OPTICAL MULTILAYERS
WITH
DIAMOND-LIKE THIN FILMS

by

GLENN ANDREW CLARKE

B.Sc., Queen's University, 1988

M.A.Sc., University of British Columbia, 1990

A THESIS SUBMITTED IN PARTIAL FULFILMENT OF

THE REQUIREMENTS FOR THE DEGREE OF

DOCTOR OF PHILOSOPHY

in

THE FACULTY OF GRADUATE STUDIES

Department of Physics

We accept this thesis as conforming

to the required standard

THE UNIVERSITY OF BRITISH COLUMBIA

October 1995

In presenting this thesis in partial fulfilment of the requirements for an advanced degree at the University of British Columbia, I agree that the Library shall make it freely available for reference and study. I further agree that permission for extensive copying of this thesis for scholarly purposes may be granted by the head of my department or by his or her representatives. It is understood that copying or publication of this thesis for financial gain shall not be allowed without my written permission.

(Signature)

Department of Physics

The University of British Columbia
Vancouver, Canada

Date Oct 16/95

DE-6 (2/88)

Abstract

A series of studies were performed to aid in the development of a magnetron sputter system which would have the ability to deposit protective optical multilayers for operation in the infrared. Diamond-like carbon was to be used as the top protective layer, while germanium carbide was chosen for the underlying layers due to its tunable refractive index.

The microstructural, optical, mechanical and electrical properties of the diamond-like carbon films were investigated as a function of argon sputter gas pressure, substrate bias and reactive gas partial pressure (H_2 , O_2, and N_2). The films were characterized by spectroscopic ellipsometry, scanning and transmission microscopy, electron diffraction, resistivity and hardness measurements, along with infrared spectroscopy.

It was found that the pseudo-bandgap and IR transparency increased with an increase in the sputter gas pressure, along with a decrease in the hardness. This appeared to be, in part, due to an increase in the amount of hydrogen incorporation and the development of a polymer phase in the film matrix. It was felt that the primary source of hydrogen was outgassing from surfaces inside the vacuum deposition chamber. Increasing the substrate bias resulted in an increase in the film density only.

The optimum diamond-like films were deposited at low sputter gas pressures (1 Pa). A widening of the pseudo-bandgap was observed for an increase in the H_2 partial pressure up to a value of 0.1 Pa. The films deposited in a nitrogen/argon mix exhibited up to an order of magnitude increase in the deposition rate over the films deposited in pure argon. The optical

properties of these materials were intermediate to those for the hydrogenated and unhydrogenated films.

Germanium and carbon multilayers were deposited to determine if interdiffusion between the individual layers would result in germanium carbide. The purpose of this investigation was to attempt to overcome the limitations on the carbon alloy fraction in conventional sputter techniques due to a poisoning of the germanium target from the hydrocarbon gas. The optical and microstructural properties of the multilayers were studied as a function of pressure and substrate bias through in-situ ellipsometry. It was found that a good deal of interdiffusion occurs at higher pressures (2 Pa) but at the cost of an increase in the film porosity.

A novel control system was developed by monitoring the film growth through in-situ ellipsometry. This routine has the capability to determine both the thickness and the optical constants of the individual layers in a multilayer stack. A Fabry-Perot filter consisting of 21 quarter-wave layers was deposited with a peak transmission of 65 %. It is shown how this routine can be extended to optically absorbing materials such as carbon.

TABLE OF CONTENTS

LIST OF TABLES

LIST OF FIGURES

ACKNOWLEDGEMENTS

First I would like to thank my research supervisor, R.R. Parsons for all of his help, friendship and support over the years of my thesis. In addition I would like to thank all of the members of the lab for the help and the support they have given me, Norman Osborne for his technical expertise, Al Kleinschmidt for his excellent work on the in-situ ellipsometer and Samir Aouadi for his discussions on x-ray multilayers. In addition I would like to thank John Eldrige and Yidan Xie for the work performed on the infrared spectroscopy measurements.

I would also like to acknowledge the excellent technical services in the department. I would not have been able to able to complete this thesis otherwise.

In addition I would like to thank Brian Sullivan of the National Research Council of Canada for his helpful discussions on ellipsometry.

Finally I would like to acknowledge the financial assistance of R.R. Parsons, the University of Columbia, Microtel Pacific Research and the Science Council of British Columbia

INTRODUCTION

1.1 General

The objective of this thesis is to develop the ability to deposit protective infrared optical multilayers which employ diamond-like films for use over the wavelength range of 1 to 12 μm. Diamond-like films have a number of properties which make them suitable for this application. These properties include good IR transparency,[1] high hardness,[2] chemical inertness[3] and impermeability to moisture penetration.[4]

Diamond-like films in general are amorphous with a mixture of sp^2 (graphitic) and sp^3 (diamond) bonds and, in the majority of cases, are fabricated containing between 20% and 60% hydrogen.[5] There is, however, a growing interest in diamond-like films that have been deposited without hydrogen, since these materials are typically harder[6] and, ideally, do not posses C-H resonance absorptions in the infrared.[7] The main disadvantage of these materials is that they generally have a lower optical bandgap than the hydrogenated films, though this is not necessarily a problem for IR coatings. In addition, there is a small but growing body of literature concerning diamond-like films with nitrogen incorporation,[8,9] due to the potential very high hardness of the material.

There are a good number of current and potential applications for protective optical coatings using diamond-like films. These include protective coatings for germanium,[10] zinc sulfide,[11] and salt optics[12] in the mid infrared range, coatings for front surface aluminum mirrors,[13] and photothermal conversion of solar energy.[14] In addition, there is a wide range

of non-optical applications for diamond-like films. These include wear resistant overcoats in magnetic recording,[15] passivation layers,[16] dielectric p-n junctions,[17] and hard coatings for steel and carbide tools.[18]

In many cases, for protective optics, one also desires that the coating be anti-reflecting in order to maximize the transmission through the optical element of interest. With a single layer coating, this property can only be achieved at discrete wavelengths and when the refractive index of the film is the square root of that of the substrate.[19] As a result, multilayer films are required for general broad-band anti-reflection coatings.[20] For coatings of this nature diamond-like films can be employed as the top protective layer and other materials with different refractive indices are required for the intermediate layers.[21]

An ideal material for the intermediate layers in the infrared region is germanium carbide.[22] Germanium carbide is an alloy with a tunable refractive index from approximately 4.1 to 1.8, making it very desirable for the above application. In addition, the material is quite hard if a significant fraction of the material is carbon. As a result, GeC can also be used as thick, protective, refractive index-matched initial layer in the overall multilayer design.

Germanium carbide develops an appreciable absorption in the near-infrared which limits its range of applications if thick layers are required. However, the useful optical range of GeC overlaps with many materials which are also transparent in the visible, such as SiO_2 and Ta_2O_5, which are also fairly hard. As a result, it should be possible to find suitable intermediate materials over the entire infrared range specified.

One important requirement during the deposition process is thickness control, as the

resulting properties of the optical coating are dependent upon the thickness of the individual layers.[20] In addition, for materials such as carbon and germanium carbide, one may also be required to monitor the refractive index, as this factor is dependent upon the deposition conditions.[23]

There are a number of different methods currently in practice which are used to deposit diamond-like films. These methods are outlined in the next section along with a brief history of the development of diamond-like films.

1.2 History and State of the Art of Diamond-like Films

The current interest in diamond-like films has evolved out of efforts to deposit diamond films at low pressures.[24,25] In a typical deposition procedure for diamond, a hydrocarbon gas is dissociated either through a hot filament[26] or through a high frequency plasma discharge.[27] The carbon atoms then condense onto the substrate, which is usually kept at a temperature on the order of 800° C. The presence of hydrogen is thought to etch away the graphitic phases causing the resulting material to be predominately diamond.[28]

Though thin films of diamond would appear to be ideal for optical applications there are a number of drawbacks to the material in its present form. One problem is that diamond can only be deposited at relatively high substrate temperatures, effectively eliminating a wide range of potential applications. Another problem is that, currently, the material is polycrystalline with surfaces too rough for optical applications. As a result there has been a good deal of interest in the ability to grow diamond-like films as these can be deposited at

relatively low substrate temperatures and with very smooth surfaces.

The first case of diamond-like films in the literature was reported by Aisenberg and Chabot.[29] In their technique, diamond-like films were deposited from a beam of carbon ions. Work of this nature was continued by Spencer *et al.* [30] throughout the seventies. An important advancement in the field was the development of the r.f. self-bias method by Holland,[31] which at present is the most widely used deposition technique for diamond-like carbon. This method and a number of others currently in practice are outlined below.

- R.F. self bias/Chemical vapour deposition method[21, 32]

  In this method, an r.f. glow discharge is sustained in a mixed argon / hydrocarbon gas. Typical hydrocarbons used in this technique are methane, ethane, butane, propane and benzene. In the r.f. discharge, the hydrocarbons are partially ionized and cracked, which results in the positively charged particles being accelerated towards the r.f. biased substrate. The resultant film properties depend upon the deposition pressure and the substrate bias. A number of variations of this method exist including a dc process which is more applicable for scale-up.[3]

- Ion Beam plating[33, 34]

  In this technique, electrons which are emitted from a hot tungsten cathode are accelerated through an anode grid with energies up to 200 eV. The electrons then enter the deposition chamber where they ionize hydrocarbon gas molecules through collisions; creating a plasma. The positively charged ions within the ion sheath region are then accelerated towards the negatively biased substrate, and form a carbon film.

- Arc Deposition[35, 36]

  In this method, the carbon film is deposited by the condensation of a highly ionized carbon plasma (70%) onto a substrate. The energy of the depositing ions are typically on the order of several tens of electron volts. The plasma is created through an arc discharge between a cathode and an anode, both of which are made of carbon. A current problem with this technique is the inclusion of graphitic macroparticles in the film. One potential solution to this problem is a magnetic filter which separates the ions from the feedstock material.

- Laser Ablation[37, 38]

  A typical laser ablation system[39] operates as following. A Nd-YAG laser delivers 250-1400 mJ to a graphitic feedstock in a ultrahigh vacuum system at 10 Hz. The beam is focused to ensure a high intensity at the target surface. As a result an intense, highly ionized, plasma is formed. The substrate is placed so it is exposed to the plasma to allow for the deposition of a film. This procedure has the problem of unwanted graphitic particles in the film.

- Magnetron Sputtering [12, 40]

  In the sputter process, a negatively biased carbon target in a plasma discharge is bombarded by positive ions. This results in the ejection of both carbon atoms and plasma sustaining secondary electrons. The sputtered carbon atoms then condense onto a substrate, creating a film. Though the deposition rate is low in this technique, large industrial scale-ups are relatively straightforward. In addition, a wide range of materials

are readily sputtered, making the method suitable for multilayer deposition. For example, magnetron sputtering is the only technique which is used to deposit hard carbon overcoats for magnetic recording applications.[41]

1.3 Deposition Technique

The method chosen to deposit the optical multilayers in this thesis was magnetron sputtering.[42] As described above, this technique is highly versatile allowing for the deposition of a wide range of materials. Therefore, for optical multilayers, one can deposit all of the required materials through the one method. In addition, films deposited through magnetron sputtering exhibit excellent film uniformity, smooth surfaces, good adhesion and near bulk-like properties; all which are of importance for optical coatings. Also, development work performed on a small research-size system can be readily extended to large scale production processes.

1.4 Goals of the Thesis

There are essentially three goals in this thesis. The first is the determination of the optimum conditions for the deposition of magnetron sputtered diamond-like carbon for infrared optical coatings. At present, these conditions cannot be determined from the literature.

The processes investigated in this thesis are intended to be directly applicable to industry and allow for the deposition on as wide a range of substrates as possible. Therefore,

only dc sputtering is examined to allow for a large degree of scale-up. In addition, no heating or cooling of the substrate is to be applied. The deposition parameters to be varied are the substrate bias, sputter gas pressure and the partial pressures of the reactive gases.

The second goal of the thesis is to develop a method of depositing germanium carbide through magnetron sputtering over the entire refractive index range of 4.1 to 1.8, which is currently limited from 4.1 to 3 due to poisoning of the target.[43]

The final goal of the thesis is to develop a control system for optical multilayers which can determine both the thickness of the individual layers and their corresponding optical constants. This control routine is intended to be applicable for both absorbing and non-absorbing materials.

1.5 Characterization Methods.

There are three main characterization methods used in the course of this thesis. These techniques are spectroscopic ex-situ ellipsometry, single wavelength in-situ ellipsometry and infrared spectroscopy.

Spectroscopic ellipsometry[44] is an ambient, non destructive optical technique which allows for the analysis of such thin film microstructural properties as surface roughness,[45] voids,[46] phase fractions,[47] and intermediate layers.[48] In addition, for high quality films, the technique can also determine such intrinsic properties as optical constants[49] and band-gaps.[50] The optical range of the ellipsometer used in this thesis is 1.5 to 6 eV.

In single wavelength in-situ ellipsometry, the film properties are measured as a function of layer thickness, rather than photon energy. Measurements of this nature can determine such factors as layer interdiffusion,[51] film inhomogeneities and roughness evolution,[52] as well as the optical constants at the monitoring wavelength.[53] In addition, the thickness of the film can be determined for control purposes.[54]

Infrared spectroscopy can be used to provide a chemical analysis of the thin film of interest through an examination of the molecular bond vibrations.[55] This factor is useful in determining the presence and nature of the hydrogen and nitrogen incorporation. In addition, this technique can solve for the optical constants in the infrared, allowing for a determination of the technical feasibility of the material.

Additional characterization methods used during the course of this thesis were scanning and transmission electron microscopy, electron diffraction, hardness and resistivity methods, as well as reflection/transmission measurements in the visible/UV. These techniques are discussed in greater detail in the later chapters.

1.6 Chapter Organization

The thesis is divided into seven chapters. Chapter 1 is an introduction to the thesis topic. Chapter 2 outlines the necessary optical theory required for the subsequent analysis in later chapters. The purpose of the third chapter is two-fold. The first purpose is to describe the main instrumentation used during the course of the thesis. The second is to discuss the accompanying analytical techniques.

The experimental results along with the accompanying analysis and discussion are given in the fourth, fifth and sixth chapters. Chapter 4 deals with the diamond-like films. Amorphous carbon films (a-C) and amorphous carbon films containing hydrogen (a-C:H) and/or nitrogen (a-C:N) are all examined and compared in terms of their feasibility for optical coatings. Chapter 5 looks at a novel approach in depositing germanium carbide and compares this technique with more conventional methods. A control routine for the deposition of optical multilayers is developed in chapter 6 using in-situ ellipsometry. The routines are initially developed for dielectric films and are then extended to allow for those which exhibit absorption.

Chapter 7 concludes the thesis.

OPTICAL THEORY

2.1 Introduction

The purpose of this chapter is to provide the basic optical theory required in the remainder of the thesis. When necessary, the theory presented here is developed in greater detail in the later chapters. Three main topics are discussed. The first is the concept of optical polarization. A number of representations are given including the Jones calculus. The second topic deals with the calculation of the reflection and transmission properties of single and multilayer films. It is shown how the process can be simplified through the use of a matrix method. Finally, some practical configurations for optical coatings are presented.

2.2 Optical Polarization

For a monochromatic plane wave traveling in free space the electric field can be written as

$$E(r,t) = \mathrm{Re}\left(\tilde{E}\, e^{i(kz-\omega t)}\right), \tag{2.1}$$

where k is the wavevector, ω the angular frequency and $\tilde{E}$ the complex field vector. For the remainder of the thesis the complex notation is used and it is implicitly assumed that the real part is to be taken. As the electric field vector under the above condition is transverse, $\tilde{E}$ can be represented by two components along the x and y axis

$$\tilde{E}_x = E_x\, e^{-i\phi_x}\hat{x}, \tag{2.2a}$$

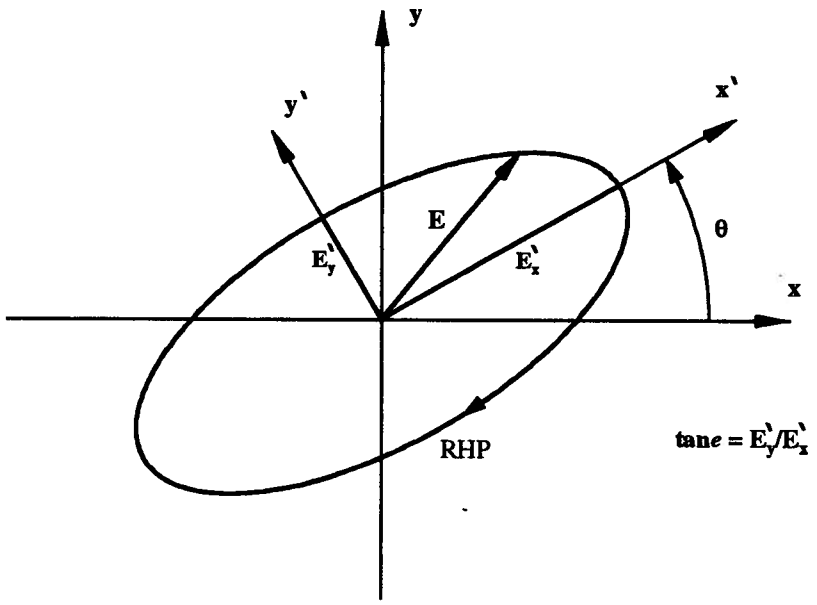

Figure 2.1 Polarization ellipse for light propagating in the z direction. The field vector is right-handed polarized.

$$\tilde{E}_y = E_y \, e^{-i\phi_y} \hat{y}, \tag{2.2b}$$

where E_x , E_y are the amplitudes and ϕ_x , ϕ_y are the phases of the field vectors. The relationship between the amplitudes and the phases of the two field vectors is referred to as the polarization of the light (defined below).

The solution of Eq. 2.1 for a fixed value of z shows that the tip of the electric field vector sweeps out an ellipse in the x-y plane at a radial frequency ω. This effect is illustrated in Fig. 2.1. The rotational direction of the field vector is referred to as the handedness of the light. The light is defined to be right-hand polarized if the electric field vector rotates in the

clockwise direction looking into the source, and left-hand polarized if it rotates in the opposite direction.

A convenient form for defining the polarization, χ, of the electric field vector is through the ratio between the complex amplitudes

$$\chi = (E_y / E_x)\, e^{i(\phi_y - \phi_x)} . \tag{2.3}$$

Hence the polarization is represented by a single complex number. One can then determine the form of the ellipse in Fig. 2.1 through the relation

$$\chi = \frac{\tan\theta + i \tan e}{1 - i \tan\theta \cdot \tan e}, \tag{2.4}$$

where θ is the angle between the major axis (x') of the polarization ellipse and the reference x- axis; and ellipticity, *tane*, is the ratio of the minor/major axis. The term, e, is referred to as the ellipticity angle.

There are two important forms of the polarization. For the case where the field vectors are in phase, χ is real and the light is linearly polarized. For the case where $\chi = \pm i$ the light is circularly polarized. A positive or negative sign before the i determines whether the polarization is left-handed or right-handed respectively. This condition also holds for elliptically polarized light.

Another representation for the polarization is through a Jones vector,[56] J, where

$$J = \begin{bmatrix} \tilde{E}_x \\ \tilde{E}_y \end{bmatrix} \tag{2.5}$$

In this notation the vectors are normalized so that

$$J^* \cdot J = 1. \tag{2.6}$$

As the vector space is two dimensional, it can be represented through a choice of two orthogonal vectors. All forms of the polarization can then be written as a combination of these two vectors. The two most common representations are light linearly polarized along the x and y-axis where

$$J_x = \begin{bmatrix} 1 \\ 0 \end{bmatrix}, \quad J_y = \begin{bmatrix} 0 \\ 1 \end{bmatrix}, \tag{2.7}$$

and left-handed and right-handed circularly polarized light where

$$J_L = \frac{1}{\sqrt{2}} \begin{bmatrix} 1 \\ i \end{bmatrix}, \quad J_R = \frac{1}{\sqrt{2}} \begin{bmatrix} 1 \\ -i \end{bmatrix}. \tag{2.8}$$

One other advantage of the Jones representation is that the individual optical elements of a system can be represented through a 2×2 matrix.[57] If the effects of reflection off the individual components is ignored, then the sum effect of N optical elements in series on the output polarization can be determined through the relation

$$J_{out} = (C_N \ldots C_2 C_1) J_{in} = (T) J_{in} = \begin{bmatrix} T_{11} & T_{12} \\ T_{21} & T_{22} \end{bmatrix} \begin{bmatrix} J_1 \\ J_2 \end{bmatrix}_{in}, \tag{2.9}$$

where C is the Jones matrix of an individual component and T the product matrix. The output polarization can be written in complex number form through the bilinear transformation[58]

$$\chi_o = \frac{T_{22}\chi_i + T_{21}}{T_{12}\chi_i + T_{11}}. \tag{2.10}$$

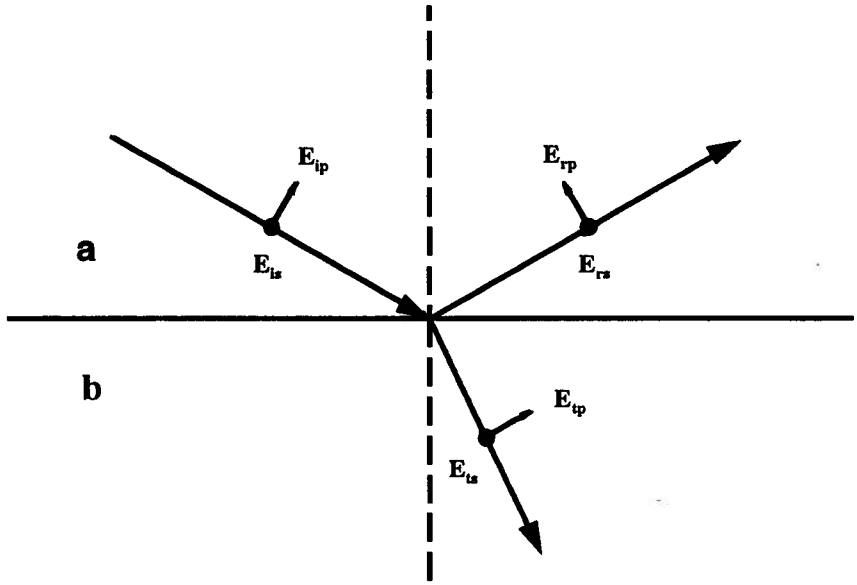

Figure 2.2 Reflection and transmission at an interface between two media *a* and *b*. Both the *p* and *s* polarizations are shown. The dashed line represents the normal to the interface.

2.3 Reflection and transmission

Fig 2.2 shows the reflection and transmission of light at an interface between two media, *a* and *b*. In this system, the orthonormal vectors for the electric field are chosen to be linearly polarized along the *p* (parallel to plane of incidence) axis and along the *s* (perpendicular to the plane of incidence) axis. The polarization of the individual rays can then be represented through the notation

$$\chi = (E_p / E_s)\, e^{i(\phi_p - \phi_s)}, \tag{2.11}$$

or alternatively through the vectors in Eq. 2.7, if the subscripts *s* and *p* are substituted for *x* and *y*.

The reflectance and transmittance at an interface for an electromagnetic wave is determined through the consideration of the boundary conditions for the tangential components of the electric and magnetic field vectors.[59] In a non-magnetic medium the magnetic field vector $\tilde{H}$ is related to the electric field vector through the relation

$$\tilde{H} = \sqrt{\varepsilon} \cdot \sqrt{\varepsilon_0 / \mu_0}\ \hat{s} \times \tilde{E} = \tilde{N} \cdot \sqrt{\varepsilon_0 / \mu_0}\ \hat{s} \times \tilde{E}, \tag{2.12}$$

where $\hat{s}$ denotes a unit vector in the direction of propagation, ε_0 and μ_0 are the permittivity and the permeability of free space respectively, and ε is the dielectric function where the conductivity of the medium has been included. Equation 2.12 also includes a term, $\tilde{N}$, the complex refractive index where

$$\tilde{N} = \sqrt{\varepsilon} = n + ik \tag{2.13}$$

where n is the refractive index and k is the attenuation constant. In the remainder of the thesis the term "complex refractive index" will be denoted by $\tilde{N}$, and n will be referred to as the refractive index.

Consideration of the boundary conditions for the electric and magnetic fields gives the values for the reflectance coefficients, r_p and r_s for p and s polarized light respectively through the relations

$$r_s = \frac{\tilde{N}_a \cos\phi_a - \tilde{N}_b \cos\phi_b}{\tilde{N}_a \cos\phi_a + \tilde{N}_b \cos\phi_b}, \tag{2.14a}$$

$$r_p = \frac{\tilde{N}_a \cos\phi_b - \tilde{N}_b \cos\phi_a}{\tilde{N}_a \cos\phi_b + \tilde{N}_b \cos\phi_a}, \tag{2.14b}$$

where ϕ is the angle of incidence of the propagation vector from the normal. The value of ϕ_i, where i is the film index, is determined through the consideration of the phase relationships at the boundary or equivalently through Snell's law

$$\tilde{N}_o \sin\phi_o = \tilde{N}_i \sin\phi_i \,, \tag{2.15}$$

where the subscript o represents the ambient medium. As the two reflection coefficients are for orthogonal components, the above relations can be used for any polarization.

An important factor in optics is the ratio between r_p and r_s. To demonstrate this, consider the calculation of the polarization of the reflected beam through the Jones matrix

$$\begin{bmatrix} E_p \\ E_s \end{bmatrix}_r = \begin{bmatrix} r_p & 0 \\ 0 & r_s \end{bmatrix} \begin{bmatrix} E_p \\ E_s \end{bmatrix}_i , \tag{2.16}$$

or alternatively though Eq. 2.10

$$\chi_o = (r_p / r_s)\chi_i . \tag{2.17}$$

This ratio is referred to as the complex reflectance ratio, ρ, and is given by

$$\rho = r_p / r_s = \rho_r + i\rho_i = \tan\psi \, e^{i i\Delta} , \tag{2.18}$$

where $tan\psi$ is the relative amplitude attenuation and Δ the phase difference of the polarization upon reflection from an interface. Hence, the value of ρ acts as a transfer function between the input and output polarizations.

The derivation of the reflection and transmission coefficients for a thin film system is complicated by interference effects between the individual layers. However, consideration of the boundary conditions at each film interface allows for the system to be analyzed as a series of matrices. In this method, each interface is represented through a reflection matrix ,U, where

$$U_{ab} = \frac{1}{t_{ab}} \begin{bmatrix} 1 & r_{ab} \\ r_{ab} & 1 \end{bmatrix}. \tag{2.19}$$

where $t = 1 - r$ is the transmission coefficient. In addition, a phase matrix, P, is used to describe the propagation through a film , f, by

$$P_f = \begin{bmatrix} e^{-i\beta_f d} & 0 \\ 0 & e^{i\beta_f d} \end{bmatrix}, \tag{2.20}$$

where

$$\beta_f = (2\pi/\lambda) \cdot \sqrt{(\tilde{N}_f^2 - n_o^2 \sin^2 \phi_0)}, \tag{2.21}$$

where λ is the wavelength of interest. For a N-layer system, the electric field components at the input and output of the system are then related through the relation

$$\begin{bmatrix} E_{1i} \\ E_{1r} \end{bmatrix} = U_{01} P_1 U_{12} P_2 \ldots P_N U_{N,N+1} \begin{bmatrix} E_{N+1,i} \\ E_{N+1,r} \end{bmatrix} = \begin{bmatrix} m_{11} & m_{12} \\ m_{21} & m_{22} \end{bmatrix} \cdot \begin{bmatrix} E_{N+1,i} \\ E_{N+1,r} \end{bmatrix}, \tag{2.22}$$

where the subscript, $N+1$, denotes the substrate; which, in this case, is assumed to be infinitely thick. As the value of $E_{N+1,r} = 0$ under these conditions the coefficients for reflection and transmission are

$$r = \frac{m_{21}}{m_{11}}, \tag{2.23a}$$

$$t = \frac{1}{m_{11}}. \tag{2.23b}$$

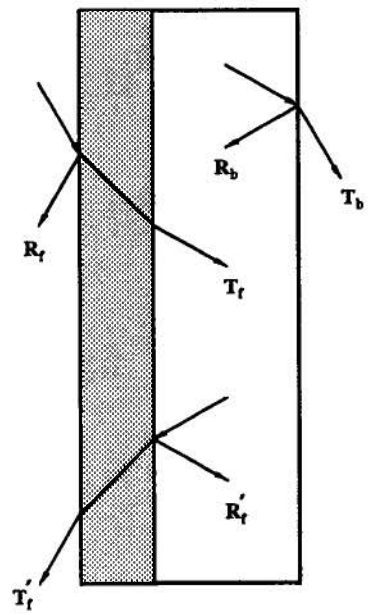

Figure 2.3 Thin film system on a thick transparent substrate. The film system is the shaded area. The reflection and transmission components are for light incident on the ambient side of the film system, light incident on the substrate side of the film system and light incident on the back face of the substrate.

The intensity of the reflected and transmitted electromagnetic radiation can then be determined through the relations

$$R = r \cdot r^* , \tag{2.24a}$$

$$T = \frac{n_s}{n_0} t \cdot t^* . \tag{2.24b}$$

The inclusion of the refractive indices in Eq. 2.24b is to compensate for the difference in the ratio between the electric and magnetic fields in the two media. It should also be noted that Eq. 2.23b is only applicable when the substrate is transparent. Hence the matrix method

outlined above can be used to determine the reflection, transmission, and the complex reflectance ratio of a thin film system.

The above derivations make the assumption of coherent interference which is usually valid for films with a thickness on the order of the wavelength of light. This assumption cannot necessarily be made when the effects of a thick transparent substrate are included in the calculation of the reflection and transmission values. In this situation it becomes necessary to average the phase change across the substrate.[60] The intensities are then given by the relations

$$R = R_f + \frac{T_f \cdot T_f' \cdot R_b}{1 - R_f' \cdot R_b}, \tag{2.25a}$$

$$T = \frac{T_f \cdot T_b}{1 - R_f' \cdot R_b}, \tag{2.25b}$$

where the terms are as shown in Fig. 2.3.

2.4 Optical Multilayers

Interference effects in thin film multilayers allow for the deposition of a wide range of passive optical devices. Three of these devices, which are of importance in this thesis, are described below. These are antireflection coatings, dielectric mirrors and Fabry-Perot bandpass filters.

One of the simplest thin film coatings is the single antireflection layer on a substrate. If we consider the substrate to be infinite, then the reflection and transmission of the system is given by the product of the matrices

$$M = U_{af} \cdot P_f \cdot U_{fs} \tag{2.26}$$

where a, f, and s denote the ambient, film, and substrate respectively. For a dielectric film on a transparent substrate, where the ambient is taken to be free space, the conditions for 100 % transmission are

$$n_f = \sqrt{n_s}\,, \tag{2.27a}$$

$$n_f d = (2m+1) \cdot \lambda_0 / 4\,, \qquad m = 0,1,2... \tag{2.27b}$$

where λ_o is the wavelength of interest, d is the film thickness, and n_f and n_s are the film and substrate refractive indices respectively.

The single layer antireflection coating has a number of drawbacks. One problem is that the range of useful wavelengths is quite narrow. Also, it is often not possible to find a coating material with the required refractive index.

The above problems can be solved through the application of a broadband multilayer antireflection coating. Coatings of this nature usually consist of 3 to 6 layers and are made up of 2 to 3 materials with different refractive indices. These systems are too numerous to describe here and the reader is referred to an excellent summary by G. F. Dobrowolski.[61] However, one of the most popular designs is given by the relations

$$n_1 d_1 = n_3 d_3 = \lambda_o/4, \quad n_2 d_2 = \lambda_o/2, \tag{2.28a}$$

$$n_3 = \sqrt{n_1 n_s}\,, \tag{2.28b}$$

$$n_1 > n_s\,, \quad n_2 > n_3\,, \tag{2.28c}$$

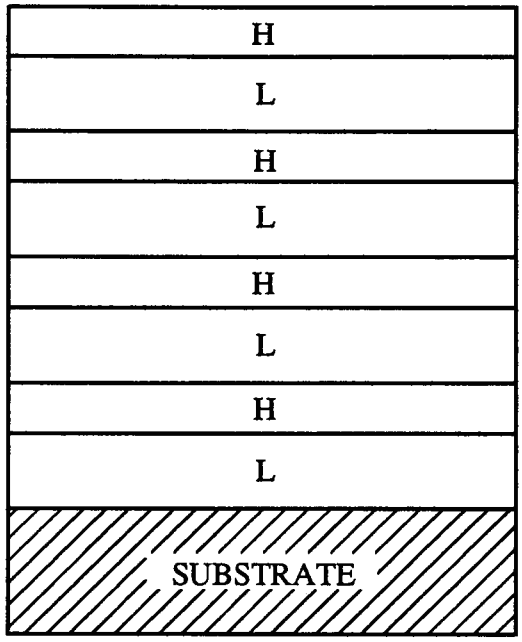

Figure 2.4 Quarter-wave stack of low and high index of refraction materials on a substrate. The low index of refraction layers are physically thicker in order to achieve the same optical thickness as the high index of refraction material. If the substrate is also of a low refractive index, often an additional high index of refraction layer is sandwiched between the substrate and the displayed stack.

where n_1, n_2, n_3, denote the refractive indices of the topmost, second and third layers respectively and n_s is the refractive index of the substrate. The above equations illustrate the need for films with different refractive indices when depositing antireflecting coatings.

At the other extreme, to achieve high reflectance values a dielectric mirror, or "quarter-wave stack" is typically used. This multilayer system consists of alternating layers of two materials with high and low refractive indices (Fig 2.4), each a quarter-wave thick ($nd = \lambda/4$). Under these conditions, the reflected waves off each interface interfere constructively leading to very high reflectivities, typically higher than those which can be achieved with metal films.

For a multilayer of x high and x low layers the reflectance at the wavelength of interest is given by

$$R = \left[\frac{n_a - \dfrac{n_H^{2x}}{n_L^{2x-2} n_{sub}}}{n_a + \dfrac{n_H^{2x}}{n_L^{2x-2} n_{sub}}} \right]^2 , \tag{2.29}$$

where n_L and n_H are the refractive indices of the low and high medium respectively. The effective wavelength range may be derived from

$$\frac{\lambda_0}{\Delta\lambda} = \frac{2}{\pi} \sin^{-1} \left[\frac{n_H - n_L}{n_H + n_L} \right] . \tag{2.30}$$

Hence, theoretically one can achieve as high a reflectance as desired, though the useful range is limited by the contrast between the refractive indices. Outside of this region the intensity drops off rapidly and there is a series of small maxima, called side bands.

The half-wave thickness, $\lambda/2$, is also important in the design of optical filters. From an examination of Eq. 2.22, the phase matrix becomes equal to -1 under this condition. Hence the deposition of a half-wave layer has the effect of reversing the sign of the reflection coefficient of the underlying multilayer. This effect allows for the deposition of a Fabry-Perot filter. In this device, a half-wave layer is sandwiched between two identical quarter-wave stacks. Hence the reflection from one stack will be 180° out of phase with the other and the two mirrors will interfere destructively. This leads to a high transmission at the wavelength of interest. Away from the primary wavelength, the two dielectric mirrors are no longer 180° out of phase and the transmission drops off rapidly.

3. INSTRUMENTATION AND ANALYTICAL TECHNIQUES

3.1 Introduction

The purpose of this chapter is two-fold. The first is to provide a description of magnetron sputtering. Both the instrumentation and the mechanics of sputtering are discussed. This technique is described in some detail as a thorough understanding is required for the subsequent analysis in later chapters.

The second part of the chapter describes the main instrumentation used to characterize the films and the accompanying analytical techniques. The most important technique discussed is that of ellipsometry. Two types of ellipsometers are described. The first is a high precision spectroscopic ex-situ ellipsometer. The second is a single wavelength in-situ ellipsometer capable of real time measurements. The corresponding methods for data analysis are then investigated. The chapter ends with a discussion of infrared spectroscopy.

3.2 Magnetron Sputtering

3.2.1 Deposition Mechanisms

Magnetron sputtering is the sole deposition technique used in this thesis. The sputter process is essentially one of momentum transfer whereby the material of interest for deposition, or target, is bombarded by energetic ions. This bombardment causes the ejection of target atoms, a portion of which condense onto a substrate, resulting in a film.

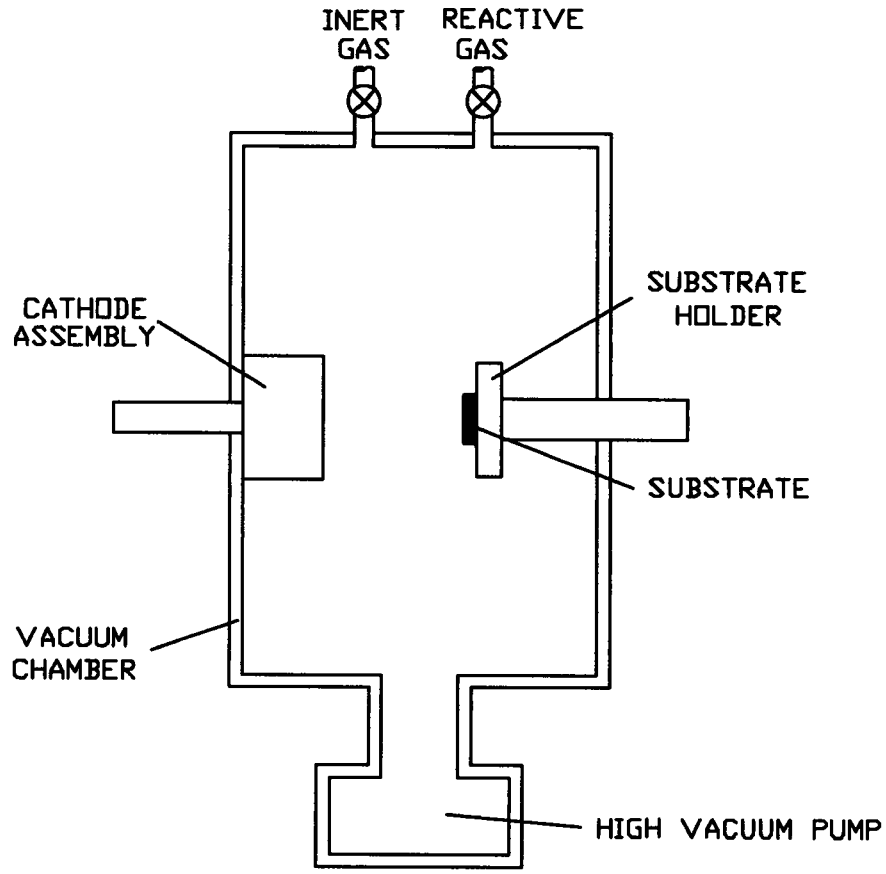

Figure 3.1 Schematic of a magnetron sputtering system. The cathode assembly is shown in greater detail in Fig. 3.2.

A schematic of the deposition chamber is shown in Fig. 3.1 and a more detailed drawing of the cathode assembly in Fig. 3.2. During the deposition process the vacuum chamber is initially pumped with a roughing pump from atmospheric pressure to approximately 3 Pa, then taken down to a pressure of approximately 1×10^{-4} Pa through diffusion pumping. The diffusion pump is aided by a liquid nitrogen cold trap which freezes out the water vapour. An inert gas, usually argon, is then introduced to raise the pressure to 0.5 to 8 Pa. Reactive gases such as nitrogen, oxygen or hydrogen can also be supplied, allowing for the deposition of

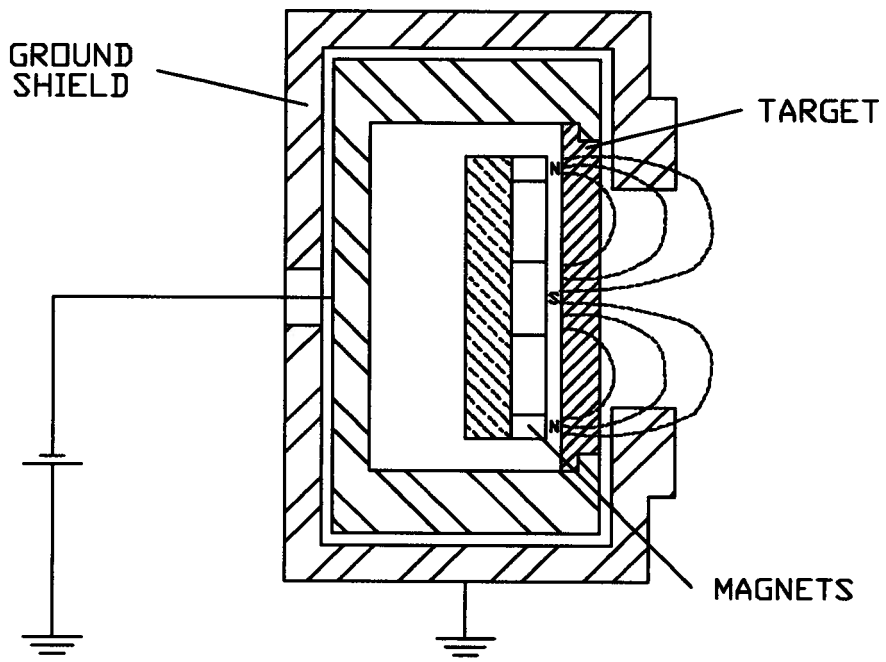

Figure 3.2 Schematic of the cathode assembly of the magnetron system, which also shows the magnetic field lines. Also included is the electrical biasing.

a film of a different chemical composition than the target.[62] After the gas is at the desired pressure, a negative potential is applied to the target while the chamber and part of the target assembly are grounded, creating a plasma discharge. Positive ions in the plasma bombard the target surface, resulting in the ejection of both neutral atoms and secondary electrons, as well as other species such as negative ions and reflected neutrals. A portion of the ejected target atoms condense onto the substrate, typically located at a distance of 4 to 10 cm from the target, producing a film.

An important factor in the sputtering process is sustaining the plasma discharge. In order to achieve this, the loss of ion-electron pairs needs to be overcome. This loss results

from ion-electron recombination on the chamber walls, ion neutralization on the target, and electron loss through the grounded surfaces.

The loss of ion-electron pairs can be overcome through the emission of secondary electrons during the process of ion bombardment of the target. The secondary electrons are initially accelerated away from the target surface and gain kinetic energy through the applied electric field. The electrons undergo collisions with the gas atoms, which often involve excitation and/or ionization. The newly created ions, in turn, bombard the target surface producing more secondary electrons, making the process self-sustaining.

The efficiency of the above process is aided by the application of a magnetic field parallel to the target surface. Under these conditions the electrons are initially accelerated away from the surface, but are forced back towards the target by the Lorentz force. In addition, the electrons undergo cycloidal motion with a drift velocity in a direction perpendicular to both the electric and the magnetic field ($\vec{E} \times \vec{B}$).

For the magnetron assembly shown in Fig. 3.2, the field source consists of an annular and centre magnet mounted on a high permeability pole piece. As the outer magnet completely surrounds the inner magnet, the $\vec{E} \times \vec{B}$ drift has a closed path. This traps the electrons close to the target surface and increases their effective path length. This mechanism leads to a sufficient ionization to sustain the discharge and also contains the plasma to within the vicinity of the target.

Ideally all of the magnet field lines originating on the annular magnet should return to the centre magnet in order to maximize the electron trap (Fig. 3.2). This configuration is

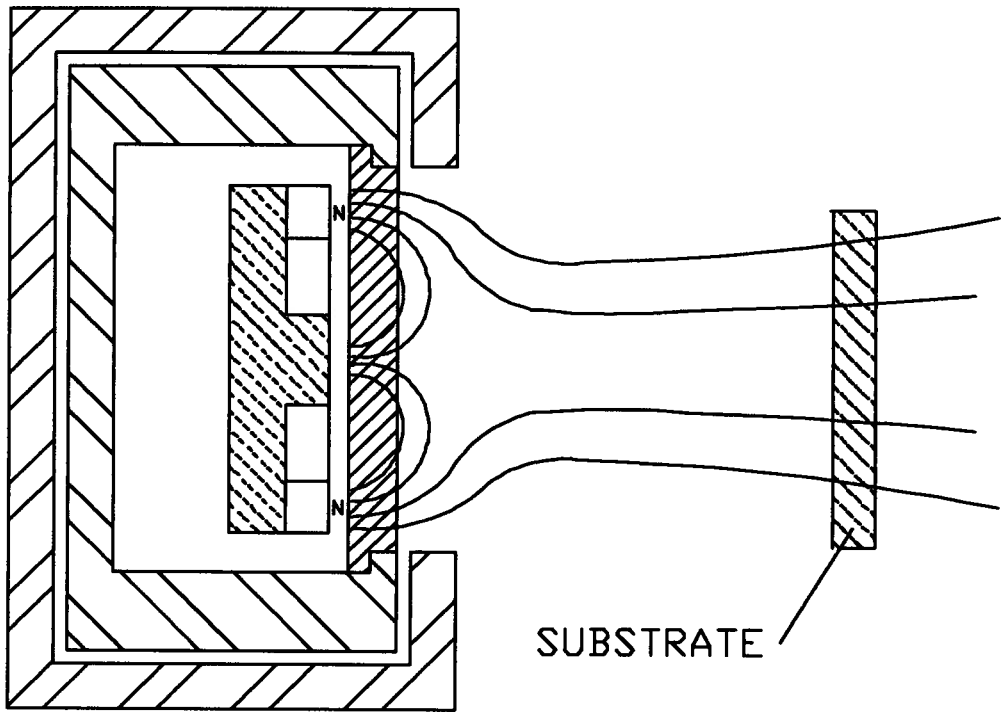

Figure 3.3 Schematic of a cathode assembly with an unbalanced magnetron. Note that the first surface that intersects the field lines is the substrate.

referred to as a balanced magnetron. Balanced magnetics are not possible in practice for a planar magnetron due to fringing effects, though this effect can be approximated by equalizing the strength of the centre and annular magnets.

A different type of plasma discharge results if the annular magnet is made much stronger and/or with a larger area than the centre magnet (Fig. 3.3). The magnetron configuration described above is referred to as an unbalanced magnetron. Under these conditions, a large portion of the field lines intercept the substrate. As a result, the substrate can undergo a significant electron and ion bombardment.[63] The electron flux is usually of a

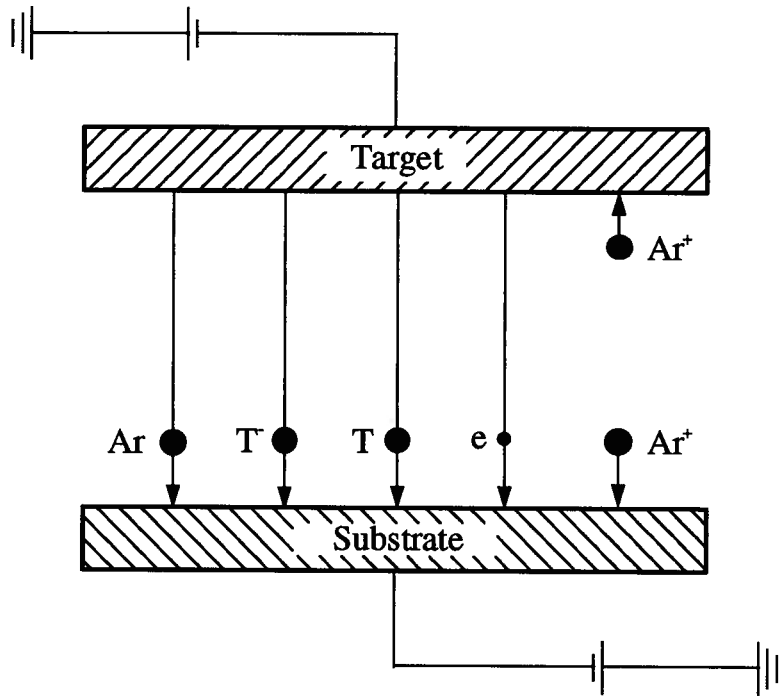

Figure 3.4 Main species at the target and substrate. The lines show the origins of the species. The species shown are the reflected neutrals (Ar), negative target ions (T^-), target atoms (T), electrons (e) and positive ions (Ar^+).

low energy and, therefore, can be repelled by applying a small negative bias (–10 to –35 V) to the substrate. Therefore one can control the density of the plasma in the vicinity of the substrate through a proper design of the magnetic assembly.

Fig. 3.4 shows the main species at the target and at the substrate. The two main bombarding species at the substrate are the reflected neutrals and the plasma ions. The prospect of negative ions is ignored as these are unlikely in the case for carbon. The reflected neutrals originate at the target and can bombard the growing film with energies up to the target voltage (300 to 600 eV). The positive ions originate in the plasma in the vicinity of the

substrate and travel on average a distance equal to the Debye length,[64] typically on the order of a few millimeters. These ions bombard the substrate with an energy equal to difference in voltage between the plasma and the substrate. As previously mentioned, the ion current can be controlled through proper magnetron design.

Energetic particle bombardment can be desirable under the proper conditions as it can enhance the quality of the deposited films. To understand this, it necessary to understand the various growth mechanisms of thin films, which are explained in the next section.

3.2.2 Energetic Particle Bombardment

Films that are deposited under conditions where the growth temperature is less than about 30% of the melting point of the bulk material have what is referred to as a zone-1 microstructure.[65] At these temperatures the film initially grows around preferred nucleation sites located at areas of substrate inhomogeneities and roughness. Atoms reaching these sites are initially loosely bound to the film lattice and are referred to as adatoms. The mobility of the adatoms is low under the above conditions and they will not be able to travel between the nucleation sites. As the nucleation sites grow in size they will prevent further depositing atoms from reaching the substrate through shadowing effects. Hence the microstructure is characterised by long columns separated by significant voids. The resulting film has a large surface roughness and properties that are quite unlike that of the bulk material and is often unsuitable for many applications. A zone-1 microstructure results in poor quality optical coatings as the refractive index can change under different atmospheric conditions due to moisture penetration. [66]

Different microstructures result at higher deposition temperatures. For temperatures between 30 and 50% of the melting point, the mobility of the adatoms increases to the point where they can undergo significant diffusion on the grain boundaries. The film microstructure then consists of columnar grains separated by intercrystalline boundaries and is referred to as zone-2. For substrate temperatures above 50% of melting point of the deposited material the result is a zone-3 microstructure where diffusion within the grains leads to a film characterized by equiaxed grains.

Though films with a zone-2 or zone-3 microstructure have desirable properties for a number of applications, the deposition conditions required often makes this method of film growth impractical, especially if the substrate has a melting point lower than that of the film or can be damaged at high temperatures. Also polycrystalline films often make poor optical films due to light scattering at the grain boundaries. Fortunately, high quality optical films can be grown at ambient temperatures if the substrate is subjected to particle bombardment during the deposition process. The bombarding particles, either the ions or energetic neutrals, will both impart energy into the growing film, increasing the adatom mobility, and forward sputter the film material. The above processes result in a microstructure consisting of densely packed fibrous grains. This microstructure, referred to as zone-T, results in films with smooth surfaces, high densities and properties close to that of the bulk values.

Energetic particle bombardment can also affect the film properties through changing the chemical composition of the film,[67] either through preferential sputtering of the different types of atoms, or by altering the bonding configuration of the individual atoms. Both of these effects are

important in the deposition of diamond-like films. The first effect alters the film properties when a dopant gas is added during the film deposition. The second effect is of importance as ion bombardment is thought to alter the sp^3/sp^2 bond ratio.[68]

In conclusion magnetron sputtering is a versatile technique capable of depositing a wide range of materials. However, the nature and resulting quality of the films is highly dependant upon the deposition conditions.

3.3 Ellipsometry

3.3.1 Introduction

Ellipsometry is a technique whereby the change in polarization is measured upon reflection from a sample.[44] This allows for a determination of the complex reflectance ratio ρ (section 2.3). As ρ is dependent upon both the individual layer thicknesses and the optical constants, measurements of this kind can be used to determine such parameters as film thickness, porosity, and surface roughness; i.e. discriminate between zone-1 and zone-T films (section 3.2.2). Ellipsometric measurements can also solve for the dielectric function of individual films. Hence ellipsometry can provide both microstructural analysis and information about the optical bandstructure.

Two ellipsometers were used in the course of this thesis. The first was a spectroscopic ex-situ ellipsometer used to analyze the samples upon removal from the deposition chamber.

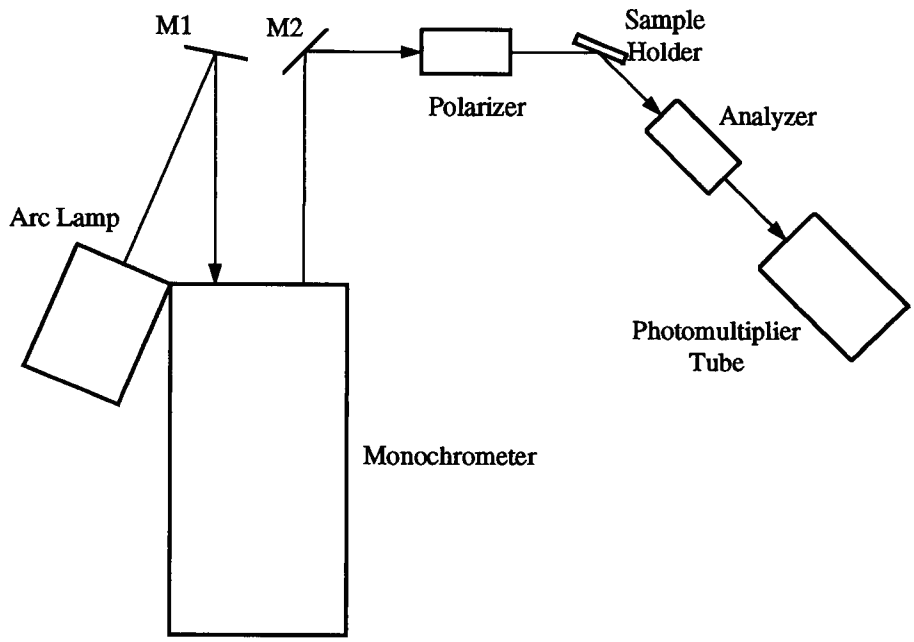

Figure 3.5 Schematic of the spectroscopic ex situ ellipsometer used in this thesis.

The second was a single wavelength in-situ ellipsometer which collected measurements as the films were being deposited.

The remainder of the section describes the two ellipsometers in some detail then discusses the methods used to analyze the data. The analytical methods discussed are limited to those used for the ex-situ measurements as these are by far the most general. The techniques used to analyze the in-situ data are quite specific and are discussed in the relevant sections in chapters 5 and 6.

3.3.2 Ex-situ Ellipsometer

A rotating analyzer ellipsometer with a spectroscopic range from 1.5 to 6 eV was used during the course of this thesis. This instrument was designed and built by Brian Sullivan as part of his Ph.D. thesis.[69]

A block diagram of the ex-situ ellipsometer is presented in Fig. 3.5. A 75 Watt xenon arc lamp is used for the light source. A concave mirror is used to focus the image of the arc lamp onto the entrance slit of the double prism monochrometer which, in turn, selects the desired wavelength. The bandwidth of the monochrometer is proportional to the slit width and is usually on the order of 3 nm. Upon exit from the monochrometer the mirror system, *M2*, focuses the image of the exit slit onto the sample. A rochon polarizer, capable of .005 ° steps, linearly polarizes the light at a selected angle from the *p*-axis of the sample. A vacuum chuck, capable of .02 ° rotational steps, is used to hold the sample. The analyzing stage consists of a rotating rochon polarizer (or analyzer) followed by a photomultiplier tube. Once the data are collected, a discrete Fourier transform is performed at twice the frequency of revolution. The ellipticity of the light incident on the face of the analyzer can then be evaluated from the second harmonics. As the incident polarization, *P*, on the sample is known, the value of ρ can then be determined through the relations[70]

$$\tan\psi \cdot \left|\cot(P)\right| = \left[(1+a_2)/(1-a_2)\right]^{1/2}, \qquad \textbf{(3.1a)}$$

$$\cos\Delta = b_2\left(1-a_2^2\right)^{-1/2}, \qquad \textbf{(3.1b)}$$

where a_2 and b_2 are second cosine and sine harmonics respectively. The error in the second harmonics can be reduced through signal averaging over a number of cycles of the rotating analyzer. It should be noted that the handedness of the light can not be determined through this configuration as one solves for $cos\Delta$ rather than Δ.

Though ellipsometry is a very powerful analytical technique, it is quite sensitive to relatively small amounts of misalignment and miscalibration.[71] To compensate for this factor, the ex-situ ellipsometer can be aligned and calibrated to a high degree of accuracy through a number of automatic routines. After each calibration, measurements are made on a Si substrate which has also been measured at AT &T labs by D.E. Aspnes. The disagreement in complex reflectance ratio is typically on the order of 10^{-3}. This amount corresponds to approximately a 1 Angstrom difference in the oxide thickness on a silicon substrate.

3.3.3 In-situ Ellipsometer

In-situ ellipsometry measures the complex reflectance ratio as a function of thickness during the growth of a film. This technique has been used for the control of x-ray multilayers,[72] the determination of chemical composition in quantum well devices,[73] interface analysis[74] , process control,[75] and the spectroscopic investigation of diamond films.[76] An in-situ ellipsometer was designed and built during the course of this thesis through a collaboration with A. Kleindschmidt as part of his Masters Thesis.[77] This author's role was to aid in the initial basic design and help develop the alignment and calibration routines.

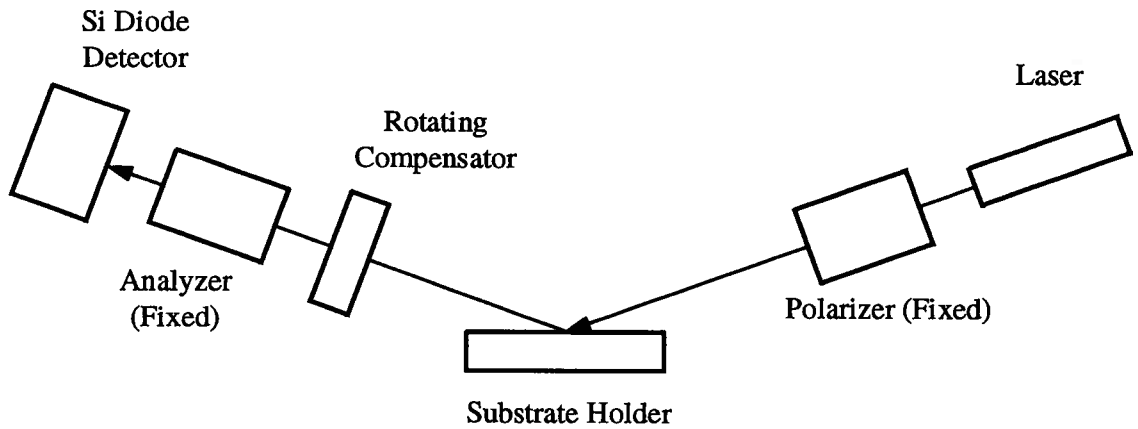

Figure 3.6 Schematic of the in-situ ellipsometer used in the course of this thesis.

The ellipsometric configuration decided upon was a single wavelength rotating compensator ellipsometer (RCE). An outline of the instrumentation is given in Fig. 3.6. A HeNe laser is used for the light source. A laser has the dual advantage over an arc lamp through eliminating the need for a monochrometer and being relatively easy to align. The main disadvantage of this configuration is the loss of spectroscopic information. However, it now possible to analyze the film properties as a function of thickness.

The laser light is linearly polarized through a Glan Taylor polarizer capable of 0.1° steps. The sample stage is mounted onto three adjustable feed-throughs on the back of the deposition chamber. The analyzer optics consist of a rotating compensator (quarter-wave at 632.8 nm) and an analyzer module identical to that of the polarizer. The resultant beam

intensity is measured by a silicon photodetector. An optical filter is placed in front of the detector in order to eliminate the background radiation from the plasma discharge. The measured signal is then Fourier transformed to give both the second and fourth harmonics.

The rotating compensator ellipsometer possesses a number of advantages over the rotating analyzer configuration. The first is the ability of the RCE to determine the handedness of the polarization upon reflection from a sample. This ability is crucial when analyzing optical multilayers as the complex reflectance ratio can lie in all four quadrants of the complex plane. The second advantage is that the RCE can make precise measurements when the ellipticity of the reflected light is small. This ability allows for accurate measurements during the initial growth of materials on silicon and glass. The final advantage is that the instrument is free of any polarization effects from the source and detector due to the fixed analyzer and polarizer.

The main disadvantage of the RCE configuration over that of the RA and RP is that the compensator characteristics are wavelength dependant. As a result, the instrument has a useful range of approximately $\pm \lambda_c/4$ where λ_c is the compensator quarter wavelength, which for the above instrument is 632.8 nm. However, as this particular instrument is operated at a single wavelength, in this case, this is not a drawback.

During the development of the in-situ ellipsometer one other disadvantage was, that unlike the rotating analyzer configuration, there did not exist a good calibration routine in the literature for this type of instrument. To address this problem, a calibration routine was developed and is given in A. Kleinschmidt's thesis. However the routine has been expanded

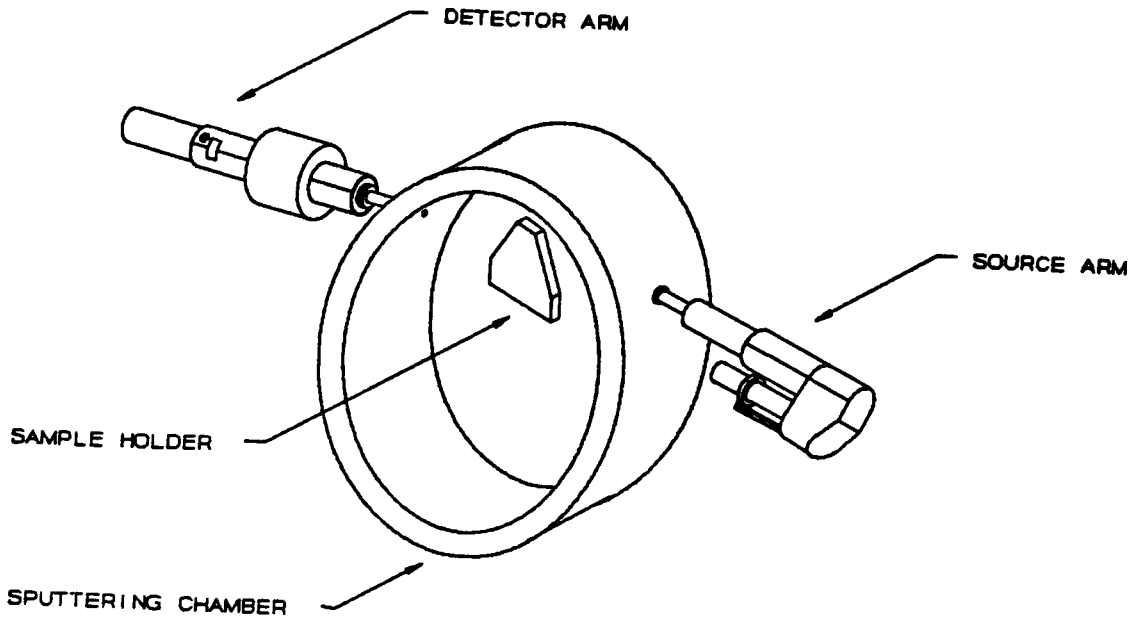

Figure 3.7 In-situ ellipsometer and its attachment to the sputtering chamber.[77]

upon since to include the effects of the vacuum port windows.[78] The complete routine is given in appendix A.

Fig. 3.7 shows the ellipsometer mounted onto the deposition chamber designed for this specific application. The deposition chamber has an adjustable substrate holder for alignment purposes and rotatable targets. This configuration eliminates one problem associated with in-situ ellipsometry, that of substrate wobble. In conventional systems, in order to ensure good film uniformity, the substrates are toggled during the deposition. However; this method introduces an error in the ellipsometric measurements due to small variations in the angle of

incidence. In the system used in this thesis, the targets are toggled while the substrate stays fixed, eliminating the above source of error.

One further advantage of this system is that it lends itself well to the optical monitoring of multilayers. As the substrate stays fixed, only one ellipsometer is needed, greatly simplifying the process over systems where two or more ellipsometers are required.[72]

3.3.4 Ellipsometric Analysis

Spectroscopic measurements of the complex reflectance ratio allow for an analysis of thin film properties through the use of an *N*-layer model.[79] As shown in Chapter 2, the theoretical value of ρ for a multilayer film can be calculated through a matrix method. For a thin film on a substrate, such factors as diffusion and surface roughness can be modeled as individual layers. Information on the film structure can then be deduced by fitting the theoretical value of ρ to the experimental data.

It is important, then, to be able to derive the optical constants of the individual layers. If the bulk optical properties are known, an effective medium theory[80] can be used to predict the individual layer optical constants. If the bulk optical constants are not known, then the optical properties can be determined through the choice of an appropriate parametric model. The next two sections discuss the concepts of effective medium theories and the modeling of optical constants.

3.3.5 Effective Medium Theory

The macroscopic equation for an applied electric field, E, in matter is given by

$$D = \varepsilon E = 4\pi P + E, \tag{3.2}$$

where D is the resultant displacement field, P is the polarization field and ε is the dielectric function. The dielectric function is related to the complex refractive index through the relation

$$n + ik = \sqrt{\varepsilon_r + i\varepsilon_i}, \tag{3.3}$$

where ε_1 and ε_2 are the real and the imaginary parts of the dielectric function respectively. The dielectric function, then, is dependent upon the polarizability of the medium. In order to derive the macroscopic dielectric constant from the film constituents, it is necessary to consider the effects of the field at the microscopic level. For a cubic dielectric lattice with a polarizabilty, α, at each lattice site, the macroscopic dielectric function is related to the microscopic through the Clausius and Mosotti relation

$$\frac{\varepsilon - 1}{\varepsilon + 2} = \frac{4\pi}{3} n\alpha, \tag{3.4}$$

where n is the volume density of the lattice points. The above relation is well known and is usually derived from the cavity method.[81] For a random distribution of two different polarizabilities a similar derivation[82] leads to

$$\frac{\varepsilon - 1}{\varepsilon + 2} = \frac{4\pi}{3}(n_a\alpha_a + n_b\alpha_b). \tag{3.5}$$

Equation 3.5 can be extended to three or more constituents but this is rare in practice for thin film systems. As the individual polarizabilities are not directly measurable, the above equation is often written in the more convenient form

$$\frac{\varepsilon - 1}{\varepsilon + 2} = f_a \frac{\varepsilon_a - 1}{\varepsilon_a + 2} + f_b \frac{\varepsilon_b - 1}{\varepsilon_b + 2}, \tag{3.6}$$

where f_a and f_b are the volume fractions of the individual phases. Eq. 3.6 is the Lorentz-Lorenz effective medium expression.[83,84]

The Lorentz-Lorenz expression becomes unsatisfactory when the two phases consist of regions large enough to have their own characteristic dielectric response. Under these conditions the assumption that the background dielectric is the ambient is no longer valid and one typically substitutes a host dielectric, ε_h . One other factor which must also be considered is the screening effect of the individual grains. In general, for a two phase system, the effective medium expression is given by[85]

$$\frac{\varepsilon - \varepsilon_h}{\varepsilon + \kappa_z \varepsilon_h} = f_a \frac{\varepsilon_a - \varepsilon_h}{\varepsilon_a + \kappa_z \varepsilon_h} + f_b \frac{\varepsilon_b - \varepsilon_h}{\varepsilon_b + \kappa_z \varepsilon_h}. \tag{3.7}$$

where κ_z is the screening factor.[86] For a three dimensional isotropy $\kappa_z = 2$. For magnetron sputtered films, when a columnar growth pattern is present, a two dimensional isotropy where $\kappa_z = 1$ is often more appropriate.

For a random dispersion of the two constituents a suitable choice for the host dielectric is the effective dielectric function itself. This leads to the Bruggman effective medium approximation[87] (EMA) :

$$f_a \frac{\varepsilon_a - \varepsilon}{\varepsilon_a + \kappa_z \varepsilon} + f_b \frac{\varepsilon_b - \varepsilon}{\varepsilon_b + \kappa_z \varepsilon} = 0, \tag{3.8}$$

Though the effective medium approximation is applicable in a large number of cases, it is important to consider its limitations. One potential problem is the assumption of a random dispersion of the constituent phases. For example if phase *b* is encapsulated in phase *a* then the choice of $\varepsilon_h = \varepsilon_a$ in Eq. 3.7 is a more suitable one. This choice results in the Maxwell-Garnet effective medium theory.[88] A more serious problem arises when the grain size can effect the dielectric functions of the individual phases, as is the case for semiconductors and metals. Also, the EMA can underestimate the amount of screening between a metal and dielectric if the individual dielectric phases are sufficiently connected. In this particular case it is more appropriate to use a model by Sen, Scala and Cohen[89,90] (SSC):

$$\frac{\varepsilon_v \cdot (\varepsilon_m - \varepsilon)}{\varepsilon \cdot (\varepsilon_m - \varepsilon_d)} \cdot \frac{1}{(1 + \kappa_z)} = f_d, \tag{3.9}$$

where ε_m and ε_d represent the dielectric function of the metal and the dielectric phases respectively.

Given the large number of effective medium models, and the problems associated with each of them, it is desirable to have a method whereby one can determine if the measured dielectric function can result from a chosen set of phases. This ability is especially important when changes in the dielectric function of one or more of the constituents are possible under different deposition conditions. The above requirement can be achieved through the examination of the theoretical bounds to the resultant dielectric function. These bounds can be

determined through the consideration of the effects of screening. For the case of no screening, which would correspond to long needle-like grains aligned with the electric field, the resultant dielectric function is given by

$$\varepsilon = f_a \varepsilon_a + f_b \varepsilon_b . \tag{3.10}$$

In the case of plate-like grains aligned against the field, we have the maximum possible screening and the resulting dielectric function is given by

$$\varepsilon^{-1} = f_a \varepsilon_a^{-1} + f_b \varepsilon_b^{-1} . \tag{3.11}$$

As the above conditions represent the limits to the possible amount of screening, equations 3.10 and 3.11 form the boundaries in the complex ε plane for the resultant dielectric function from two distinct phases. These limits are commonly referred to as the Wiener bounds.[91]

3.3.6 Parametric Modeling.

If one desires to solve directly for the optical constants of the deposited material then there can be only two unknowns at each wavelength of interest. For the case of a transparent film, the two unknowns are the refractive index and the film thickness. However, in practice, it is often difficult to solve for n directly over the entire range of interest as even small imperfections due to surface roughness, film inhomegeneity and film-substrate interdiffusion can lead to relatively large errors in the solution of the refractive index at certain wavelengths. This situation becomes even more complicated for absorbing films, when one desires to solve

for both n and k, as the film thickness typically has to be measured to a degree of accuracy beyond that of mechanical devices.[92]

The situation described above can be simplified if a parametric model is used to determine the optical constants. In this case the thickness of the film can also entered into the model and the resulting value compared with other methods of measurement such as profilometry. The model chosen depends on the material in question. Some of the more popular models are described below.

For a simple metal, the primary optical absorption mechanism is intraband excitations of the conduction electrons. In this circumstance the Drude approximation[93] is often used:

$$\varepsilon_{Drude} = \varepsilon_o - \left[\Omega_p^2 / \omega\left(\omega + i/\tau\right)\right], \tag{3.12}$$

where $\hbar\omega$ is the photon energy, Ω_p the plasma frequency of the electrons, τ the intraband relaxation time and ε_o the free space dielectric constant. The Drude approximation cannot be used in regions when the interband transitions of the core electrons become significant.

For dielectric films, dispersion in the refractive index is often modeled through the Sellmeier approximation:[94]

$$n^2 = A + \sum_{i=1}^{N} \frac{B_i \lambda^2}{\lambda^2 - \lambda_i^2}, \tag{3.13}$$

where A and B_i are constants and λ_i represents an electronic transition wavelength. As one approaches a value of λ_i, the absorption becomes appreciable, and an expression for k must also be included in the model.

Semiconductors are often the most difficult to model as the dielectric function in the near-infrared to UV region depends upon both the short and long range order of the material. A suitable model for this region has been developed by Farouhi and Bloomer.[95] This model derives the value of k through a method based on the quantum mechanical theory of absorption, then determines n through a Kramers-Kronig transformation. This method is applicable for both crystalline and amorphous solids, however only the amorphous case is required for this thesis.

The absorption coefficient at a given frequency ω is defined as

$$\alpha(\omega) = 2\omega k/c = \Theta\Phi/I_o, \tag{3.14}$$

where Φ is the probability that an electron will undergo a transition to an excited state and Θ is the number of possible transitions. The value of Φ is derived through time dependent perturbation theory through the consideration of an electronic transition between a bonding (σ) and an antibonding (σ*) state :[96]

$$\Phi(\omega) = \frac{4\pi\hbar}{3c} e^2 \omega I_o \left|\langle \sigma^* | x | \sigma \rangle\right|^2 \left(\frac{\gamma}{\{E_{\sigma*} - E_\sigma - \hbar\omega\}^2 + \hbar^2\gamma^2/4} \right), \tag{3.15}$$

where E is the energy of the state, x is the electron position vector, γ is the reciprocal of the finite lifetime of the state and $\langle \sigma^* | x | \sigma \rangle$ is the dipole matrix element between the initial and final states. The maximum probability of transition occurs when $\hbar\omega = E_{\sigma*} - E_\sigma$.

The value of Θ depends upon the product of the number of occupied states in the valence band times the number of unoccupied states in the conduction band separated by an

energy $\hbar\omega$. Let $\eta_v(E_v)$ and $\eta_c(E_c)$ stand for the density of states as a function of energy in the valence band and the conduction band respectively. The value of Θ can be then be determined through the relation

$$\Theta \propto \int \eta_v(E_v) f_v(E_v) \eta_c(E_v + \hbar\omega)[1 - f_c(E_v + \hbar\omega)] dE_v . \tag{3.16}$$

If a low temperature approximation to the fermi functions f_c and f_v is made then the above equation can be written as

$$\Theta \propto \int \eta_v(E_v) \eta_c(E_v + \hbar\omega) dE_v . \tag{3.17}$$

To solve for Eq. 3.17 a further assumption is made that the density of states in the conduction and valence bands can be approximated by parabolic functions where

$$\eta_v(E) = const(E_v^{top} - E)^{1/2} , \tag{3.18a}$$

$$\eta_c(E) = const(E - E_c^{bottom})^{1/2} . \tag{3.18b}$$

The solution to Eq. 3.16 is then

$$\Theta = const(\hbar\omega - E_g)^2 , \tag{3.19}$$

where

$$E_g = E_c^{bottom} - E_v^{top} \tag{3.20}$$

is the difference between the lowest energy in the conduction band and the highest energy in the valence band.

The value for k can then be written as

$$k(E) = \frac{A(E - E_g)^2}{E^2 - BE + C} , \tag{3.21}$$

where the coefficients A, B and C represent the terms in Eq. 3.15 through the relations

$$A = const\left|\langle \sigma^* | x | \sigma \rangle\right|^2 \times \gamma\,, \tag{3.22a}$$

$$B = 2(E_{\sigma^*} - E_\sigma), \tag{3.22b}$$

$$C = (E_{\sigma^*} - E_\sigma)^2 + \hbar^2\gamma^2/4. \tag{3.22c}$$

The refractive index $n(E)$ is related to $k(E)$ through the Kramers-Kronig dispersion relation

$$n(E) - n_\infty = \frac{1}{\pi} P\int_{-\infty}^{\infty} \frac{k(E') - k_\infty}{E' - E}\, dE', \tag{3.23}$$

where P denotes the principle part of the integral. One obvious problem with the above equation is it requires a knowledge of k over all frequencies rather than the limited range described above. This is not a problem if the other absorption mechanisms are far in terms of energy as they will enter into the solution of Eq. 3.23 essentially as a constant.

Substituting Eq. 3.21 into Eq. 3.23 results in a solution

$$n(E) = n(\infty) + \frac{B_\alpha E + C_\alpha}{E^2 - BE + C}. \tag{3.24}$$

The coefficients B_α and C_α are represented as

$$B_\alpha = \frac{A}{Q}\left(-\frac{B^2}{2} + E_g B - E_g^2 + C\right), \tag{3.25a}$$

$$C_\alpha = \frac{A}{Q}\left(\left(E_g^2 + C\right)\frac{B}{2} - 2E_g C\right), \tag{3.25b}$$

where

$$Q = 1/2\left(\sqrt{4C - B^2}\right). \tag{3.26}$$

3.3.7 Nonlinear Optimization

Once the appropriate effective medium theories and/or parametric methods have been chosen for the N-layer model, the individual parameters must be adjusted to optimize the fit to the experimental data. Typically, this type of procedure is performed through a Chi-square minimization of the function

$$\chi^2(\hat{a}) = \sum_{i=1}^{N}\left|\frac{y_i - y(x_i;\hat{a})}{\sigma_i}\right|^2, \tag{3.27}$$

where x_i are the independent variables, $\hat{a}$ the model parameters and y_i and $y(x_i, \hat{a})$ are the experimentally measured and theoretical determined values respectively. Equation 3.27 also contains a term for the random experimental errors σ_i. In ellipsometry, the term σ_i in Eq. 3.27 is usually ignored as errors due to the imperfections in the model and systematic errors due to such factors as misalignment are almost always larger than the statistical errors. The function to be minimized is then

$$F(\hat{a}) = \sum_{i=1}^{N}\left|y_i - y(x_i;\hat{a})\right|^2. \tag{3.28}$$

The minimization technique is outlined below.

An initial assumption is made that Eq. 3.28 can be expanded out to the second order through the relation

$$F(\hat{a}+\delta\hat{a}) \approx F(\hat{a}) + d^T \cdot \delta\hat{a} + \tfrac{1}{2}\delta\hat{a}^T \cdot D \cdot \delta\hat{a}, \tag{3.29}$$

where d is the vector of first derivatives with respect to the individual parameters of $\hat{a}$ and D the Hessian matrix of second derivatives. Around the minimum of Eq. 3.29, the first derivatives are expected to be zero; hence the function should be minimized through the step

$$\hat{a}_{\min} = \hat{a} + D^{-1} \cdot \left[-\nabla F(\hat{a})\right]. \tag{3.30}$$

In practice several steps of the type in Eq. 3.30 are required for convergence.

The gradient and Hessian of Eq. 3.28 are derived as follows. The first partial derivatives of the function F with respect to the individual parameters are

$$\frac{\partial F}{\partial a_j} = -2\sum_{i=1}^{N}\left[y_i - y(x_i;\hat{a})\right]\frac{\partial y(x_i;\hat{a})}{\partial a_j}, \tag{3.31}$$

and the second derivatives are determined through

$$\frac{\partial^2 F}{\partial a_j \partial a_k} = 2\sum_{i=1}^{N}\left[\frac{\partial y(x_i;\hat{a})}{\partial a_j}\frac{\partial y(x_i;\hat{a})}{\partial a_k} - \left[y_i - y(x_i;\hat{a})\right]\frac{\partial^2 y(x_i;\hat{a})}{\partial a_j \partial a_k}\right]. \tag{3.32}$$

In practice the second term in Eq. 3.32 is usually ignored as the term in brackets close to the minimum is expected to be small and average out to zero over the summation. If one then uses the representation

$$\beta_j = -\frac{1}{2}\frac{\partial F}{\partial a_j}, \tag{3.33a}$$

and

$$\alpha_{jk} = \frac{1}{2}\frac{\partial^2 F}{\partial a_j \partial a_k}, \tag{3.33b}$$

then the steps to minimize F can be found through solving the linear equations

$$\sum_{k=1}^{M} \alpha_{jk} \delta a = \beta_j \,. \tag{3.34}$$

Once the parameters which minimize Eq. 3.28 are found, it is necessary to assign errors to the parameters and examine the goodness of fit. For ellipsometric models optimized through Eq. 3.28 an independent goodness of fit is not possible and a relative term, the unbiased estimator σ, is used:

$$\sigma = \sqrt{\frac{2}{(N-p-1)} F_{\min}(x)}\,, \tag{3.35}$$

where N is the number of data points and p the number of wavelength independent parameters. The unbiased estimator allows for a comparison between different models and is approximately equal to the $\sqrt{2}$ times the average absolute difference between the experimental and the theoretical values. The calculation of the Hessian also allows for a determination of the covariance matrix,[97] V, where

$$V = \alpha^{-1}\,. \tag{3.36}$$

The 90 % confidence limits, δa, for each individual parameter can then be found through the relation[98]

$$\delta a_j = 1.67 \cdot \sqrt{V_{jj}}\,\sigma\,. \tag{3.37}$$

Also a correlation matrix,[79] C_{ij}, between the individual parameters can be determined through the covariance matrix by the relation

$$C_{ij} = \frac{V_{ij}}{\sqrt{V_{ii}V_{jj}}} \cdot \tag{3.38}$$

The elements of the correlation matrix can be examined in order to determine the degree c independence of the individual parameters. Perfectly independent parameters have a cros term value of zero while strongly correlated values have an absolute value close to 1.

Eqs. 3.35 to 3.38 allow for the establishment of a set of criterion which can be used determine the validity of a particular model. If two different models have an equal numbe parameters, then the general rule is to choose the one with the smallest unbiased estima The introduction of an additional parameter into the model should only be accepted if the a significant reduction in the unbiased estimator, typically on the order of 2. In addition error bounds on the individual parameters should be reasonable and not increase wi addition of new parameters. Finally, the individual parameters should not be too st correlated, though this requires some discretion on the part of the user.

3.4 Infrared Spectroscopy

3.4.1 Introduction

A Fourier-transform infrared spectrometer was used to examine the infrare properties of the films. This allowed for both a determination of the optical consta

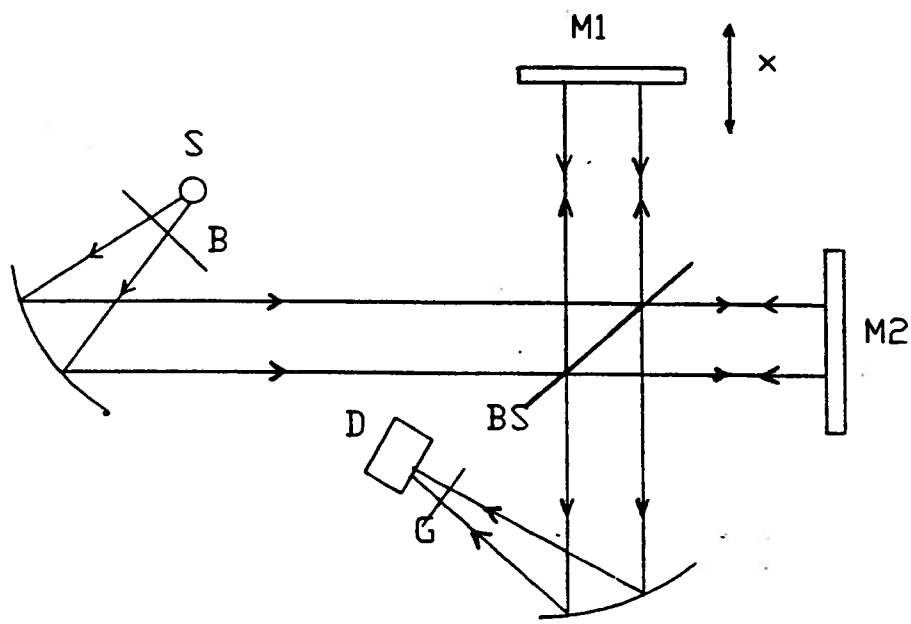

Figure 3.8 Schematic of a Michelson Interferometer.[100] S: source, B: chopper, BS: beamsplitter, M1: moveable mirror, M2: fixed mirror, G:sample, D: detector, x: mirror displacement.

infrared and a chemical analysis through an examination of the molecular bond vibrations.[99] The infrared measurements and analysis in this thesis were performed in collaboration with Yidan Xie as part of her Masters thesis.[100]

The next sections describe the experimental apparatus and the techniques used to analyze the resulting data.

3.4.2 Infrared Spectrometer

The main component of the infrared spectrometer is a Michelson interferometer. A schematic of the interferometer is shown in Fig. 3.8. The operation of the instrument is

described below.

Light from the source, S, is chopped, collimated, then focused onto a beamsplitter, B_s. The divided beam is then reflected from the mirrors $M1$ and $M2$ and recombined at the beam splitter. The resultant intensity is then measured at the detector, D. For the sake of simplicity it is convenient to initially consider the light source to be monochromatic. The intensity measured by the detector is then

$$I(x) = I_o(1 + \cos 2\pi \nu x), \tag{3.39}$$

where x is the total optical path difference between the two beams, I_o is the individual beam intensity and ν is the wavenumber of the infrared radiation.

In practice, the source is polychromatic and the measured intensity as a function of x is

$$I(x) = \int_0^\infty I(\nu)(1 + \cos 2\pi\nu x)d\nu, \tag{3.40a}$$

$$= \frac{1}{2}I(0) + \int_0^\infty I(\nu)\cos 2\pi\nu x d\nu. \tag{3.40b}$$

Equation 3.40 can be converted to a Fourier transform through the following observations. As the intensity, $I(\nu)$, is real we have the relation

$$\int_{-\infty}^0 I(\nu)e^{i2\pi\nu x}d\nu = \int_0^\infty I^*(\nu)e^{-i2\pi\nu x}d\nu. \tag{3.41}$$

As a result, Eq. 3.40 can be written as

$$I(x) - \frac{1}{2}I(0) = \tfrac{1}{2}\int_{-\infty}^\infty I(\nu)e^{i2\pi\nu x}d\nu. \tag{3.42}$$

Hence the wavelength spectrum can be determined through the reverse transform

$$I(\nu) = 2\int_{-\infty}^{\infty} I'(x)e^{-i2\pi\nu x}dx, \tag{3.43}$$

where $I'(x) = I(x) - I(0)$. The value of $I(\nu)$ can only be determined from Eq. 3.43 if the intensity is measured over all values of x. In practice the intensity is discretely sampled and an approximation to Eq. 3.43 must be made:

$$I(n\Delta\nu) = \sum_{n=0}^{N-1} I(n\Delta x)\exp(i2\pi\, n\Delta x / N), \tag{3.44}$$

where

$$\Delta\nu = 1/(N\Delta x). \tag{3.45}$$

In order to obtain an accurate determination of the infrared spectrum, the intensity must be sampled at the required intervals with a high degree of precision. This requirement is accomplished through HeNe laser tracking. By sampling at the intensity minimums of the laser one can achieve a highly accurate position measurement.

Equation 3.44 does not give the true Fourier transform as the sampling is discrete and over a finite distance x. The problems associated with this, such as aliasing and apodization, and how they are compensated for are discussed in detail in Bell.[101]

The Fourier-transform spectrometer is operated in two distinct ranges. The first, between 800 to 4000 cm^{-1}, is referred to in the remainder of the thesis as the mid-infrared. The second range, between 4000 to 9000 cm^{-1} is referred to as the near-infrared.

For the mid-infrared range, a globar source was used and a tungsten-filament was employed in the near-infrared region. The beam splitters consisted of thin films on substrates. For the optical range of 800 to 4,000 cm^{-1} a Ge film on KBr substrate was used while a

CaF_2 substrate was used in the 4,000 to 9,000 cm^{-1} region. For the intensity measurements a Mercury-cadmium-telluride (MCT) detector and a InSb detector were employed in the mid-infrared and the near infrared respectively.

3.4.3 Infrared Optical Analysis

Once a spectral measurement of the reflectance and transmittance of a thin film system is made, it is necessary to solve for the optical constants in order to perform a chemical analysis. However, unlike the visible-UV region, no simple model exists for the dielectric function of carbon films in the mid-infrared due to the large number of molecular resonance oscillations. Given the large degree of parameters necessary to describe the optical constants over the wavenumbers of interest, it is simpler to solve for $\tilde{N}$ directly. Once the values of n and k are determined, one can then analyze the chemical structure of the film by fitting the individual resonances to an appropriate model. The next two sections discuss the methods used to solve for the optical constants and to perform the subsequent chemical analysis.

3.4.4 Newton-Raphson Method

In order to determine the optical constants *(n, k)* of the system at each wavelength of interest, it is necessary to simultaneously solve the equations

$$R_{Th}(n,k,d) - R_E = 0, \tag{3.46a}$$

$$T_{Th}(n,k,d) - T_E = 0, \tag{3.46b}$$

where R and T are the values of the reflection and transmission and the subscripts Th and E represent the theoretically determined and the experimentally measured values respectively. As there can be only two unknowns at each wavelength, the thickness, d, must be determined through an alternate method.

Eqs. 3.46a and 3.46b are not invertable in terms of n and k and must be solved through a numerical technique such as the Newton-Raphson method. The general case of this method for N unknowns is described below.

Let X represent a vector of N variables, x_i, which result in the zeros of the N equations, y_i. In the region around the zeros, the functions y_i can be expanded out to the first order through the relation:

$$y_i(X+\delta X) = y_i(X) + \sum_{j=1}^{N} \frac{\partial y_i(X)}{\partial x_j} \delta x_j. \tag{3.47}$$

By setting the term on the right hand side to zero, the value of X can then be found through iterative solutions to the set of equations

$$\sum_{j=1}^{N} \alpha_j \delta x_j = \beta_i, \tag{3.48}$$

where

$$\alpha_{ij} = \frac{\partial y_i}{\partial x_j}, \tag{3.49a}$$

$$\beta_i = -y_i. \tag{3.49b}$$

Though the form of Eqs. 3.49a and 3.49b is quite similar to that of Eqs. 3.31 and Eqs. 3.32, the Newton-Raphson method is inherently much more problematic than nonlinear

optimization. This is the direct result of having to solve for n and k at each individual wavenumber, rather than over the entire spectral range.

The difficulties associated with the Newton-Ralphson method are best illustrated in the spectral region around some multiple of the half-wave thickness. At the half-wave thickness, Eqs. 3.46a and 3.46b are independent of n, resulting in an infinite continuum of multiple solutions.[102] As a result, in the neighborhood around the half-wave thickness, the solution of n is highly sensitive to small measurement errors. In nonlinear optimization these factors are compensated for by the regions around the quarter-wave thickness where $\partial R/\partial n$ and $\partial T/\partial n$ are large. This property allows for an accurate determination of n over the entire of spectral region, providing the choice of model is a good one.

Despite the problems in determining the value of n at specific wavenumbers using the Newton-Ralphson method, it is still possible to investigate the bonding structure in these regions. This is accomplished through fitting the chosen model to the absorption coefficient, α, given by

$$\alpha = \frac{4\pi k}{\lambda} \tag{3.50}$$

which is inherently less sensitive to measurement errors and film imperfections. This technique is discussed in the next section.

3.4.5 Optical models in the Mid-Infrared

For non-metallic materials, the primary absorption mechanisms in the mid-infrared are

DIAMOND-LIKE FILMS

4.1 Introduction

This chapter provides a thorough investigation of the diamond-like films to be used as a protective overlayer for infrared multilayer coatings. The main goals of this chapter are to allow for a comprehensive understanding of the basic mechanisms of the deposition process which affect the properties of the diamond-like films and to provide a set of physical measurements useful to the optical designer.

The initial set of films studied were deposited in an argon atmosphere. This process simplified the analysis and allowed for a comparison with previously published works. This also served as a guide for the films studied later in the chapter. In addition, it was felt that these potentially useful films had not been examined in enough detail in the literature. The optical, infrared, electronic, tribological and microstructural properties of the films were investigated.

Once the films deposited in a argon atmosphere were characterized, the effects of the addition of reactive gases of H_2, O_2 and N_2 during the sputter process were investigated. The same analytical methods used for the amorphous carbon films were employed.

The final section of the chapter discusses the feasibility of using the investigated materials in infrared optics.

4.2 Amorphous Carbon Films

4.2.1 Introduction

A study was undertaken to understand the properties of amorphous carbon (a-C) films as a function of pressure and substrate bias.[105] The goals of this study were twofold. The first was to allow for a comparison with the results in the literature and to provide a more complete knowledge of the film properties relevant to protective optical coatings The second goal was to provide a better understanding of how the individual deposition mechanisms affected the properties of the films. A number of the more important studies in the literature of this nature are outlined below.

Rossnagel *et al.*[106] studied the optical and electrical properties of carbon as a function of deposition pressure. This was correlated with an in depth study of the plasma characteristics of the sputter gas. Their results showed that there was an increase in the transparency and the resistivity of the films with increasing pressure accompanied by a decrease in the plasma density and the electron temperature at the substrate. These effects were attributed to a decrease in the deposition energetics with increasing pressure. The paper did not investigate the infrared properties of the materials nor did it give any indication of the relative hardness of the films.

I. Petrov et al.[107] performed a comprehensive study of the effects of the substrate bias and the deposition pressure on the resistivity of carbon films. It was found that the resistivity of the films was maximized at the highest deposition pressures and when the substrate bias was

at the electrically floating potential. When the substrates were grounded during the deposition process, the film resistivity was on the order of 1 Ω -cm over the entire range of pressures examined (0.8 to 4 Pa). There was a small decrease in the film resistivity when the magnitude of the negative substrate bias was greater than that of the floating potential.

A detailed investigation was performed by Window and Savvides.[108] In this study, the properties of diamond-like films were examined as a function of deposition power. In their results, the films became more transparent and nonconducting with decreasing power. This effect was attributed to an increase in the bombarding ion/deposition flux ratio, which, in turn, increased the amount of energy delivered to each arriving atom. Preliminary tests of this nature were performed during the course of this thesis with comparable results. However, due to the extremely low deposition rates at the lower powers, it was felt that this technique was impractical and it was not pursued further.

Though the studies in the literature showed that changes in the sputtering gas pressure and the substrate bias altered the film properties, there was no clear understanding of how each of the individual deposition mechanisms affected the properties of the diamond-like films. Also, the studies were not comprehensive enough for the purpose of this thesis; in particular, there was a serious lack of information on the infrared properties.

The initial tests performed in this thesis were centered about the ellipsometric results. Once the necessary analytical software was written, the ellipsometric analysis could be performed with relative ease compared to the complementary techniques. This factor allowed for an extensive study. The complementary methods used were scanning and transmission

microscopy (SEM and TEM), electron diffraction (ED), and hardness and resistivity measurements. Infrared measurements were not included in the initial investigations for two reasons. The first was that the IR measurements and analysis routines were quite time consuming compared to the ellipsometric methods. It was felt it was better to use the above techniques to determine which of the deposition conditions warranted further study. Also, at the time of this study, the infrared measurements were being set up as a collaborative effort and could not be performed until a later date.

4.2.2 Experimental

The planar magnetron system described in section 3.2 was used for the diamond-like film deposition. The target material was pyrolytic graphite. An unbalanced magnetron was employed in order to supply a substantial ion current at the substrate.[109]

All of the films were deposited at a 100 W sputtering power. The substrate to target distance was 8 cm. As carbon has the ability to absorb large quantities of impurity gases,[110] the target was presputtered for 1 hour before each deposition run. The base pressure prior to sputtering was below 2×10^{-4} Pa. During the sputter process, the argon gas pressure was increased by varying the argon flow rate while keeping the pumping speed fixed. This helped to keep the base pressure constant at all times. In addition, the back pressure of the diffusion pump was kept below 60 mTorr at all times. This consideration is important as the pumping efficiency can drop dramatically if the back pressure goes above 100 mTorr. Whenever possible all the films used in a study, such as ellipsometric measurements as a function of

pressure, were deposited in the same run. This procedure helped eliminate such possible sources of nonrepeatability as drifts in the pressure gauges, differences in the target thickness and differences in the base pressure.

Highly polished silicon substrates, with a manufacturers[111] specified "roughness" of 4 Angstroms, were used for the ellipsometric, SEM, and the hardness measurements. Corning glass substrates, 1 inch in diameter, were used for the resistivity measurements. For the TEM measurements, the films were deposited onto freshly cleaved NaCl, floated off in distilled water and placed onto copper grids.

An important factor in thin film deposition is the cleanliness of the substrate. To ensure clean substrates the following procedure was used. First the substrates were mechanically polished by hand using methanol and lens paper for approximately 1 minute. Next, ultrasonic cleaning was employed. In this procedure the substrates were first immersed in a beaker of acetone, then trichlorylethelene, followed by methanol for approximately 3 minutes each. After each step the substrates were rinsed with de–ionized water then blown dry with N_2 gas. Ellipsometric measurements revealed this to be a more effective cleaning method than that of mechanical polishing alone. Cleaning was not necessary for the freshly cleaved NaCl substrates.

Ellipsometric measurements were performed on the spectroscopic rotating analyzer ellipsometer described in section 3.3. The films were analyzed immediately upon removal from the deposition chamber in order to help reduce any error in measurement resulting from a hydrocarbon overlayer buildup from the atmosphere.[112] If more than one sample was removed

from the chamber at a time, the remainder of the samples were stored in containers containing pure N_2 until measurement.

The hardness measurements were determined through the scratch method.[113] In this procedure, the films were scratched with an indenter under increasing loads. The depths of the scratches were then measured through profilometry. The rate of increase in scratch depth vs. load gave an indication of the relative hardness between the films. The depth of the scratches did not exceed more than 10% of the film thickness ($1.5 \pm .1$ μm) in order to prevent the substrate from influencing the results.[114]

Initially, the substrate adhesion was poor for the films deposited at the higher pressures. As a result, the scratch method would remove the films from the substrate. In addition, the films deposited at higher pressures failed the tape test.[113] However, if the films were initially deposited at a pressure of 0.5 Pa for approximately 1 minute, all of the films showed excellent adhesion. This effect was attributed to an increase in the bombardment from the reflected neutrals, which has been shown to be beneficial for this aspect.[115]

Resistivity measurements were made with a four point probe.[116] Ion currents at the substrate were determined by biasing a 2.5 cm diameter probe,[117] centred on the magnetron axis, at −100 V. The probe was placed on the substrate table which was also biased at −100 V during the measurements. The same probe was also used to determine the floating voltage of an electrically isolated substrate. The significance of these measurements is explained below.

For a floating surface in a plasma, an electron and ion flux impinges upon the surface. Initially the magnitude of the flux of each species, J_s, is given as[118]

$$J_s = .6 n_e \left(\frac{kT_e}{m_s} \right)^{\frac{1}{2}}, \tag{4.1}$$

where n_e is the electron density in cm^{-3}, T_e the electron temperature in degrees Kelvin and m_s the mass of the species, s, in grams. As the initial electron flux is greater than the ion flux, the surface will charge negative with respect to the plasma until the two fluxes are equal. At this point the voltage of the surface reaches a value V_f, typically between -10 to -35 V, where

$$V_p - V_f = \frac{kT_e}{2e} \ln\left(\frac{m_i}{2.3 m_e} \right), \tag{4.2}$$

where V_p is the plasma potential, which is typically on the order of a few volts. If a voltage on the order of -100 V is placed on the detector it has a sufficient negative bias to repel nearly all of the electrons in the plasma but not enough to cause a significant secondary electron emission from the bombarding ions.[63] At this voltage, the current is equal to the ion current, giving a measurement of the magnitude of the ion bombardment. The determination of the floating voltage, in turn, gives a measurement of the average energy of the bombarding species.

4.2.3 Results

a) Pressure

Diamond-like thin films were investigated over the pressure range of 1 to 8 Pa. The films were deposited onto electrically isolated (floating) substrates. Below 1 Pa it was found that the films were under considerable compressive stress and would delaminate from the substrate when the thickness was over 0.5 μm.

The deposition parameters are shown in Table 4.1. The magnitude of both the target voltage and the substrate floating voltage decreases with increasing pressure. The decrease in the target voltage is due to an increase in the sputtering efficiency at the higher pressures. The decrease in the substrate voltage is attributed to a lower electron temperature; the result of scattering. A lower electron temperature is also one possible reason for the decrease in the ion current (Eq. 4.2), though a reduction in the plasma density could also be a contributing factor (Eq. 4.1). The deposition rate first increases then decreases with pressure which is common for films deposited at the same power.[119]

The optical constants and the individual thickness of the films were determined by fitting the ellipsometric measurements to the Forouhi and Bloomer interband model described in section 3.3 which has been shown in the literature to be appropriate for diamond-like films.[120] In addition to solving for the optical constants, the model can determine additional information about the bandstructure. This ability is best illustrated by considering the mechanisms for absorption in carbon in the visible-UV range as illustrated below.

Table 4.1 Deposition parameters of films deposited as a function of pressure onto electrically isolated substrates.

Pressure (Pa)	Target Voltage (V)	Substrate Voltage (V)	Ion Current (mA)	Deposition Rate (nm/min)
1	-531	-25	0.53	4.2
2	-516	-23	0.51	4.7
4	-499	-18	0.45	4.6
8	-479	-12	0.43	3.3

A schematic of the theoretical band structure[121] for diamond-like carbon is shown in Fig. 4.1, with contributions from both the bonding and the antibonding π and σ bands. The σ contribution comes from both sp^2 and sp^3 hybridized bonds and is usually centered around 15 eV. The π bands have lower transition energy which can range from 0 to 5 eV. The origins of the different bonding structures in carbon are described below.

In its ground state the carbon atom has the electronic configuration $2s^2\ 2p^2$. In diamond, 4 sp^3 hybridized bonds form a tetrahedral structure. In graphite, there are three hybridized sp^2 orbitals and one p_z orbital. The sp^2 orbitals lie in a plane at 120° from each other. The electrons in the p_z orbitals between the graphite sheets overlap and form delocalized π bonds. The bonding and antibonding π bands in turn overlap, which is the cause of the opaque nature of graphite. Disorder in the graphitic structure is thought to lead to both the creation of sp^3 bonds and the localization of the π electrons.[122] The localization of the electrons can result in a separation of the π bands creating a bandgap. Ultimately, an increasing number of sp^3 bonds would result in a material whose properties were close to

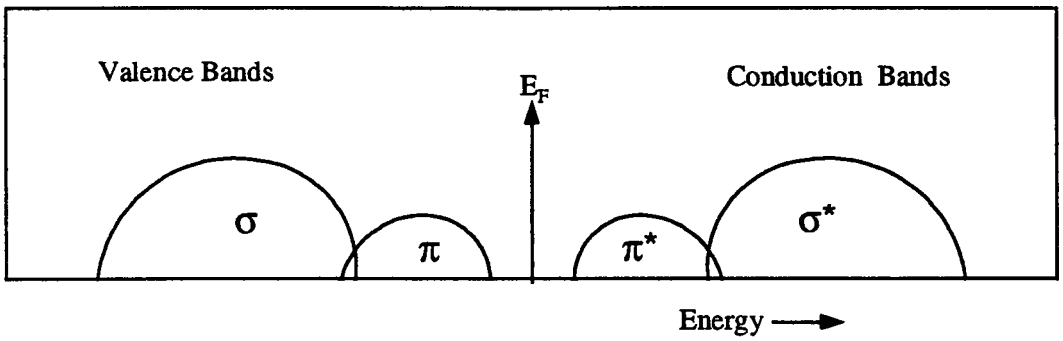

Figure 4.1 Schematic representation of the bandstructure of amorphous carbon.

diamond.

In this study, the only absorption mechanism considered was interband transitions between the bonding and the antibonding π bands. It was assumed that the σ bands would have a negligible contribution over the photon energy range measured (1.5 to 6 eV) and the addition of five extra parameters in the model would cause an unnecessary complication.

The experimentally determined and the theoretically calculated values of the complex reflectance ratio, ρ, are shown in Fig. 4.2 for the films deposited at 1, 4 and 8 Pa. The optical constants derived from the interband model are shown in Fig. 4.3 for the films deposited at 1, 2, 4 and 8 Pa. Table 4.2 shows the thickness, model parameters and the unbiased estimator for each of the films. The thickness of the films were also measured through profilometry to within ± 5 nm and in each case the measurements agreed to within error with the results shown in Table 4.2.

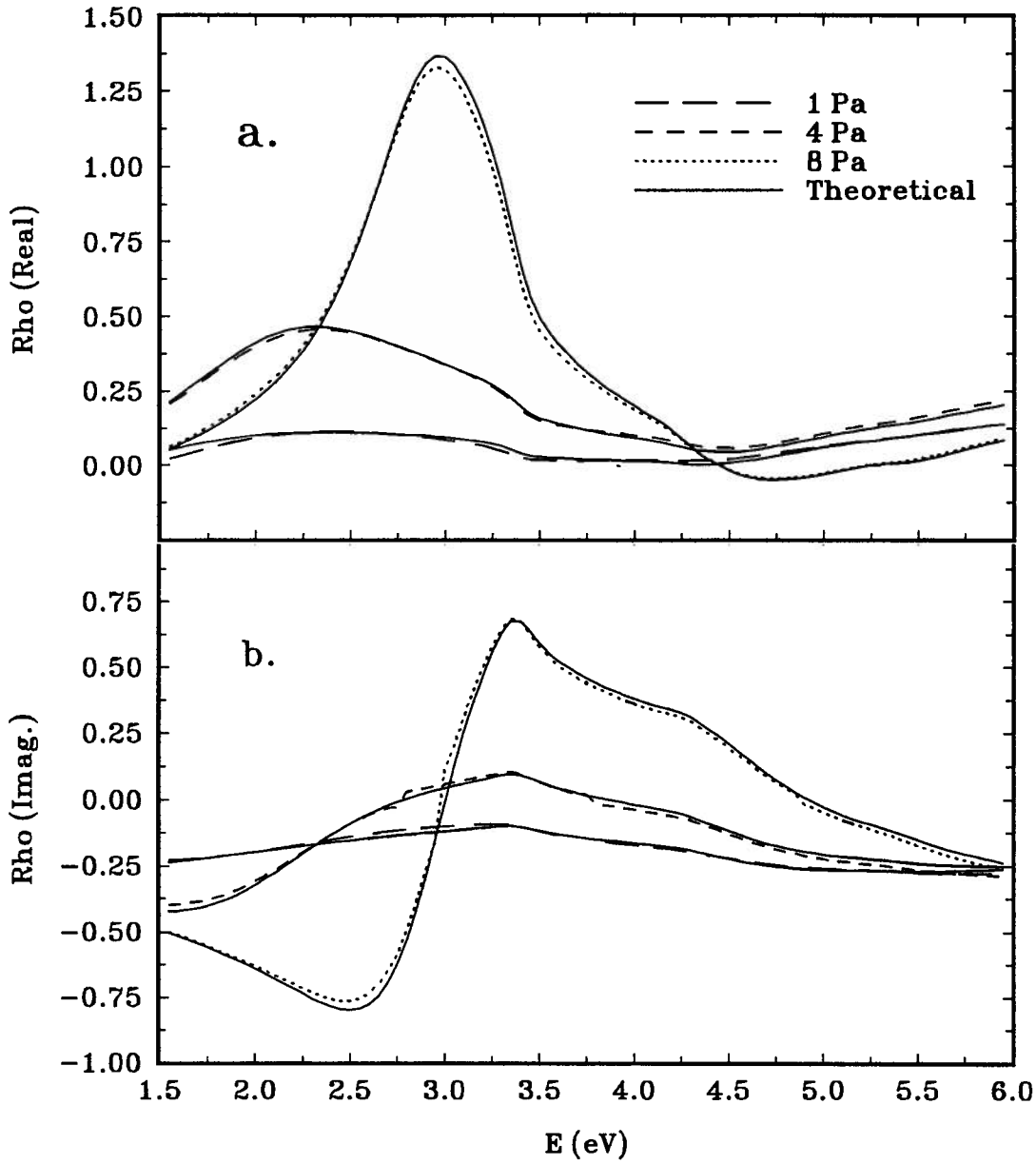

Figure 4.2 Experimentally determined and theoretically calculated values of the real (a) and imaginary (b) parts of the complex reflectance ratio for films deposited at 1, 4 and 8 Pa.

Table 4.2 Farouhi and Bloomer interband model parameters and the unbiased estimators for films deposited as a function of pressure onto electrically isolated substrates.

Pressure (Pa)	Thickness (nm)	n_∞	a	b	c	σ
1	72.0 ± 2.1	1.75 ± .04	.51 ± .05	2.2 ± .4	3.9 ± .8	.030
2	78.3 ± 1.7	1.64 ± .03	.42 ± .03	2.0 ± .2	3.2 ± .5	.024
4	84.2 ± 1.3	1.52 ± .01	.32 ± .02	2.3 ± .3	5.2 ± .7	.026
8	76.4 ± 0.8	1.40 ± .01	.23 ± .01	3.9 ± .5	15 ± 1	.024

Table 4.2 omits the parameter E_g in the modeling results. It was found that the value of E_g was highly correlated with the values of B and C resulting in large errors in all three parameters. In each optimization, the value of E_g was close to zero so it was subsequently set to zero and treated as a constant during the fitting procedure. This discrepancy with respect to the theoretical development in section 3.3 is due to a breakdown in the parabolic band assumption close to the minimum and the maximum of the conduction and valence bands respectively. For amorphous solids, below the expected optical bandgap, there exist a series of localized tail states which increase exponentially with photon energy.[123]

Though a well defined bandgap does not exist for amorphous semiconductors a "pseudo-bandgap" can be deduced through the fitting of the imaginary part of the dielectric function in the linear region above the tail states to the relation

$$\sqrt{\varepsilon_2}E = B^{1/2}(E - E_T), \tag{4.3}$$

where B is a constant and E_T the pseudo-bandgap. The above equation is known as the Tauc relation.[124] Tauc plots for the above films are shown in Fig. 4.4. The tail states are clearly

Table 4.3 Measured properties of films deposited as a function of pressure onto electrically isolated substrates.

Pressure (Pa)	Pseudo - Bandgap (eV)	Resistivity (ohm-cm)	Relative Hardness
1	0.3	30	1
2	0.4	400	.54
4	0.7	2000	.28
8	1.2	$>10^5$	.14

visible for the film deposited at 8 Pa. The least squares fit lines are extrapolated back to the x-axis in order to determine the values of E_T which are presented in the second column of Table 4.3 along with the resistivity of the films in the third column.

The plots of the scratch depth vs. load are shown in Fig. 4.5 along with the corresponding least squares fit. The relative hardness between the films, which is the ratio of the slopes, is given in the last column of Table 4.3.

Scanning electron micrographs of fracture cross-sections and transmission electron micrographs of films deposited at 1 and 8 Pa are shown in Fig. 4.6. and in Fig. 4.7 respectively. The thickness of the TEM films is approximately 600 Angstroms. The films deposited at 1 Pa appear dense and featureless. For the 8 Pa films there is direct evidence of columnar growth and an open voided structure. The films deposited at 4 Pa appeared very similar to those deposited at 8 Pa. The films deposited at 2 Pa were intermediate in microstructure compared to those deposited at 1 and 4 Pa.

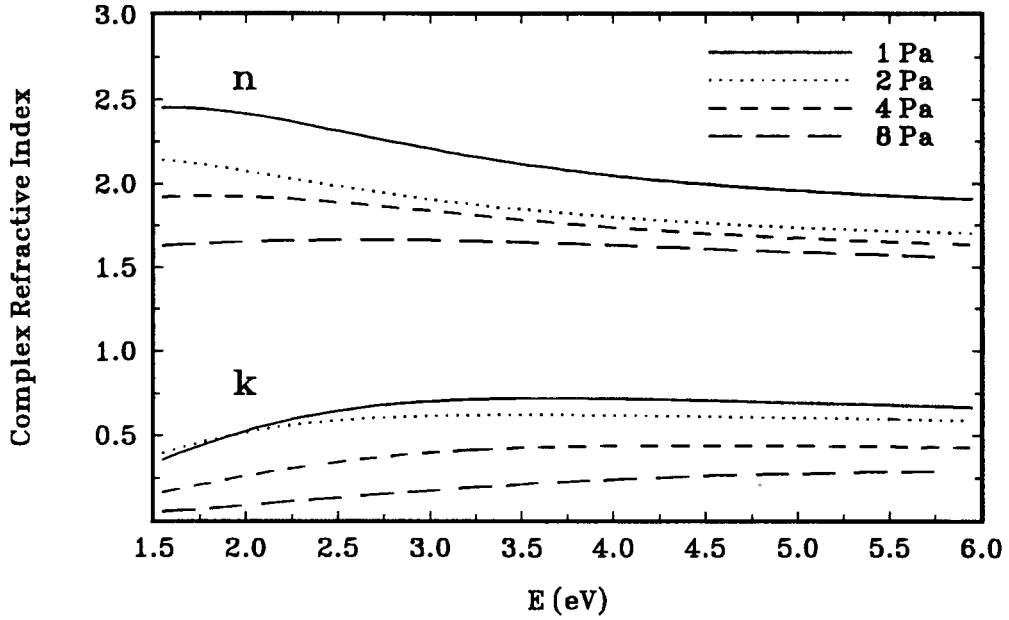

Figure 4.4 Real (n) and imaginary (k) refractive indices for films deposited at 1, 2, 4 and 8 Pa.

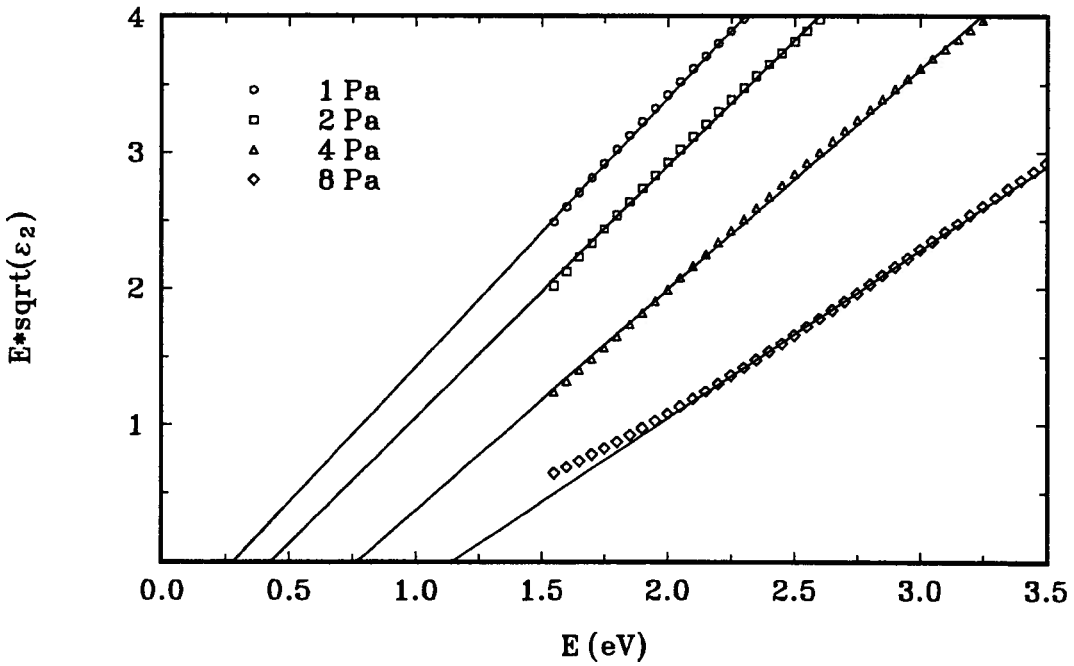

Figure 4.3 Tauc plots as a function of pressure for the amorphous carbon films. The linear fits have been extrapolated back to the origin in order to determine the pseudo-bandgap.

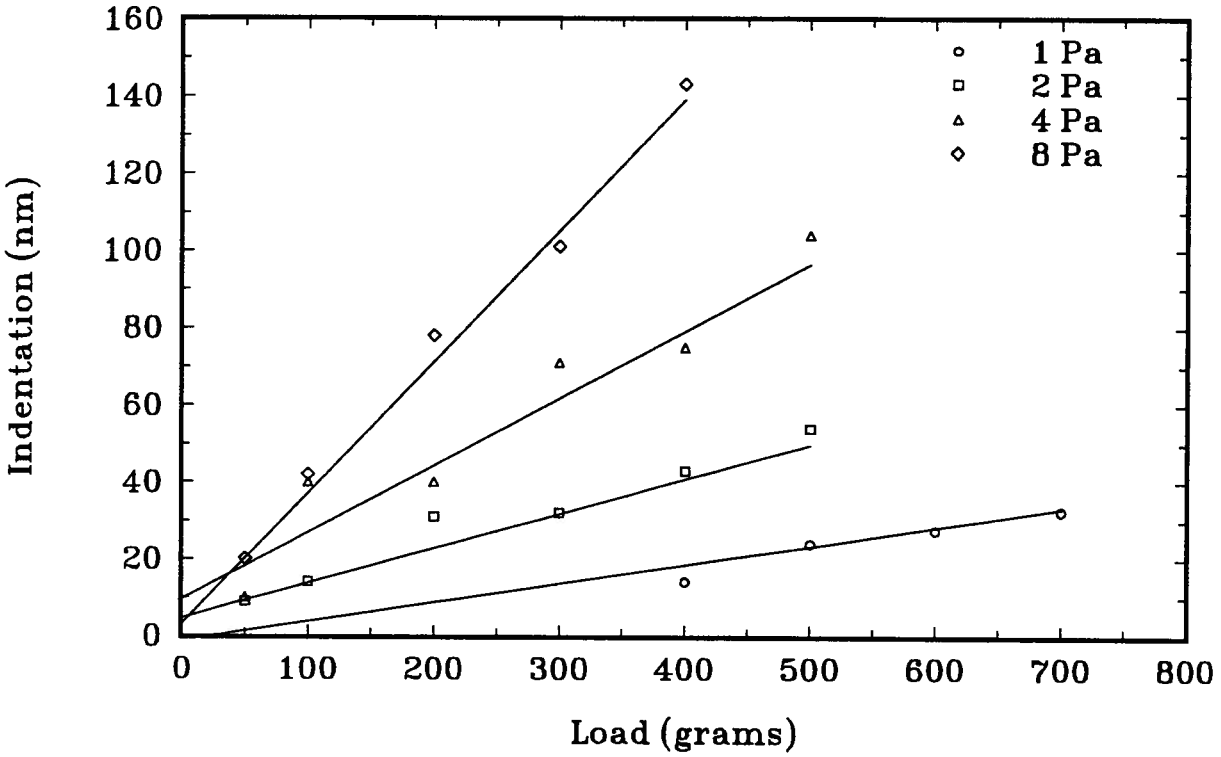

Figure 4.5 Scratch depth vs. load for films deposited at 1,2, 4 and 8 Pa. The corresponding linear least squares fit is also shown.

(a)

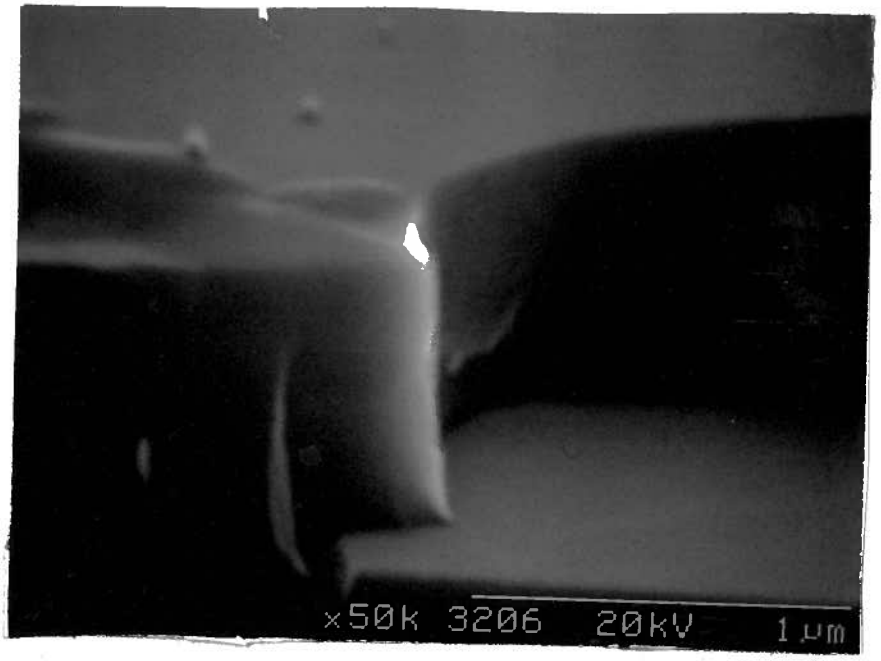

(b)

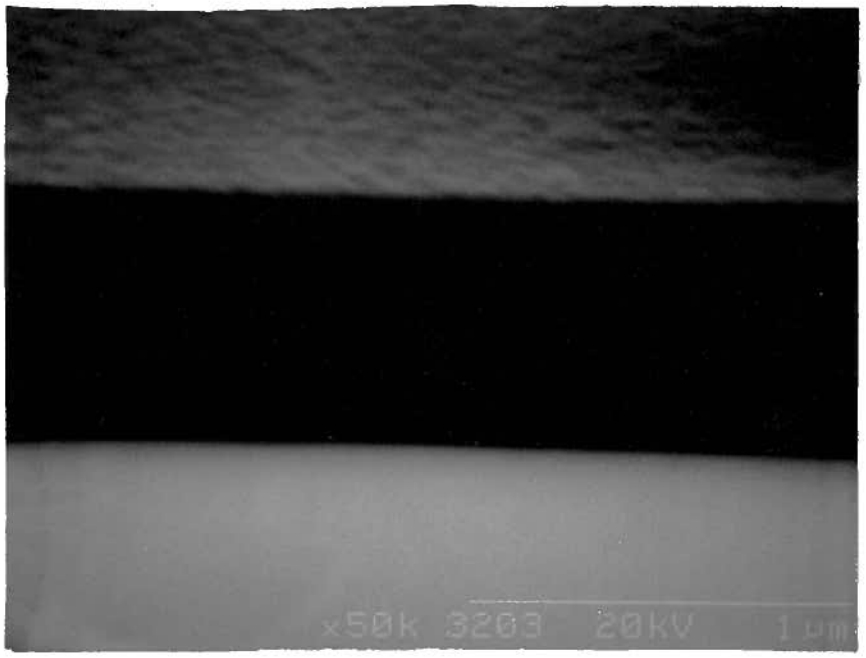

Figure 4.6 SEM fracture cross-section photographs of films deposited at (a) 1 Pa, and (b) 8 Pa . The scale is indicated on the figures.

(a)

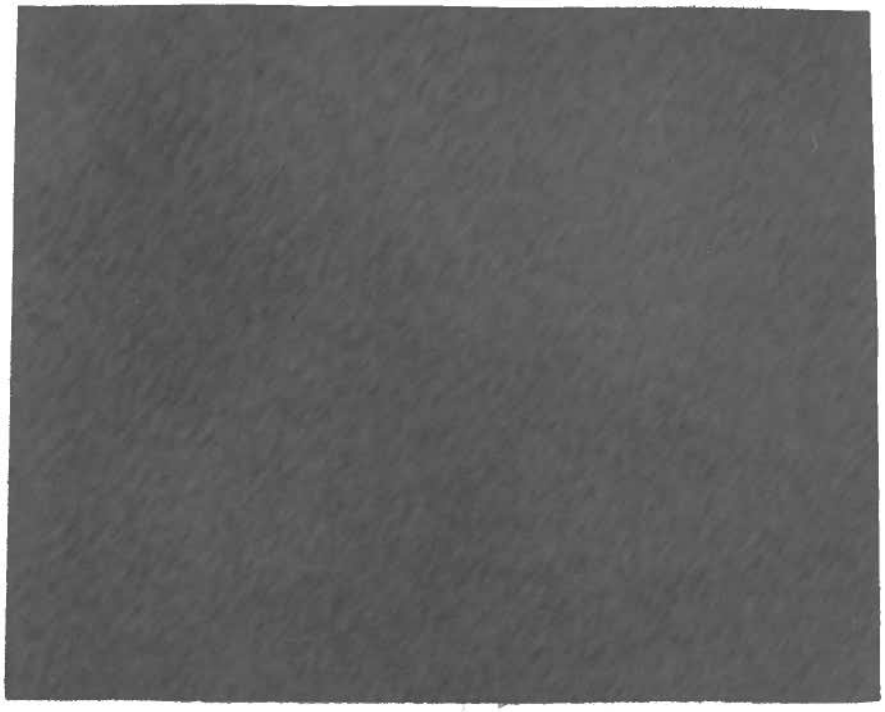

(b)

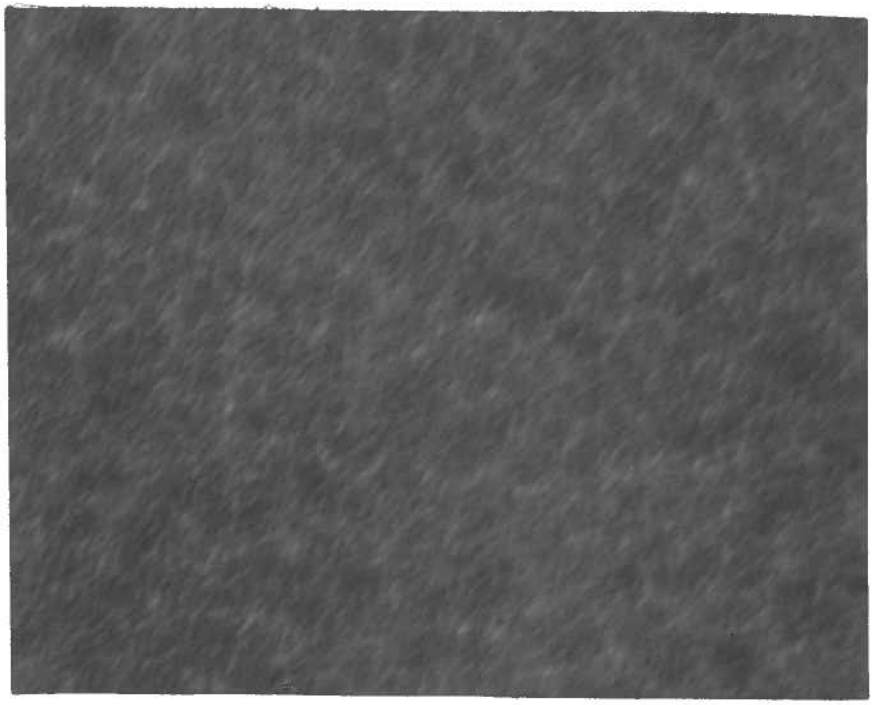

Figure 4.7 TEM photos of films deposited at (a) 1 Pa, and (b) 8 Pa. The films were approximately 600 angstroms thick. The scale is approximately 50 nm/inch.

The electron diffraction results for all of the films appeared identical and featured two broad diffuse rings. This property indicated that all of the films were amorphous without any long range order.

b) Substrate Bias.

Two sets of films deposited at argon pressures of 1 and 8 Pa were studied as a function of substrate bias. For each set of films it was found that above a substrate bias of −50 V the films appeared to be under considerable compressive stress and would delaminate from the substrate upon removal from the deposition chamber.

Ellipsometric studies of the films deposited at 1 Pa were shown to be identical in terms of there optical properties. There was no discernible difference in the optical properties of the films deposited at 8 Pa at substrate biases greater than −30 V.

The refractive indices of two 8 Pa films, one deposited at −12V (floating potential) and one at −30 V bias, are shown in Fig. 4.8. The SEM photo of the film deposited at −30 V appeared very similar to that of the film deposited at 1 Pa and at a floating potential. The hardness of the film deposited at −30 V was to within error (10%), the same as that at −12 V.

The substrate bias and ion currents were also altered by changing the magnetics of the sputter source through the use of a balanced magnetron. Over the pressure range of interest, the replacement of the magnetics caused an increase in the magnitude of the target voltage of 10 to 20 V. The ion currents decreased on average by a factor of 2, and the floating voltage

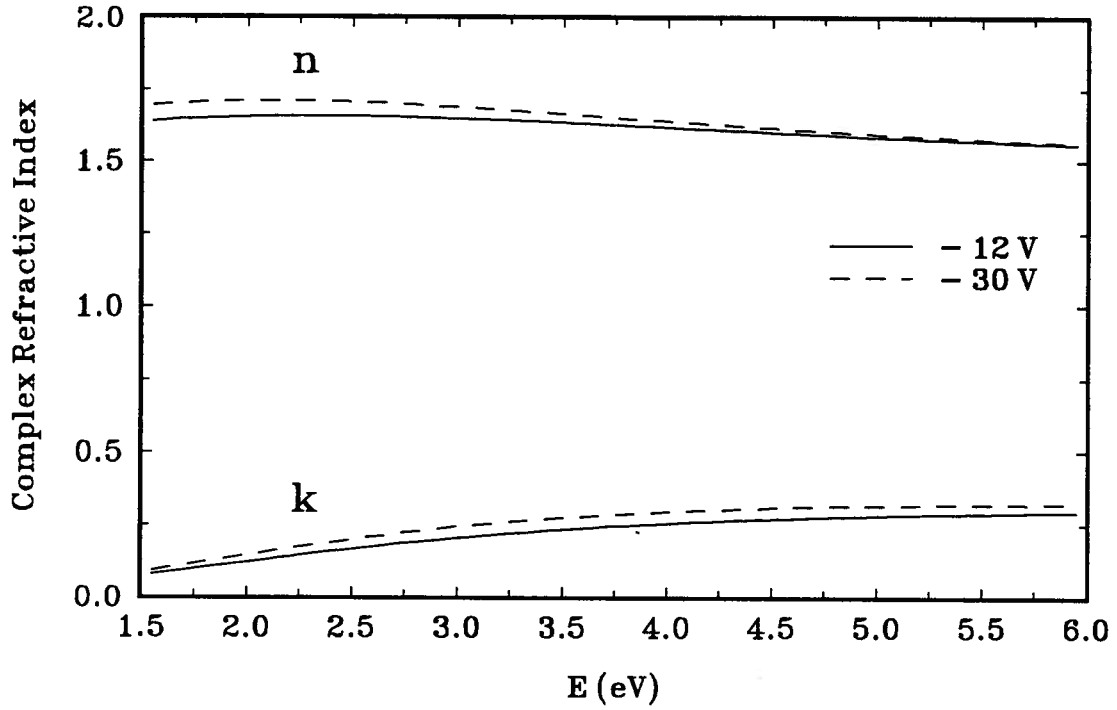

Figure 4.8 Real and imaginary refractive indices for films deposited at 8 Pa with substrate biases of (a) −12 V and (b) − 30 V.

by a factor of 20%. A set of films were deposited as function of pressure and their optical properties determined through ellipsometry. After depositing the films the unbalanced magnetron was replaced and the above measurements were repeated. The ellipsometric model parameters for both sets of measurements agreed to within error.

4.2.4 Discussion

The electron microscopy results show that with increasing pressure the films develop a more voided microstructure. This trend is well known for magnetron sputtered films and is attributed to a decrease in the deposition energetics. At low pressures there is a considerable

energy flux resulting from the reflected neutrals at the target surface, and the bombarding ions from the plasma in the vicinity of the substrate. As discussed in section 3.2.2, the bombarding particles both impart energy into the growing film, which increases the adatom mobility and forward sputter the film material into voids and interstitial sites. The sputtered atoms also arrive directly at the substrate with several eV's of energy. These factors result in a densely packed film. At higher pressures, increased gas scattering results in a more thermalized and oblique deposition flux as well as a reduction in the energy of the neutrals due to a lower target voltage. In addition, there is a decrease in the energy of the ions due to a reduction in the floating potential of the substrate.

With increasing pressure there is also a substantial change in the ellipsometric measurements. Microstructural changes alone can result in large changes in the optical properties of thin films and this effect is often used to deduce such factors as void fractions and surface roughness through ellipsometric modeling.[125] For carbon films, however, there is the added complexity of the possibility of a change in the chemical bonding configuration or the localization of the π bonds. For example, energetic particle bombardment results in high temperature/pressure "spikes" which are believed to result in the creation of sp^3 bonds.[126]

It was attempted to determine whether the changes in optical properties for films deposited at different pressures could be explained solely in terms of microstructure alone or if an accompanying change in the molecular bonding configuration was also necessary. To accomplish this, the ellipsometric data at 8 Pa was fit to an N-layer model where the Bruggman effective medium approximation was used to determine the dielectric function of

each layer. Both a 3 dimensional and a 2 dimensional isotropy were considered. The dielectric function of the film deposited at 1 Pa was used as the reference data. All of the models attempted predicted void fractions in excess of 50 %, which seemed large given the electron microscopy results, and unbiased estimators an order of magnitude larger than that for the interband model.

For metallic films deposited at high pressures, the SSC model is a often a more suitable choice than the Bruggman effective medium approximation.[89] At higher deposition pressures, voids in the film can become connected, enhancing the screening of the metallic phase. As the films deposited at low pressures were reasonably conducting, the above study was repeated using the SSC model. However, it was found that with this technique there was at best a few percent improvement in the unbiased estimator and about a 5 % reduction in the void fraction. It was felt that this relatively small effect was the result of the dielectric contrast between the film material and the ambient being small compared to that with a metal.

Though a suitable model for the dielectric function of the 8 Pa film could not be found, this does not necessarily mean that the resultant dielectric function cannot be arrived at from the chosen set of phases. To investigate the this factor further, the Wiener bounds (Section 3.3.5) to the resultant dielectric function were applied at three separate photon energies: 1.5, 3.5 and 6 eV's. The results are shown in Fig. 4.9. Also shown are the bounds between the EMA and SSC models for a film with a 2 dimensional isotropy. It can be seen that the value for the 8 Pa film lies within the dielectric bounds for the last case only and in this instance still

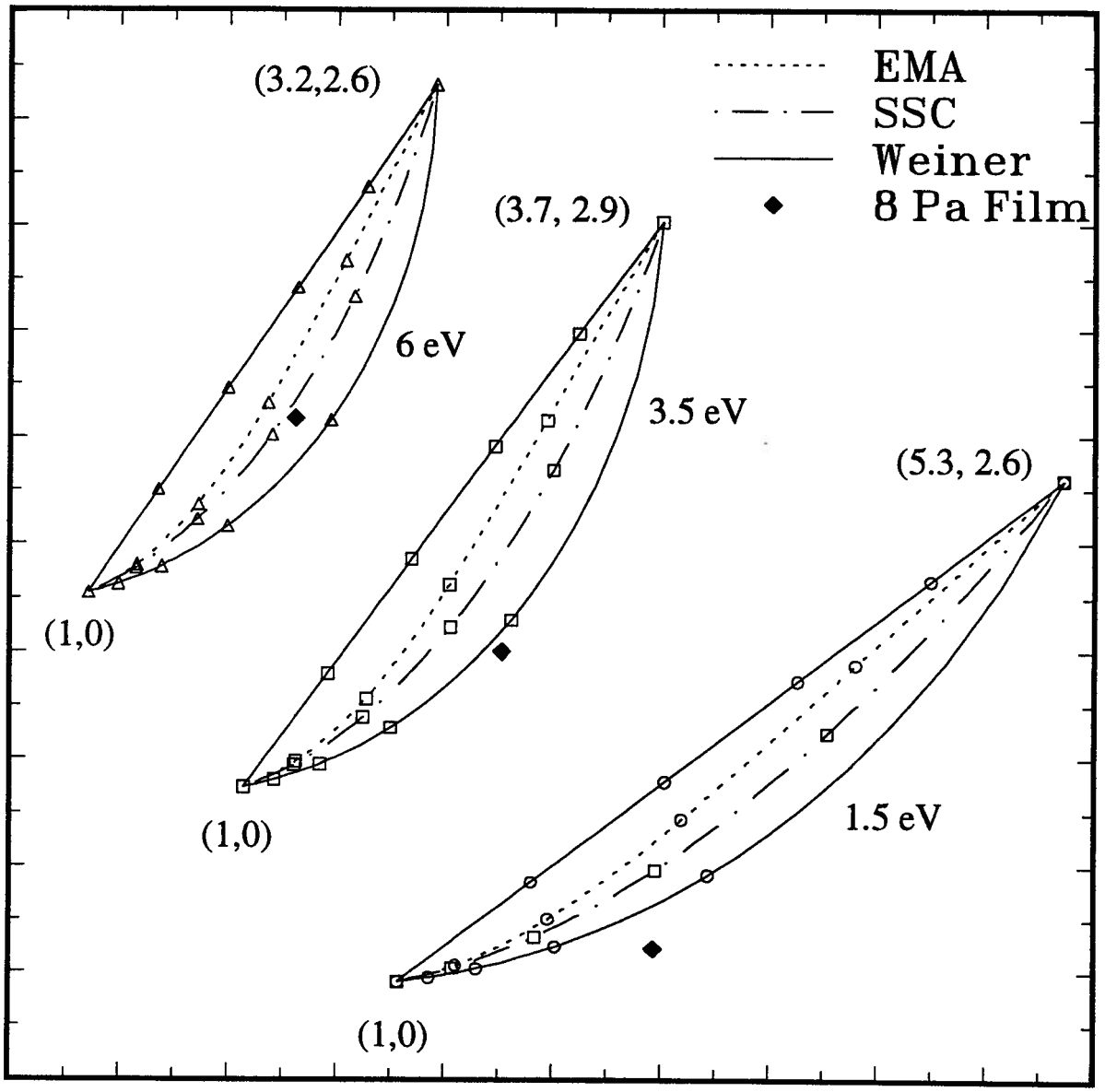

Figure 4.9 Theoretical Wiener bounds when the two phases are the ambient and the amorphous carbon film deposited at 1 Pa (Ar) at the photon energies 1.5, 3.5 and 6 eV. The The data points are spaced at intervals corresponding to a 20 % change in the constituents. The bounds at each energy have been displaced for presentation purposes. Also shown are the dielectric functions for the EMA and SSC models. In addition, the dielectric values for the film deposited at 8 Pa at the above photon energies are presented.

lies outside the region expected for an isotropic film. Hence, it can be concluded that the difference in the optical properties between the 8 Pa and 1 Pa film can not be explained in terms of the difference in the microstructure alone. This result correlates well with large variations in the resistivity and hardness measurements.

One other factor which can influence the ellipsometric results is surface roughness. The Farouhi-Bloomer model was used to determine the dielectric function of the individual films when surface roughness was included in the film structure model. In this case a two layer model was used. The top roughness layer contained 50 % voids and the Bruggman effective medium approximation was used to determine the resultant dielectric function. The thickness of both layers was allowed to vary.

It was found that the inclusion of surface roughness into the model for the high pressure film did not result in a reduction of the unbiased estimator and caused only minute changes in the dielectric function. This factor was attributed to the small dielectric contrast between the film and the ambient. For the low pressure film the inclusion of surface roughness resulted in a 20 % improvement in the unbiased estimator (for a surface roughness of 30 Angstroms) and the general effect of increasing the real part of the dielectric function and lowering the imaginary part. However, when the Wiener bounds were examined it was found that this was not enough of a change for the results of the 8 Pa film to lie within the required dielectric bounds.

Though it can be concluded that the changes as a function of pressure are the result of a change in the bandstructure, it cannot be said, at this point, whether or not the changes are

the result of an increase in the number of sp^3 bonds. Though this is often cited as the reason for more diamond-like properties[126,127] another valid reason is the localization of the π electrons. One other important consideration is that the above diamond-like properties do not necessarily indicate a large fraction of sp^3 bonds. These two factors are best understood by considering a number of the theoretical studies in the literature, which are outlined below.

An excellent theoretical discussion of the properties of amorphous carbon is given by J. Robertson.[128] In this study, he compares the difference between a number of random network models with different sp^2/sp^3 bonding ratios and models which consist primarily of graphitic islands linked by sp^3 bonds. The graphitic island structure was chosen as it was found that the formation of 6-fold rings during the deposition process was thermodynamically favourable over a number of other naturally occurring configurations. The chosen microstructure consisted of graphitic islands with complete breaks in the π bonding at the edges.

The optical properties of the models were determined through a tight-binding approximation,[129] which included both the first and the second nearest neighbour interactions. In addition, the optical properties for the diamond and graphite structures were also predicted through the above method. The tight-binding approximation gave reasonable results for both the diamond and graphite bandstructures and predicted the values for the optical bandgaps of these materials.

There was a distinct difference in the optical properties of the random network and the graphitic island models. It was shown for the random networks that, even for the 100% sp^3

bond model, an optical bandgap did not exist. For the graphitic island structure, however, the presence of medium range order in the material resulted in a bandgap which was inversely proportional to the island size.

Hence, according to Robertson's study, an increasing bandgap alone does not necessarily indicate an increase in the number of sp^3 bonds. The results in this thesis would seem to support this as the films become softer as the optical bandgap increases.

Another theoretical study of amorphous carbon was performed by Tamor and Wu.[130] Their assumption was that the diamond-like properties of a-C resulted from imperfections in the graphite lattice. In their model, the parallel graphite sheets were linked by sp^3 bonds. Percolation theory [131] was used to determine the percentage of sp^3 bonds required for the material to change from a metal to an insulator, which was found to be 8.3 %. The maximum allowed number of diamond bonds in the above model was shown to be approximately 10%.

A theoretical simulation which complements the above studies was performed by G.Gali *et al.* .[132] In this study, the structural and electronic properties of amorphous carbon are generated through a molecular-dynamics method.[133] The model starts with a random array of carbon atoms at 5000K which are subsequently quenched to room temperature. This model simulates the effects of ion bombardment which causes high temperature/pressure spikes.

The theoretical results predicted 85% sp^2 sites and 15% sp^3 sites. The general structure was one of intersecting planes of 5, 6 and 7 fold rings. These properties correlate well with the two models above. In addition, the theoretical electronic density of states was in good agreement with experimental values in the literature.

It should be noted that the above discussion is not meant to show that a large degree of sp^3 bonding cannot exist in amorphous carbon films, only to point out they are not necessarily required to explain what are commonly referred to as "diamond-like" characteristics.

One method for determining the presence of π electrons in carbon is through the examination of the energy loss function, $-\mathrm{Im}(1/\varepsilon)$, where[134]

$$-\mathrm{Im}(1/\varepsilon) = \varepsilon_2/(\varepsilon_1^2 + \varepsilon_2^2), \tag{4.4}$$

Peaks in the energy loss function occur for plasma oscillations when both ε_1 and ε_2 are small, as is the case for carbon. For amorphous carbon there are generally two peaks, a lower peak which results from the π electrons and one which includes the effects of all of the valence electrons ($\pi + \sigma$). To a first order approximation, the position of the peaks, $\hbar\omega_p$, is given by the relation [135]

$$\omega_p = (ne^2/\varepsilon m)^{1/2} \tag{4.5}$$

where n is the electron density, e the electron charge, ε the permativity of free space and m the electron mass.

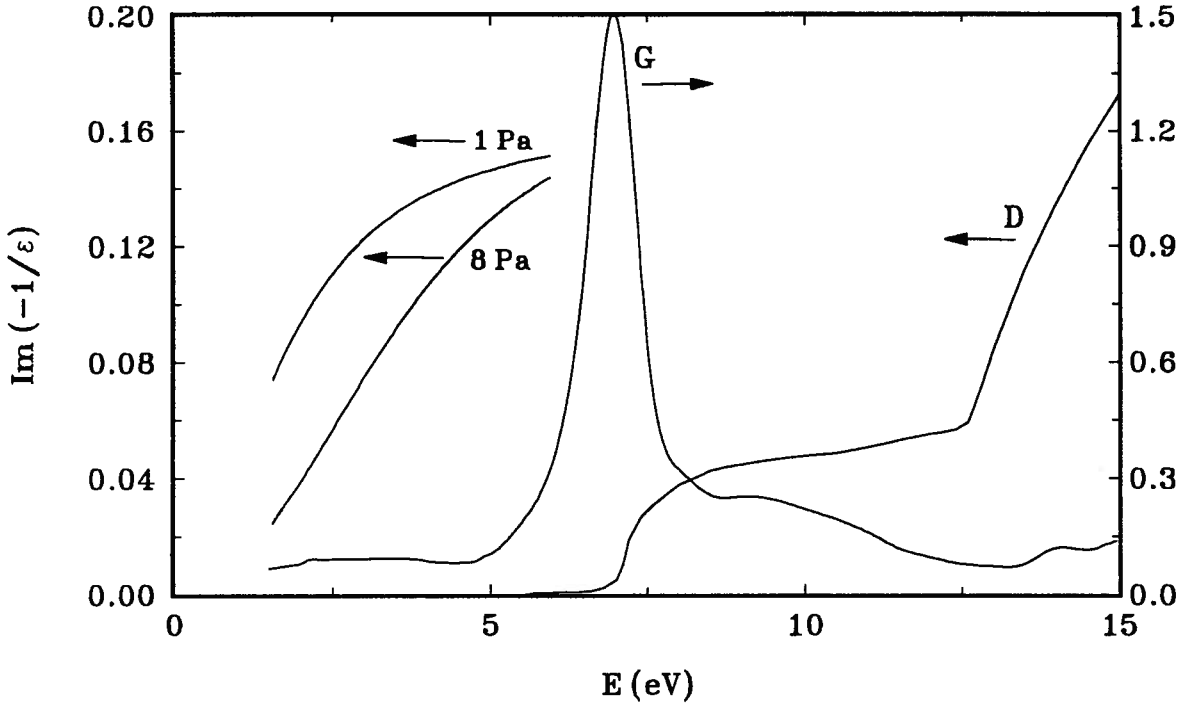

Figure 4.10 The energy loss function Im (-1/ε(ω)) vs. photon energy for the films deposited at 1 and 8 Pa . Also included is the loss function for diamond and graphite (E⊥c).

Fig. 4.10 gives the energy loss functions for both graphite and diamond along with the loss function for the films deposited at 1 and 8 Pa. The π plasmon peak for graphite is centered around 7 eV which is beyond the range of the instrumentation used in this thesis. However, from a visible inspection of Fig. 4.10, it can be seen that the energy loss functions for both the 1 and the 8 Pa films have not reached a maximum by 6 eV. This factor indicates a substantial amount of sp^2 bonding in the films. In addition, there does not appear to be an appreciable difference in the peak positions, suggesting that there is not a large difference in the density of the π electrons in the two materials.

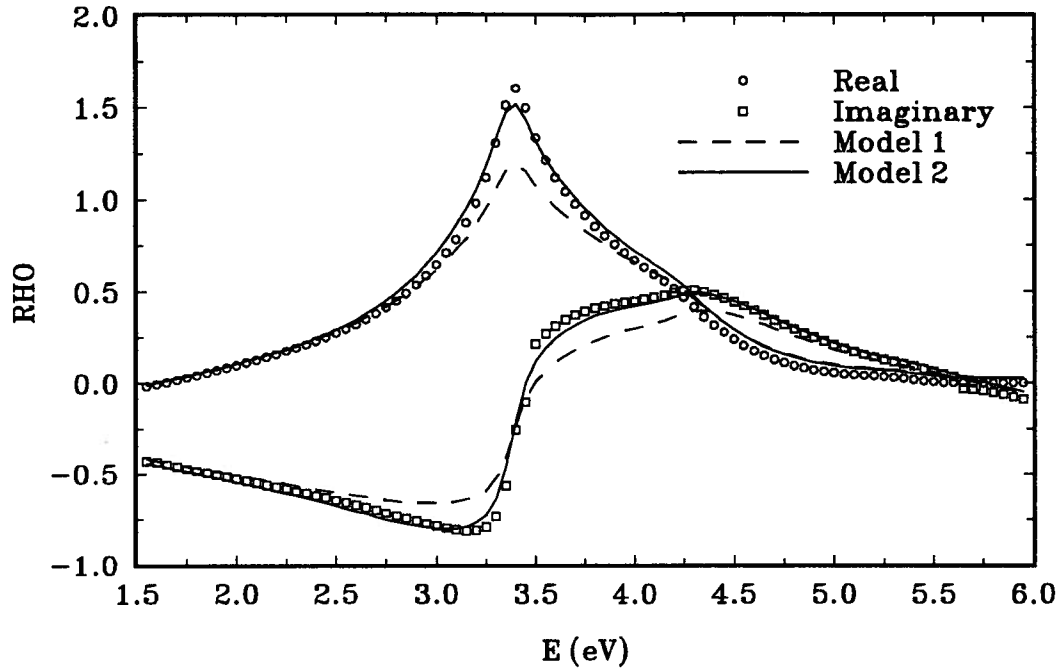

Figure 4.11 Real and imaginary values of the experimentally determined complex reflectance ratio of a film deposited at 8 Pa on an electrically isolated substrate and two theoretically modeled fits. The first model assumes no voids while the second contains 10% voids.

Unlike the films deposited as a function of pressure, the films deposited as a function of substrate bias do not exhibit large differences in their optical properties. For the films deposited at 8 Pa there is, however, a substantial change in the microstructure which appears to undergo a transition from zone-1 to zone-T with an increasing substrate bias. This effect is attributed to the bombarding ions. Ellipsometric modeling was once again used to determine if the difference in optical constants could be explained solely in terms of changes in the microstructure of the films. In this case, the dielectric function of the film deposited at –30 V bias was used to fit the ellipsometric data of the film deposited at the floating potential. The results for two different EMA models are shown in Fig. 4.11. The first model assumed no

voids and allowed the thickness of the film to vary. The introduction of voids into the second model resulted in a relatively good fit withan unbiased estimator of 0.06 and a void fraction of $0.1 \pm .01$. Given the good correlation between the electron microscopy and the ellipsometric results, it would appear that an increase in the energy of the bombarding ions over the range studied results in a change in the microstructure only. This result correlates well with the results of I. Petrov *et al.*[107] which showed a small increase in the conductivity of their films with an increasingly negative substrate bias indicating an increase in the density of their films.

Table 4.1 shows that the magnitude of the floating voltage and the energy of the argon ions increases with decreasing pressure. However, given the results for films as a function of substrate bias, it appears unlikely that this effect alone would explain the large change in the film properties. One other possible mechanism is the difference in the energetics of the reflected neutrals. As discussed in section 3.2, unlike the relatively low energy ions, these particles can have energies up to the target voltage. Few studies have been performed on determining the magnitude of the reflected neutrals but it appears to be an approximately an order of magnitude lower than that of the ions.[136] The energy of the bombarding particles in other deposition methods such as chemical vapour deposition[21] (> 100 eV) and laser ablation[137] (>50 eV) indicate that relatively high energies are required for the formation of diamond-like films.

4.3 Infrared Studies of Amorphous Carbon Films

4.3.1 Introduction

To understand the nature of the amorphous carbon films further a study was undertaken where the infrared properties were measured as a function of deposition pressure.[138] The effects of substrate bias on the infrared properties was not investigated as it was felt that this procedure resulted in an increase in the film density only.

The goal of this study was two–fold. The first was to measure the absorption coefficient in the infrared in order to determine if the films were suitable for optical applications. The second goal was to perform a chemical analysis of the films through the examination of the nature of the molecular bond vibrations.

4.3.2 Experimental

The films to be investigated through infrared spectroscopy were deposited onto double polished semi-insulating GaAs substrates, which were transparent in the range of 700 to 10,000 cm^{-1} . The measured infrared reflection and transmission spectra for a GaAs substrate is presented in Fig. 4.12. Also shown in this figure is the residue ($1-R-T$). As the ideal absorption is zero, the residue, with a range from -1 % to 0%, gives an indication of the accuracy of the method.

The reflection measurements were made in reference to an aluminum mirror adjacent to the sample of interest. As the aluminum mirror would cloud easily when the samples were

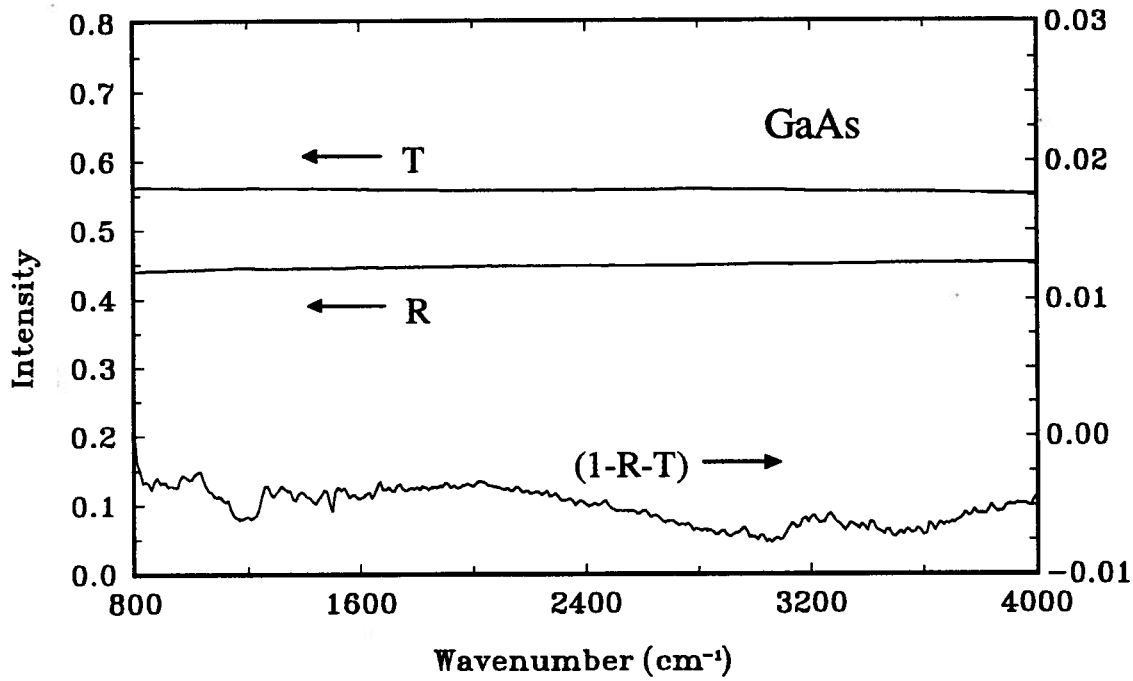

Figure 4.12 Mid-infrared reflection (*R*) and transmission (*T*) spectra for a semi-insulating GaAs substrate. Also shown is the residue: 1-*R* -*T*.

changed between measurements, this presented another potential source of error. As the adherence of the aluminum film to the glass substrate was poor, cleaning the mirror proved difficult and often resulted in a small degree of scratching. The solution to the above problem was to include a third surface in the measurements, that of a GaAs substrate. As the surface of the GaAs substrate was highly polished and easily cleaned, it provided a reliable check for the reflection measurements.

The samples were measured over the range of 800 to 9000 cm^{-1} . In this thesis, the range from 800 to 4000 cm^{-1} is denoted as the mid-infrared and from 4000 to 9000 cm^{-1} the

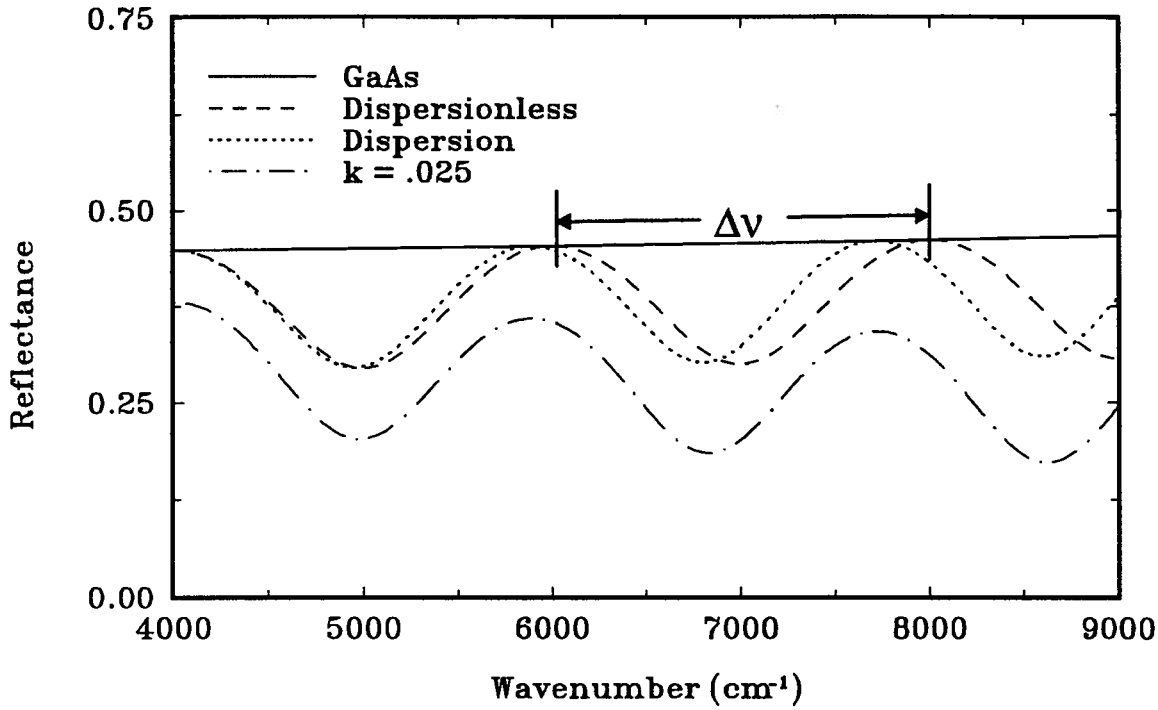

Figure 4.13 Theoretical reflection spectra of a 1.25 μm thick film with a refractive index of 2 on GaAs along with the reflection spectra of the substrate. Also shown is the reflection spectra of a film with dispersion and one that in addition has a value of $k = .025$. The value of $\Delta\nu$ represents the distance between the reflectance maxima.

near-infrared. For carbon films, absorption peaks due to molecular resonance vibrations lie primarily in the mid infrared. Though the near-infrared does not provide information about the chemical bonding structure, it can be used to deduce the film thickness. The technique used to determine the thickness of the film is described below.

For a transparent film on a substrate, the envelope method[139] is often used to deduce the value of n and the film thickness, d. Fig. 4.13 shows the theoretical reflection spectra of a 1.25 μm thick film with a refractive index of 2 on GaAs along with the reflection spectra of the

substrate. Also included is the theoretical reflection spectra for a film with a linear dispersion of

$$n = 2 + (\nu - 4000)/9000\, cm \tag{4.6}$$

and a film with the above dispersion which also has a value of k equal to 0.025. For the transparent dispersionless film, the solution of n and d is quite straightforward. The value of the optical thickness, nd, can be determined through the relation

$$nd = \frac{1}{2\Delta\nu}, \tag{4.7}$$

where $\Delta\nu$ is the difference in wavenumber between the reflectance maxima. The value of n can then be determined by examining the difference in intensity, ΔI, between the minimum and maximum values through the relation:

$$\Delta I = \left(\frac{n_s - 1}{n_s + 1}\right)^2 - \left(\frac{n_f^2 - n_s}{n_f^2 - n_s}\right)^2, \tag{4.8}$$

where n_f and n_s are refractive indices of the film and the substrate respectively.

The above method becomes more complicated when dispersion is included in the refractive index. However, if a suitable model for the refractive index is chosen, the envelope method can be used to determine an appropriate set of starting values for the fitting routines.

Fig. 4.13 shows that the additional presence of absorption in the films does not, in this case, visibly affect the distance between the interference maximum but has the general effect of lowering the overall reflectance of the film/substrate system. The inclusion of absorption can

also affect the value of ΔI, ultimately reducing it to zero. However, as long as a significant amount of interference remains in the films, it should still be possible to deduce the optical constants and the film thickness from the choice of an appropriate model.

Ideally, then, the films should be thick enough to ensure interference fringes in the near infrared, but not so thick as to be completely opaque. Another limiting factor for the thickness is the problem of multiple solutions to the optical constants in the mid-infrared. In general, the thicker the film, the greater the number of possible solutions.[102] At the other extreme, the limits to the instrumentation accuracy require total absorption levels of at least several percent in order to guarantee an accurate determination of the absorption coefficient. The optimum thickness range was determined to be approximately 0.8 μm for the most absorbing films and 1.4 μm for the most transparent ones.

A set of films were deposited as a function of pressure for the purpose of infrared measurements. The films were deposited at argon pressures of 1, 2, 4 and 8 Pa in order to allow for a comparison with the experimental results in the previous section.

4.3.3 Results

The reflection (R) and transmission (T) measurements for the film deposited at 1 Pa is shown in Fig. 4.14. Also included is the calculated value of the absorbance ($1-R-T$). The peaks due to molecular vibrations can be seen in the region between 900 and 1700 cm^{-1}. Interference effects in the absorption spectrum are also present. The elimination of this artifact

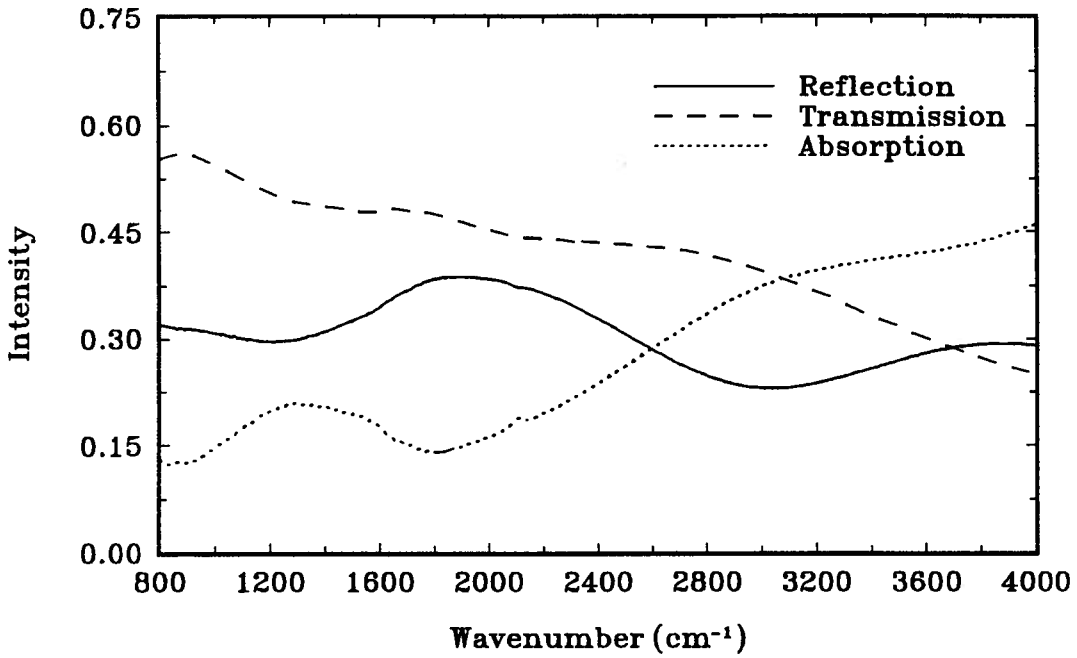

Figure 4.14 The mid-infrared reflection and transmission spectra for a film deposited at 1 Pa in argon. Also included is the calculated value of the absorbance (1-R-T).

in the solution of the absorption coefficient provides a check on the accuracy of the thickness determination.

The Forouhi–Bloomer model was chosen to determine the optical constants and film thickness in the near-infrared. The reflection measurements and the modeled fits are shown for the films deposited at 1 and 8 Pa in Fig. 4.15. The modeling results appear to account for the dispersion in both n and k for the two films.

The values of k for the films in the near- infrared are given in Fig. 4.16. The values of n are essentially those in the infrared region of Fig. 4.5. The results show a general reduction

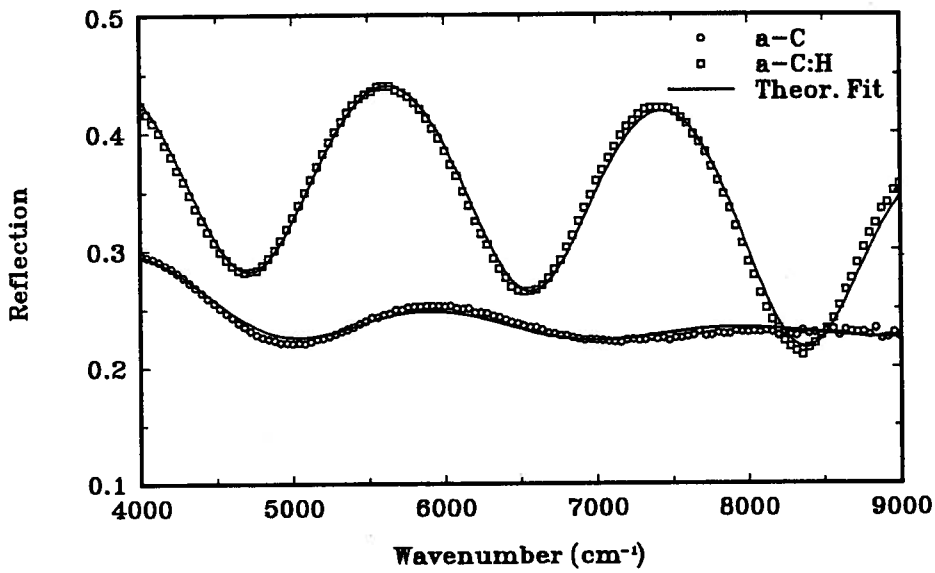

Figure 4.15 The near-infrared reflection measurements and the modeled fits are shown for the films deposited at 1 and 8 Pa.

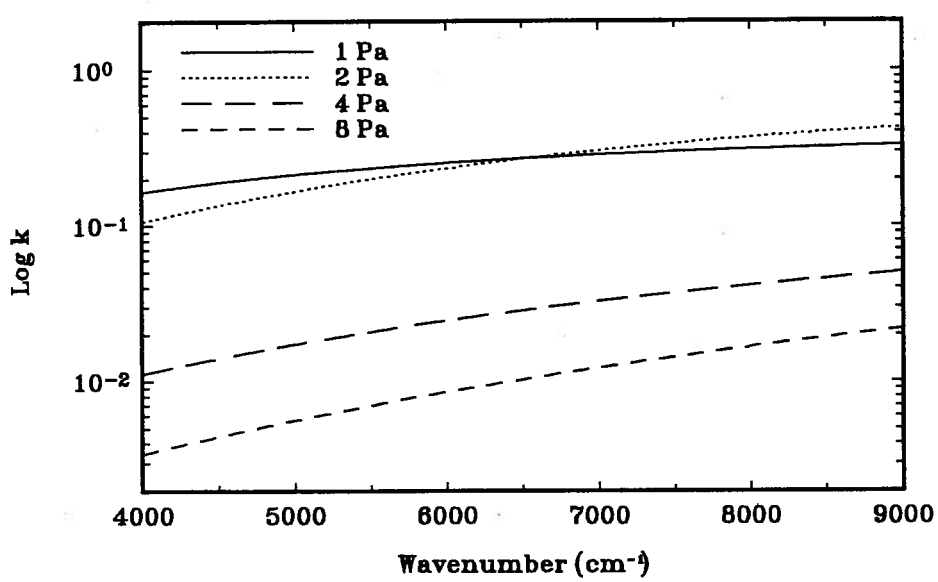

Figure 4.16 Log of k vs. wavenumber for films deposited at 1,2,4 and 8 Pa in the near infrared. The values of k were determined through fitting the reflection spectra to the Farouhi-Bloomer model.

of absorption with increasing pressure. A notable exception to this trend is observed for the 2 Pa film where the absorption is greater than the 1 Pa film at the higher wavenumbers. This anomaly is also observed for the optical constants in Fig. 4.5 at the lower end of the energy spectrum.

Once the thickness of each of the films was determined, the optical constants could be solved for in the mid-infrared. This procedure proved to be somewhat difficult due to the presence of multiple solutions. The most effective way found to solve for the optical constants of the films is outlined below.

In order to employ the Newton-Rhaphson method, an initial guess of the solution set must be supplied. In the procedure used in this thesis, the initial value of k at each wavenumber, ν, is determined through the relation

$$k = \frac{-\ln(1-A)}{4\pi\nu\, d}, \tag{4.9}$$

where A is the measured absorption and d is the thickness of the film. Equation 4.9 is derived by ignoring interference effects in the film and the reflection off the back of the substrate. A set of solutions is then found at each wavenumber using the above value of k and a range of n values centered about that derived in the near infrared. The correct solutions at each wavenumber can then be determined by looking for a continuum across the entire spectrum.

In general, the errors in n were quite large, so a continuum was sought in the values of k only. However, there were still regions where a solution could not be found. In order to

remedy the above situation, a new set of initial values was determined by interpolating between the accepted values of k and the above procedure was repeated. After one or two iterations a solution for the entire range could be found.

Once the absorption coefficient as a function of wavenumber was determined, a theoretical fit to the data was performed using Eq. 3.53. The experimentally determined absorption coefficient and the corresponding theoretical fit as a function of wavenumber for the films deposited at 1, 2, 4 and 8 Pa are shown in Figs. 4.17 through 4.20. The modeling parameters are given in Table 4.5.

An important factor is the overall accuracy of the absorption coefficient. Using Eq. 4.9 we can estimate the error as

$$\Delta\alpha = \frac{\Delta A}{(1 - A)\cdot d} \tag{4.10}$$

where ΔA is the uncertainty in the absorption. Equation 4.10 tends to overestimate the error in α as it ignores the effect of multiple reflections in the film which enhances the overall absorption (except at the quarterwave thickness) for a given absorption coefficient. The lowest measured amount of absorption in the films is approximately 5 %. Given a maximum value of 1% for ΔA (Fig 4.13) this results in an absolute error of 70 cm^{-1}. It is important to note that this is a systematic error rather than a random one and hence will tend to offset a good part of the spectrum. As a result the error in the terms in Table 4.4 will partially be absorbed by the Urbach tail. However this value does place a limit on how accurately one can measure the optical window where no molecular absorptions are present.

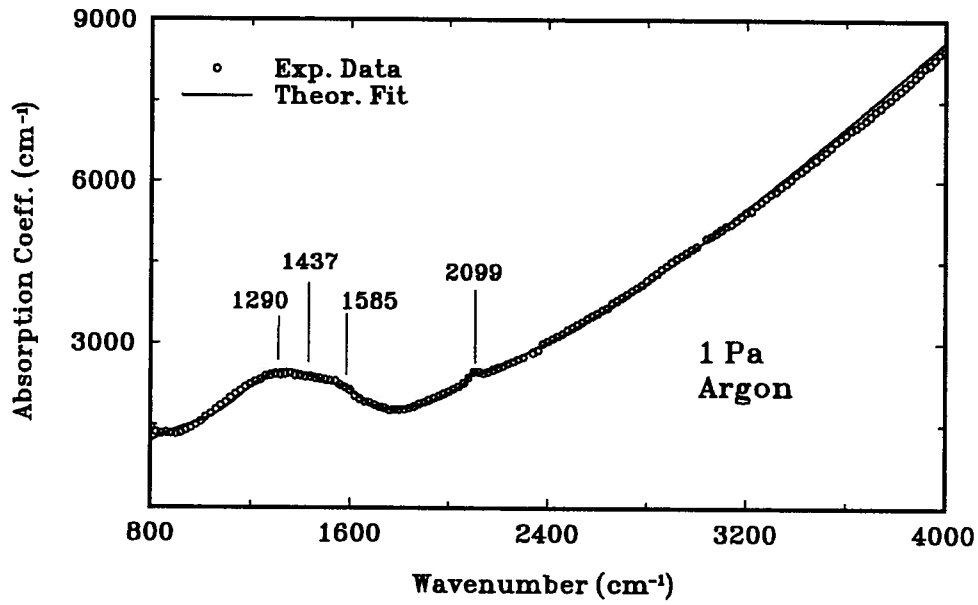

Figure 4.17 Experimentally determined and theoretically calculated absorption coefficient of the film deposited at 1 Pa in argon. The theoretical fit was determined through equations 3.51 and 3.52

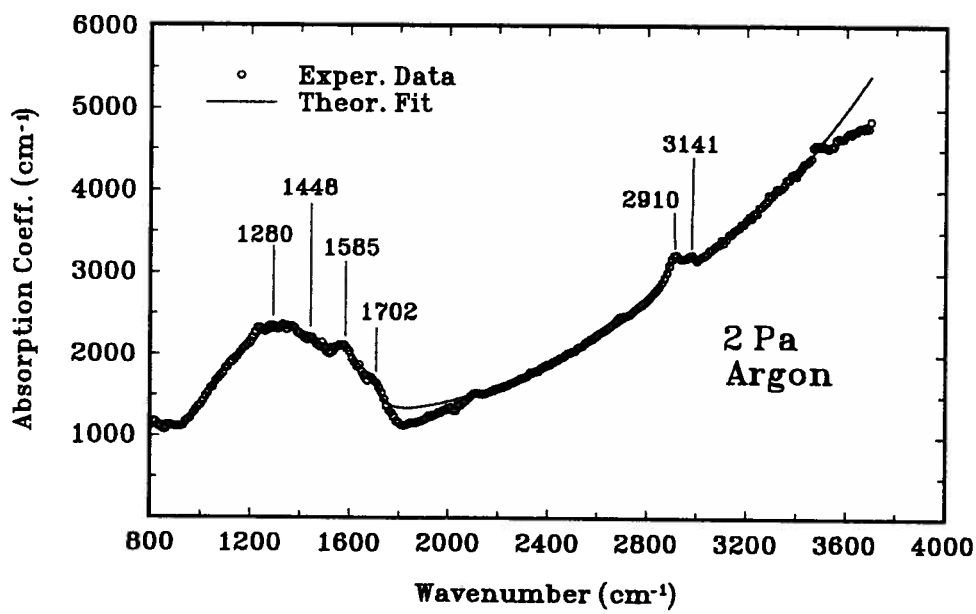

Figure 4.18 Experimentally determined and theoretically calculated absorption coefficient of the film deposited at 2 Pa in argon. The theoretical fit was determined through equations 3.51 and 3.52.

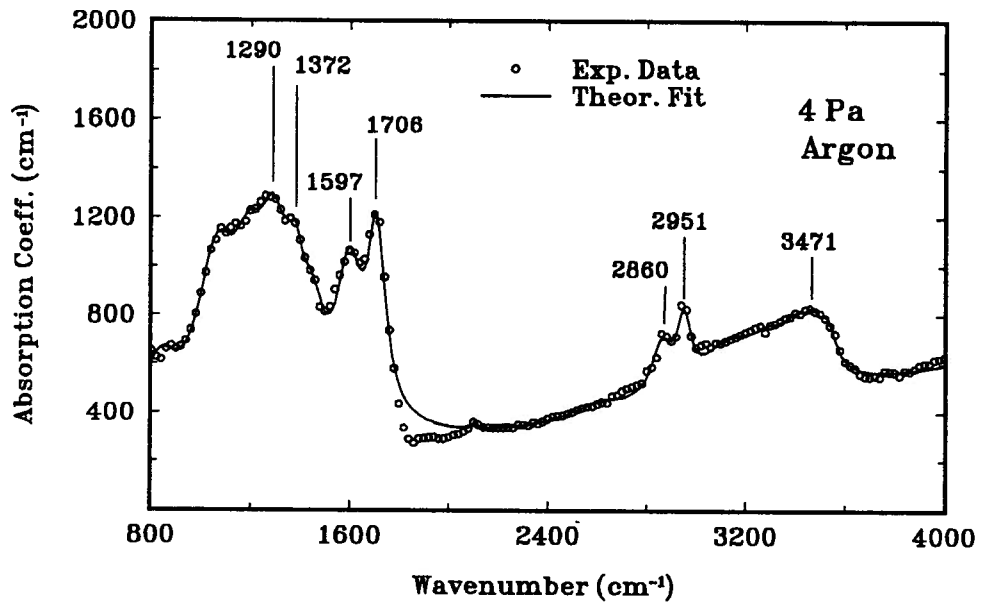

Figure 4.19 Experimentally determined and theoretically calculated absorption coefficient of the film deposited at 4 Pa in argon. The theoretical fit was determined through equations 3.51 and 3.52.

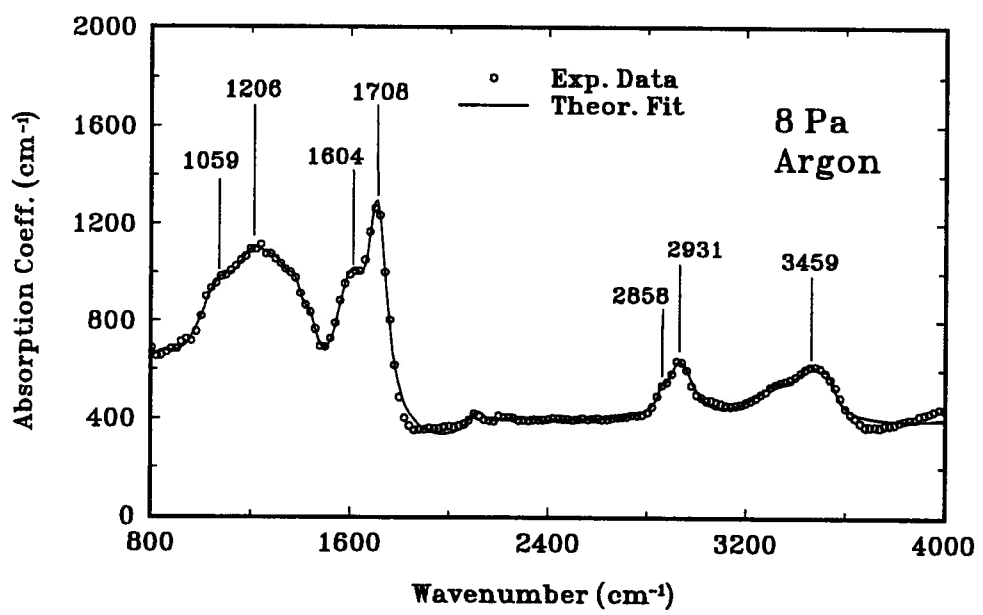

Figure 4.20 Experimentally determined and theoretically calculated absorption coefficient of the film deposited at 8 Pa in argon. The theoretical fit was determined through equations 3.51 and 3.52.

Table 4-4: Fitting Parameters and Possible Bonding Configurations for Films Deposited in Argon as a Function of Pressure

Possible Bonding	1Pa			2 Pa			4 Pa			8 Pa		
	ν_0	J	Γ	ν_0	J	Γ	ν_0	J	Γ	ν_0	J	Γ
(1)							3530	2.19	42.6	3514	1.38	38.0
							3471	1.50	39.2	3459	2.16	46.5
							3409	3.60	67.8			
(2)							3300	5.90	112.1	3324	3.72	87.2
(3)				3141	1.72	65.6	3129	11.6	156.1			
(4)				2975	0.26	6.4	2951	3.27	33.3	2931	5.45	60.5
				2910	8.23	59.4	2860	4.82	56.4	2858	0.29	15.2
(5)	2099	0.40	12.5				2106	0.13	4.79	2110	0.005	0.6
(6)				1707	3.95	21.4	1707	20.0	43.1	1708	17.8	38.9
(7)	1585	3.91	25.7	1585	33.3	61.4	1597	26.6	64.9	1604	22.1	66.9
	1523	8.66	38.0									
(8)	1437	22.9	68.9	1448	40.3	76.0	1447	14.3	61.9	1439	4.85	37.9
(9)				1382	10.9	42.4	1372	16.4	49.9	1378	7.56	39.1
(10)	1290	76.6	127.4	1280	81.4	91.7	1290	28.2	63.5	1306	17.6	60.3
				1112	133.5	133.4	1195	42.3	86.2	1206	32.2	77.7
	1067	41.7	202.4				1057	75.8	102.8	1059	53.3	108.2
				810	75.5	107.2	823	53.8	103.9	793	47.8	122.0

For the samples deposited at higher pressures, the mid-infrared can be divided into three regions. The first is the C–C network and CH_x deformation region at wavenumbers below 1700 cm^{-1}. Aside from the C=C stretch at around 1600 cm^{-1} it is difficult to identify any particular resonance. Hence the assignment of the bonding configurations given in Table 4.4 in this region are not the only possible ones. Adjacent to this region is a strong C=O resonance at around 1700 cm^{-1}.

The second region is a low absorption window between 1900 and 2700 cm^{-1}. This region is of interest for optical applications. The small peak at around 2100 cm^{-1} is attributed to nitrogen impurities. The third region is the result of CH_x and O–H stretch modes. There is also evidence of a weak Urbach tail.

The films deposited at lower pressures show evidence of a much stronger Urbach tail. This factor correlates well with the high absorption values in the visible regions. For the film deposited at 1 Pa there is no evidence of any CH, CO or OH bonds.

4.3.4 Discussion

The IR results show that with increasing pressure there is a general trend towards a lower overall absorption in the films. The spectroscopic results also show that there is unintentional hydrogen and oxygen incorporation in the films.

The most probable source of the impurities is the finite base pressure, which in turn, is primarily due to outgassing from the surfaces in the chamber. After several hours of diffusion

pumping, the outgassing consists predominately of water vapour (assuming good care is taken to keep the chamber clean which was the case during the course of this thesis). This factor would explain the presence of both oxygen and hydrogen in the films.

The incorporation of impurities at higher pressures is attributed to a change in the energetics at the substrate surface. It is not attributed to a change in the base pressure as care was taken to ensure that this was constant over the entire pressure range. At lower pressures the impurity atoms may be sputtered off due to the energetic impacts from the reflected neutrals. The carbon atoms remain due to the higher C-C bond strength (607 KJ/mol) than that of the C–H (338 KJ/mol) or the C=0 bond (532 KJ/mol in 0=C0).[140] The impurities due to nitrogen are still present due to the C≡N bond having a strength (754 KJ/mol) which is greater than the C–C bond.

A number of attempts were made to lower the impurity level of the deposition chamber, through baking and longer pumping times (several days). However, it was found that the system was operating at the optimum conditions.

Table 4.4 divides the possible bonding configurations into 10 separate types. In the region between 2700 cm^{-1} and 3350 cm^{-1} there are the resonance vibrations due to CH stretch modes. Configuration 2 is contributed to hydrogen bonded to sp^1 (acetlynic) carbon.[141] which is present in the films deposited at 4 and 8 Pa. Lower in wavenumber are a number of resonance vibrations due to hydrogen bonded to sp^2 carbon (configuration 3).[142] In addition, there are a number of vibrations at wavenumbers usually assigned to either CH_2 and CH_3 stretch modes in organic molecules or hydrogen bonded to sp^3 carbon.[143]

There are also two indications of oxygen in the films. The first is due to H–O resonance vibrations in the region from 3400 to 3550 cm^{-1} , which are present in the films deposited at 4 and 8 Pa. Values in this region are more typical of those found for bonding in organic molecules than that for H_2O (3675 cm^{-1} symmetric and 3756 cm^{-1} antisymmetric). There is also a strong peak in the higher pressure films at around 1700 cm^{-1} due to C=O bonding and a relatively low one for the film deposited at 2 Pa.

Of particular interest is the C=C bond around 1600 cm^{-1}. This has two possible sources. The first is from the presence of organic molecules in the film matrix. The second possible source is the single phonon vibration in graphite.[34]

The last three assignments, configurations 8,9 and 10 are somewhat arbitrary as there is a high degree of overlapping between the various resonances. Hence it is difficult to perform any type of analysis with the results in these regions.

The infrared results for the films deposited at high pressures have a number of similarities with those in the literature deposited under different deposition conditions but which also exhibit low absorption in the visible.[1,34] In all of these cases there is the presence of hydrogen in the films. The effects of hydrogen incorporation in diamond-like films is explained below.

In amorphic 4-fold coordinated solids such as silicon and germanium, the incorporation of hydrogen is thought to passify dangling bonds.[144] As a result, hydrogenated forms of these materials are generally less optically absorbing. Amorphous carbon films are inherently more complicated than silicon and germanium due to the additional ability of the material to form

sp^2 type bonds. In this case an additional role for hydrogen is to allow for different sp^3/sp^2 bonding ratios.

A theoretical study was performed by J. Angus and F. Jansen[145] where the amount of hydrogen incorporation in carbon was predicted using a random covalent network. In this case the role of the hydrogen was to ensure that the network was properly constrained, that its the number of constraints per atom equaled the number of degrees of freedom: 3.

The results of the model gave an upper limit and lower limit for hydrogen incorporation of 60% and 20 % respectively. Above 60 % the carbon matrix would be underconstrained resulting in a soft polymer-like material. Below 20 % hydrogen incorporation, the material would be overstrained and reconstruct, possibly into graphitic clusters. Therefore with decreasing percentage of hydrogen the graphitic island model of Robertson would appear to be more appropriate.

The theoretical results matched those in the literature quite well for films with a higher hydrogen content.[146] However, for the lower hydrogen films, the films were less graphitic than predicted. It was felt that this was the result of the presence of medium range order in the materials which would also reduce the stress in the films.

The incorporation of hydrogen at low levels is also thought to reduce the number of dangling bonds in sp^3 carbon and reduce the bonding between the graphitic clusters.[147] This, in turn, would also reduce the mobility of the π electrons. The resulting material would be more transparent, have an increase in the resistivity and be softer. It would also allow for a

smaller island size, by allowing for the creation of more sp^3 bonds, increasing the optical bandgap.

One possibility for the increase in transparency for the films deposited at higher pressures, then, is the incorporation of hydrogen. This factor is also a possible explanation for the observed decrease in hardness and the increase in the resistivity. However from Table 4.4 and from Figs. 4.18 to 4.20 there does not appear to be a large degree of difference in the degree of hydrogen concentration if the integrated area under the absorption curves for the C-H stretch vibrations between the films deposited at 2, 4 and 8 Pa are considered. Hence it is difficult to say if the change in the transparency is the result of hydrogen incorporation alone.

A set of experiments which were complementary to the ones in this thesis was performed by J. Ullman *et.al.* .[148] In this study, carbon films were deposited through r.f sputtering in a pure argon atmosphere at approximately 1.3 Pa. The target voltage was varied over the range from −1500 to −2900 V.

Ullman's results showed that the IR transparency of the films increased with decreasing target voltage. However the hydrogen concentration in the films was relatively constant at around 8 %. This level is much lower than those typically found in the literature when hydrogen is intentionally incorporated (20 to 60 %).

Ullman argued that the reason for the increase in transparency was the reduction in energy of the target reflected neutrals and of the secondary electrons. It was felt that the lower of the energetics at the substrate resulted in a reduction in the graphitic island size (assuming Robertson's model) . A lower energy environment would lead to a faster quenching time

which could possibly result in a smaller over grain size. An increase in the optical bandgap has also been observed in the literature when the substrate temperature was lowered during deposition to 77 K.[149]

The films deposited as a function of pressure in this study are consistent with the above results. The decrease in hardness could also be explained through the lowering of the bombardment energies. As the formation of sp^3 bonds is thought to be the result of ion bombardment, a reduction in this factor could decrease the amount of linking between the graphitic islands.

In addition to hydrogen there is also the incorporation of oxygen in the films. The oxygen is bonded both to hydrogen and to carbon. This factor is relatively low for the films deposited at 2 Pa but increases for the films deposited at a higher pressure. This factor suggests the presence of organic molecules bonded onto the carbon matrix or some form of polymer phase in the film which grows with increasing pressure. The latter result would be consistent with those for films deposited from chemical vapour deposition (CVD) under low energy conditions.[150]

In the CVD process the energetic bombardment is controlled entirely by the biasing of the substrate through the bombardment of ionized particles. Below approximately −100V a polymer is deposited. Above −100 V a diamond-like film is deposited with a decreasing hydrogen content with increasing bias. At approximately −600 V the bombardment energy is enough to drive off all of the hydrogen and an opaque film is deposited as a result.

The results in this study are consistent with those of the CVD process if we consider the primary source of energetics to be the reflected neutrals. At low pressures there is no evidence of hydrogen in the films. The presence of the C=C resonance vibration is most likely due to the single phonon process of graphite. As the pressure increases this vibration increases relative to the other vibrations in the region. As it is unlikely the amount of sp^2 bonding is increasing to a large degree, this factor is most likely due to the growth of an organic phase in the material. At 8 Pa the film is not completely polymerized, however, as there are still resonances associated with sp^3 carbon. This is probably due to the relatively small amount of hydrogen present compared to the CVD method.

Polymer materials deposited in CVD processes are highly transparent and have a refractive index between 1.5 and 1.8. One possibility considered was that the 8 Pa film was a combination of the material deposited at 1 Pa and a polymer. This can be discounted through the re-examination of the Wiener-bounds. In this case the dielectric function for the 8 Pa film does not lie in the boundaries required for an isotropic material. This factor is enhanced if we consider the additional effects of voids in the higher pressure films. Hence, if a polymeric phase is present, there must also be a change in the bonding configuration of the diamond-like phase.

Therefore, at this point, there appear to be three possibilities for the change in the properties of the diamond-like films as a function of pressure. The first is the incorporation of hydrogen which pacifies the dangling bonds. The second is the growth of a separate soft,

transparent polymer phase. The third is a reduction in the graphitic island size. It is possible that all three processes are happening concurrently.

4.4 Amorphous Carbon Films with Oxygen, Nitrogen and Hydrogen.

4.4.1 Introduction

A series of studies similar to those performed in the last section were undertaken for a number of films deposited in an argon/reactant gas mix. The purpose of this investigation was two-fold. The first reason was to allow for a better understanding of how the impurities observed in the infrared spectra in the previous section affected the properties of the films. In this case, the "impurities" were to be added intentionally and primarily at pressures low enough to prevent the inclusion of additional background gases. The second reason was to compare the resultant properties with those films deposited in pure argon. This would allow for a determination of the optimum deposition conditions for infrared optical applications.

The initial tests were again centered around ellipsometry, due to the relative ease of this technique at this point in the thesis. However, the complementary techniques used to analyze the films were more selective in this section. Once these were undertaken, infrared analysis was performed when deemed necessary.

The first section looks at the effects of intentionally introducing oxygen into the sputtering gas. This section is fairly brief and is intended to complement the next section

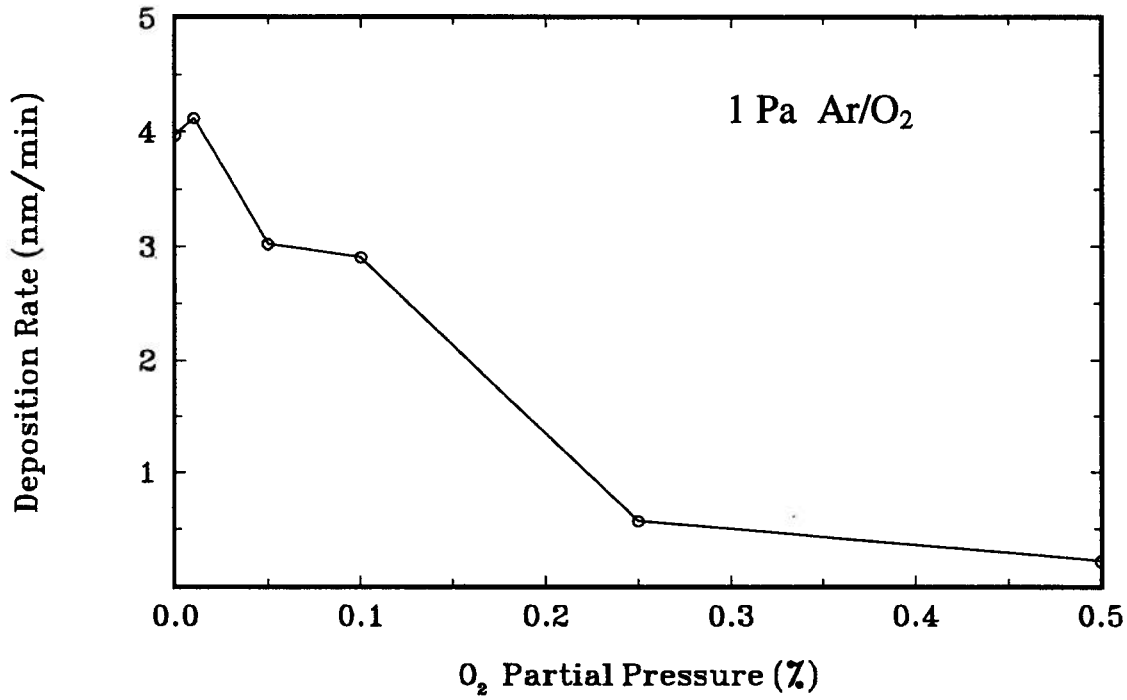

Figure 4.21 Deposition rate vs. O_2 partial pressure for amorphous carbon films deposited in a O_2 / Ar mix. The total deposition pressure was 1 Pa.

which examines the effects of hydrogen. The final section investigates the properties of films deposited in argon/nitrogen sputter gas mix.

4.4.2 Amorphous Carbon Films with Oxygen

An ellipsometric study of set of films deposited in a argon/oxygen mix was performed. The total deposition pressure was 1 Pa. The O_2 partial pressure was varied from 0.0 to 0.5 Pa.

There was a small increase in the transparency of the films with an increasing O_2 partial pressure; with approximately a 10% overall increase in the pseudo-bandgap. A more dramatic effect was observed for the deposition rate (Fig 4.21) which experienced an order of magnitude reduction at the highest partial pressure.

There are two possible explanations for the decrease in the deposition rate. The first possibility is that the oxygen is reacting with the loosely bound surface atoms at the substrate to form carbon monoxide or carbon dioxide. It has been shown that the presence of O_2^+ and oxygen atoms can etch away diamond-like films deposited through r.f. plasma decomposition.[151] A preferential etching could also be the reason for the small increase in the transparency of the film. The second reason is that the oxygen is reacting with the target surface. It is unlikely that this phenomena has any effect on the films deposited in intentionally pure argon due to the relatively low levels of the oxygen.

Infrared measurements of a film deposited in an 0.1 Pa O_2 / 0.9 Pa Ar mix were taken. The results were similar to those for the film deposited in a pure argon atmosphere at the same total pressure (Fig 4.18) , with no evidence of CO or OH bonds.

It would appear, then, that oxygen is only incorporated when there is the additional presence of hydrogen. This observation lends weight to the argument in section 4.3.4 that there are organic molecules bonded onto the carbon matrix or a polymer phase in the films deposited at high pressures in intentionally pure argon.

4.4.3 Amorphous carbon with hydrogen (a-C:H)

a) Experimental and Results

Two sets of ellipsometric measurements were performed in this section. In both cases, the optical constants of the materials were determined as a function of H_2 partial pressure. The first set of films were deposited at a total pressure of 1 Pa and the second set at a total pressure of 8 Pa. The Farouhi-Bloomer model was used to determine the optical properties of the films.

Electron diffraction results showed that the hydrogenated carbon films were amorphous. The resistivity of the films deposited at the highest hydrogen concentration in each case was greater than the maximum limit of the 4-point probe (10^5 - cm^{-1}). The film deposited at a total pressure of 8 Pa , and a hydrogen partial pressure of .03 Pa appeared to be relatively soft compared to the other films. Infrared analysis of a film deposited in a 0.9 Pa Ar and 0.1 Pa H_2 mix was performed. The experimentally determined and theoretically calculated mid-infrared absorption coefficient as a function of wavenumber is given in Fig. 4.23. The model parameters are given in Table 4.5 along with those for the films deposited in pure argon at 1 and 8 Pa. The near infrared *k* values of this set of three films are given in Fig 4.24.

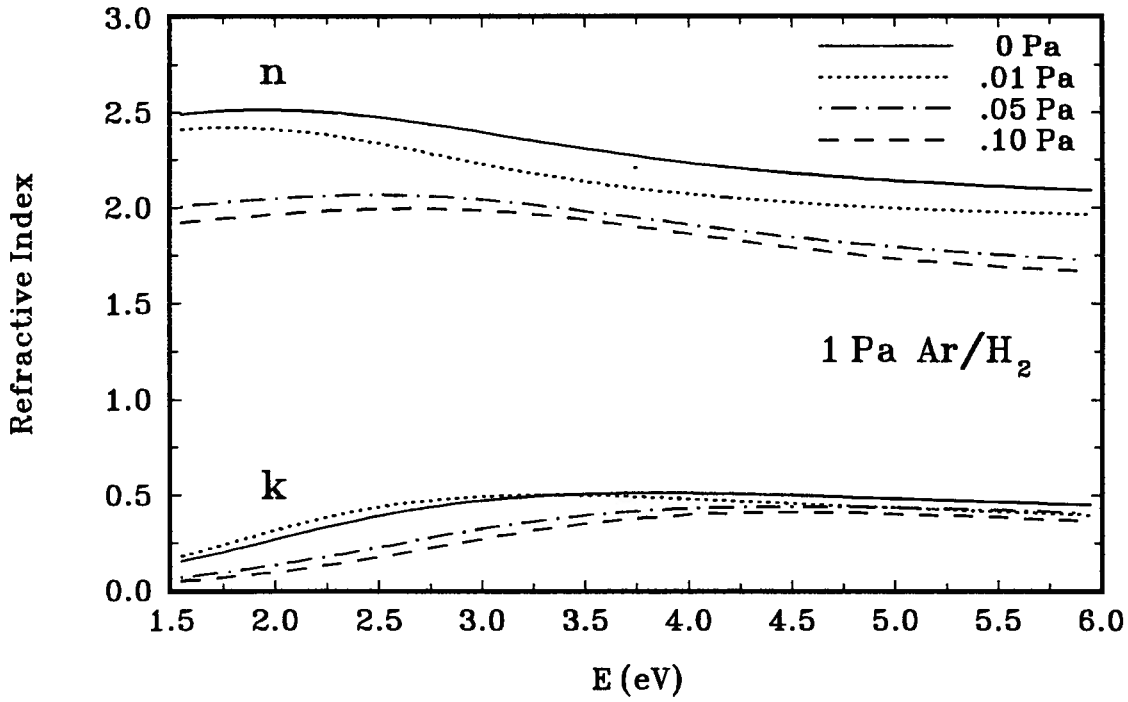

Figure 4.22 Real (n) and imaginary (k) refractive indices vs. photon energy for carbon films deposited in an Ar/H_2 mix for a number of different partial pressures of hydrogen. The total deposition pressure was 1 Pa.

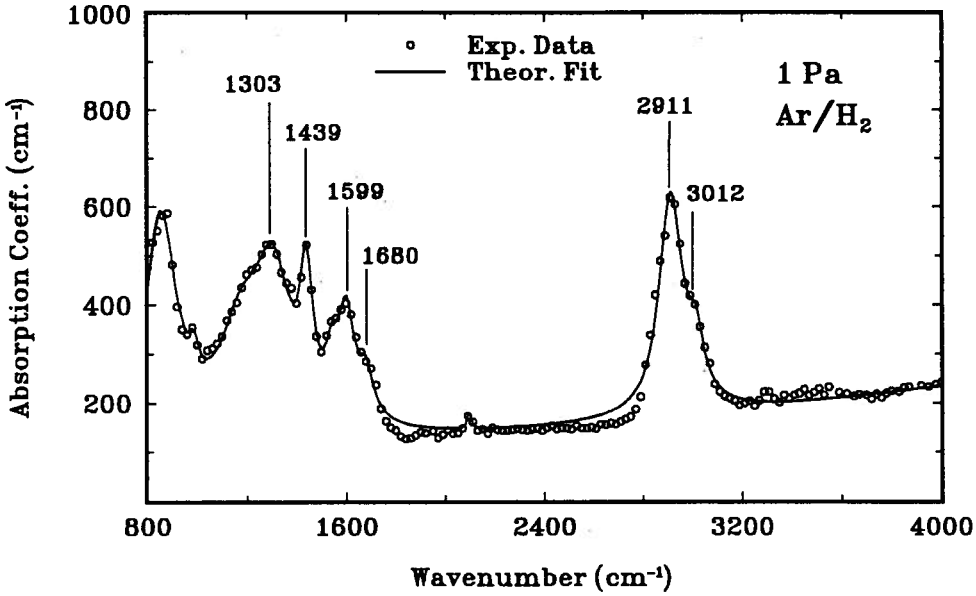

Figure 4.23 Absorption coefficient of the film deposited in 0.1 Pa H_2 and 0.9 Pa Ar. The theoretical fit was determined through equations 3.52 and 3.53.

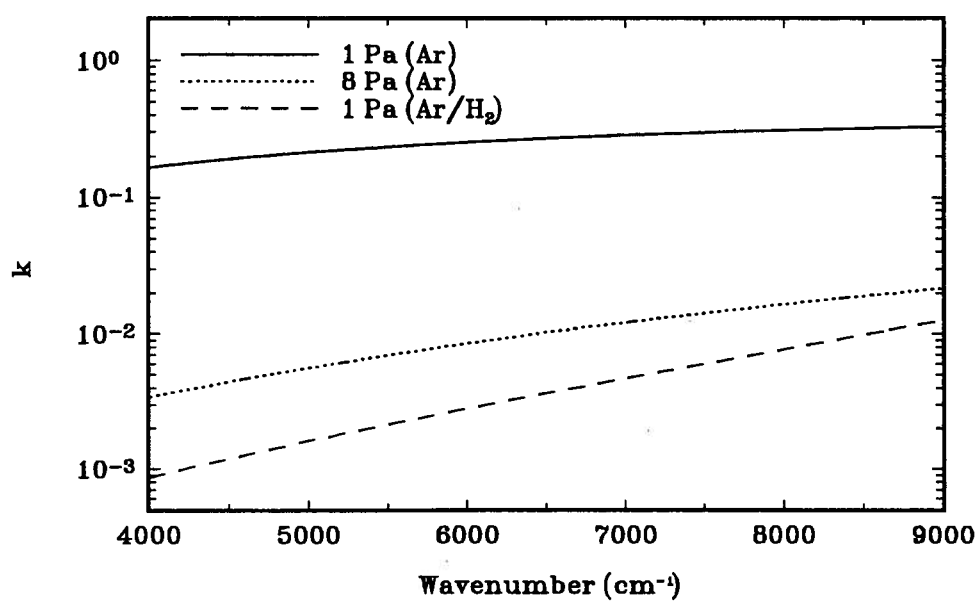

Figure 4.24 Log of k vs. wavenumber for films deposited at 1 and 8 Pa in pure argon and for a film deposited in 0.1 Pa H_2 and 0.9 Pa in argon. The values of k were determined through fitting the reflection spectra to the Farouhi-Bloomer model.

Table 4.5 Fitting Parameters and Possible Bonding Configurations for Films Deposited in Argon and in an Argon / Hydrogen Mix.

Possible Bonding	1Pa (Ar)			8 Pa (Ar)			1 Pa (Ar/H_2)		
	ν_0	J	Γ	ν_0	J	Γ	ν_0	J	Γ
(1)				3514	1.38	38.0			
				3459	2.16	46.5			
(2)				3324	3.72	87.2			
(3)							3012	1.69	39.2
(4)				2931	5.45	60.5	2911	9.65	56.4
				2858	0.29	15.2			
(5)	2099	0.40	12.5	2110	0.005	0.6	2095	0.16	6.8
(6)				1708	17.8	38.9	1680	1.84	32.6
(7)	1585	3.91	25.7	1604	22.1	66.9	1599	6.22	41.9
	1523	8.66	38.0				1541	1.69	27.4
(8)	1437	22.9	68.9	1439	4.85	37.9	1439	5.61	28.9
(8)				1378	7.56	39.1			
(9)	1290	76.6	127.4	1306	17.6	60.3	1303	21.5	89.9
(10)				1206	32.2	77.7	1175	24.1	118.7
	1067	41.7	202.4	1059	53.3	108.2	985	1.42	21.2
				793	47.8	122.0	847	49.5	78.0

1): H-O (sretch) (2): hydrogen bonded to sp^1 hybridized carbon (stretch) (3):hydrogen bonded to sp^2 hyberdized carbon (stretch) (4): hydrogen bonded to sp^3 hyberdized carbon (stretch) (5) C≡N (6): C=O stretch (7): C=Cstretch (8): C-H rock or CH_2 deformation (9): CH_2 symmetric bending (10): sp^2 - and sp^3 - hybridized carbon.

The optical constants for the films deposited at 1 Pa total pressure are presented in Fig 4.23. The pseudo-bandgap increased from 0.3 to 1.4 eV over the range of H_2 partial pressures. The maximum bandgap was achieved at a hydrogen partial pressure of 0.1 Pa.

For the set of films deposited at 8 Pa the maximum bandgap was achieved at a hydrogen partial pressure of .03 Pa, increasing from 1.2 to 1.5 eV. A higher hydrogen partial pressure did not result in a change in the optical properties of the films.

b) Discussion

The infrared results for the film deposited in an argon/hydrogen mix differ in nature from those for the films deposited in the last section which also show the presence of hydrogen. A comparison of the C–H stretch bands for these films is given in Fig 4.25 where the spectrum for each film has been displaced by a constant amount for comparison purposes.

An important criteria is the integrated area under the absorption spectra,[152] α_o :

$$\alpha_0 = C_0 \int \alpha(\nu) d\nu \tag{4.11}$$

where α is the absorption due to the C–H bonds and C_0 a proportionality constant. The value of α_0 gives the amount of bonded hydrogen in the films.

The value of α_0 for the individual films has not been calculated for two reasons. The first is that the constant of proportionality is difficult to determine and there is some controversy over its exact value, due to various types of carbon bonding.[153] The second reason is that the additional presence of a strong Urbach tail for a number of the films makes the evaluation of the integral quite difficult. However, a visual inspection of the spectra shows that there is a larger amount of hydrogen present in the film deposited in a Ar / H_2 atmosphere than the other films, all which appear to have roughly the same amount of C–H bonds in the sp^3 region.

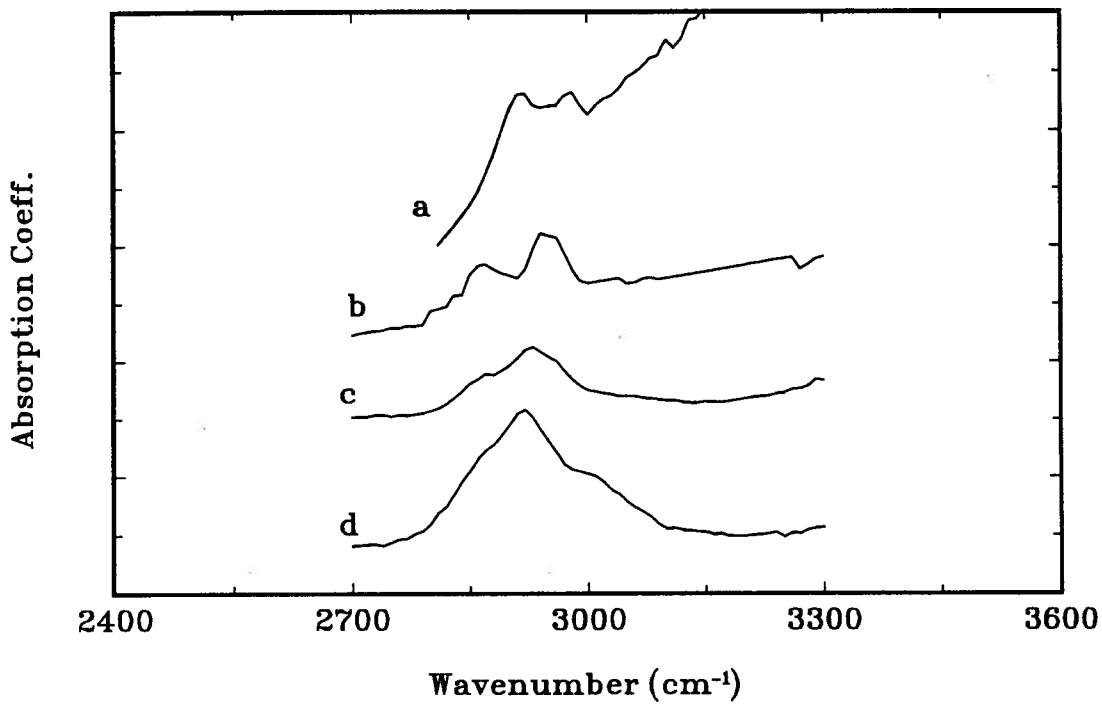

Figure 4.25 C–H stretch vibrations for films deposited in pure argon at a) 2 Pa, b) 4 Pa c) Pa and d) 0.1 Pa H_2 and 0.9 Pa argon. The spectra has been shifted for comparison purposes.

One other feature of interest in this region is the nature of the stretch vibrations. Unlike the films deposited at 4 and 8 Pa in argon, there are no resonaces due to sp^1 bonding in the films deposited in an H_2/Ar atmosphere (Tables 4.4 and 4.5). In addition, the low ratio of hydrogen bonded to sp^2 and sp^3 carbon respectively appears closer to that of the 2 Pa film rather than the films deposited at higher pressures.

From Tables 4.4 and 4.5 it can be seen that the degree of oxygen incorporation is much less for the film deposited in a hydrogen/argon mix than that of the high pressure films. In

addition the peak due to the C=C bond is also smaller and comparable to the film deposited at 1 Pa in pure argon.

The above results indicate that either a polymer phase is not present in the film deposited in an H_2 / Ar atmosphere or that it is much less than that in the higher pressure films. In addition, most the hydrogen appears to be bonded to sp^3 carbon. Therefore, under these conditions, the hydrogen appears to be the reason for the more diamond-like properties of the films.

The ellipsometric results indicate that the incorporation of hydrogen is more easily achieved at higher pressures. This observation lends weight to the argument that the presence of hydrogen is due to a change in energetics at the substrate rather than an increase in the base pressure. In addition, the softness of the film deposited with intentional hydrogen incorporation at high pressures indicates that a polymer phase does grow under low energy conditions.

A similar study was performed in the literature for magnetron sputtered films where hydrogen was intentionally introduced at low overall pressures (though without the mid-infrared results).[6] It was found that there were no measurable changes in the properties of the films when the H_2 partial pressure was greater than 5 %. In addition there was a reduction by a factor of three in the hardness between the a-C and a-C:H films. As the hardness of the films in this thesis decreased by a factor of about 7 when the pressure was varied between 1 and 8 Pa, this would also indicate that there is a softer phase in the high pressure films.

One possible explanation for the trend observed for the films deposited as a function of pressure is as follows. At low pressures, hydrogen is not easily incorporated into the film due to the highly energetic reflected neutrals. However, a limited amount of sp^3 bonding occurs due to high pressure/temperature spikes. As the pressure increases the hydrogen present in the chamber can now be incorporated into the film. As the majority of the hydrogen initially appears to be bonded to sp^3 carbon, this is similar to the case where hydrogen is purposely introduced at lower pressures. However the lower amount of hydrogen present prevents the same degree of change in the optical properties of the film.

As the pressure increases further, it becomes increasingly easy to incorporate hydrogen, which can further stabilize sp^3 bonding. However the lower energetics at the substrate result in a decrease in the probability of the creation of diamond bonds. As a result, an organic or polymer phase also occurs due to the presence of hydrogen and oxygen.

4.4.4 Carbon Nitride Films

a) Introduction

Recently there has been good deal of interest in the ability to deposit carbon nitride films. This interest is primarily due to a theoretical study by A.Y.Liu and M.L.Cohen[154] which predicted that the hardness and thermal conductivity of the phase β-C_3N_4 was on the order of that of diamond. At the time of the writing of this thesis the above material had not

been synthesized though a number of attempts to deposit thin films of β-C_3N_4 had been made. A number of the studies in the literature relevant to this thesis are outlined below.

A comprehensive investigation was performed by C.J. Torn *et. al.* .[155] In this study, the properties of the films deposited through r.f. sputtering were examined as a function of N_2 partial pressure. The optical band-gap was observed to increase from 1.1 to 1.4 eV for a maximum nitrogen incorporation of 10%. An internal reduction in stress was also reported for the films.

An increased incorporation of nitrogen of up to 40 % was reported for films deposited through dc sputtering[156] and through ion assisted deposition.[157] In addition, the hardness of the films was shown to be comparable to the a-C:H films in the literature.[156]

One additional study showed that the nitrogen in the a-C:N films was chemically bonded to the carbon atoms through both infrared and Raman spectroscopy.[8] However, the optical constants in the infrared were not determined.

A study was undertaken in this thesis to examine the optical properties of a-C:N films in more detail. The properties of the films were investigated as a function of N_2 partial pressure and total deposition pressure.

b) Experimental

A set of ellipsometric studies was performed both as a function of N_2 partial pressure and total pressure. The preparation techniques were the same as outlined in section 4.2.2. The optical constants were determined through the Forouhi-Bloomer model.

The films deposited at high N_2 partial pressures exhibited poor adhesion on both silicon and gallium arsenide substrates. By introducing a carbon intermediate layer between the substrate and the film, the overall adhesion could be improved. However, films on the order of a micron could still not be grown on the GaAs substrates, which prevented IR measurements from being performed for this material.

c) Results and Discussion

The optical constants for a number of films deposited in Ar and N_2 are presented in Fig. 4.26. Shown are the values as a function of photon energy for a film deposited at 1 Pa in pure argon and for films deposited in pure nitrogen at 1, 2 and 4 Pa.

For the films deposited as a function of N_2 partial pressure at low overall pressures there was a noticeable change in the optical properties as illustrated in Fig. 4.26. However it was found that at 50 % partial pressure the pseudo-bandgap had increased to 90 % of its final value. The relative change in the optical properties as a function of nitrogen partial pressure decreased with increasing overall pressure until at 8 Pa no difference could be observed.

One noticeable effect was a dramatic increase in the deposition rate as a function of nitrogen partial pressure. This factor is illustrated in Fig. 4.27 for a set of films deposited at 1 Pa overall pressure where an eight-fold increase in the deposition rate is observed. This factor is an important technological advantage as the deposition rate of sputtered carbon is relatively low when compared to the more predominate CVD process.

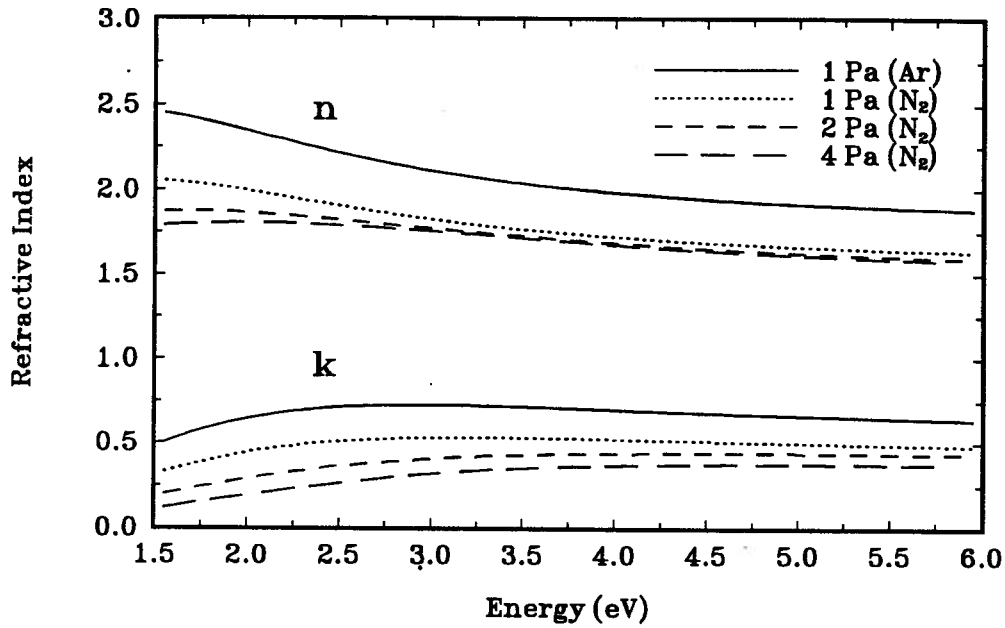

Figure 4.26 Refractive index measurements for films deposited in argon and N_2 . The refractive indices were determined through the Forouhi-Bloomer model.

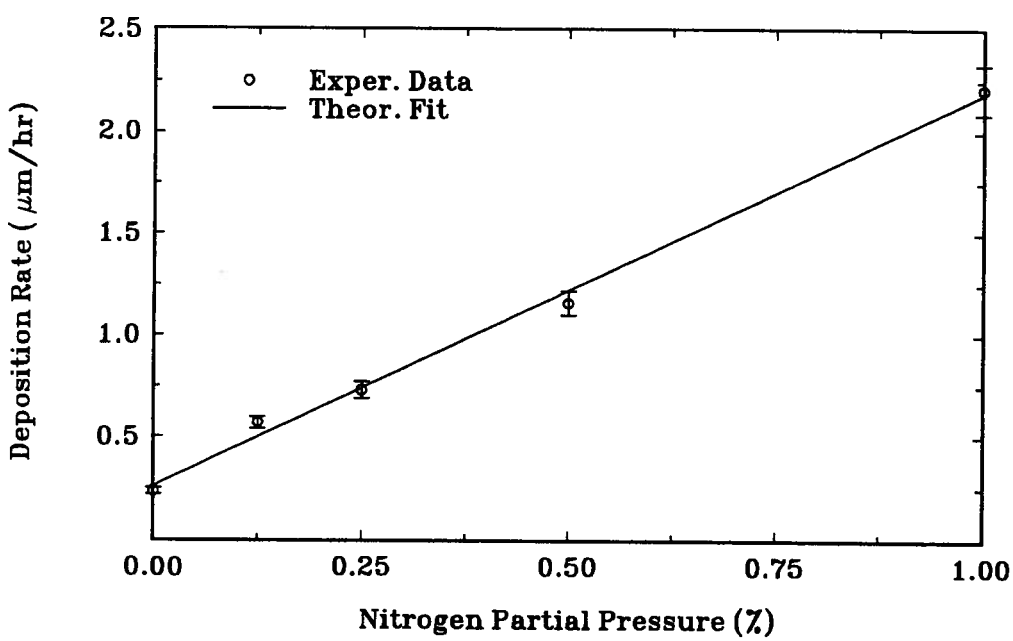

Figure 4.27 Deposition rates vs. N_2 partial pressure for films deposited in a nitrogen / argon mix. The deposition power was 100 W and the total pressure was 1 Pa.

As the maximum degree of nitrogen incorporation observed in the literature is approximately 40 %, the above increase can not be explained in terms of nitrogen incorporation alone. The increase in the deposition rate is also attributed to chemical sputtering of the target.[158] In this method, the bombarding ions react with the target atoms, increasing the overall sputter rate.

From the above ellipsometric results it would appear that the incorporation of nitrogen does not result in same degree of change in the optical properties as that of hydrogen at lower pressures. In addition, from the results at higher pressures, it would appear that nitrogen does not enhance the optical properties once hydrogen is also present. This is in good agreement with a study in the literature which showed that the presence of nitrogen caused a small decrease in the optical bandgap for diamond-like films deposited through chemical vapour deposition.[159]

The main advantage of a-C:N films, then, appears to be the relatively high deposition rates. However, the additional presence of a large CN resonance at 2100 cm^{-1} in the middle of the optical window could also be problematic.

4.5 Technical Feasibility

One of the most important coatings is the single layer anti-reflection coating (Eq. 2.29). As discussed previously, diamond-like carbon films are well suited as anti-reflection coatings on germanium optics as the latter material has a refractive index of approximately 4.1 in the infrared.[160]

A theoretical study was undertaken to examine the feasibility of using the films studied in this chapter for the above purpose. The model assumed a single layer coating on one side of a germanium window. The thickness, d, at each wavelength, λ,. was given by

$$d = \frac{\lambda}{4n} \tag{4.11}$$

where n is the refractive index of the given material. The value of n for each material was essentially a constant and equal to that in the near infrared red.

The reflection, transmission and absorption at the quarter-wave thickness at each wavelength was calculated for the films deposited at 1, 2 , 4 and 8 Pa in argon, and for the film deposited at 1 Pa in an argon/hydrogen mix. One problem for the last two films was that there was a discontinuity in the k-values at the boundary between the near and mid-infrared. This was attributed to the small error in the fit for the model in the near infrared. As the value of k is very sensitive to this factor when its overall value is small, this leads to large relative errors. The near infrared values of k for these two films were then determined by interpolating between the value measured at 4000 cm^{-1} in mid infrared studies and the value measured at 9000 cm^{-1} in near infrared ones.

As the films were antireflecting, the value of R at each wavelength was approximately that of the back surface of the germanium substrate, 37 %. The absorption values ($1-R-T$) are given in Fig. 4.28., except for the 2 Pa film which were very similar to the those for the film deposited at 1 Pa.

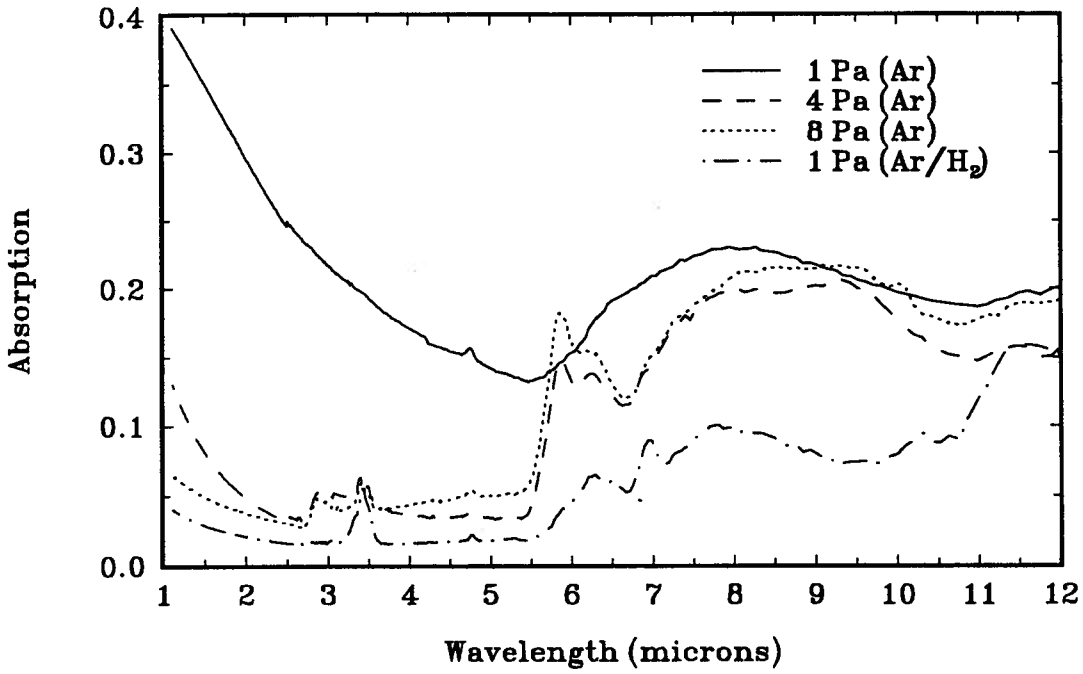

Figure 4.28 Theoretical absorption as a function of wavelength for quarter-wave carbon films on germanium. Note that the thickness is not constant as a function of wavelength but that of Eq. 4.11.

Aside from the film deposited at 1 Pa, there is a relatively low absorption window between 2 to 5 Pa, discounting the C-H absorptions around 3 μm. The lowest values are for the film deposited in a Ar/ H_2 atmosphere. Aside from the previously mentioned film, the absorptions are approximately equal in the region between 8 to 12 μm. Though the value of the absorption coefficient is higher in Fig. 4.17 than in Figs. 4.19 and 4.20, this factor is partially offset by the larger refractive index which decreases the necessary physical thickness required for quarter-wave conditions.

If the main criterion is the maximum possible transmission, then the film deposited in a Ar/ H_2 atmosphere is clearly the ideal choice. As the reflection from a germanium surface is approximately 37 %, the film will enhance the transmission over the entire wavelength range. This film is also well suited to be used as termination layer for a broadband anti-reflection coatings on infrared materials in the range from approximately 1 to 6 μm.

Though the film deposited at 1 Pa appears unsuitable for optical applications, it should not be dismissed. If a 20 % reduction in transmission is acceptable, then the hardness of the material may make it the ideal choice. Many current commercially available optical filters have relatively low transmissions; typically on the order of 60% or less.[161]

GERMANIUM CARBIDE

5.1 Introduction

Once the diamond-like films were characterized the next step was to be able to deposit the intermediate materials for the optical multilayers. A suitable choice for the mid-infrared is germanium carbide, which is sometimes used in protective optical multilayers which employ diamond-like films.[14,162] Germanium carbide is an alloy which can range from pure carbon to pure germanium. The desirable properties of this material are outlined below.

The most important property of germanium carbide is its tunable refractive index, which varies almost linearly with the carbon fraction from 4.1 to 1.8.[163] This factor allows for a good deal of flexibility in the design of optical coatings. Infrared studies have shown that there is Ge-C bonding over the entire alloy range,[164] indicating that this property is not merely the result of a dielectric average of the individual carbon and germanium phases. The material is also quite hard if a sufficient fraction of the material is carbon.[164]

There are two main methods for depositing germanium carbide, plasma assisted chemical vapour deposition (PACVD)[165] and reactive sputtering.[166] In the PACVD method, germane (GeH_4) and a hydrocarbon gas, typically methane, are used as the source of germanium and carbon. The main disadvantage of this method is the very high toxicity of the germane gas. In the reactive sputtering method, a germanium target is sputtered in an argon/hydrocarbon mix. A serious drawback to this method is that an increasing methane fraction will ultimately poison the target, leading to the deposition of either diamond-like

carbon or a polymer. This factor limits the attainable refractive index range from 4.1 to approximately 3.

As the goal of this thesis is to develop the ability to deposit multilayers through magnetron sputtering alone, the restriction on the refractive indices is a potential problem. One possible solution is through co-sputtering of two targets of carbon and germanium oriented at an angle.[167] One can then tune the refractive index through adjusting the power ratio to the targets. If absorption due to dangling bonds is a problem, then hydrogen gas can be introduced into the chamber.

Despite its simplicity, there are a number of drawbacks to the above configuration. The oblique angle of incidence of the deposition flux results in shadowing effects. In addition the deposition rate is reduced under these conditions. Finally, this method makes the design of larger systems quite complicated.

An alternative method, which is examined in this thesis, is to deposit alternate layers of germanium and carbon. If the layers are thin enough, interdiffusion between the layers should result in the formation of germanium carbide. This method would lend itself well to a system with either rotating substrates or targets. The same chamber could also be used to deposit the diamond-like films. This technique can also compensate for the relatively low sputter rate for carbon compared to germanium by having a greater number of carbon targets. In addition, the deposition rate could be enhanced by introducing methane into the sputter gas which would decrease the required thickness of the carbon layers.

Interdiffusion between the individual layers has been studied extensively in x-ray multilayer systems.[168,169] However, the focus of these studies has been to have as sharp an interface as possible.

Two factors have been found which affect the amount of diffusion between the individual materials in multilayer systems. The first is the degree of energetic particle bombardment. In general, an increase in the deposition energetics results in an increase in the amount of diffusion. The second factor is surface roughness. An increase in surface roughness in one material results in a mixed layer as the second material is deposited. The atoms in this mixed layer can then interdiffuse.

A study was performed to examine the degree of interdiffusion as a function of substrate bias and deposition pressure. An increase in substrate bias increases the energy of the bombarding ions, but reduces the amount of surface roughness. In turn, an increase in pressure results in a larger degree of surface roughness but reduces the energy of the reflected neutrals. Therefore, in both cases, there are two competing factors which can effect the amount of diffusion.

The germanium and carbon multilayers were analyzed through in-situ ellipsometry. The significance of these techniques with respect to the above systems is discussed in the next section.

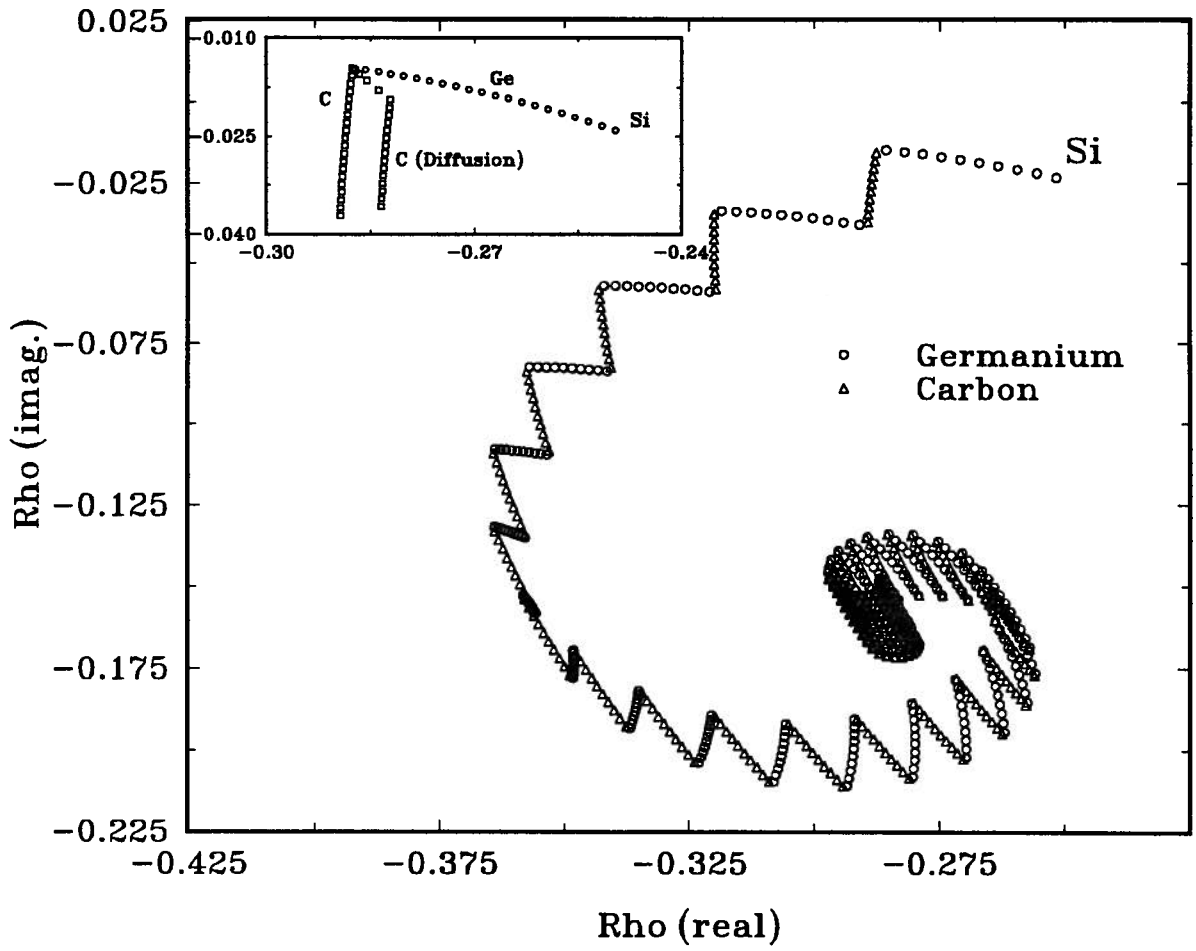

Figure 5.1 Theoretical trajectory for a germanium/carbon multilayer deposited onto silicon. The thickness of the individual layers is 2.0 nm. The inset shows the difference between a sharp and diffuse layer.

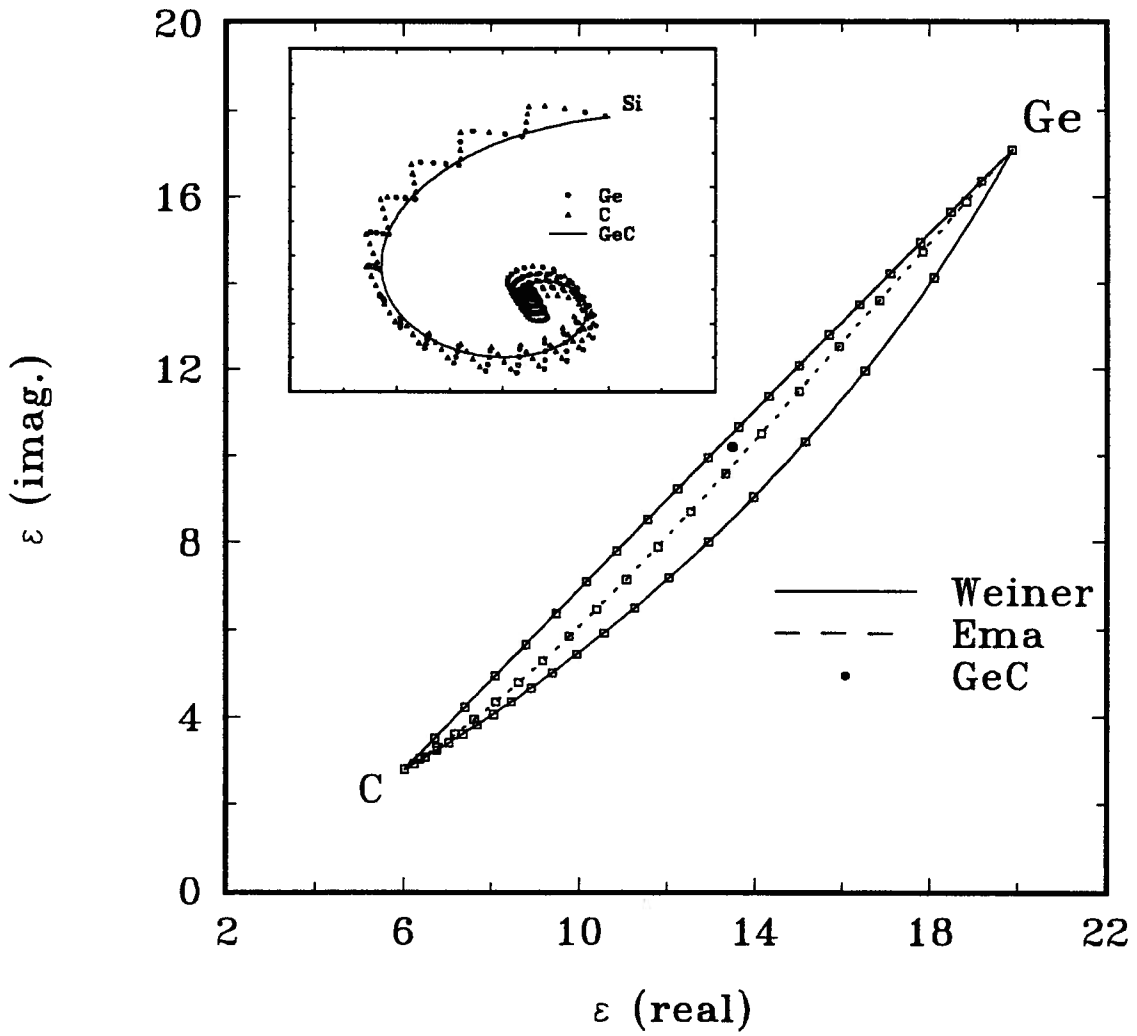

Figure 5.2 Wiener bounds for the germanium and carbon phases in Fig. 1. The data points correspond to a 5% change in the constituents. Also shown is the expected dielectric values assuming the Bruggman effective medium theory with a three dimensional isotropy. The inset shows the ellipsometric trajectory of Fig 5.1 along with that for a film with the same pseudo-dielectric function. The value of the pseudo-dielectric function, GeC, is also shown on the main figure.

5.2 Analytical Methods

Fig. 5.1 shows the theoretical ellipsometric trajectory as a function of thickness for an eighty layer stack with alternating layers of germanium and carbon at the HeNe wavelength. The complex refractive index is taken to be (4.8, 1.78) for the germanium layers and that for the carbon layers, (2.52, 0.56). Each layer is 2 nm thick and the data points are spaced 0.2 nm apart. The angle of incidence is 67.8°. Hence the trajectory is simulating what one would expect to see through in-situ ellipsometry.

There is, initially, a good deal of contrast between the carbon and the germanium layers. As more layers are deposited, this contrast decreases and the trajectory appears to converge. If the system is thick enough to be opaque at the wavelength of interest, the ellipsometric trajectory will form a closed path between the endpoints of the germanium and the carbon layers.

One advantage to the above technique is that there is marked difference between a sharp and diffuse interface in the ellipsometric trajectory in the ρ plane. This effect is illustrated in the inset of Fig. 5.1. Here the data points are spaced 0.1 nm apart. The initial carbon layer on germanium is shown for the case of a perfect interface. In addition, the trajectory for an intermediate layer, 0.5 nm thick, with a linear diffusion gradient between the carbon and germanium layers is also shown. The model assumes that the carbon smoothes out the surface roughness of the germanium layer. Hence, the overall thickness of the multilayer does not increase for the first 5 data points. Other forms of diffusion will have different trajectories in the complex plane and this factor is exploited in the later sections.

An infinite amount of layers will form a closed path in the ellipsometric plane approximately around the value of ρ equal to (-.286,-.158). This corresponds to value of ρ given by a semi-infinite substrate with a dielectric function of (13.5, 10.2) at the wavelength of interest. Fig. 5.2 shows the Wiener bounds for the range of dielectric functions which can result when the constituents of germanium and carbon have the optical constants given above. It is assumed that there is no chemical bonding between the individual materials, as this could affect the dielectric functions. The data points are spaced at intervals corresponding to a 5 % change in the amount of each constituent. Also shown is the resultant dielectric function for a three dimensional isotropy when the Bruggman effective medium approximation is assumed. The value corresponding to the pseudo-dielectric function of an infinite stack is given as the data point GeC. The pseudo-dielectric function of a multilayer structure is defined as that of a semi-infinite substrate which would give the same complex reflectance ratio at the angle of incidence of interest.

The pseudo-dielectric function of an infinite stack lies between the EMA and the Wiener bound corresponding to minimum screening. This is to be expected due to the angle of incidence and the anisotropic nature of the material. At an angle of incidence of approximately 68° the larger of the electric field components is aligned parallel to the grains (in this case the individual layers). Hence the overall screening is reduced from that of a random three dimensional structure.

Ideally, one would expect the pseudo-dielectric function to be aligned aside the point corresponding to an equal fraction of germanium and carbon, given that the volume fractions

of the constituents are equal. However, the theoretical data point is a few percentage points away from this value, indicating a greater amount of germanium in the system than is present. This anomaly is due to the arbitrary choice of choosing a point in the middle of a layer deposition. As a result the top bilayer, which has the largest effect on the measured value of ρ, is germanium rich.

The above analysis does not apply when the thickness of the layers become appreciable on the order of the wavelength of the light. In this case the infinite wavelength approximation used in the determination of the effective medium theories breaks down and interference effects between the layers must be considered.

If there is mixing between the constituents, without a change in the chemical bonding configuration, then the multilayer will become more isotropic and the pseudo-dielectric data point will move towards the value given by the Bruggman effective medium theory. If chemical bonding occurs and results in an overall change in the dielectric function, then the data point may not lie within the expected dielectric bounds.

The inset of Fig. 5.2 shows the stack of Fig. 5.1 with the data points spaced 0.5 nm apart. In addition, the theoretical trajectory of a uniform layer of GeC with a dielectric function of (13.5, 10.2) is shown. It can be seen that the trajectory of the uniform layer follows that of the stack quite closely, especially as an increasing number of layers are deposited. Hence one can determine the pseudo-dielectric function of the stack to a good deal of accuracy without depositing an infinite amount of layers.

The above theory can be applied to spectroscopic ellipsometry. The modeling techniques used the previous section can be used to determine the nature of the multilayer. In this case an 2 or 3 dimensional isotropy can not be assumed and the screening parameter , κ_z, must be allowed to vary. If a good degree of chemical mixing is present, then the Forouhi-Bloomer model may provide a better fit to the ellipsometric data.

5.3 Experimental

The germanium carbide films were deposited in the chamber with the rotating targets and the fixed substrate holder. This system is described in greater detail in section 3.3. A germanium and a pyrolytic carbon target were used. The substrate holder was electrically isolated from the grounded chamber in order to allow for the application of a substrate bias. The substrate preparation techniques were the same as those described in section 4.2.2. Diffusion pumping with a liquid nitrogen cold trap was used to maintain a low base pressure during the deposition process.

The films were monitored during the deposition process through in-situ ellipsometry. During the ellipsometric monitoring of the film growth, it was desired to take a data-point at each Angstrom of film growth in order to observe the effects of diffusion to a good deal of precision. However, it was initially found that the deposition rate of germanium was too high to accomplish this given that the data collection and process time for the in-situ ellipsometer was on the order of 3 seconds. In order to reduce the deposition rate of germanium, a mask

was placed in front of the target. The deposition rate of carbon was low enough not to require this procedure.

The "target" thickness of the individual layers in the stacks was approximately 2.0 nm. Forty layers were deposited in all. In addition, individual layers and bilayers several tens of nanometers in thickness were also deposited in order to determine the dielectric functions of the individual materials.

Two sets of experiments were conducted, one as a function of pressure and the other as a function of substrate bias. The deposition pressures were 0.5, 1.0 and 2.0 Pa. In the system used in this study, it was necessary to achieve these pressures by increasing the throttling of the diffusion pump. Hence, there was an increase in the base pressure by a factor of 2–3 from 2×10^{-4} Pa over the experimental range. During the deposition process, the substrates were electrically isolated. Balanced magnetrons were employed in order to reduce the effects of the plasma ions.

A set of individual films and multilayers were also deposited as a function of substrate bias. In this case, the pressure was held constant at 1.0 Pa and the films were deposited at substrate biases of −22 V (floating) , −50 V and −100V. In this set of experiments, unbalanced magnetrons were used in order to ensure a good ion flux at the substrate.

5.4 Films Deposited as a Function of Pressure.

5.4.1 Results

Fig. 5.3 shows the experimentally measured and the theoretically determined ellipsometric data points for a germanium/carbon bilayer deposited at 0.5 Pa in argon. The optical constants were found to be (4.8, 1.78) for the germanium layer and (2.52, 0.56) for the carbon layer. The data were fit using the projection method, which is explained in detail in chapter 6. Essentially, in this technique, the distance in the complex plane between the experimental data points and the theoretical trajectory is minimized. The main advantage of this method is that one need not know the thickness of the film at each data point apriori to the optimization procedure. The above procedure was repeated for films deposited at 1 and 2 Pa. The optical constants for the films deposited at 1 Pa were, to within a fitting error of ± .02, the same as those for the 0.5 Pa film for both germanium and carbon.

For the germanium film deposited at 2 Pa a single layer model could not be used to describe the ellipsometric trajectory of the film. In this case a three layer model with an increasing void fraction was used which assumed that the optical constants of the bulk material are the same as those for the film deposited at 0.5 Pa. The results of the fit are presented as the inhomogenous line in Fig. 5.4 while the void fractions, thicknesses and the resulting optical constants of the individual layers are given in Table 5.1. For comparison purposes, a homogenous model with the same optical constants as layer 1 in Table 5.1 is also shown in the figure. Finally the ellipsometric trajectory of a film with surface roughness layer

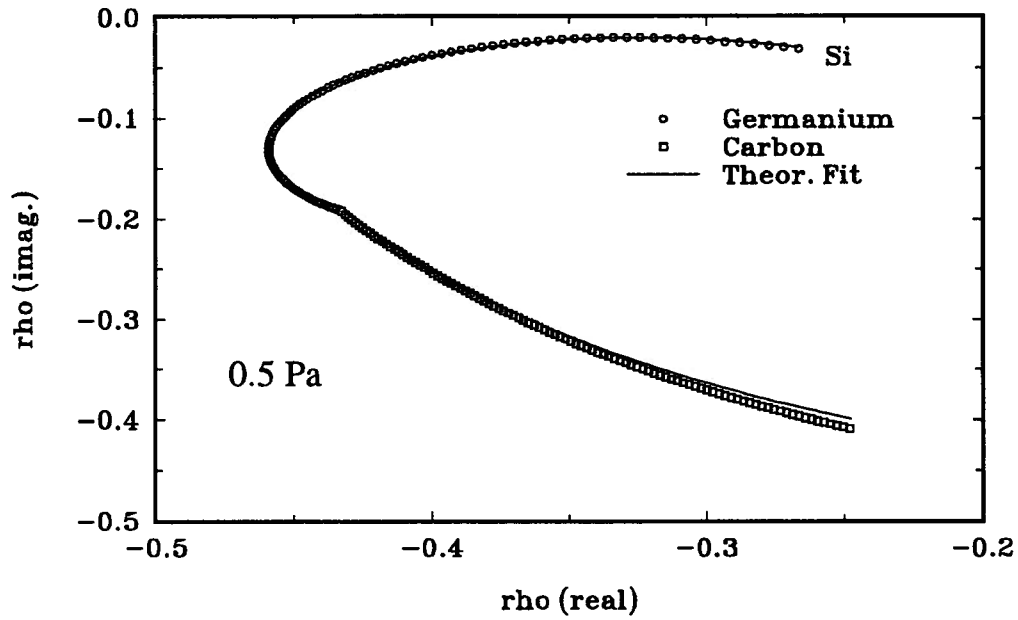

Figure 5.3 Experimental data and theoretical fit to a germanium/carbon bilayer on a silicon substrate deposited at 0.5 Pa. The optical constants were determined to be (4.78,1.78) for the germanium layer and (2.52, 0.56) for the carbon.

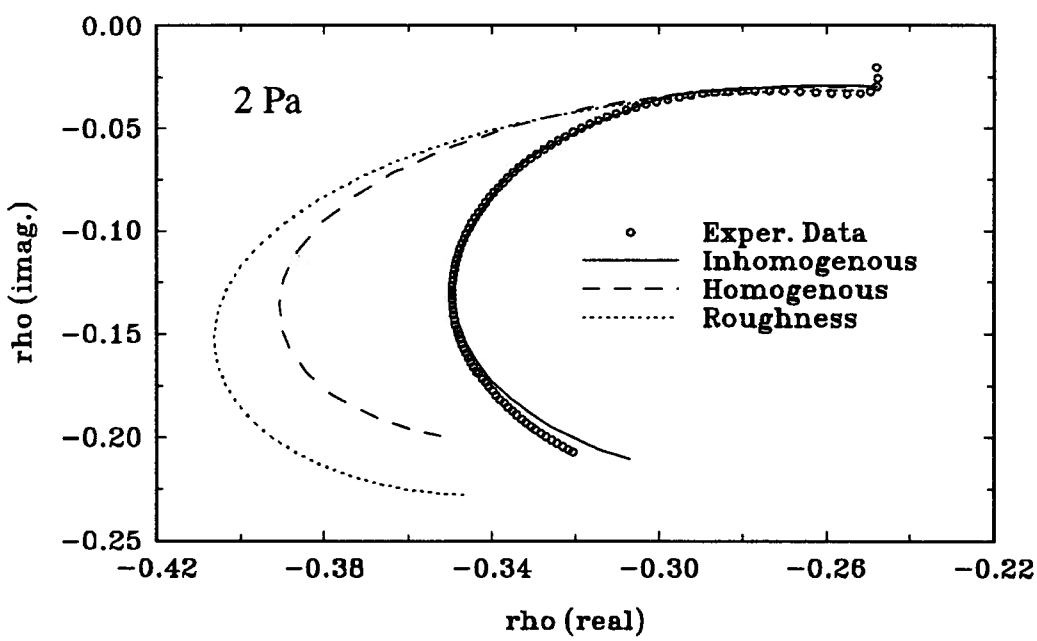

Figure 5.4 Experimental data and three theoretical models for a germanium layer deposited on silicon at 2.0 Pa. The parameters for the inhomogenous layer are given in Table 5.1

Table 5.1 Parameters for inhomogeneous model in Fig. 5.4. The bulk optical constants are that of the germanium film deposited at 0.5

Layer	Thickness (nm)	Void Fraction	Optical Constants
1	4.0	.15	(4.14, 1.49)
2	5.0	.21	(3.78, 1.32)
3	24.0	.24	(3.62, 1.24)

which initially follows the same ellipsometric trajectory as the homogenous film is presented. The model is based on the observation that a roughness layer generally evolves as[170]

$$d_r = d^s \tag{5.1}$$

where d is the total film thickness, d_r is the thickness of the top roughness layer and s is a model parameter with a value between 0.25 and 0.50. In Fig. 5.4, the value of $s = 0.5$ and the optical constants are assumed to be those of the film deposited at .5 Pa with a 12% void fraction. The optical constants for the carbon layer deposited at 2 Pa were determined to be (2.1, 0.42).

The ellipsometric trajectories for the germanium/carbon multilayers deposited at 0.5, 1.0 and 2.0 Pa are shown in Figs. 5.5, 5.6 and 5.7. Also shown is the theoretical ellipsometric trajectory for a material with the same pseudo-dielectric function as the stack. The optical constants for the material are also shown on the plots and presented in Table 5.2, along with the optical constants of the single layer films.. For the multilayer deposited at 1 Pa a two layer model was required, indicating a inhomogeneous growth pattern. The difference

Table 5.2 Optical constants vs. pressure for single layers and multilayers. More than 1 set of optical constants indicates inhomogeneities in the films.

Pressure (Pa)	Germanium	Carbon	Ge/C Multilayer
0.5	(4.78, 1.78)	(2.52, 0.56)	(4.23, 1.34)
1.0	(4.78, 1.78)	(2.52, 0.56)	(4.0, 1.30)
			(3.7,1.15)
2.0	(4.14, 1.49)	(2.1, 0.42)	(2.48,0.44)
	(3.78, 1.32)		
	(3.62, 1.24)		

between the two sets of optical constants indicates approximately a 15% increase in voids.

Due to the large degree of inhomogenities in the films, an analysis with the Wiener bounds was not performed for the films deposited as a function of pressure.

5.4.2 Discussion

The results show that there is an increasing amount of inhomogeneity in the germanium films as the pressure of the sputter gas is increased. As discussed in section 3.2.2, this is attributed to a reduction in the energy of the reflected neutrals. It should be noted that the 3-layer model used to predict the ellipsometric trajectory of the film deposited at 2 Pa is not necessarily unique and other factors, such as the presence of impurities, could also be affecting the optical properties of the film.

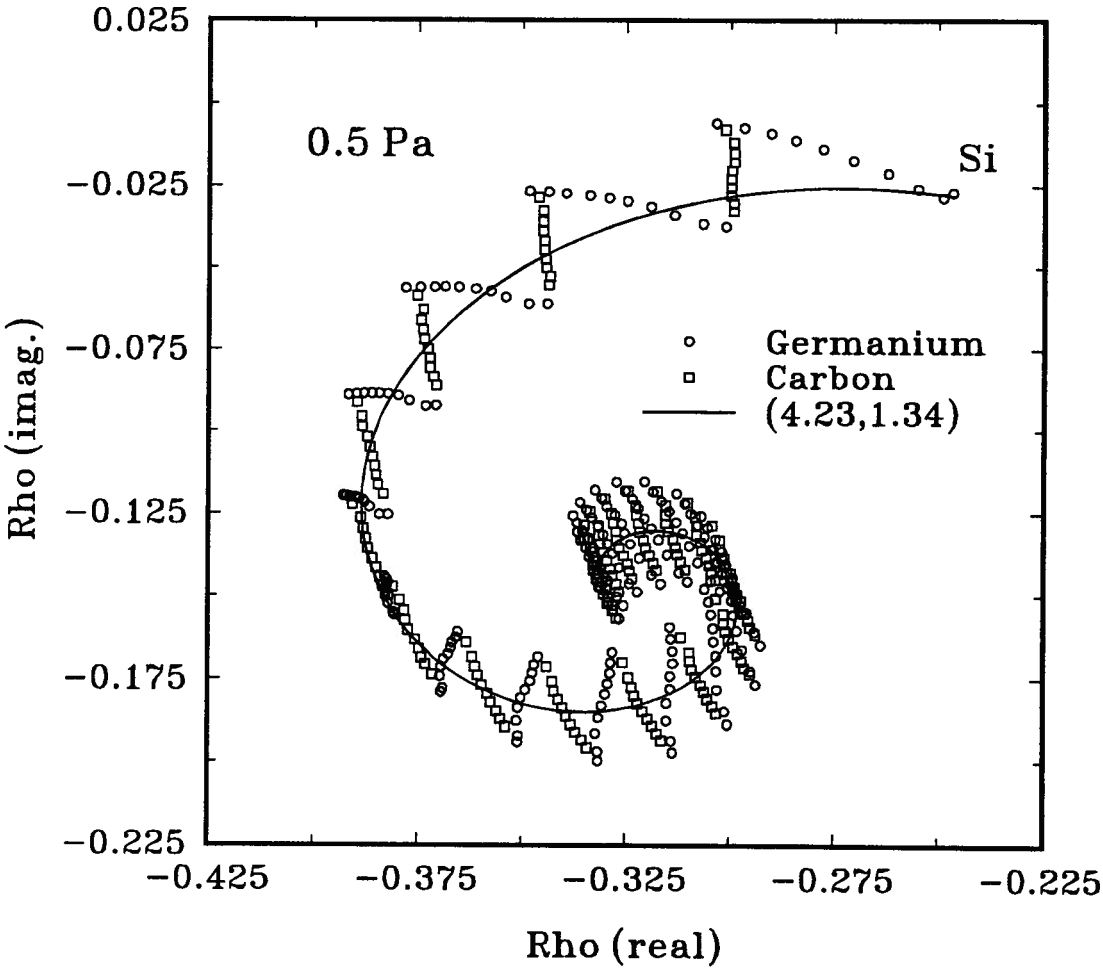

Figure 5.5 Ellipsometric trajectory of a germanium/carbon multilayer deposited onto a floating substrate at 0.5 Pa. Also shown is the theoretical ellipsometric trajectory for a material with the pseudo-dielectric function as the stack.

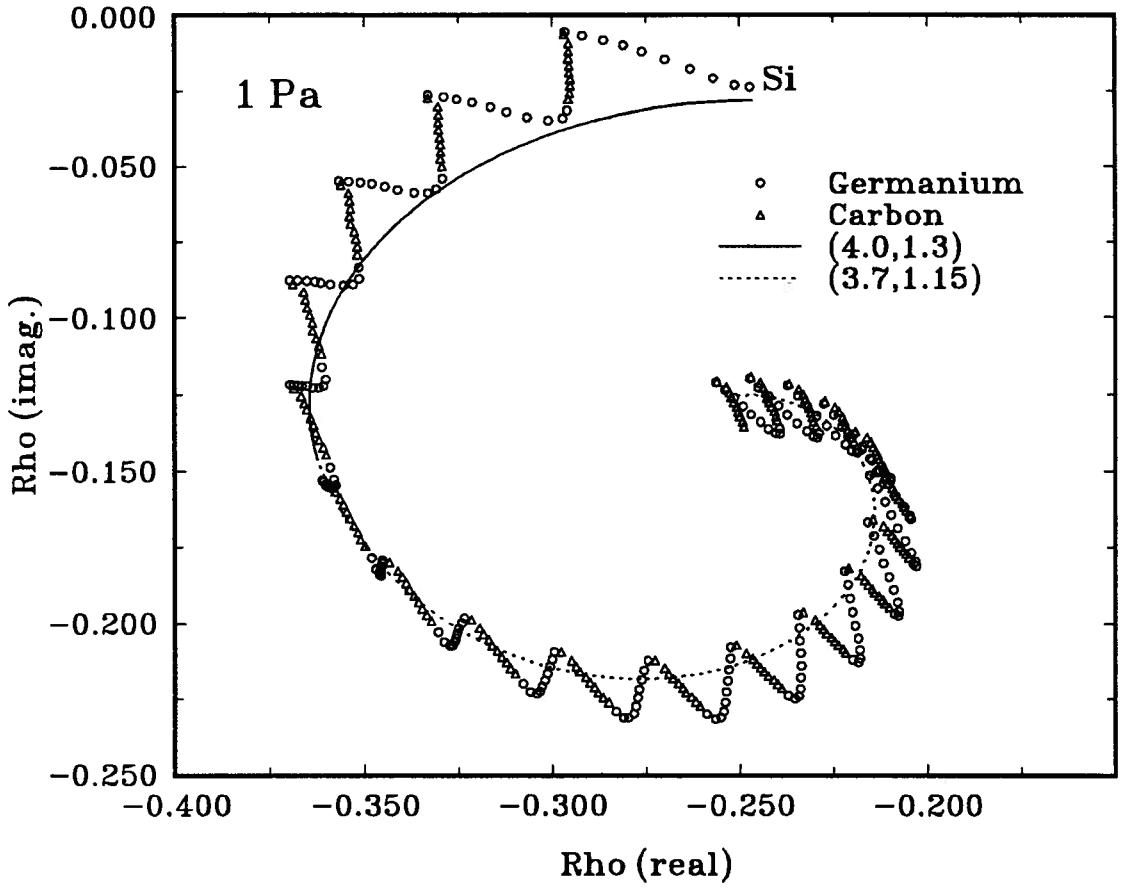

Figure 5.6 Ellipsometric trajectory of a germanium/carbon multilayer deposited onto a floating substrate at 1.0 Pa. Also shown is the theoretical ellipsometric trajectory for a material with the pseudo-dielectric function as the stack. In this case a two layer model is required.

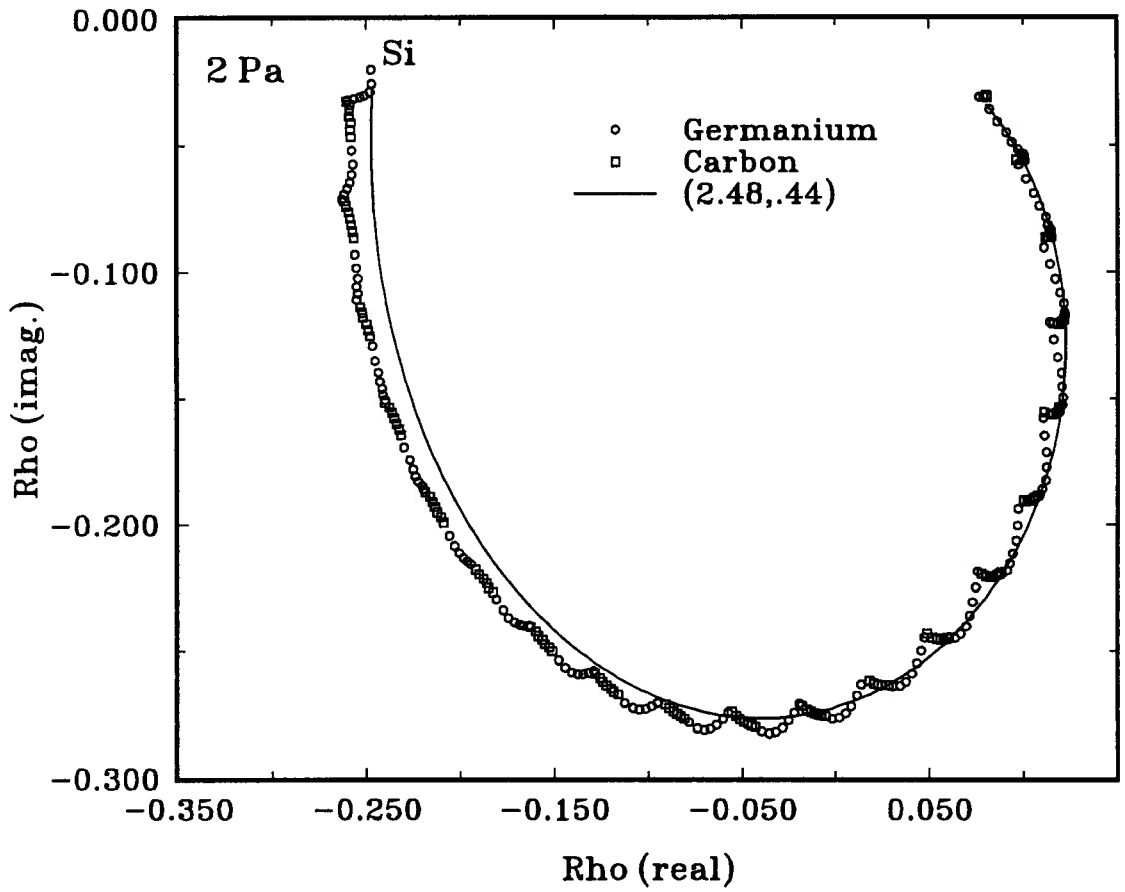

Figure 5.7 Ellipsometric trajectory of a germanium/carbon multilayer deposited onto a floating substrate at 2.0 Pa. Also shown is the theoretical ellipsometric trajectory for a material with the pseudo-dielectric function as the stack.

Inhomogeneities were not detected in the carbon films. Though thin films of carbon have been observed to be quite smooth,[171] it is also possible that inhomogenities are not detected due to the reduced dielectric contrast between carbon and the ambient. This is also a probable reason for the ability of a one layer model to describe the dielectric function of the multilayer deposited at 2 Pa.

Interdiffusion between the individual layers is clearly visible in the ellipsometric trajectories of the germanium/carbon multilayers shown in Figs 5.5, 5.6 and 5.7. The mixing of the individual layers is observed to increase as the argon pressure is increased from 0.5 to 2.0 Pa.

Fig. 5.8 shows the ellipsometric data for the first few layers of the system deposited at 1 Pa. Also shown is a theoretical simulation for the 3rd, 4th and 5th layers. Both sets of data have been displaced for comparison purposes.

The theoretical model has assumed diffusion between the 3rd and 4th and the 4th and 5th layers. The thickness of each diffusion layer is 6 Angstroms and a linear gradient between the dielectric functions of the two materials is assumed. However, the nature of the diffusion is assumed to differ at the Ge/C and at the C/Ge interface.

For the interface where carbon is deposited onto germanium, the model assumes that the germanium layer is rough and the carbon atoms initially smooth out the surface. The model simulates this effect by having the carbon atoms diffuse into the germanium layer without an overall increase in the thickness of the stack. As a result, the six initial data points

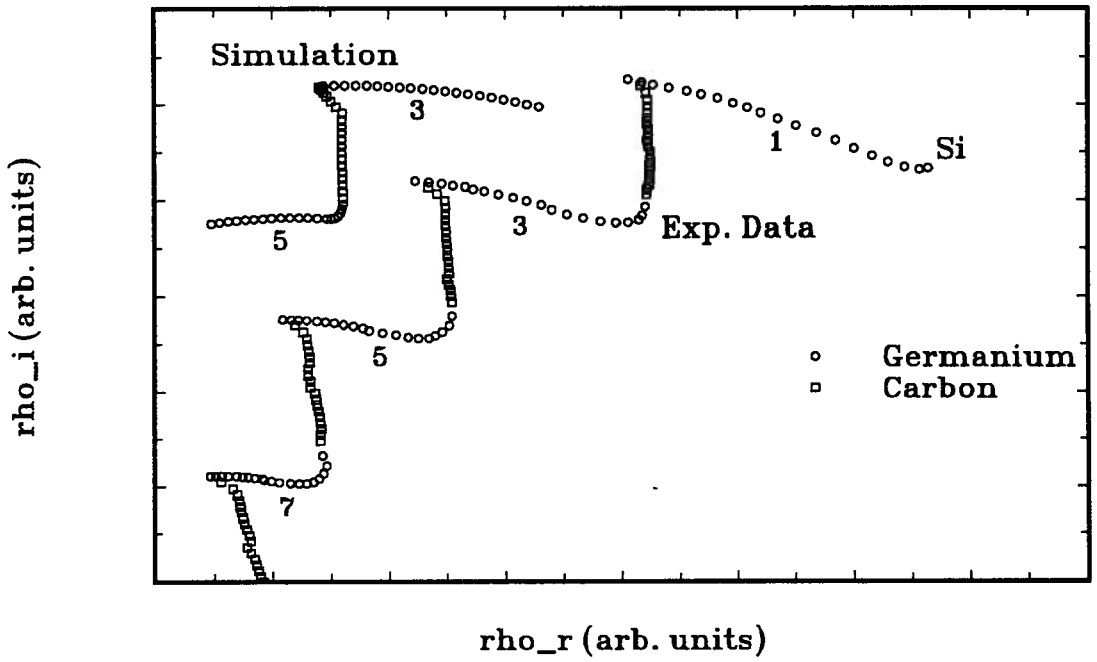

Figure 5.8 Experimental data for the first few layers of the multilayer deposited at 1 Pa. Also shown is a theoretical simulation of layers 3, 4 and 5 with diffusion between the layers. Both sets of data have been displaced for comparison purposes.

of the simulation represent an additional Angstrom of diffusion rather than one of layer growth. As the atoms diffuse into germanium, the surface becomes more carbon-rich. The overall thickness of the stack increases after the sixth data point, where a pure carbon layer is then deposited.

The theoretical results match the experimental trajectory fairly well, though the angle between the germanium trajectory and the trajectory of the diffusion layer appears to be more oblique in the former case. This could be the result of a non-linear diffusion gradient.

The nature of the interface where germanium has been deposited onto carbon is assumed to be differ from the above case. In x-ray multilayer systems it has been shown that the deposition of carbon tends to smooth out the surface of a multilayer.[54] As a result, physical intermixing is more likely due to pure diffusion and one expects the overall thickness of the multilayer to increase during the initial deposition process.

The model which most closely matched the experimental results was carbon diffusing into the newly deposited germanium layer, as shown in Fig. 5.8. In this case, each data point indicates an additional Angstrom of thickness. A linear gradient between the dielectric functions was once again assumed.

An increase in carbon diffusing into the germanium layer with increasing pressure is most likely the result of a more open voided structure in the later. The smaller carbon atoms can then readily diffuse into the germanium. This theory is supported by the modeling results for the thick germanium film deposited at 2 Pa. Models which also included germanium diffusing into the carbon layer resulted in a poorer agreement with the experimental data.

The theoretical model shows a smaller radius of curvature for the intermediate layer between layers 4 and 5 than that for the experimental data. The reason for this can be, in part, explained through an examination of the first layer of the experimental data. Ideally, the trajectory should have the same form as that of layer 3 in the simulation. However, the path initially departs from this with a small degree of curvature. This thickness, termed the critical thickness,[172] is the result of an initial anisotropic film growth. After this point the deposition becomes more uniform and the curve is closer to the ideal.

The multilayer deposited at 2 Pa appears to be fairly homogeneous with a large degree of mixing between the carbon and germanium layers. However, due to the observed voided structure for germanium (and for carbon at this pressure in chapter 4), the optical constants of the resulting film are likely to change over time due to moisture penetration.[66] Hence increasing the degree of mixing through altering the sputter gas pressure appears impractical for optical applications.

5.5 Films Deposited as a Function of Substrate Bias

5.5.1 Results

The optical constants for carbon and germanium were determined for a set of single layer films on silicon substrates which were biased at −22 V (electrically floating), −50 V, and −100 V respectively. The deposition pressure was 1 Pa.

The thickness of the individual germanium films grown as a function of substrate bias was approximately 40 nm. To within a modeling error of ± .015 for n and k, no difference in the optical properties of the above films could be observed . The complex refractive index was determined to be (4.92, 1.70).

Fig. 5.9 presents the ellipsometric trajectories for three carbon films deposited at different substrate biases along with the accompanying theoretical fits. The thickness of the films decreases from approximately 28.5 nm at the floating potential to 23.5 nm at a −100 V

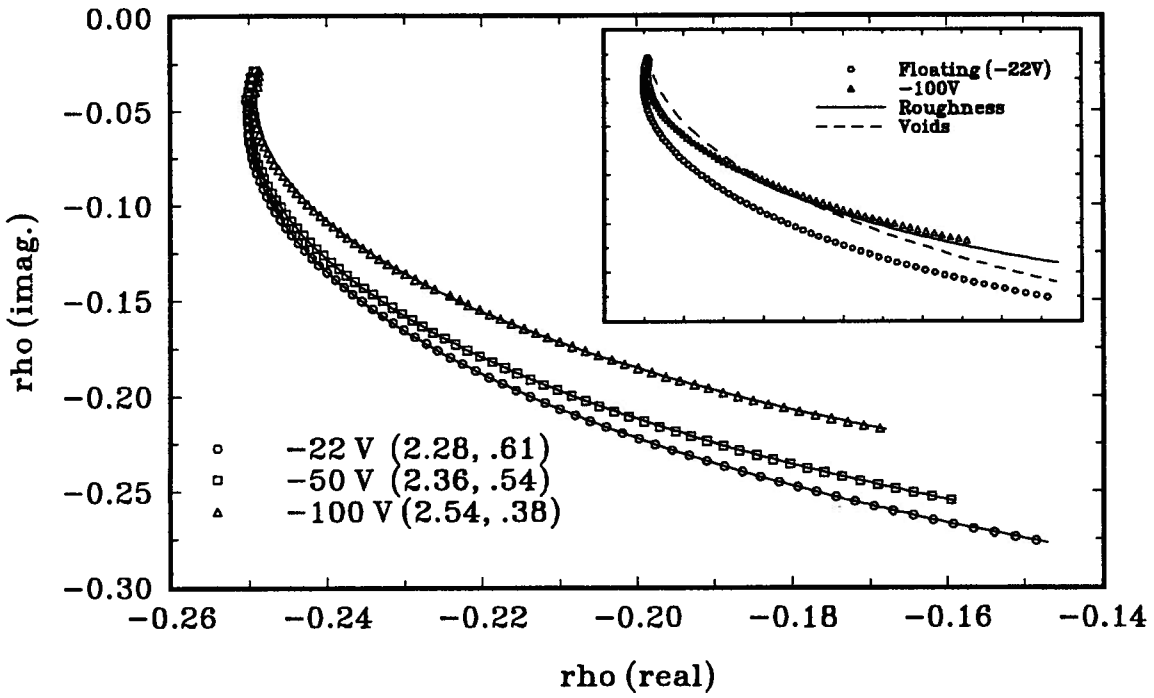

Figure 5.9 Experimental data and theoretical fits for carbon films deposited as a function of substrate bias. The optical constants of the 1 layer theoretical models are given. The inset shows two of the experimental trajectories and two theoretical models which assume the bulk material is that of the film deposited at −100 V.

substrate bias. This could be, in part, the result of an increase in the density of the film. The theoretically determined optical constants are also given in Fig 5.9 and in Table 5.3. It can be seen that the general trend with increasing substrate bias is an increase in the refractive index n, along with a decrease in the absorption and deposition rate.

The inset of Fig. 5.9 shows the films deposited at −22 V (floating) and −100 V substrate bias along with the theoretical trajectories of two models. Both models assume that the bulk material has the same optical properties as the film deposited at −100V and in each case the Bruggman effective medium approximation is used to determine the resultant

Table 5.3 Optical constants vs. substrate bias for single layers and multilayers. More than 1 set of optical constants indicate inhomogeneities in the films.

Substrate Bias (V)	Germanium	Carbon	Ge/C Multilayer
−22	(4.92, 1.70)	(2.28, 0.61)	(3.76, 1.13)
			(3.62, 1.09)
−50	(4.92, 1.70)	(2.36, 0.54)	(3.76, 1.13)
			(3.76, 1.21)
−100	(4.92, 1.70)	(2.54, 0.38)	(3.84, 1.10)

dielectric function of the individual layers. The first model has a single layer trajectory with a 20 % void fraction. The second model has a surface roughness layer with a thickness given by Eq. 5.1 where the roughness parameter, *s*, is equal to 0.5. The roughness layer consists of an even mixture of bulk material and voids. It is clear from the resulting trajectories that the ellipsometric properties of the carbon films deposited at lower substrate biases cannot be explained through microstructural changes alone.

Figs. 5.10, 5.10 and 5.12 show the ellipsometric trajectory of the germanium/carbon multilayers deposited at a substrate bias of −22 V, −50 V and −100 V respectively. Every second data point collected is shown. The thickness of the germanium and the carbon layers is approximately 2 nm.

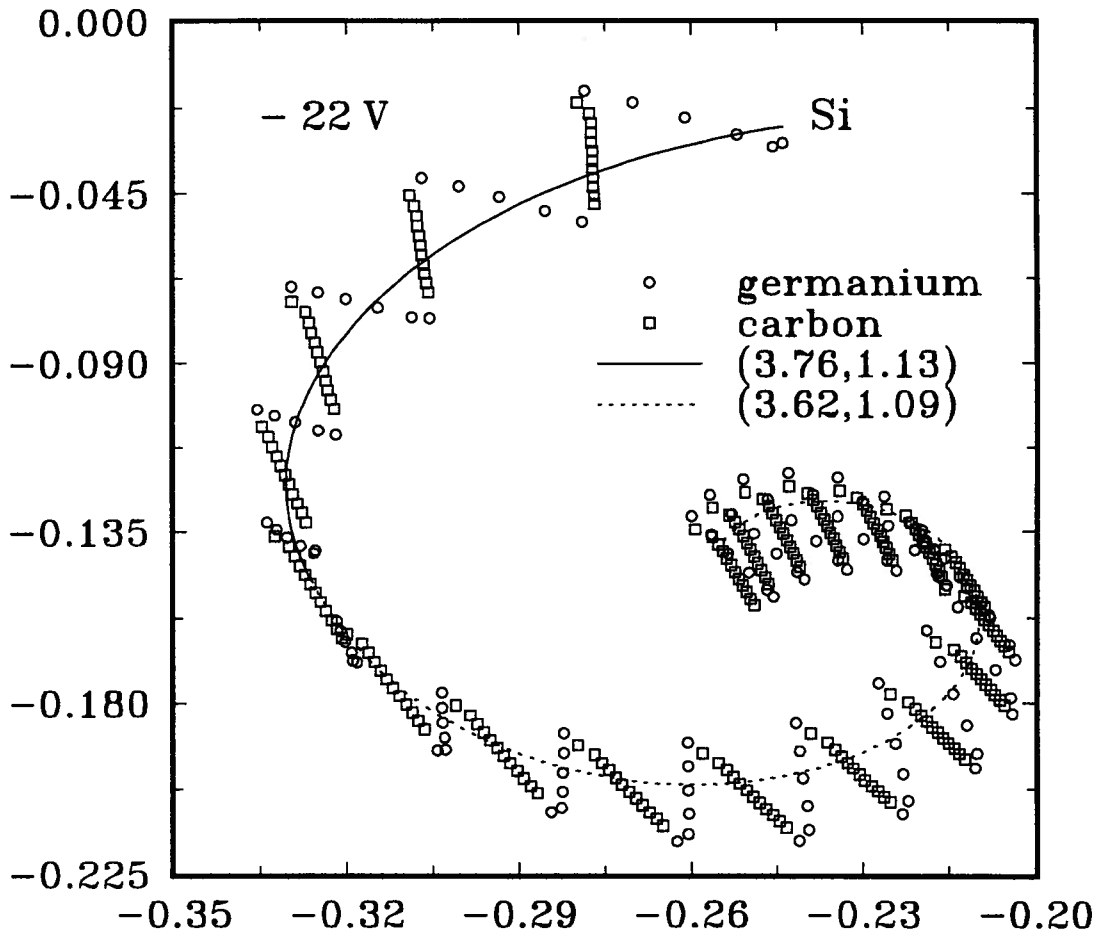

Figure 5.10 Ellipsometric trajectory of a germanium/carbon multilayer deposited onto a floating substrate (−22 V). Also shown is the theoretical ellipsometric trajectory for a material with the pseudo-dielectric function as the stack.

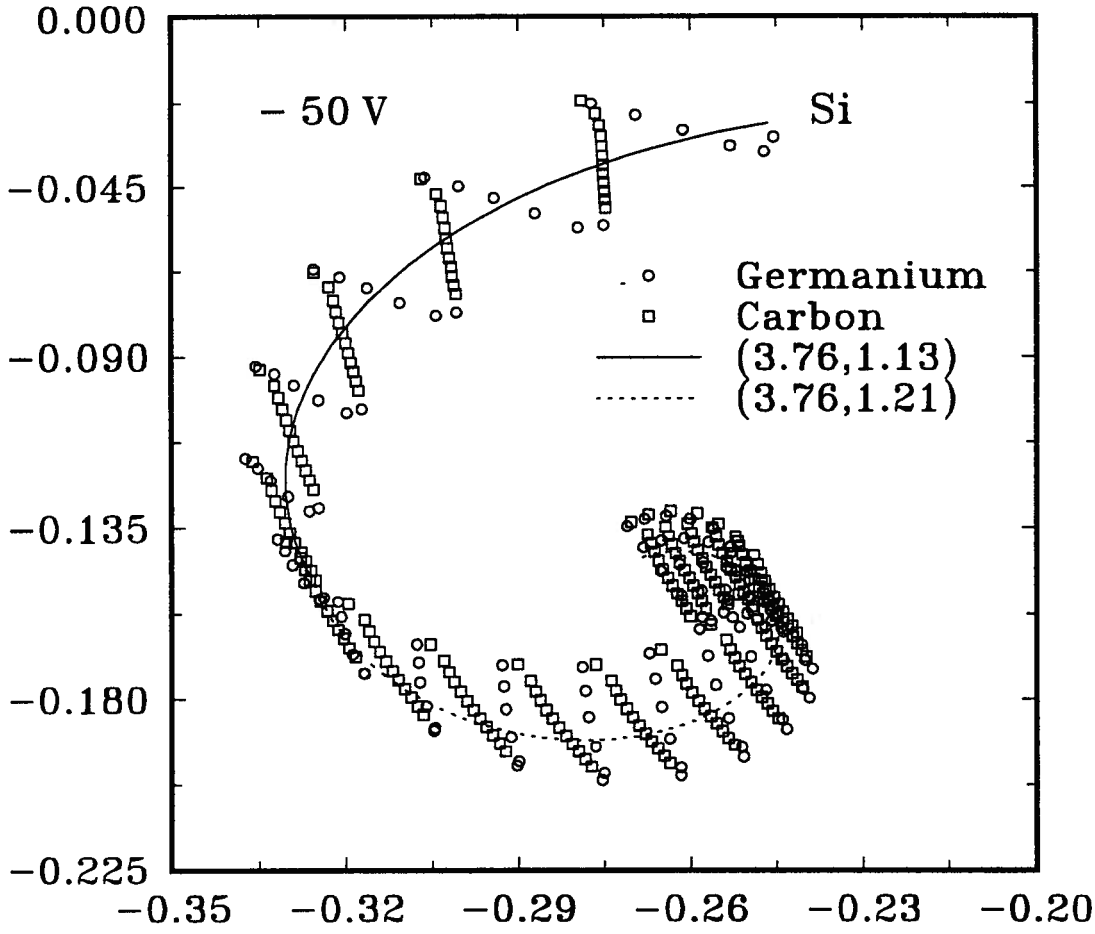

Figure 5.11 Ellipsometric trajectory of a germanium/carbon multilayer deposited onto a substrate biased at −50 V. Also shown is the theoretical ellipsometric trajectory for a material with the pseudo-dielectric function as the stack.

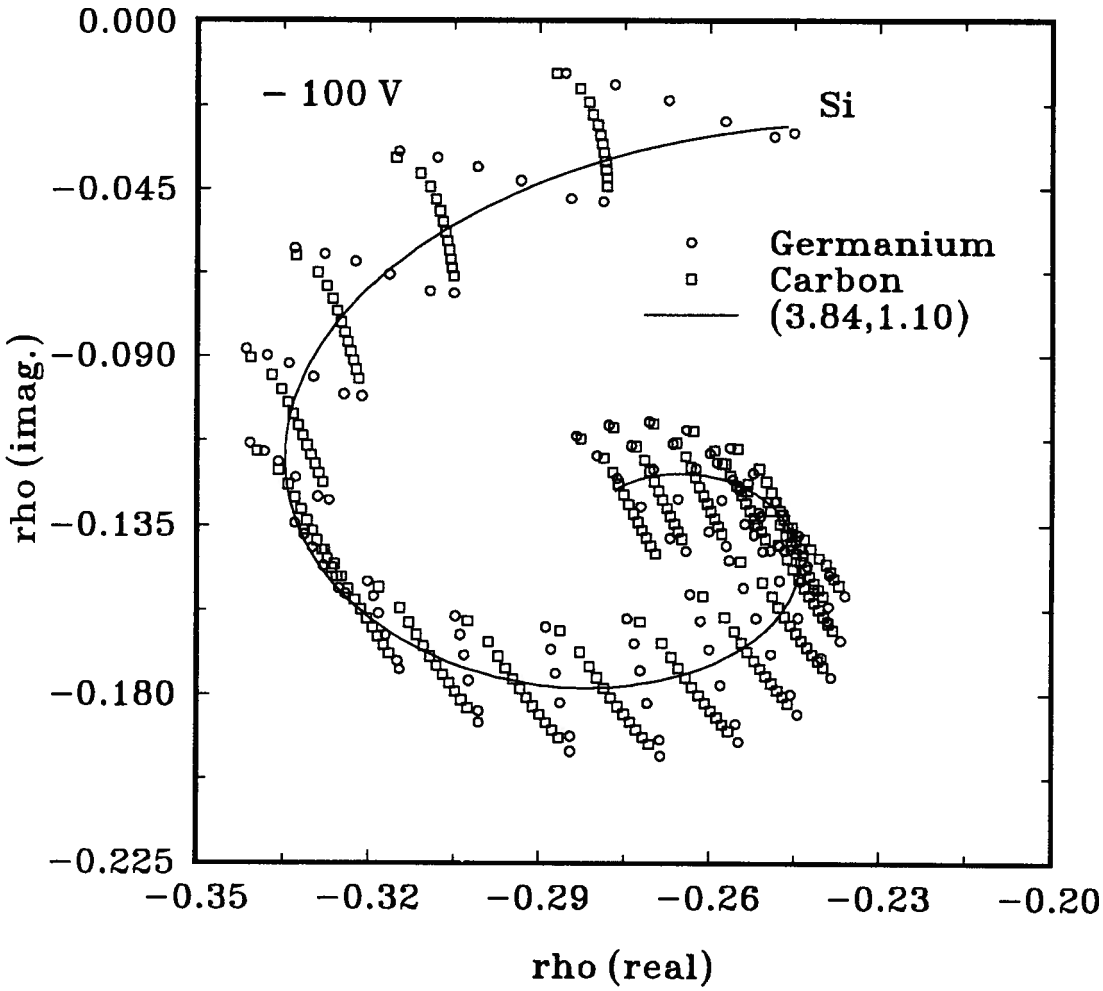

Figure 5.12 Ellipsometric trajectory of a germanium/carbon multilayer deposited onto a substrate biased at −100 V. Also shown is the theoretical ellipsometric trajectory for a material with the pseudo-dielectric function as the stack.

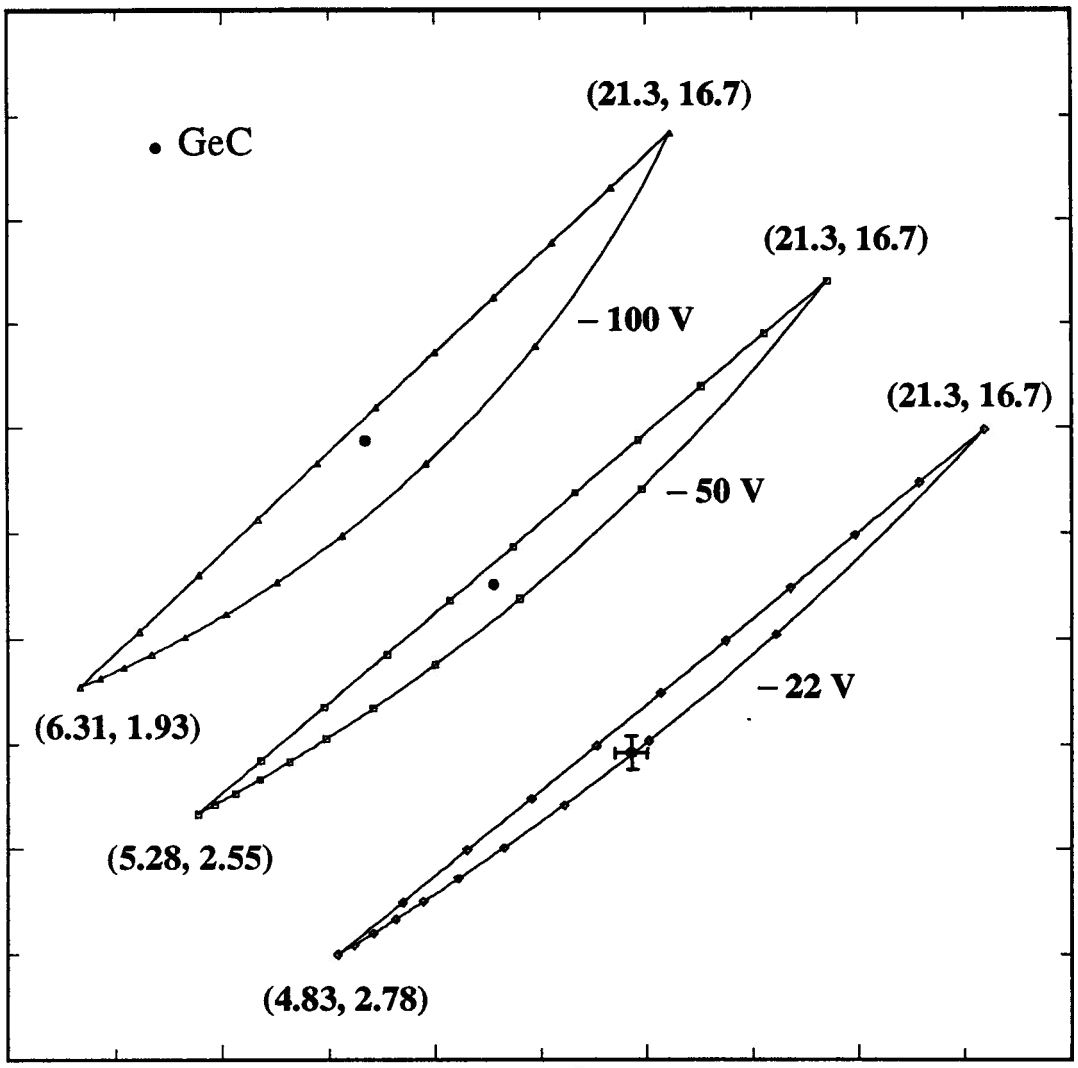

Figure 5.13 Wiener bounds for the multilayer stacks deposited as a function of substrate bias. The optical constants are determined from the single layer films. The data have been offset in each case for comparison purposes.

Also presented in the figures is the theoretical ellipsometric trajectory of a material that follows the trajectory of each multilayer. Inhomogenaties must be taken into account for the multilayers deposited at –22 V and at –50 V. The density of the system appears to be decreasing with increasing thickness for a floating bias and increasing at a bias of –50 V. The optical constants for the multilayers are presented on the figures and along with those for the single layers in Table 5.3.

It can be seen that the diffusion of carbon into the germanium layer increases with a greater substrate bias. However, the germanium/carbon interface appears to become sharper.

The Wiener bounds for the three multilayers are given in Fig 5.13 along with the pseudo-dielectric function of each system. The optical constants of the constituents are assumed to be those for the single layer films deposited at the corresponding substrate bias. The data points on the bounds represent a 10 % change in the fraction of the constituents. The three sets of bounds have been displaced for comparison purposes. Error bars are included for the dielectric function of the multilayer deposited at a floating bias. The error range for the other multilayers is on the same order as that of the previous data point. This degree of error compensates for the inhomogeneities in the films.

5.5.2 Discussion

The results for the single layers of germanium indicate that the density of the films does not change with an increase in the substrate bias. This observation correlates well with the results for the films deposited as at the lower pressures in the previous section. Hence, one

can conclude that germanium films with a zone-T microstructure are deposited at 1 Pa and at a floating potential.

Fig 5.9 indicates that the optical properties of the carbon films change with an increasing substrate bias. This effect cannot be attributed to an increase in the film density alone due to the increase in the transparency of the film material. This property was not observed in chapter 4 due to the inability to grow films under the above conditions with thickness greater than 50 - 70 nm. Carbon films in this thickness range (> 70 nm) are required for analysis by the ex-situ ellipsometer as the film thickness and the optical constants for thinner films. are highly correlated.[173]

The resulting optical constants at high substrate biases are closer to those of the amorphic diamond films produced through high energy arc deposition. Films of this nature are thought to contain a large percentage of sp^3 bonds.[174] As with the above case it is also difficult to grow relatively thick films through this technique,[175] which is a major problem in infrared applications.

Figs. 5.10 through 5.12 show that the diffusion of carbon into the underlying germanium layer increases with a greater substrate bias. However, the nature of the ellipsometric path differs from that of the films deposited as a function of pressure. In this case there appears to be a small amount of curvature outwards before the trajectory bends back in the opposite direction of the underlying layer. This is attributed to a small increase in the overall thickness of the multilayer, indicating that the germanium layer is smoother than in the previous section.

The degree of interdiffusion between the germanium/carbon boundary appears to decrease with increasing substrate bias. This is attributed to an increase in the density of the layers and overall smoother films. It is unlikely that the increase in bias will result in the germanium diffusing into the carbon due to the relatively large atomic size of the former.

Fig. 5.13 shows that in all three instances the pseudo-dielectric function of the multilayer lies within the corresponding Wiener bounds. It should also be noted that the experimental value lies very close to the expected one and within the boundaries of error. Therefore chemical mixing between carbon and germanium does not appear to effect the dielectric properties of the material.

Substrate bias which are much greater than −100 V are usually not applied in practice due to the problems of resputtering and the formation of a high compressive stress in the films. Therefore it would appear that biasing the substrate does not result in enough interdiffusion to make the deposition of alternate layers of germanium and carbon practical for optical coatings.

One potential solution to the above problems can be found through the observation that the effective medium theories apply to layers which are thin compared to the wavelength of interest. Hence, one should still be able to achieve the desired refractive index if the long wavelength approximation applies to the stack.. It should be noted that at a normal incidence maximum screening occurs and the resultant dielectric function is found through Eq. 3.11. As the two materials should be relatively transparent at the wavelength of interest the effective refractive index of the stack, n_{eff}, can approximated through the relation

$$n_{eff} = \frac{n_c n_g}{f_c n_g + f_g n_c} \tag{5.2}$$

where f_c, n_c and f_g, n_g are the volume fractions and refractive indices of the carbon and the germanium phases respectively. One potential problem to the above solution is interdiffusion between the layers over time, as this would reduce the overall screening and change the effective refractive index

5.6 Conclusions

An increase in the pressure and an increase in the substrate bias results in an increase in the interdiffusion between the carbon and germanium layers in a multilayer stack.. However, only an increase in pressure appears to allow for the required degree of mixing necessary to produce germanium carbide. Unfortunately, this also results in a film with a Zone-1 microstructure (section 3.2.2), making these coatings unsuitable for optical applications.

The results and analysis show that the required refractive index can still be achieved if the layers are thin enough for the long wavelength approximation to apply. However, this value could change over time if enough diffusion results. Therefore, one would like to make the individual layers relatively thick in order to reduce this effect.

OPTICAL MULTILAYERS

6.1 Introduction

Once the diamond-like and the germanium carbide films were characterized, a control system was required that would allow for the deposition of multilayers of these materials. It was also desired to be able to deposit dielectric multilayers in the near infrared region.

In order to deposit multilayers with the desired reflection and/or transmission characteristics, it is necessary to control the thickness of each layer to the required degree of accuracy. The simplest method of control is that of timing.[66] In this technique, the deposition rates and the optical constants are obtained from previous runs and an assumption is made that they will remain constant over the current run. As the optical constants of the diamond-like and germanium carbide films are highly dependent upon the deposition conditions, this method is inadequate for the purposes of this thesis.

A more precise form of control for the deposition of dielectric multilayers is transmission monitoring.[176] In this method, the transmittance of the multilayer is measured in-situ. As the intensity can be calculated as a function of layer thickness through the matrix method, the deposition process is halted when the desired value is obtained.

There are a number of drawbacks to the above method. As the transmission is monitored at normal incidence, for a large number of systems the intensity cannot be measured unless the deposition process is halted. A possible solution to this problem would be to

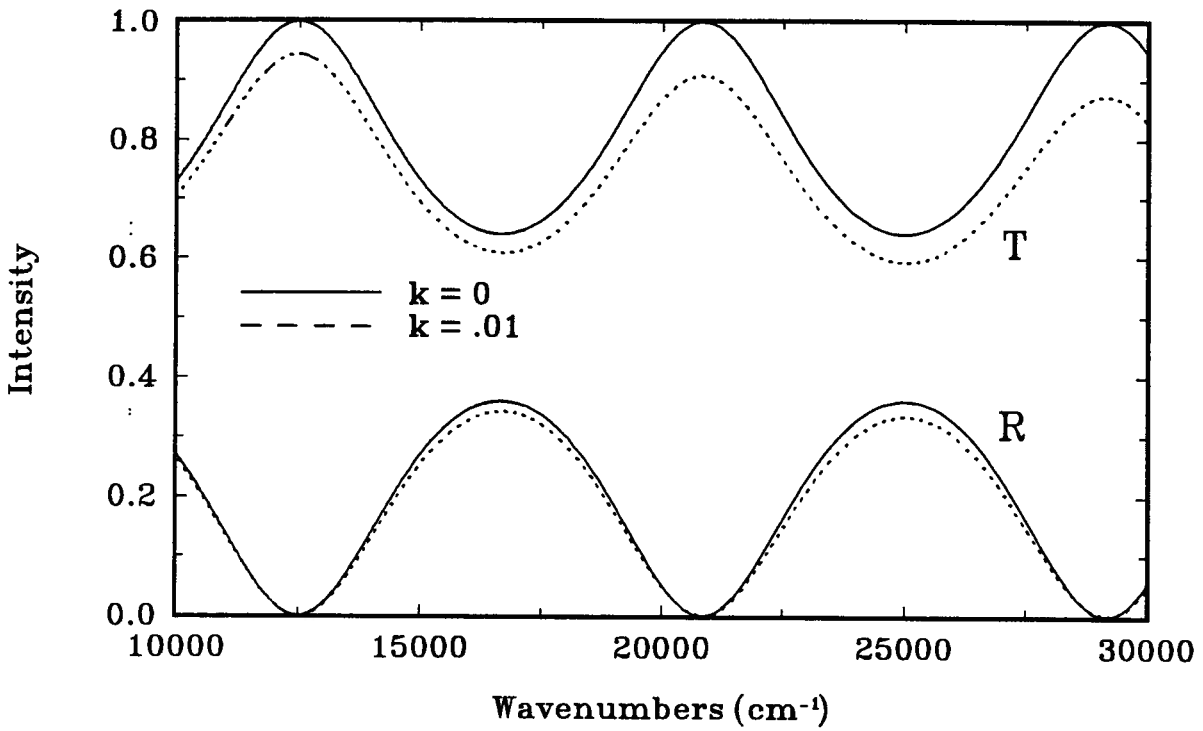

Figure 6.1 Theoretical reflection and transmission characteristics for two anti-reflection coatings on a transparent substrate with a refractive index of 4. The first film has an n and k value of (2,0) while the second has a value of (2,.01)

design a system with the targets oriented at an angle, however, as discussed in Chap 5, this results in shadowing effects. Another potential complication is caused by undesired and often unpredictable amounts of absorption in the films. Even for dielectric materials, residual impurities in the deposition chamber can result in a small value of k, typically between a value of 10^{-5} and 10^{-3}. This factor results in an overall reduction in the transmission values which increases with the number of layers. To help compensate for this effect, adaptive routines are often required which recalculate the necessary thicknesses of the remaining layers after each

individual layer deposition.[177] This problem is intensified when absorbing films such as carbon or metals are deposited.

As transmission monitoring appeared quite problematic for the purposes of this thesis, in-situ ellipsometry was chosen as the method for controlling the individual layer thickness. One advantage to this technique is that the optical properties are measured at a non-normal angle of incidence. Therefore, constant monitoring of the film growth is possible. Also, reflection measurements are inherently less sensitive to absorption in the films than transmission measurements. This property is demonstrated in Fig. 6.1 for an antireflection coating (n = 2) on a substrate (n = 4) of infinite thickness. Two cases are shown, one for a transparent film and one for a film with a value of k equal to 0.01. If we compare the maxima and minima in the intensities it can clearly be seen that the transmission is affected by a factor of at least 3 over the reflection spectra.

Another important consideration is that each ellipsometric measurement results in two pieces of information as opposed to a transmission measurement which results in only one. For dielectric coatings, this allows for a solution of n and d, giving information on both the optical thickness and the quality of the film. Ideally, for partially absorbing coatings, we would like solve for the two unknowns nd and k. Unfortunately this is not possible in practice as the complex reflectance ratio cannot written as a function of the above variables. However, as illustrated in Chapter 5, the solution of n, k and d can determined through the observation of the ellipsometric trajectory in the complex ρ plane. One final advantage is that ellipsometric

measurements are inherently more precise than intensity measurements as they are self-referencing.

At the start of this project, aside from the added instrumental complexity, the potential drawbacks to this technique were not obvious as, for optical films, this method had only been used to control the thickness of a single layer on a substrate.[178,179] There were a number of developments in the x-ray multilayer field;[72,180] but, to date, there had been no improvement over the previously mentioned timing method. Also the x-ray films were thin compared to the monitoring wavelength and highly absorbing, which made a comparison with the films used in this thesis difficult. However, given the potential applications, it was felt that this was a worthwhile project for a Ph.D. thesis.

The remainder of the chapter is as follows. The methods used to determine the optimum deposition conditions for single layer SiO_2 and Ta_2O_5 films are discussed in section 6.2. These films are to be used to test the initial control routines. The section starts with an overview of reactive sputtering, then discusses how in-situ ellipsometry was used to characterize the films. In section 6.3, the development of an optical multilayer control system for dielectric films is examined. Several iterations were required before a successful routine was implemented. In the final section the routines are extended to absorbing films.

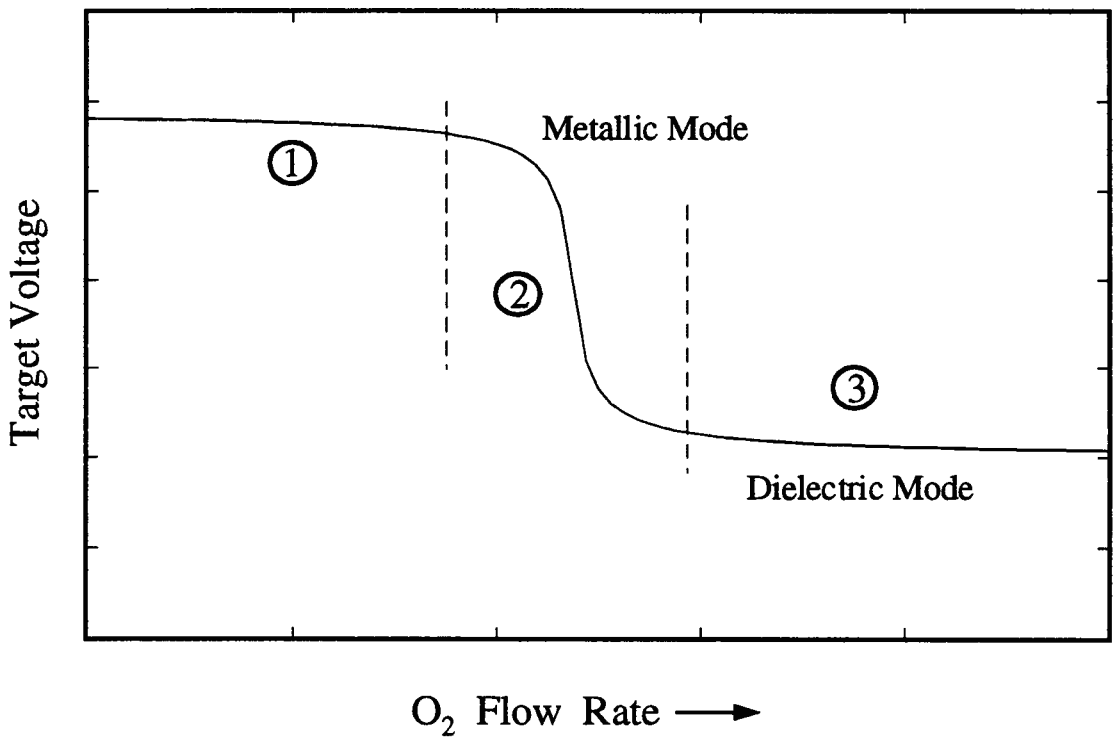

Figure 6.2 Typical target voltage vs. O_2 flow rate for reactive sputtering of silicon. The metallic mode corresponds to the region where the target is partially covered with an oxide.

6.2 Single Layer Films

6.2.1 Reactive Sputtering.

The dielectric materials used in the course of this thesis were deposited through the process of reactive sputtering.[181] In this technique, a metallic target is sputtered in an Ar/O_2 gas mix resulting in the deposition of an oxide of the target material. One of the main

advantages of this method is the high operational powers possible due to the great thermal conductivity of the metal. One other advantage is that, for conducting targets, a dc rather than an rf bias can be used; simplifying the procedure and allowing for a larger degree of scale up.[182]

Fig. 6.2 shows a typical target voltage vs. O_2 flow rate for the reactive sputtering of a silicon target. Here the flow rate of the inert gas, the sputtering power and the pumping speed are constant. In region 1, the target voltage is essentially constant and an increasing O_2 flow rate does not result in an increase in the overall pressure. These effects are due to the sputtered metal flux reacting with all of the oxygen. Typically, the film deposited in this region is a suboxide of the desired material. In region 2, the flow rate has increased to the point where all of the sputtered metal reacts with the oxygen. Under these conditions, the deposited material is either stoichiometric or very close to it. In addition the overall pressure begins to rise and the target becomes partially covered with an oxide, resulting in a drop in both the target voltage and the deposition rate. This region of operation is known as the metal mode. In region 3 the target is fully covered with an oxide, the deposition rates are fairly low and the excess oxygen results in an increase in the pressure. The excess oxygen can, for certain materials, such as titanium oxide, result in a degradation of the film quality.[183] This mode is known as the covered or dielectric mode.

The optimum deposition region then typically lies somewhere in the metal mode. However, there is a drawback to working in this region for optical coatings due to the changes in the deposition rate which result from variations in the amount of target coverage. As this region is not wide in terms of O_2 flow rate, small fluctuations in the oxygen partial pressure

can result in large changes in the deposition rate. Hence monitoring is crucial in this region if high quality optical multilayers are desired.

6.2.2 In -Situ Monitoring

Fig. 6.3 shows the ellipsometric path as a function of thickness for a number of dielectric films with different refractive indices in the complex ρ plane. The substrate material is silicon. For a dielectric film of a given refractive index, the path will follow the same trajectory each time $ndcos\phi$, where ϕ is the angle of incidence, reaches a multiple of the half-wave thickness. If the film is absorbing, the path will eventually spiral around then reach the value of ρ for an infinitely thick layer of the deposited material. This effect is shown in Fig. 6.4 for a film with refractive index of (2.0, 0.1). Hence monitoring during the film growth can be used to determine both the optical constants and the quality of the deposited material. Inhomegeneaties and surface roughness will also result in a non-closed trajectory.[184]

The ellipsometric properties described above also hold if the film is deposited onto an optical multilayer. This factor allows for a "quick and dirty" method of determining the optimum conditions. One can monitor a multilayer where the individual films are grown under a number of different deposition conditions. If the ellipsometric trajectory for a given layer returns to the same point on the complex plane, then the deposited material is of a high quality.

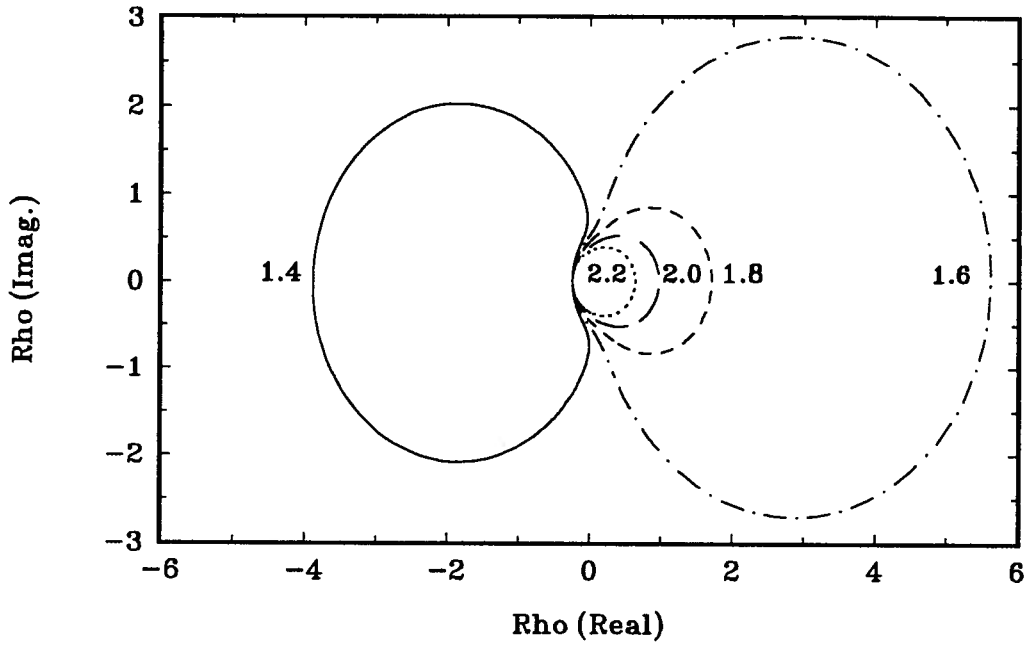

Figure 6.3 Theoretical ellipsometric trajectories for a number of dielectric films in the complex ρ plane. For a given refractive index the trajectory will follow the same spiral each time a multiple of the half-wave thickness is reached.

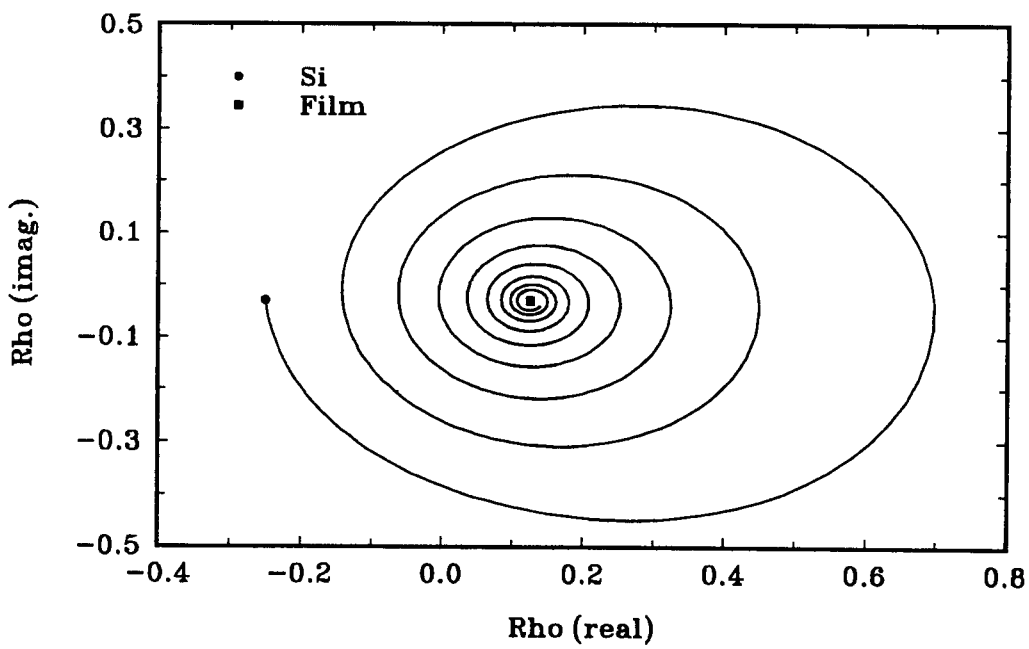

Figure 6.4 Theoretical ellipsometric trajectory for a film with a refractive index of (2.0,0.1) on silicon. Also shown are values of ρ for a silicon substrate and an infinitely thick film.

6.2.3 Silicon Oxide

The silicon target used in this study contained 5% aluminum in order to increase the electrical conductivity of the material and, therefore, allow for a more stable operation with a dc sputter source. As the refractive index of SiO_2 and Al_2O_3 are both "low", 1.45 for SiO_2, and 1.62 for Al_2O_3, the addition of aluminum had only a small effect on the optical properties of the deposited material.

Initially the films were deposited using a dc power source. However, the resulting film quality was poor with macroscopically visible pinholes. This result was attributed to occasional arcing during the film deposition, which could be observed through the port windows and through the monitoring of the output of the power supply. Arcing is caused by a thick oxide buildup on regions of the target where the sputter rate is low. During the sputter process, these regions charge up until a dielectric break-down occurs, creating an arc and often resulting in the deposition of an inferior quality film.

A solution to the above problem was found through the use of a low frequency power supply which operated at 40 kHz. Under these conditions, the bias on the target is positive for half the cycle. The period is long enough to discharge the oxide buildup but short enough not to extinguish the plasma. It should be noted that at this operating frequency the system can essentially be treated as dc because the ions are able to move completely across the plasma region within a half-period.[185]

Initial tests showed that the best films in terms of the magnitude of the refractive index were deposited at the lowest possible operating pressures. This was attributed to energetic

particle bombardment which increased the density of the film. In addition, the films appeared to be quite transparent if they were deposited in either the metal or the dielectric modes.

A set of three films were deposited onto silicon substrates to allow for a more precise study of the optical constants. The system was operated at three different points on the curve of Fig. 6.2; approximately at the boundary of the metal mode and region 1, in the middle of the metal mode, and approximately at the boundary of the dielectric and metal modes. During the deposition runs the films were monitored through in-situ ellipsometry. The operating pressure was 0.35 Pa and the sputter power was 100 Watts.

Fig. 6.5 shows the ellipsometric trajectory of the film deposited at the boundary of region 1 and the metal mode. Also included is a theoretical fit to the data assuming a homogeneous film. The theoretically determined values of the optical constants were n = 1.474 and $k = 3 \times 10^{-4}$. Fig. 6.6 shows the ellipsometric data for the film deposited in the middle of the metal mode. The results show that the film is clearly less absorbing in this region, with a value of k determined to be less than 1×10^{-4}. Also the value of n appears to be almost identical to the previous sample. However, the deposition rate under these conditions is reduced from approximately 3 Å/s to 1.5 Å/s.

For the sample deposited at the boundary of the metal and the dielectric modes, no difference in the optical constants was observed when compared to the previous sample. However, there was a further decrease in the deposition rate. Hence the deposition conditions appeared to be optimized at low pressures and in the middle of the metal mode.

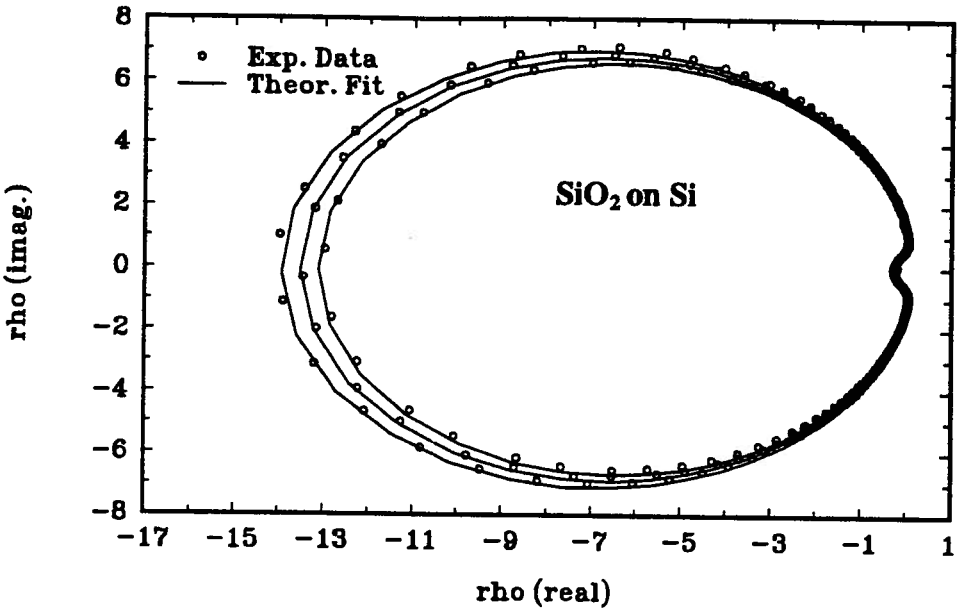

Figure 6.6 Experimental data and theoretical fit for silicon oxide on a silicon substrate as a function of film thickness. The value of k was determined to be equal to 3×10^{-4}. The film was deposited at the boundaries of region 1 and the metal mode.

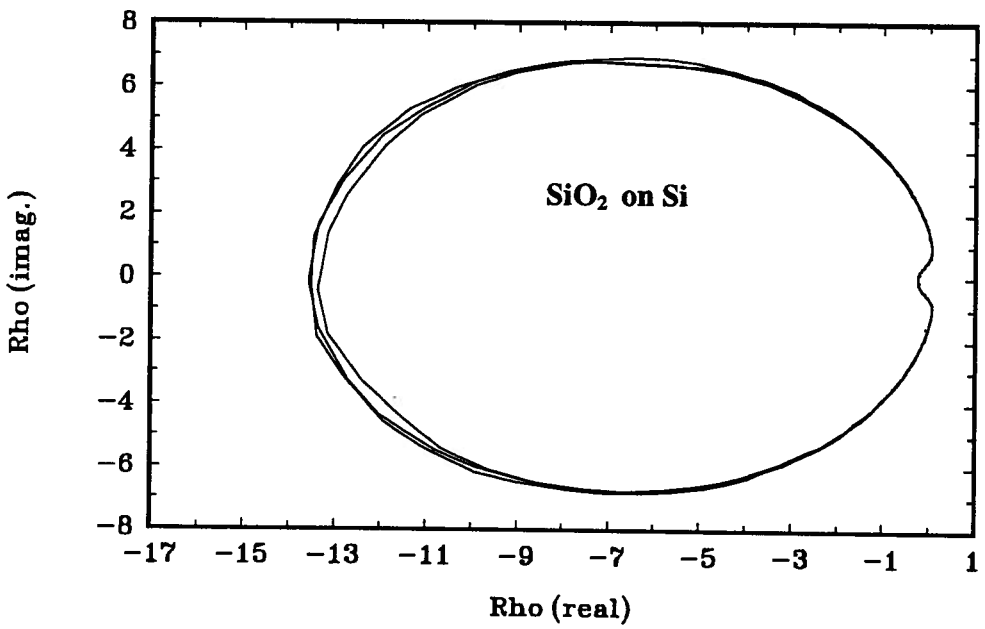

Figure 6.5 Experimental data and theoretical fit for silicon oxide on a silicon substrate as a function of film thickness. The value of k was determined to be less than 1×10^{-4}. The film was deposited in the middle of the metal mode.

Once the optimum conditions for film growth were determined, it was possible to make a comparison between the in-situ and the ex-situ ellipsometer. This allowed for an accurate determination of the window correction factor α (see appendix A, Eq. A.12).

A SiO_2 film was deposited while being monitored by the in-situ ellipsometer. When the optical thickness was approximately 120 nm thick, the deposition was halted and the film immediately removed from the chamber and measured on the ex-situ ellipsometer at the HeNe wavelength (632.8 nm). The value of ρ measured on the ex-situ ellipsometer is shown in Fig. 6.7. From this measurement the refractive index of the film was determined to be 1.472. The dotted line shows the trajectory a film of this refractive index would have if the angle of incidence of the in situ ellipsometer was the same as that of the ex-situ instrument, 67.50°.

As the complex reflectance ratio is a function of the angle of incidence it is important to determine this parameter to a high degree of accuracy. This criterion can be achieved by measuring the complex reflectance ratio of the Si substrate before deposition. In this particular case, the real part of ρ is essentially independent of small changes in the overlayer thickness, but highly dependent upon the angle of incidence. Also, as the imaginary component of ρ is small, from Eq. A.12 in the appendix, it can be shown that the real part of the complex reflectance ratio is not subject to the effects of the vacuum port windows.

The angle of incidence was determined to be 67.94 ± .03 °. Fig. 6.7 shows the theoretical ellipsometric trajectory of film with a refractive index of 1.472 at this angle. The window parameter α was adjusted until the optimum fit was achieved as shown in the graph. The value of α was determined to be .006 ±. .0005.

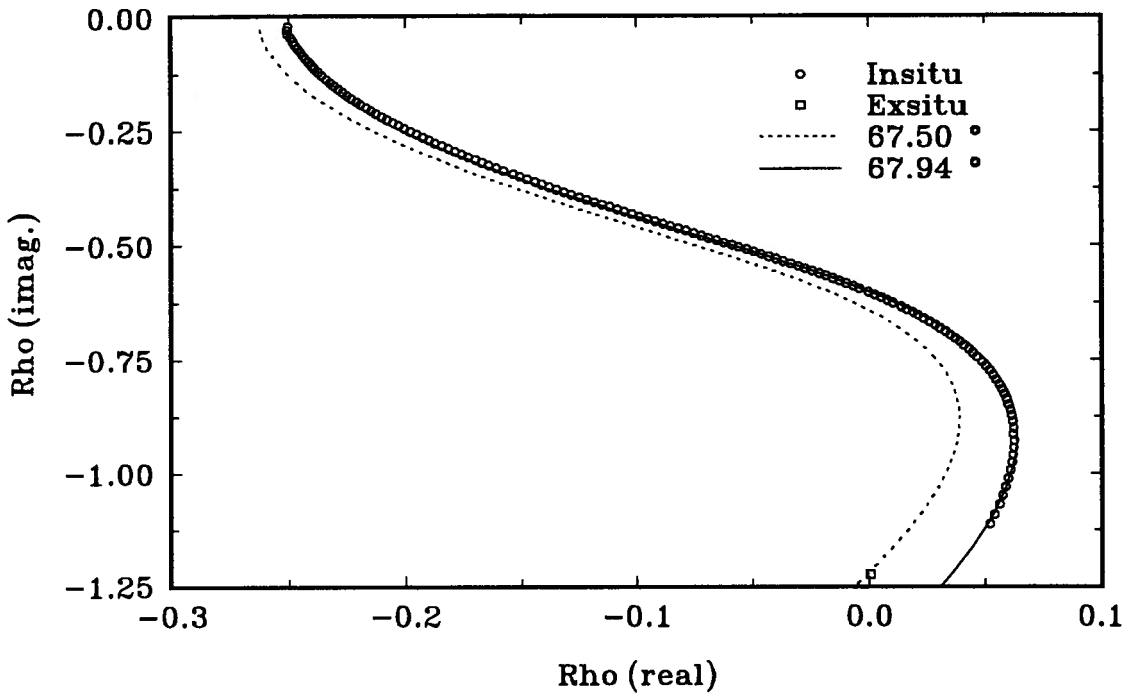

Figure 6.7 Comparison between the ex-situ and in-situ ellipsometer. Presented are the in-situ readings during the growth of a silicon layer on silicon, the ex-situ measurement of the film and the theoretical trajectories at each of the instruments angle of incidence.

It should be noted that the final n and k values given in this section were determined after all of the window correction factors were obtained.

6.2.4 Tantalum Oxide

Tantalum oxide films were investigated in order to determine the optimum deposition conditions. The method of investigation was the same as that for the SiO_2 films.

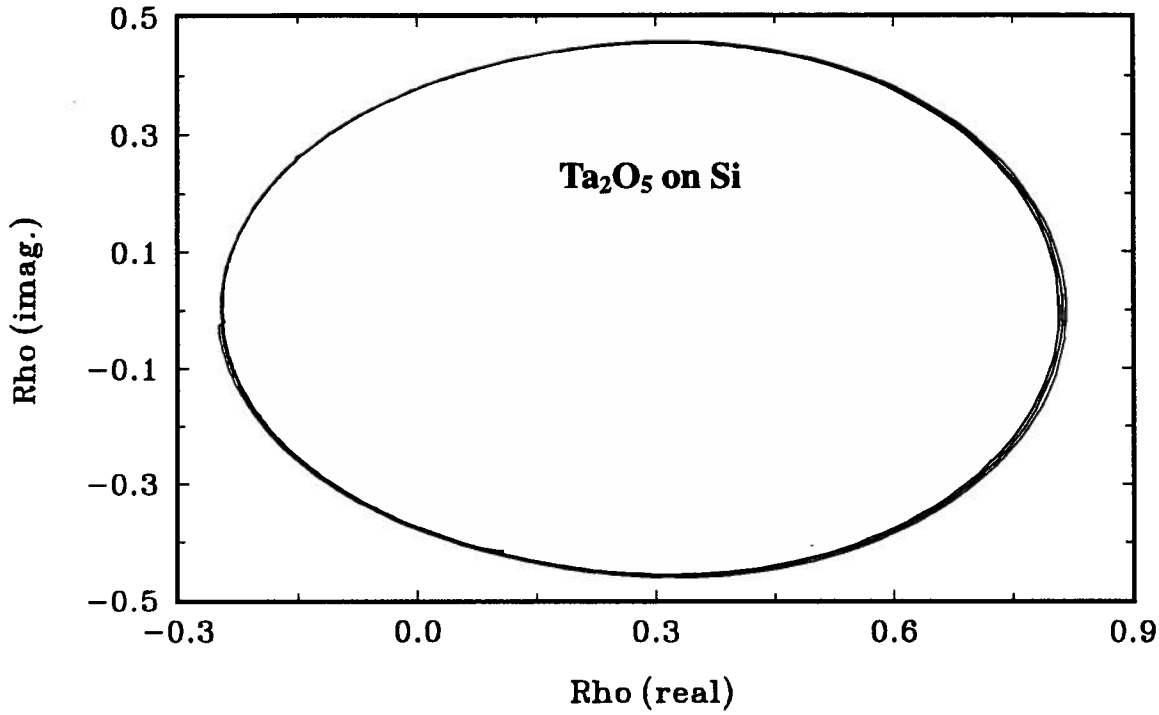

Figure 6.8 Ellipsometric trajectory for a tantalum oxide film. The results indicate very little absorption in the film.

The voltage vs. oxygen flow rate shown for silicon in Fig. 6.2 differs for tantalum. In this case there is an initial rise in the target voltage as the metal mode is approached followed by a drop as the target becomes covered with an oxide.

The refractive indices of the tantalum oxide films also increased with a decreasing pressure. However as the target voltage increases at lower pressures, the power supply, with a maximum voltage output of 500 V, limited the range of possible pressures. The operating pressure was chosen to be 0.35 Pa.

A study similar to the one performed for the SiO_2 films was undertaken for the tantalum oxide films. No measurable change in the optical constants was measured after the

target voltage had reached a maximum, however there was a decrease in the deposition rate with an increasing O_2 flow rate. Before the maximum in the target voltage was reached, the sputtered films were highly absorbing. Hence the optimum deposition region was found to be just after the peak in the voltage where the deposition rate was approximately 3 Å/s.

The ellipsometric measurement of a film deposited under the optimum conditions is shown in Fig. 6.8. The data indicate that there is very little absorption in the film.

6.3 Optical Multilayers

6.3.1 Multilayer Control Development

Once the single layer films were optimized, it was necessary to develop a control routine in order to deposit the optical multilayers. As discussed previously, the individual film thicknesses were to be determined through the method of in-situ ellipsometry.

To aid in the development of the software routines, two multilayers were deposited through the timing method while being monitored by the in-situ ellipsometer. The ellipsometric data were then used to test the subroutines before they were implemented in the control procedure.

The two multilayers deposited were quarter-wave stacks of SiO_2 and Ta_2O_5 with a 'target' wavelength of 300 nm and 632.8 nm (HeNe) respectively. The form of each of the stacks was

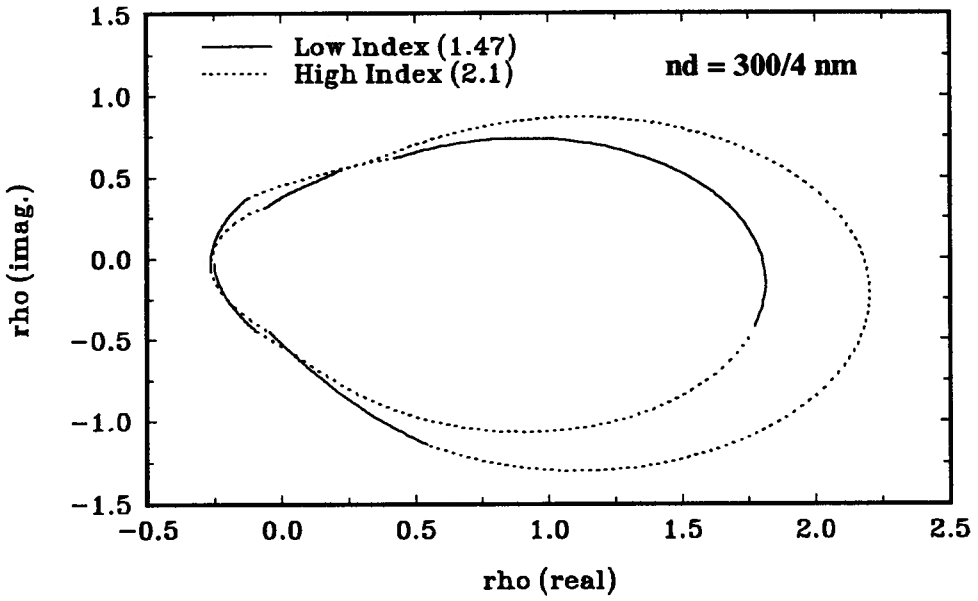

Figure 6.9 Ellipsometric trajectory of a 300 nm quarter-wave stack on a silicon substrate at the He Ne (632.8 nm) wavelength.

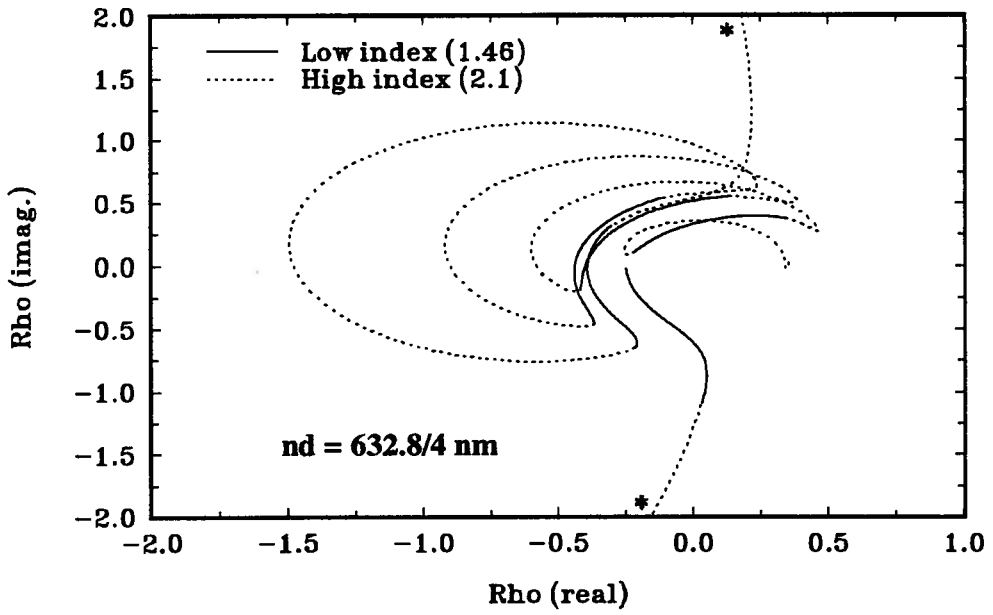

Figure 6.10 Ellipsometric trajectory of a 632.8 nm quarter-wave stack on a silicon at a wavelength of 632.8 nm. The trajectory has a maximum magnitude of approximately 20 beyond the asterisks

Air / HLHLHLHLHL / Si

The theoretical values of ρ for the two multilayers are shown in Figs. 6.9 and 6.10. The thinner of the stacks provided a relatively 'well behaved' ellipsometric trajectory to test the initial subroutines. The thicker stack allowed for the development of more robust algorithms.

Once the subroutines were developed, they were implemented in the main program which was subsequently used to control the deposition of a new quarter-wave stack at the HeNe wavelength. The reflection and transmission spectra of the stack were then measured and compared with theory.

The quarter-wave stack was deposited onto a glass substrate. As this was difficult to monitor with the in-situ ellipsometer, due to the incoherent reflections off the back of the glass, the layer thickness was monitored off an adjacent Si substrate. To ensure that the deposition was the same for each substrate the target was toggled at ± 20° or equivalently over an arc length of 14 cm. The length of the two substrates was on the order of 2 cm and they were evenly spaced about an angle of 0° with respect to the toggle.

There were a number of iterations to the control routines until a method was found that worked with a good degree of success. The next three sections outline the various methods tried and discuss the problems associated with each routine.

6.3.2 Matrix Method

The first method used to control the optical thickness of the individual layers was the direct solution of the matrix equations. As discussed in the introduction, a single

measurement of ρ allows for the solution of two unknowns. Unfortunately, the equations for ρ can not be inverted in terms of the optical constants and the film thickness and therefore are usually solved numerically through the Newton-Raphson method. As discussed in section 3.4, this method usually requires highly accurate initial values. The procedure is also time consuming, which is a potential problem for real time applications.

For a transparent film, an alternative method of solution exists which was initially developed for a single layer on a substrate.[186] For an ambient/film/substrate system the complex reflectance ratio can be written as

$$\rho = \frac{r_p}{r_s} = \frac{r_{01p} + r_{12p}\exp(2i\beta\, d)}{1 + r_{01p} r_{12p}\exp(2i\beta\, d)} \cdot \frac{1 + r_{01s} r_{12s}\exp(2i\beta\, d)}{r_{01s} + r_{12s}\exp(2i\beta\, d)}, \tag{6.1}$$

where d is the film thickness and r_{01} and r_{12} are the reflection coefficients at the ambient/film and the film/substrate interfaces respectively. The value of β is given by

$$\beta = \frac{2\pi}{\lambda}\sqrt{\tilde{N}^2 - \sin^2\phi}\,, \tag{6.2}$$

where $\tilde{N}$ is the complex refractive index, ϕ is the angle of incidence and λ is the wavelength of interest. For a dielectric film, where β is real, Eq. 6.1 can be separated into two functions where

$$F_1(n) = 0, \tag{6.3a}$$

$$F_2(n,d) = 0. \tag{6.3b}$$

Equations 6.3a and 6.3b are given in full detail in reference 186. Equation 6.3a can be solved

numerically through the use of the single variable Newton's method. Once the value of n is obtained, Eq. 6.3b can then be determined analytically for d, allowing for a solution of the optical thickness.

The above method can also be used to determine the optical thickness of a film on a known multilayer. For a multilayer system the derivation of the reflection coefficients is given by

$$r_{p,s} = \begin{bmatrix} 1 & r_{01p,s} \\ r_{01p,s} & 1 \end{bmatrix} \cdot \begin{bmatrix} \exp(i\beta d) & 0 \\ 0 & \exp(-i\beta d) \end{bmatrix} \cdot \begin{bmatrix} 1 & r_{12p,s} \\ r_{12p,s} & 1 \end{bmatrix} \cdot \begin{bmatrix} A_{p,s} & B_{p,s} \\ C_{p,s} & D_{p,s} \end{bmatrix} \tag{6.4}$$

where the right most matrix is the product of all of the underlying matrices up to but excluding the second last interface. The complex reflectance ratio can then be written as

$$\rho = \frac{r_{01p} + r'_{12p}\exp(2i\beta d)}{1 + r_{01p}r'_{12p}\exp(2i\beta d)} \cdot \frac{1 + r_{01s}r'_{12s}\exp(2i\beta d)}{r_{01s} + r'_{12s}\exp(2i\beta d)}, \tag{6.5}$$

where

$$r'_{12p,s} = \frac{(r_{12p,s} + C_{p,s}/A_{p,s})}{(1 + r_{12p,s}C_{p,s}/A_{p,s})}. \tag{6.6}$$

As Eq. 6.5 is identical in form to Eq. 6.1., Eq. 6.3a and 6.3b can also be applied to multilayer films.

One potential problem considered before the routine was implemented was the effect of a finite amount of absorption in the films. As more layers were deposited, neglecting this factor would result in an increasing error in the calculated values of $A_{p,s}$ and $C_{p,s}$. This, in

turn, would result in a large error in the determination of the optical thickness. In order to compensate for this effect, an additional routine was developed that was performed after each layer was deposited. In this procedure, nonlinear optimization was used to determine the optical constants of the deposited materials using the previous data.

The above routine has two basic assumptions. The first is that n and k for each material remains constant over the entire multilayer. The second assumption is that the deposition rate , $\dot{d}$, remains constant over an individual layer. This allows for a determination of the thickness for each measured value of ρ through the relation

$$d_i = \dot{d}(t_i - t_c) \tag{6.7}$$

where t_i is the time the data point of interest was taken and t_c a critical time period which allows for the substrates to rotate into position and for the initial nucleation process on the surface. The deposition rate can be determined by dividing the final thickness of a layer by the total deposition time minus the critical time. For an N-layer multilayer, the parameters to be fit are then

$$\left\{ n_j, k_j, t_{cj} \right\} \quad j = 1..m, \tag{6.8}$$

where m is the number of different materials.

The final algorithm for the control routines is shown in Fig. 6.11. At specific time intervals a measurement of ρ is made. The value of nd is then determined through the use of Eqs. 6.3a and 6.3b. The procedure is then repeated until the user specified optical thickness, nd_f, is reached. The deposition is then halted by rotating the targets to an

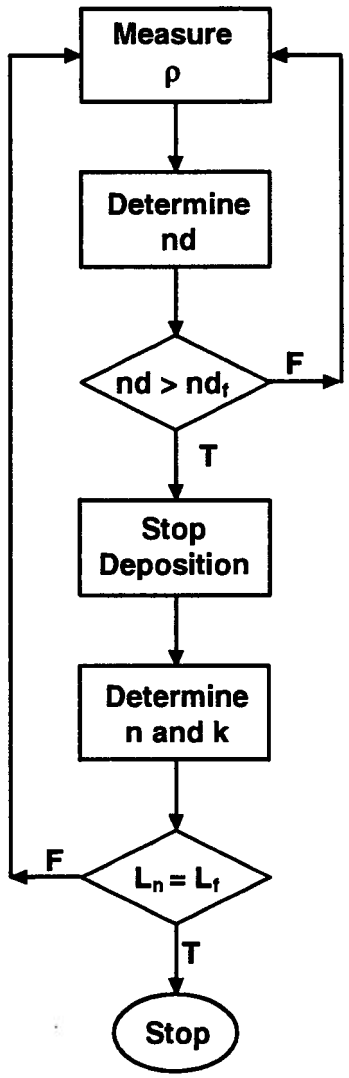

Figure 6.11 Flow diagram for the matrix method of controlling the deposition of optical multilayers

intermediate position. The nonlinear optimization routines are then performed and the values of $A_{p,s}$ and $C_{p,s}$ are updated for the next layer. The current target is then rotated into position and the above procedure is repeated until the final layer, N_f, is deposited.

Despite the simplicity of the above routines they were found to be inadequate as the optical thickness for the HeNe quarterwave stack could not be determined to any degree of accuracy beyond 4 layers. One problem was the large degree of error in the calculated values of $A_{p,s}$ and $C_{p,s}$. If the coefficients are accurate, then the solution for the initial measurement of a layer should result in an optical thickness close to zero. However, these measurements increasingly deviated from this value until at the fifth layer the error was on the order of 10 nm. As the deposition rate was on the order of 0.2 nm/s and measurements were taken approximately every 3 seconds, this large of an offset was highly unlikely.

Further investigations revealed that the assumption of a constant deposition rate over the growth of a single layer was not a good one. This was attributed to operating in the metallic mode. As a result the optimization fits were poor, resulting in a large uncertainty in the optical constants.

One further problem was that there was a large amount of noise in the calculated values of *nd* for certain regions, typically on the order of 1 nm. This degree of noise was not observed in the measured values of ρ. It was concluded that the method was too sensitive to small imperfections in the deposited material and small amounts of misalignment in the in-situ ellipsometer. To illustrate these factors, consider Fig. 6.3 again. During the initial growth of an oxide on silicon the ellipsometric path is practically independent of n. It is not, however,

simply dependent on nd but on βd. As a result an error $\delta\rho$, which can be caused by an inadequate model, miscalibration or simply noise in the system, results on an error in nd through the relation

$$\frac{\delta\, nd}{nd} = -\frac{\sin^2\phi}{n^2}\delta\, n = -\frac{\sin^2\phi}{n^2}\frac{\partial n}{\partial\rho}\delta\rho\,. \tag{6.9}$$

Therefore, in regions where $\partial n/\partial\rho$ is large, the uncertainty in the optical thickness is also large. It should be noted that $\delta\rho$ is in a direction perpendicular to the trajectory for a constant refractive index in Eq. 6.9.

6.3.3 Projection Method.

Though direct use of the matrix equations did not result in a workable control routine it was observed that the experimental data followed the theoretical trajectory quite closely. Hence the deviations from the ideal model were small. It was also noted that the refractive indices of the deposited materials were very repeatable between different runs.

The above observations led to the development of the next control routine referred to as the projection method. In this technique the optical constants determined from previous runs are specified at the beginning of the deposition of the multilayer. The optical thickness is then determined during the layer deposition by projecting the experimental value onto the closest point of the theoretical curve. As with the previous method after the individual layer deposition is completed, nonlinear optimization is performed to determine the actual optical

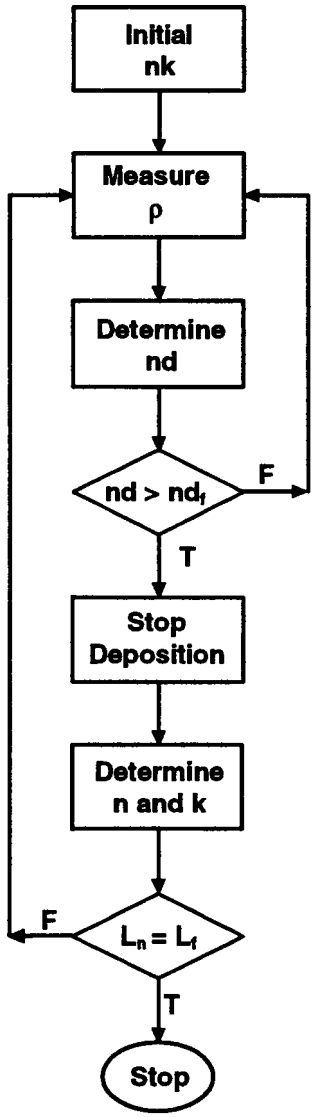

Figure 6.12 Flow diagram for the projection method for the control of the deposition method.

constants. These constants can then be used to calculate the theoretical trajectory once the particular layer material is deposited again. It should be noted that this method lends itself well to absorbing films. The algorithm for the projection method is shown in Fig. 6.12. It can be observed that the overall method is quite similar to the matrix method aside from having to specify the initial values of the optical constants. The theory for determining the optical thickness from a measurement of ρ is given below.

The difference, D, between the theoretical curve and an experimental value is

$$D(d) = \rho_{T.}(d) - \rho_E, \tag{6.10}$$

where $\rho_T(d)$ is the theoretical value as a function of thickness and ρ_E the experimentally measured data point. Rather than minimizing the absolute value of Eq. 6.10 it is simpler to minimize its square

$$|D|^2 = D \cdot D^*, \tag{6.11}$$

and hence find the zero of

$$\frac{\partial |D|^2}{\partial d} = \frac{\partial D}{\partial d} \cdot D^* + D \cdot \frac{\partial D^*}{\partial d} = 0. \tag{6.12}$$

Observation of the right hand side of 6.12 shows that we want to solve

$$\mathrm{Re}\left(\frac{\partial D}{\partial d} \cdot D^*\right) = 0, \tag{6.13}$$

or

$$\mathrm{Re}\left(\frac{\partial \rho_T}{\partial d} \cdot \left(\rho_T - \rho_{meas}\right)^*\right) = 0. \tag{6.14}$$

The projection method deals effectively with the two main problems cited in the previous section. Equation 6.9 shows that as the optical constants are determined to a good deal of accuracy, the overall error in *nd* should be small. Also no assumptions need to be made about the deposition rate in the optimization routines. In this case the function to be minimized is

$$\sigma = \sum_{i=1}^{N} |D_i|^2 \tag{6.15}$$

where N is the number of measured data points. If the number of data points becomes too large, then a fraction can be selected at some chosen interval. The parameters to be adjusted to minimize Eq. 6.15 are then

$$\{n_j, k_j\} \quad j = 1, m \tag{6.16}$$

where m is the number of material types.

The projection method worked well when analyzing the 300 nm quarter-wave stack but developed difficulties with the one deposited at the HeNe wavelength. There were problems due to inaccuracies when calculating the substrate coefficients as before, though not as serious. At the eighth layer the initial measurement of ρ gave an *nd* value of approximately 4 nm. This indicated that the simple model used to describe the stack was not sufficient.

Potential deviations from the chosen model include interdiffusion between the layers and inhomogeneities in the layers themselves. One other potential problem results from changes in the optical constants over the deposition run. This effect is possible, for example, if the base pressure does not remain constant, which can alter the value of k. Also drifts in the overall pressure can affect the value of n, though this factor is expected to be small.

Aside from the non-idealities in the films, another potential source of error is misalignment and miscalibration of the ellipsometer itself. This will also contribute to errors in the deduced values of the substrate coefficients.

Aside from problems with the chosen model another error arises from the nature of the function in Eq. 6.5 These errors result from problems with projecting onto the abrupt turns in the ellipsometric trajectory shown in Fig. 6.9. This problem is better illustrated through the examination of the eighth layer of the HeNe quarter-wave stack presented in Fig. 6.13. Here the experimental data points are shown on the continuous line at intervals of approximately 4 nm (every fifth data point measured is shown). Also shown is the theoretical trajectory predicted from the previous optimization routines. It can be seen that the experimental results follow the theoretical trend fairly closely aside from an offset that appears in part due to a small error in the determination of the substrate optical properties. However, at the point where the trajectory makes a sharp turn a more serious problem arises. Here the experimental curve intersects the theoretical one at the wrong branch. If the minimal distance method were used the resulting optical thickness would appear to initially be getting smaller after reaching this point. We have found that, depending on the exact orientation of the two curves, the experimental data can continue to be projected onto the wrong branch of the theoretical curve. Also, it can be seen that the change in ρ is relatively insensitive to thickness after the turn, hence the offset error in this situation can be quite problematic. The nature of the path of ρ can also be a problem during the optimization routines. From Fig. 6.13 it is evident that the

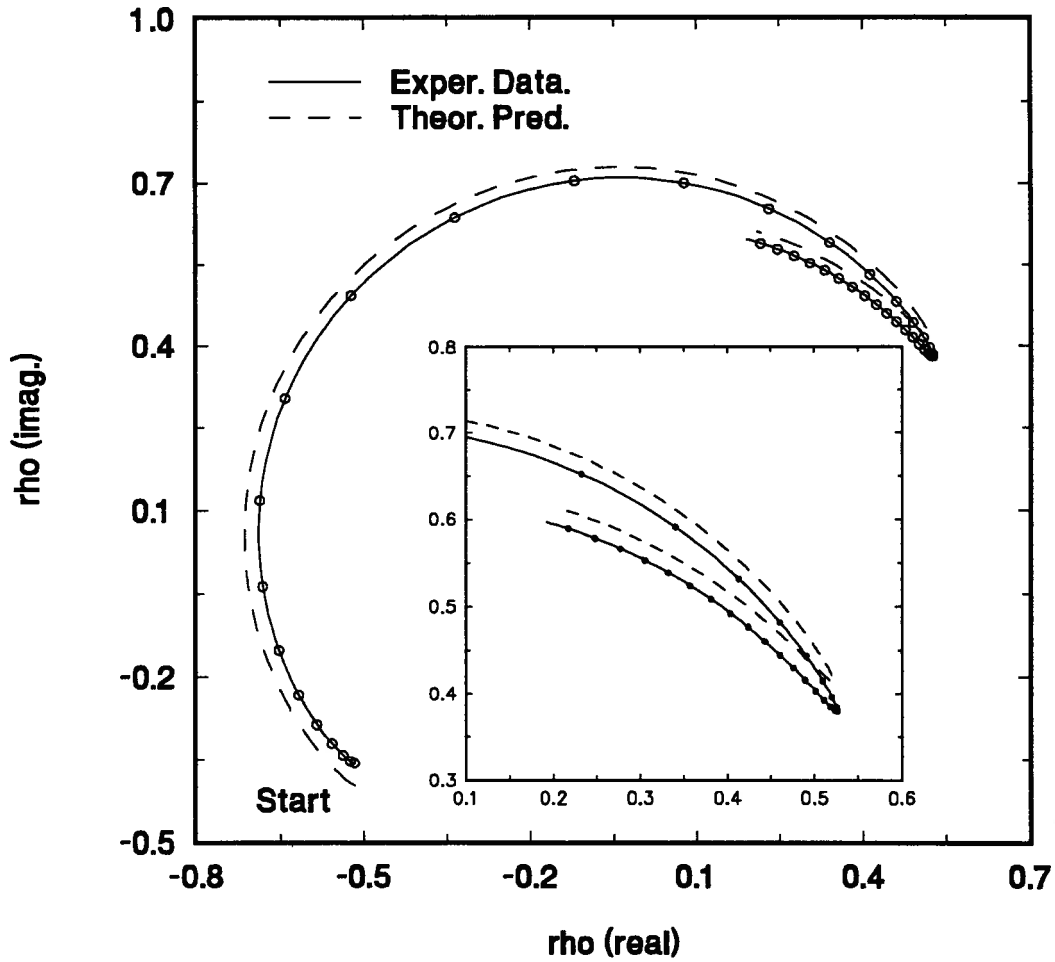

Figure 6.13 Experimentally measured and theoretically predicted ellipsometric trajectories for the eighth layer of the quarter-wave stack controlled by the projection method.

that the program can easily converge to a local rather than the global minima. This, in turn would lead in an error in the determined values of n and k.

An 8 layer quarter-wave (HeNe) stack was deposited through this method and its reflection and transmission spectra measured. The maximum in reflectance was found to be at approximately 580 nm indicating an average layer optical thickness of 145 nm rather than 158.2 nm

6.3.4 Transform method

The projection method discussed above appeared to be too sensitive to the accumulative errors in the substrate parameters. Also the ellipsometric trajectory of the complex reflectance ratio was both difficult to fit through nonlinear optimization due to the presence of local minima and to project onto for the determination of the optical thickness, nd.

What was needed was a method that could accommodate the imperfections in the substrate. Also, it was desired to be able to transform ρ into a form that could easily be optimized. A solution was found through a transform method for a single layer on a substrate developed by Yousef and Zaghloul.[187] Through Eq. 6.5 , the above method can be extended to multilayers. The transform is described below.

From Eq. 6.5, the thickness of the topmost layer affects the complex reflectance ratio through the term

$$x = \exp(2i\beta\, d). \tag{6.17}$$

For a transparent film, Eq. 6.17 is that of a unit circle with a phase factor of $2\beta d$. For an absorbing film, Eq. 6.17 will spiral in towards the origin. Equation 6.5 can be thought of as a transform that maps a value from the complex x plane onto to the complex ρ plane. As Eq. 6.17 is a much more "well behaved" function than Eq. 6.5, one possibility is to use an inverse transformation to project a measured value of ρ back to the x plane and determine the phase factor directly. This can be done in practice however it turns out to be preferable to work through an intermediate transformation given by

$$z = \frac{c + gx}{1 + abx}, \tag{6.18}$$

where

$$a = r_{01p}, \quad b = r'_{12s}, \quad c = r_{01s}, \quad g = r'_{12p}. \tag{6.19}$$

The value of z is then mapped onto the ρ plane through the transform

$$\rho = Wz + \frac{X}{z} + Y, \tag{6.20}$$

where

$$W = \frac{b \cdot (a^2 - 1)(ab - cg)}{\sqrt{g - abc}}, \tag{6.21a}$$

$$X = \frac{g \cdot (c^2 - 1)(bc - ag)}{\sqrt{g - abc}}, \tag{6.21b}$$

$$Y = \frac{(g + abc)(b + acg) - 2bg \cdot (a^2 + c^2)}{\sqrt{g - abc}}. \tag{6.21c}$$

Equation 6.18 is a linear fractional or Möbius transform which has the important property of mapping circles onto circles.[188] Hence, for a dielectric film, the transform of the measured data points back to the z plane should result in a circular arc.

If one assumes a perfect alignment and calibration then deviations from a circular arc for an experimentally measured set of data are the result in an error in the calculated values of W, X and Y. The data can then be fit to Eq 6.20 through an adjustment of

$$\{n_1, n_2, C'_p, C'_s\}, \tag{6.22}$$

where n_1 and n_2 are the refractive indices of the topmost and the second topmost layer and

$$C'_p = \frac{C_p}{A_p}, \quad C'_s = \frac{C_s}{A_s}. \tag{6.23}$$

The main problems discussed in the last section have now been addressed. Rather than adjusting the optical constants to fit all of the preceding data, the values of n and the coefficients of the product of the matrices are adjusted until the spectra of the topmost layer has the proper form. This factor helps prevent a propagation of the errors of the substrate. Also, as the data is presented in the form of a circular arc, it is relatively simple to project onto the theoretical curve and to fit through nonlinear optimization.

As previously mentioned, the above method can be applied to Eq. 6.17 rather than Eq. 6.18. However, one advantage to the using the z transformation is illustrated in Fig. 6.14. Here the z-transforms of the values of ρ in Fig. 6.10 are presented. It can be seen that there is graphical representation for a quarter-wave stack at this wavelength in the z- plane. This

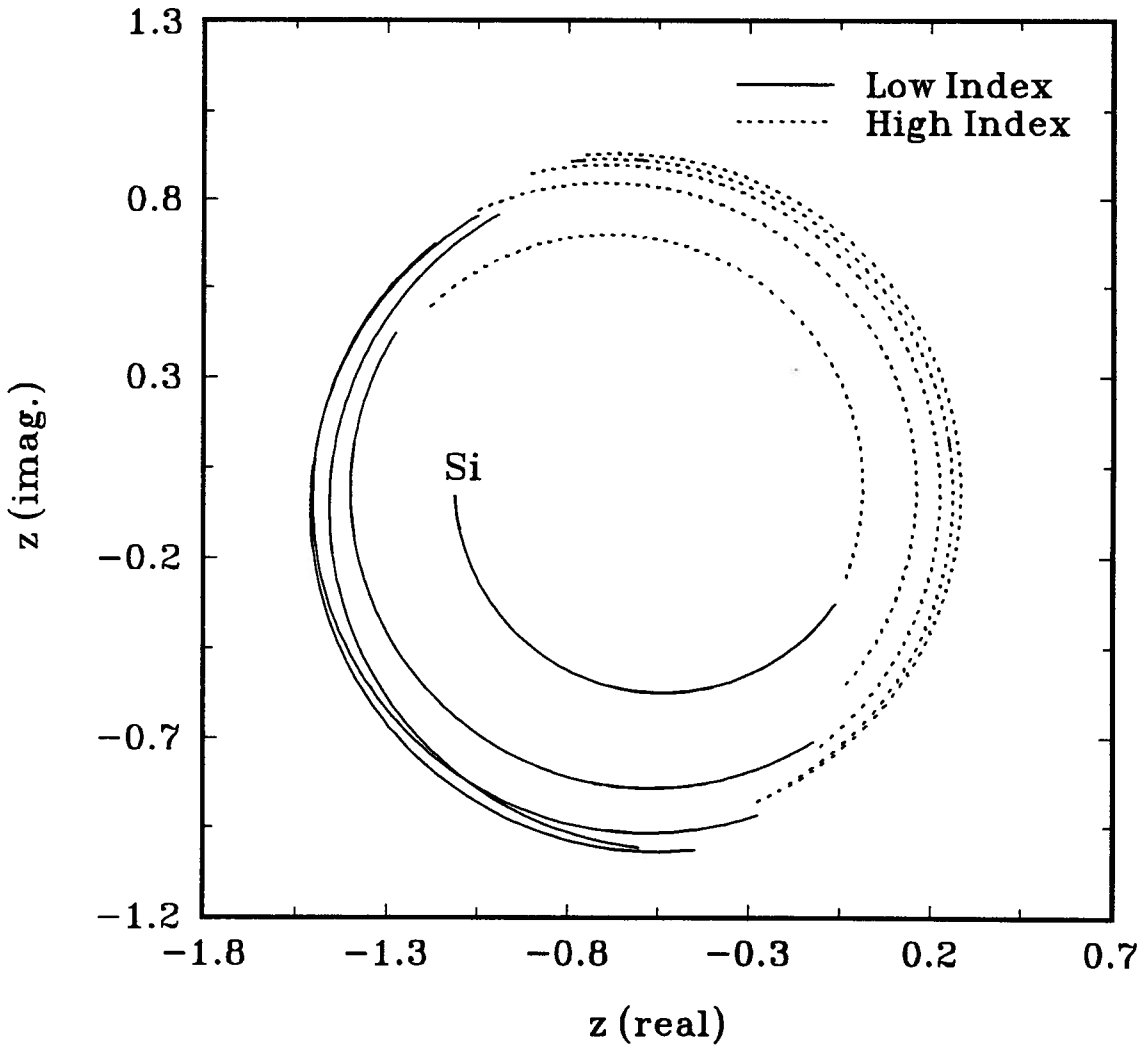

Figure 6.14 Projection of the theoretical data of Fig. 6.10 onto the z plane. The data always progress counter clockwise. The radius of the curves increase with a greater number of deposited layers. The value of the Si substrate is also shown.

representation differs for alternate forms of multilayer coatings. Hence the z-plane provides information on the nature of the multilayer and its imperfections. This cannot be said for working in the x -plane which provides information on the arc length only.

Fig. 6.15 shows the algorithm used for the solution of the optical thickness of each layer. This routine contains one more step than the previous one with the transformation onto the z-plane. The routine was found to be successful when tested on the sample data. The method was then used to control the deposition of a quarter-wave stack at the HeNe wavelength of the form

Air / HLHLHLHLH / Glass

The target optical thickness of each layer was 158.2 nm.

The ellipsometric results in the z-plane are shown in Fig. 6.16. The agreement between the experimental and theoretical curves is quite good even at the ninth layer. Table 6.1 gives the determined values of the film thickness, refractive indices, and substrate parameters before and after the fitting the data after each layer deposition. The initial optical thicknesses are all greater than 158.2 nm due to the finite time taken to rotate the targets out of position. The largest adjustment in the optical thickness occurs for the first layer. This is also accompanied with a relatively large alteration in the substrate parameters. This affect is attributed in part to the initial deposition of an absorbing layer several monolayers thick onto the silicon substrate, which we have observed through the ellipsometric trajectory.

Another reason for the large adjustment is illustrated in Fig. 6.17. Here we present the curves for the first three layers. By examining the beginning of the first arc we can see that

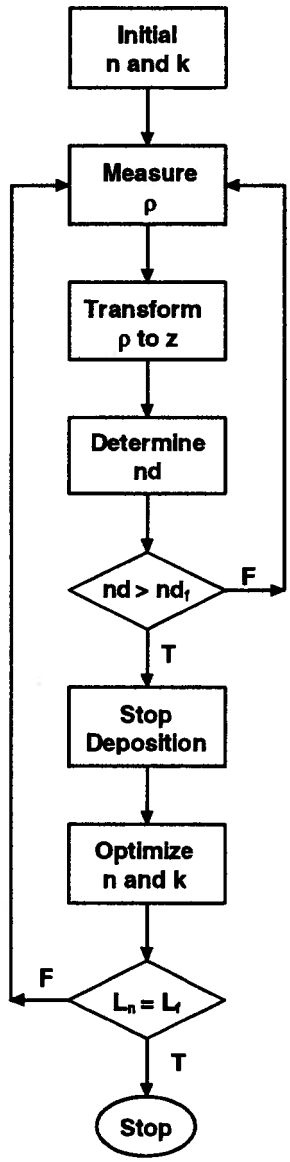

Figure 6.15 Flow diagram for the first iteration of the z-transform method for the control of the deposition of optical multilayers.

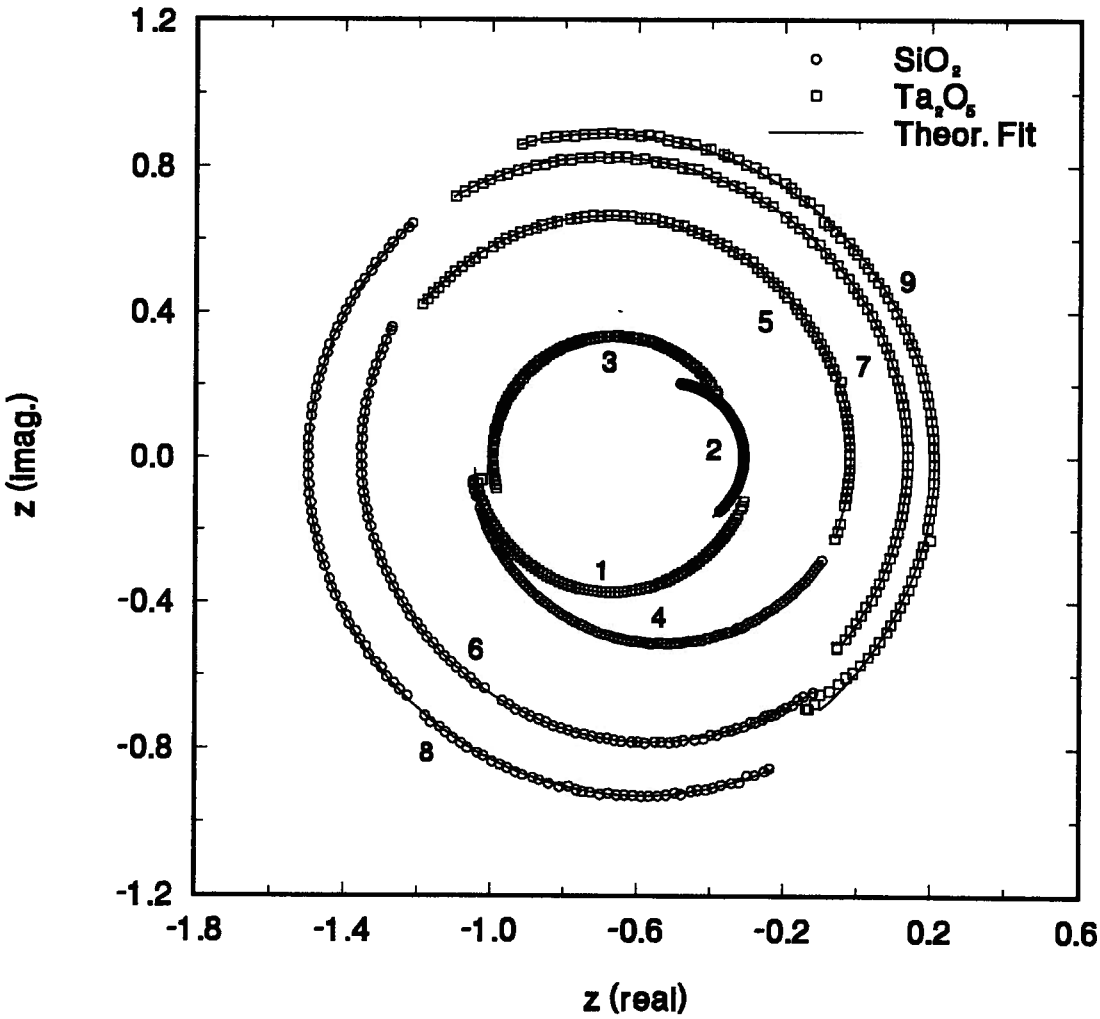

Figure 6.16 Ellipsometric data in the z-plane for the layers in the quarter-wave stack deposited through the z-transform method.

Table 6.1 Initial and final optical thicknesses, refractive indices and substrate parameters for a quarterwave stack deposited at the HeNe wavelength. The ellipsometric transform is shown in Fig 6.16

Layer	Material	Thickness (nm)	n (SiO_2)	n (Ta_2O_5)	C'_{sr}	C'_{si}	C'_{pr}	C'_{pi}
1 (initial)	Ta_2O_5	158.4	1.472	2.100	0.000	0.000	0.000	0.000
1 (final)	Ta_2O_5	153.7	1.472	2.096	-0.027	-0.028	0.013	-0.014
2 (initial)	SiO_2	158.3	1.472	2.096	0.342	-0.112	-0.249	0.114
2 (final)	SiO_2	159.7	1.474	2.096	0.340	-0.143	-0.250	0.129
3 (initial)	Ta_2O_5	159.0	1.474	2.096	0.022	-0.187	0.031	0.198
3 (final)	Ta_2O_5	159.8	1.474	2.096	0.031	-0.178	0.032	0.189
4 (initial)	SiO_2	158.4	1.474	2.096	-0.314	-0.076	0.128	0.157
4 (final)	SiO_2	159.0	1.471	2.096	-0.292	-0.035	0.129	0.149
5 (initial)	Ta_2O_5	159.1	1.471	2.096	0.405	-0.297	-0.270	0.038
5 (final)	Ta_2O_5	159.4	1.471	2.071	0.406	-0.289	-0.268	0.035
6 (initial)	SiO_2	158.7	1.471	2.071	-0.503	0.399	0.331	-0.141
6 (final)	SiO_2	160.0	1.471	2.071	-0.496	0.406	0.330	-0.141
7 (initial)	Ta_2O_5	160.4	1.471	2.071	0.342	-0.665	-0.244	0.363
7 (final)	Ta_2O_5	162.7	1.471	2.050	0.337	-0.663	-0.241	0.371
8 (initial)	SiO_2	158.8	1.471	2.050	-0.446	0.666	0.240	-0.427
8 (final)	SiO_2	159.5	1.471	2.050	-0.441	0.681	0.239	-0.427
9 (initial)	Ta_2O_5	159.2	1.471	2.050	0.203	-0.835	-0.012	0.530
9 (final)	Ta_2O_5	160.3	1.471	2.050	0.192	-0.829	-0.004	0.534

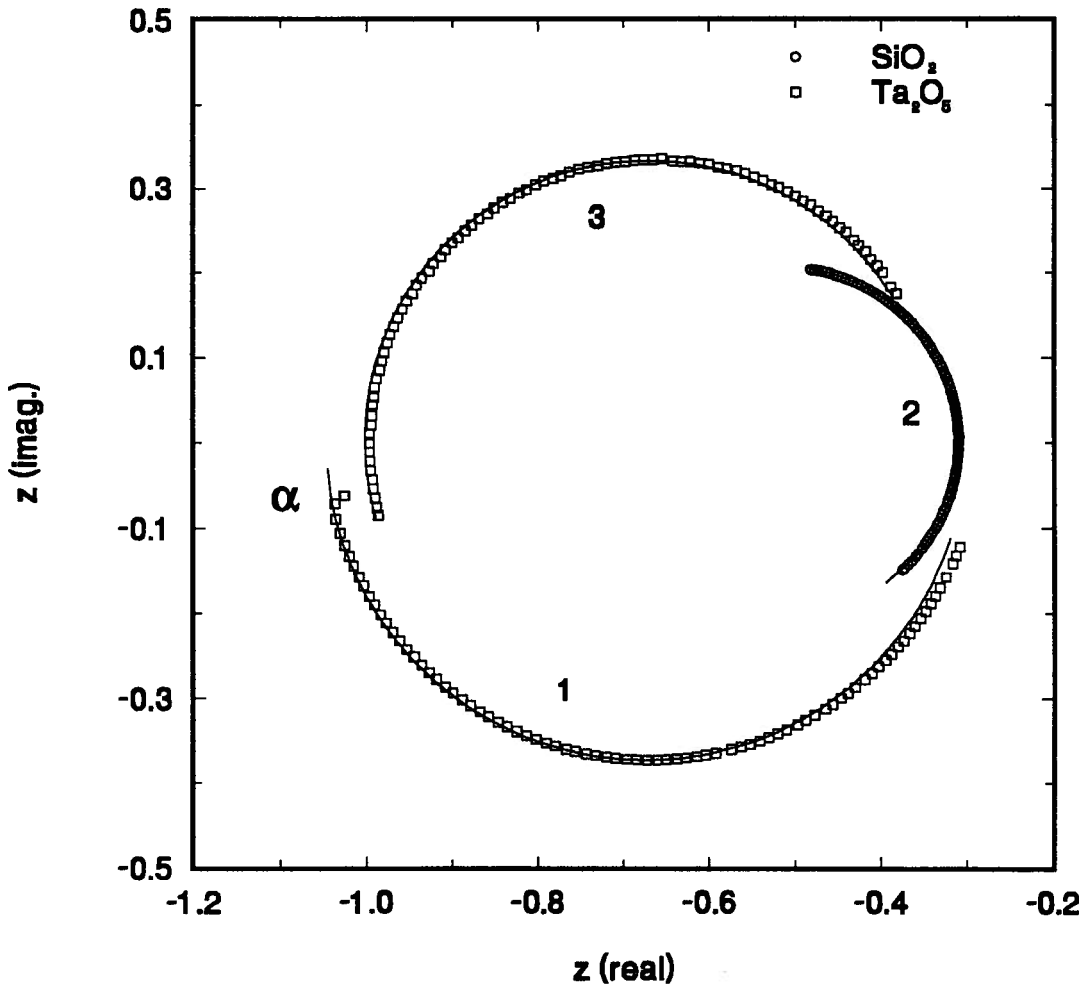

Figure 6.17 Ellipsometric data in the z-plane for the first three layers in the quarter-wave stack deposited through the z-transform method.

the experimental points do not coincide with the start of the theoretical trajectory but at a relative angle of α. This is one drawback to the fitting routines in that as we are projecting

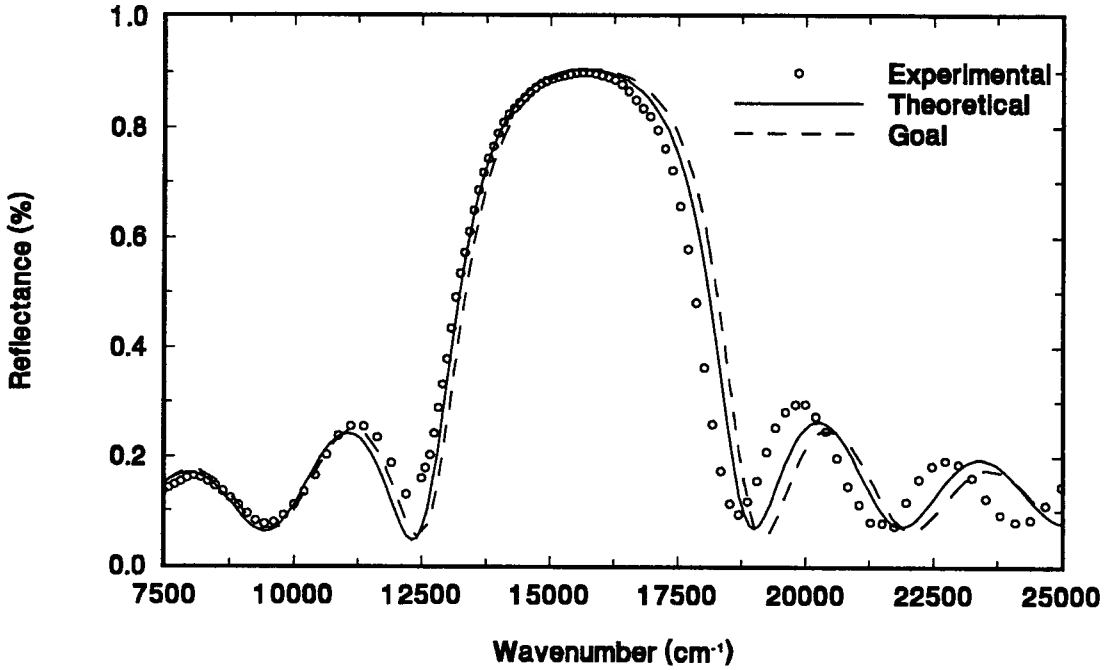

Figure 6.18 Experimentally measured and theoretically determined reflection spectra for a 5 period (HeNe-15,800 cm^{-1}) quarter-wave stack deposited through the transform method. The theoretical curve is calculated using the final thickness for layer in Table 6.1. Also shown is the theoretical spectra for an ideal stack.

onto the theoretical curve, the radius of curvature is correct but not necessarily the arc length. This will manifest itself in a non-zero original reading. This effect is still seen in the second trajectory but not the third, indicating that the error is not necessarily propagating.

The reflectance of the dielectric mirror is presented in Fig. 6.18 along with two theoretical spectra. The dashed line represents the target reflectance assuming all the optical thicknesses were 158.2 nm. The solid line is calculated using the final theoretical values in Table 6.1. The theoretical curve is shifted downwards slightly towards the infrared, which is to be expected given that the majority of the optical thicknesses are greater than 158.2 nm.

The theoretical spectra matches the experimental data quite well in the infrared and up to the HeNe wavelength (15,800 cm^{-1}). Above this point, the experimental curve appears to be shifted downward at an increasing rate as we go into the ultraviolet (UV). This effect is attributed to dispersion in the optical constants which was neglected in the theoretical calculations. As dispersion is negligible in these materials in the near infrared, the results agree well in this region. In the visible-UV regions the value of n increases with increasing wavenumber resulting in a larger value of nd. This results in the side bands being spaced closer together.

At this point the z-transform method appeared to be much more successful than the previous two methods. However it was felt that there were still two improvements which could be made. The first was to optimize the transform parameters at some point during the layer deposition rather than at the end of the run. This would result in a final optical thickness that was closer to the target thickness. The second was to determine the optical thickness from the experimental arc length, rather than from the theoretical curve. This would help reduce the error resulting from a different starting angle. To simplify the procedure, the offset error was simply subtracted off the determined value of nd. Though this is not strictly valid, as arc length is not conserved when transforming from the x to the z-plane, this should result in a first order improvement.

The final algorithm for the control routines is shown in Fig. 6.19. In this case the user decides at what point, nd_m , during the growth of an individual layer that the deposition is

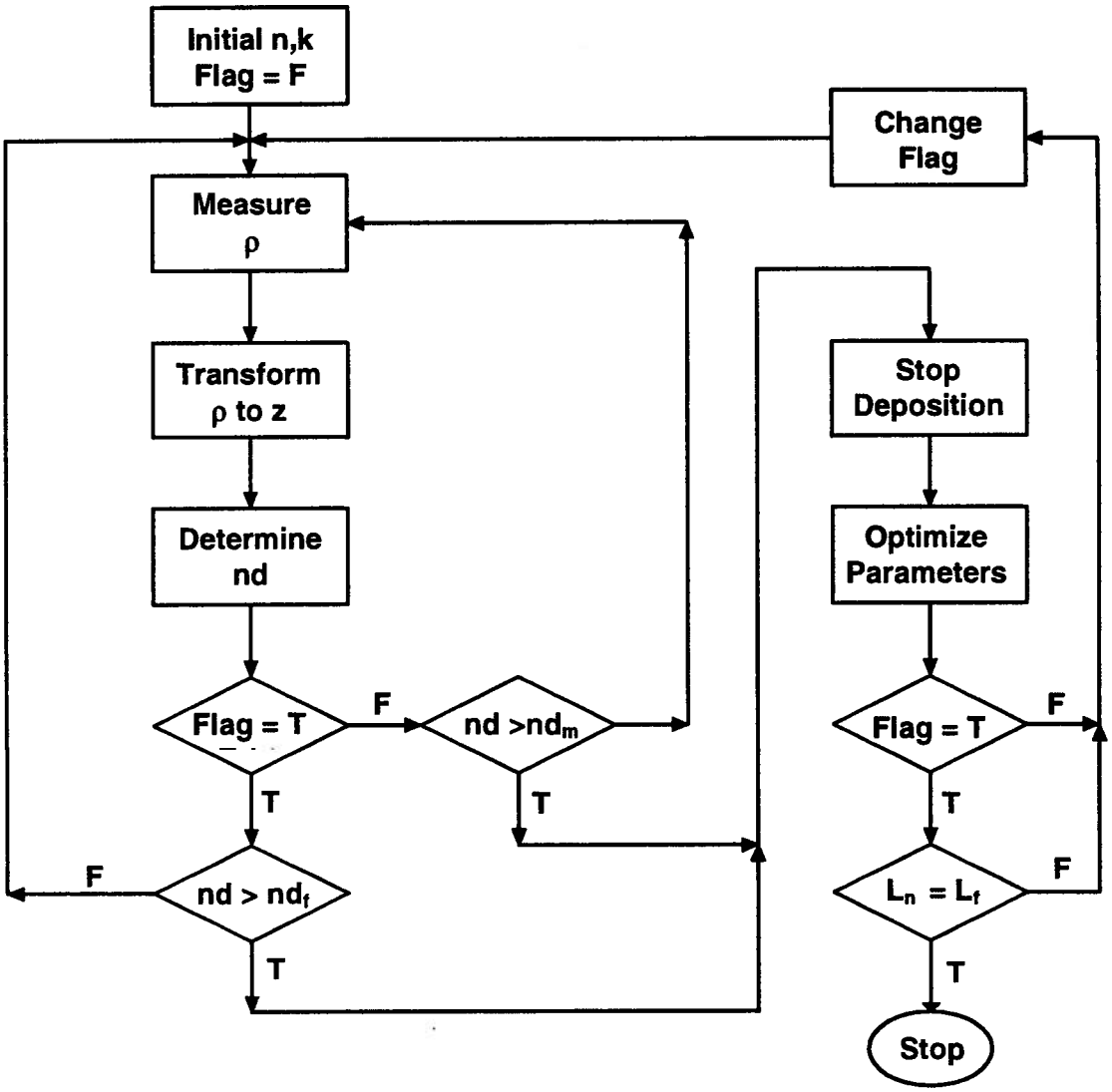

Figure 6.19 Flow diagram for the second iteration of the z-transform method for the control of the deposition of optical multilayers.

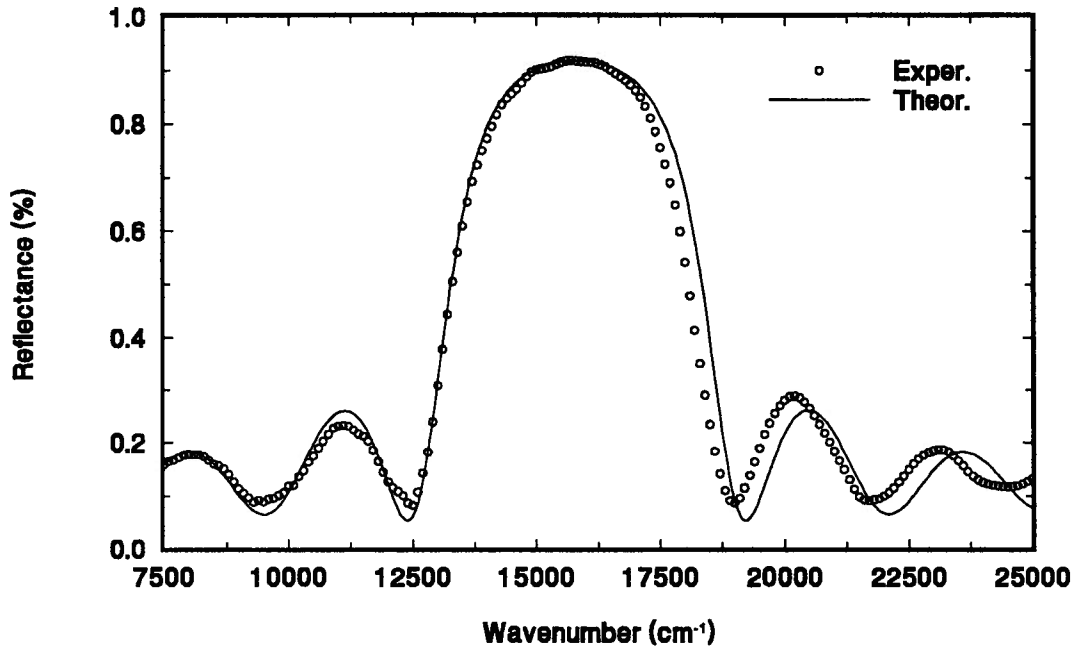

Figure 6.20 Experimentally measured and theoretically determined reflection spectra for a 5 period (HeNe-15,800 cm^{-1}) quarter-wave stack deposited through the revised z-transform method. The theoretical curve is calculated assuming a perfect stack.

halted and the model parameters updated. The refinement procedure is repeated at the endpoint in order to update the substrate coefficients for the next layer.

The experimental reflectance spectra for a quarter-wave stack identical in design to the previous sample but deposited through the final control routine is shown in Fig. 6.20. Also shown is the theoretical spectra for a perfect stack. In this case, the reflection spectra is closer to the ideal than that in Fig. 6.18, indicating that the final algorithm is an improvement over the previous one.

In order to test the routines further, a Fabry-Perot filter was deposited. As discussed in Chapter 2, a Fabry-Perot filter consists of a half-wave layer sandwiched between two

quarter-wave stacks. As a result, the conditions for high transmission at the desired wavelength require a high degree of matching between the two stacks.[189]

The design of the Fabry-Perot filter was

$$Air\ /\ LH\ /^{5}\ LL\ /\ HL\ /^{4}\ H\ /\ Glass.$$

Hence the subroutines had to control the deposition of 21 quarterwave layers.

The Fabry-Perot filter was deposited under the same conditions as the quarter-wave stack. Once the filter was removed from the deposition chamber, a colour shift along one direction of the sample was observed. This effect was attributed to a non-uniform thickness which, in turn, was attributed to a non-uniform deposition flux which is inherent in magnetron sputtering.[190] This effect was not noticeable to the same degree for the quarter-wave stack due to the lower number of layers.

One solution to the above problem would be to design a mask to allow for a uniform deposition across the surface. As this would result in a decreased deposition rate, another possible solution would be to have the targets also move along the radial direction of the chamber. However both these procedures would be quite time consuming.

As the beam-width of the spectrophotometer was approximately 7 mm the non-uniform thickness had the effect of broadening the transmission peak in the measured spectra. In order to compensate for this factor, a 2 mm wide slit was placed in front of the filter. The slit was positioned relative to the sample by finding the maximum transmission through the filter for a HeNe laser. The resulting position on the filter corresponded, within a 2 mm error, to that of the monitoring laser.

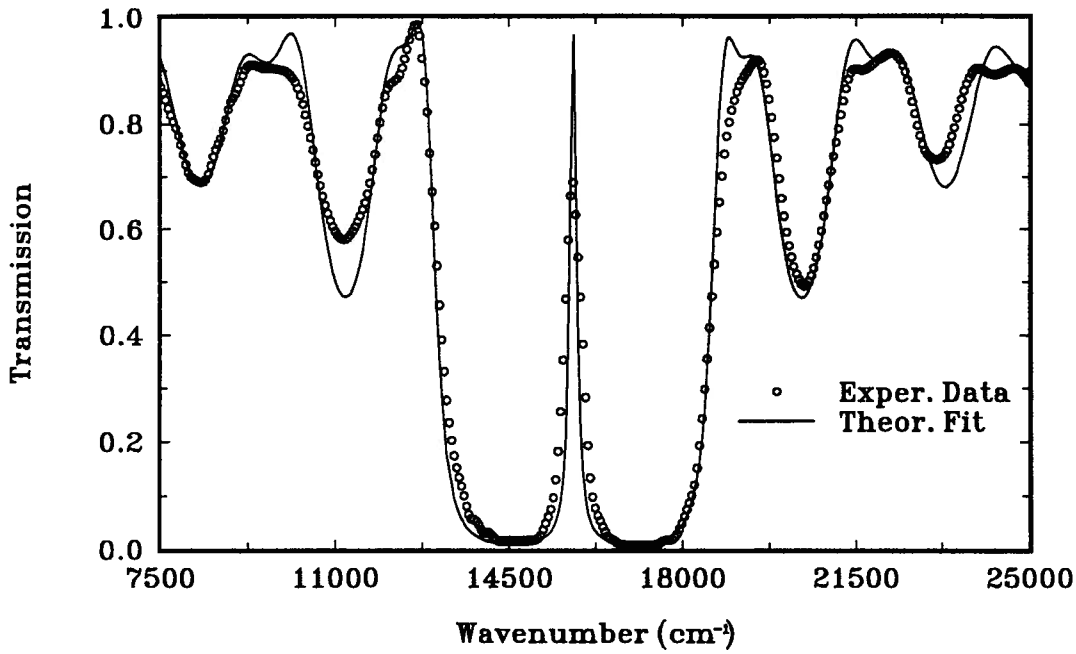

Figure 6.21 Experimentally measured and theoretically determined transmission spectra for a 5 period (HeNe-15,800 cm^{-1}) Fabry-Perot filter deposited through the revised z-transform method. The theoretical curve is calculated assuming a perfect stack.

The experimental and the theoretical spectra for the Fabry-Perot filter are shown in Fig. 6.21. The fit between the two spectra is fairly good, however, there are a number of discrepancies, the most important being those at the HeNe wavelength (632.8 nm). One problem is that the peak transmission is too low, 66 % rather than the theoretical 95 % (the ideal transmission is less than 100 % due to the glass substrate). This can be in part attributed to the non-uniformity of the sample and the finite bandwidth of the spectrophotometer (1 nm) given that a measurement with a .5 mm beam-width HeNe laser resulted in a transmission of 75 %. The measured FWHM of 17 nm is also larger than the ideal 6 nm.

One potential source of the above errors can be observed by examining a number of the theoretical fits in the z-plane to the experimental data (Fig. 6.22). The first layer presented is the tenth which, ideally, is a half-wave (316.4 nm) thick. A good theoretical fit to the data is achieved for this important layer. However, a problem arises with the next layer. At one point along the trajectory, the experimental data points can be seen to increase in radius then curl back along the theoretical curve.

In order to compensate for the above problem, the routines reject transformed data points which are a percentage greater than the theoretical radius. Under these circumstances the routines revert to the timing method until the data points fall back onto the theoretical curve. From Fig. 6.22, it can be seen that for the high index of refraction layers this problem becomes more serious with an increasing number of layers. For the final layer (SiO_2), however, the data is continuous along the entire theoretical curve.

The source of the error illustrated in Fig. 6.22. can be understood by examining the theoretical trajectory of the last two layers of the Fabry-Perot filter in the complex ρ plane (Fig. 6.23). The data points are spaced 4 nm apart and the positions on the high refractive index trajectory corresponding to four different optical thickness are also presented.

Fig. 6.23 shows that there are two regions of insensitivity in terms of $\partial\rho/\partial nd$; the first is approximately between 8 and 36 nm, and the second approximately between 96 and 140 nm. As the absolute rate of change of z with respect to optical thickness is practically constant in these regions, the value of $\partial z/\partial\rho$ is expected to be large. Hence small

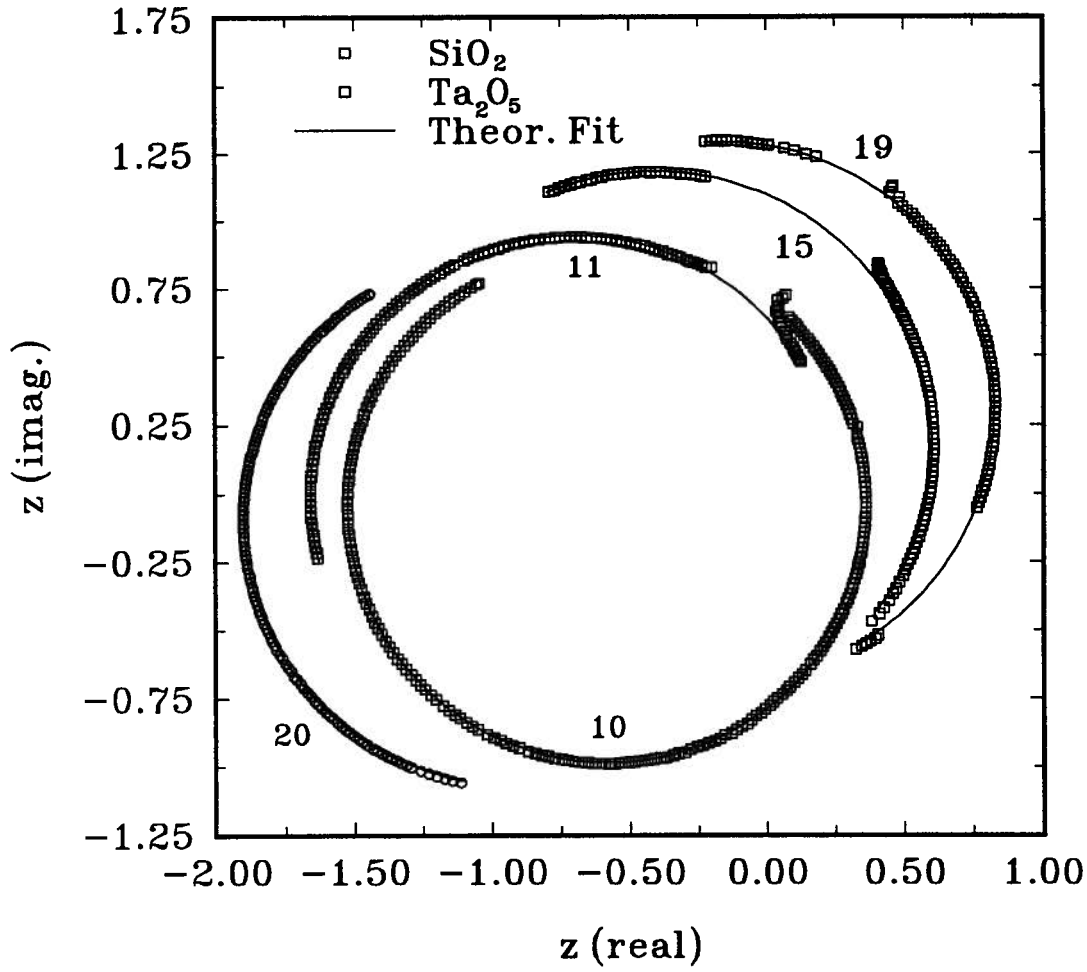

Figure 6.22 Ellipsometric data in the z-plane for a number of the layers of the Fabry-Perot filter deposited through the revised *z*-transform method. The theoretical curve is calculated assuming a perfect stack.

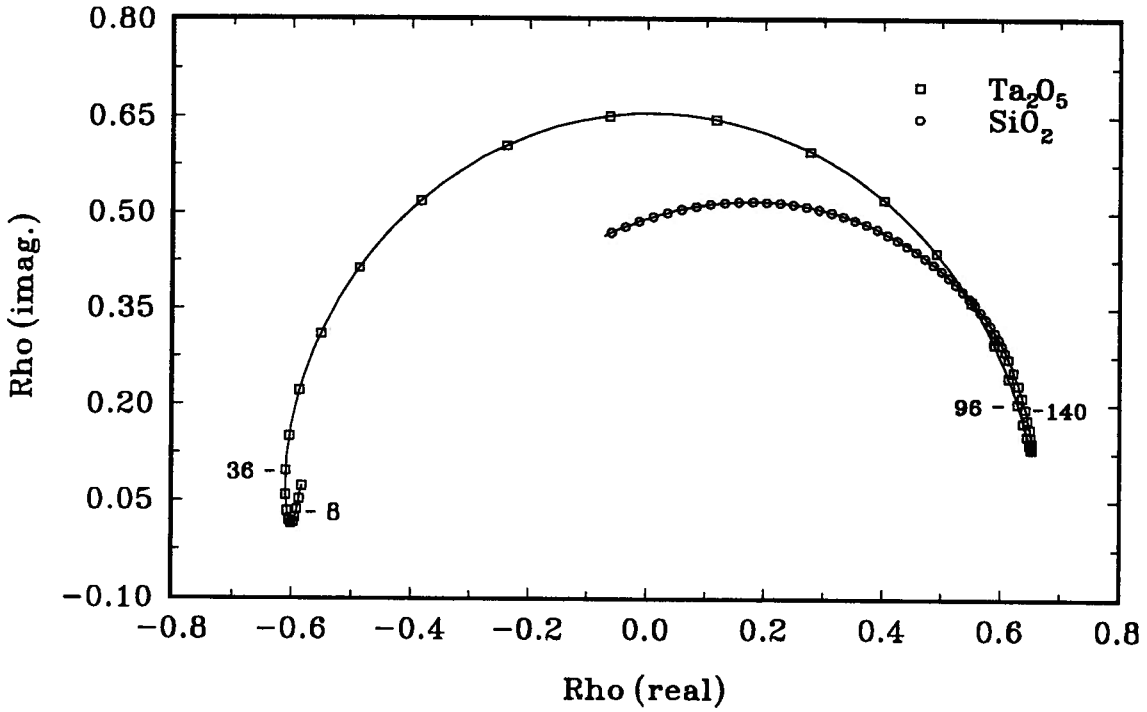

Figure 6.23 The theoretical trajectory in the ρ plane of the last two layers of the Fabry-Perot filter. The data points are spaced 4 nm apart. The optical thickness of the tantalum oxide layer is presented at a number of points along the curve.

measurement errors, small errors in the model parameters or film imperfections will lead to large errors in the value of z. These effects can clearly be seen in Fig. 6.22. The final SiO_2 layer is free of these regions resulting in good overall fit.

Though one of the main problems cited in the section on the projection method appears to be carried through in the z-transform, it is less problematic in this technique. One advantage of the z-transform method for dielectric films is that the data points should ideally all lie on the same circle. As a result, one can reject data points whose radius is greater or less than the theoretical value by some predetermined value. This simplifies the optimization

procedure due to the reduced number of local minima. Therefore reasonable values could still be achieved allowing for the good fits of the low index of refraction layers.

Since, however, an ideal fit is never achieved, Fig. 6.22 shows that the possibility exists of errors in the model parameters or misalignment and calibration errors. One other possible source of error which also must be considered is the effects of imperfections in the film itself. In order to determine this, a number of sets of data for the nineteenth layer were generated assuming a linearly decreasing refractive index gradient or some degree of surface roughness. The data were then fit to a theoretical curve in the z-plane using the above routines. The starting parameters where those used to generate the theoretical data. In the case of the inhomogeneous films the refractive index at the midpoint of the layer was used.

Fig. 6.24 shows the optimization results for a set of data with a refractive index gradient from 2.15 to 2.05. The data sets with less inhomogeneity resulted in better fits. Also shown is the actual data for the nineteenth layer, displaced by a constant factor for comparison purposes.

The above set of tests were reperformed on a number of sets of data with a surface roughness which was a percentage of the total thickness. The void fraction of the surface layer was 50 %. One set of results are also shown in Fig. 6.24 for the case where the surface roughness was 10 % of the total thickness. In this case the above effects are less than that for experimental case.

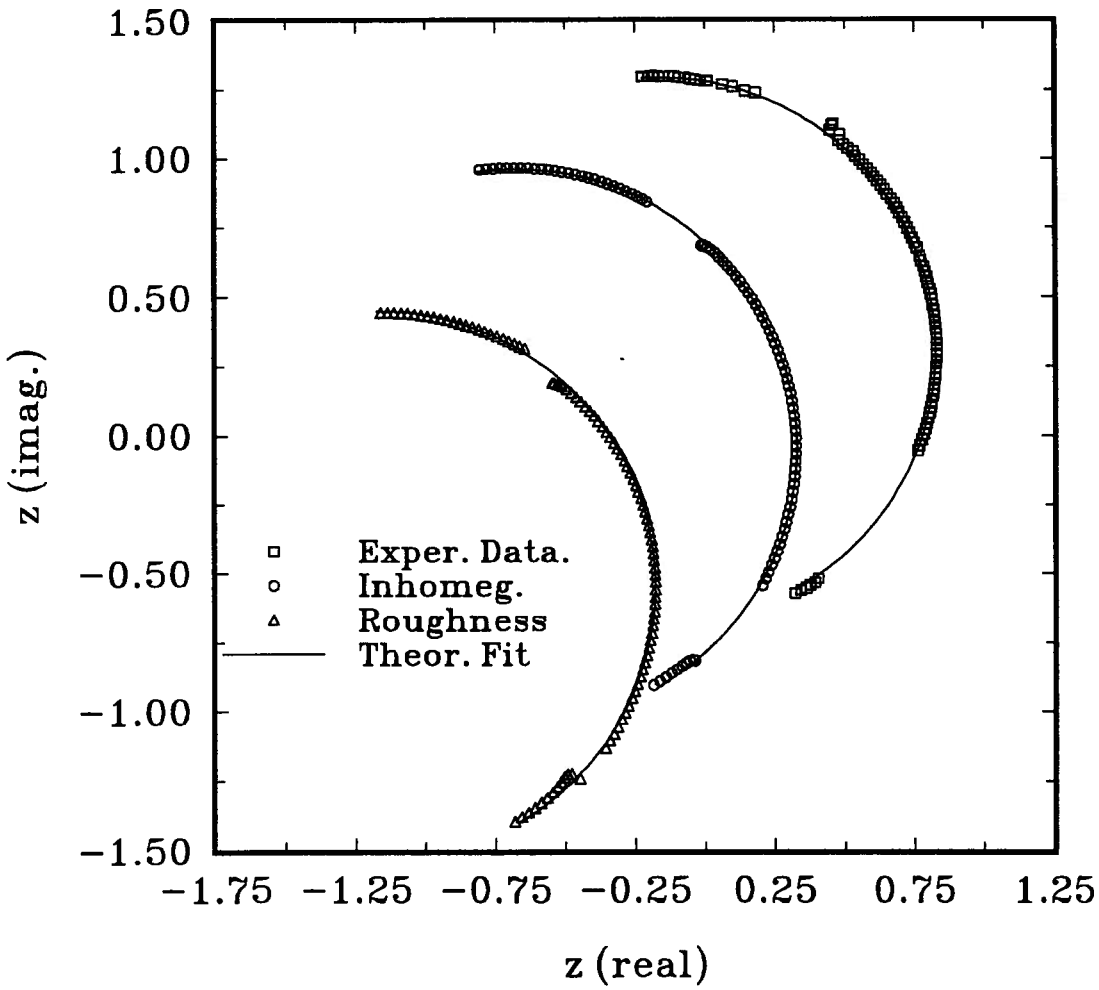

Figure 6.24 The optimized fits to two generated sets of data in the z-plane for the nineteenth layer of the Fabry-Perot filter. The first assumes 10 % inhomogeneities and the second has a surface roughness layer equal to 10 % of the total thickness. The optimization model assumes an ideal film. Also shown is the experimental data. The curves have been offset for presentation purposes.

The imperfections in the two models shown in Fig. 6.24 are somewhat large for a material such as tantalum oxide especially considering that the layer was deposited under conditions where a zone-T microstructure would be expected. As a result, it is possible that the errors in the fit are in part due to imperfections in the instrumentation or problems in the algorithms.

Miscalibration or misalignment errors are the result of limitations in the design of the in-situ ellipsometer. One improvement in the instrumentation would be to increase the angular resolution of the polarizers to that of the ex-situ machine (.005°). Another possible source of error is the birefringence of the port windows. Though this effect is reduced through the calibration routines, it would be better to deal with the problem at the source. Since the development of the in-situ ellipsometer, a low birefringent window material developed at AT&T labs[191] has become commercially available. One final improvement to the instrument would be to have the angle of incidence determined through some method other than a measurement off the Si substrate, as this procedure does not allow for an independent calibration check.

Another possible source of error are the optimization routines themselves. The techniques used in this project were kept fairly simple as the goal was to demonstrate a proof of principle, rather than deposit state of the art optical coatings. One disadvantage to the above technique is that the outlier points are ignored. More robust routines and careful weighting could be applied to achieve a more realistic fit. Also, we have not taken full advantage of the form of the z-transform in the optimization routines. A more sophisticated mathematical

treatment could be used to eliminate more of the local minima (such as when the phase angle is incorrect).

Even if the above improvements are implemented they cannot handle the case where an endpoint lies in the a region of insensitivity. Though the timing method can in part compensate for this factor, as previously discussed, the assumption of a constant deposition is not always valid. A potential solution is to use more than one wavelength. At the beginning of each layer deposition the software can choose the optimum monitoring wavelength. Multiwavelength in-situ ellipsometers are now commercially available.[192]

One final note should be made on the lack of adaptive routines which are often required to deposit high quality optical multilayers. As previously mentioned, each type of optical multilayer system has its own set of curves in the z-plane. It would interesting to see after each layer deposition, if it would be possible to recalculate the required thicknesses of the remaining layers in order to achieve the final trajectory and if this correspondingly would give the correct reflection and/or transmission characteristics for the system.

6.4 Optical Monitoring of Absorbing Coatings

Once the algorithms were developed for dielectric routines, it was necessary to extend the routines in order to be able to monitor and control absorbing layers. As discussed previously, determining the layer thickness and optical constants for absorbing films is inherently more difficult than that for dielectric coatings due to the additional unknown at each data point.

For single layers on a substrate a technique that is often used is to solve for two data points at once.[193,194] In this case, there are an equal number of equations and unknowns allowing for the employment of such numerical techniques as the Newton-Raphson method. These techniques are time consuming and often highly sensitive to noise. In addition, they generally require a knowledge of the substrate to a high degree of precision making the techniques unsuitable for multilayers.

A method has been developed for superlattices which allows for the solution of both the optical constants and the layer thickness.[195] This technique has been applied primarily for determining alloy fractions in such materials as aluminum gallium arsenide. However the technique requires prior knowledge of the optical constants as a function of alloy composition and cannot deduce these values independently. As a result, this method is not suitable for such materials such as carbon which can take on a wide range of values.

The method for determining the optical constants and the thickness of the films used in this thesis was essentially the same as that for the transparent films, that is project onto the theoretical curve then use an optimization routine to determine the optical constants more precisely. Of course this requires some estimate of the optical constants prior to deposition, however, with a well controlled system, this should not present a problem.

Though the above technique proved problematic for dielectric multilayers with more than ten layers, the same difficulties do not exist for 3 to 4 layers of partially absorbing materials. In this case the path in the ρ plane is generally more well behaved due to the dampening of the interference effects. The use of z-transforms is often unnecessary under

these conditions and a modified version of the projection method can be used. In this technique one projects onto the theoretical curve generated by Eqs. 6.5 and 6.6 and performs the optimization on a single layer using the set of parameters given in Eq. 6.22.

The method was tested using two carbon films deposited onto silicon. The first film was deposited at 1 Pa in argon at 100 W while the second was deposited at the same pressure and power but with a 33% CH_4 / 67% Ar sputter gas mix.

Fig. 6.25 shows the experimental data and theoretical fit for the carbon film deposited in pure argon. The resulting optical thickness was determined to be 160.9 nm and the optical constants (2.19,.337). In addition, theoretical trajectories for dielectric films of the same optical thickness with refractive indices of 2.1, 2.19 and 2.3 are also shown. The trajectory of the absorbing coating is clearly distinct from the three dielectric curves, indicating that the presence of absorption can be detected by observing the trajectory in the complex plane.

Fig. 6.26 shows the initial trajectories of Fig. 6.25 in greater detail. The first data point is not that of the silicon substrate due to the presputtering of the target before deposition. Initially all of the dielectric trajectories essentially lie on the same curve. However the absorbing film has a clearly distinct initial path. Hence the effects of absorption can be detected for relatively thin coatings.

Initially, the experimental trajectory of Fig 6.26 does not follow the theoretical curve. This factor is attributed to an intermediate layer between the silicon and carbon, possibly of silicon carbide.

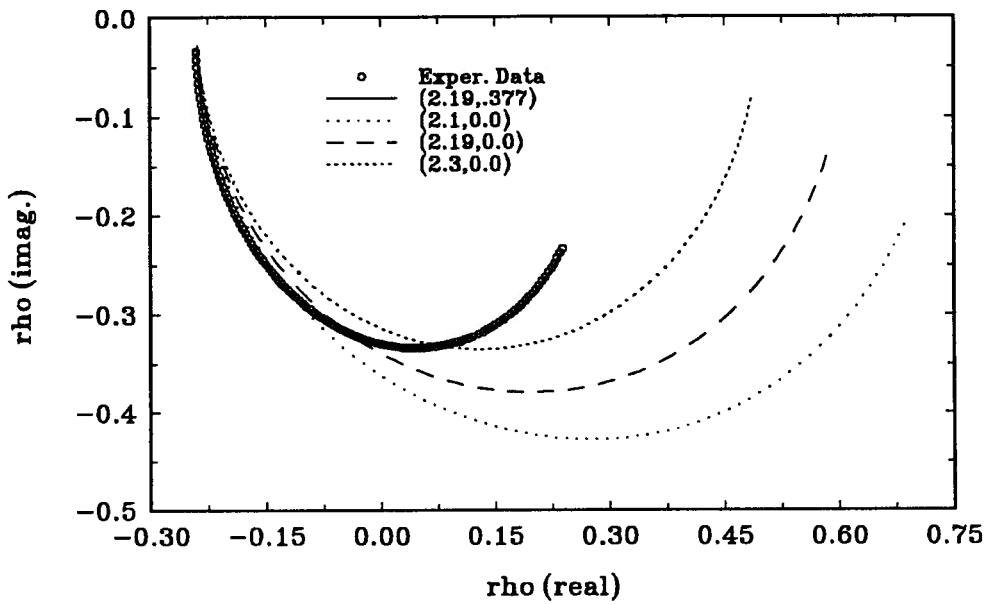

Figure 6.25 Experimental data and theoretical fit with a refractive index of (2.19, .377) for a carbon film deposited in argon. Also shown are the theoretical trajectories for three dielectric films.

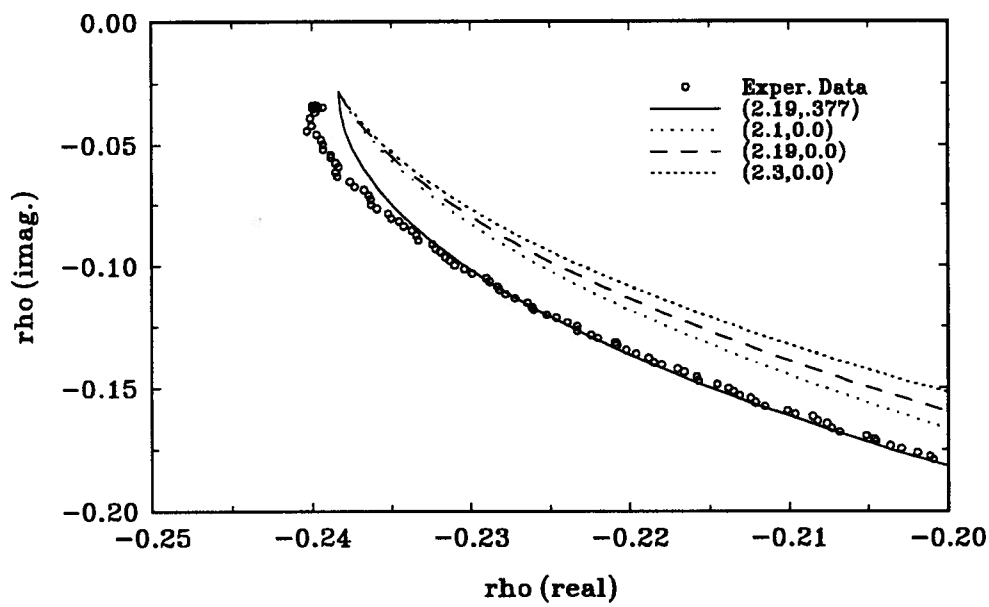

Figure 6.26 The initial values of the data and models presented in Fig. 6.26.

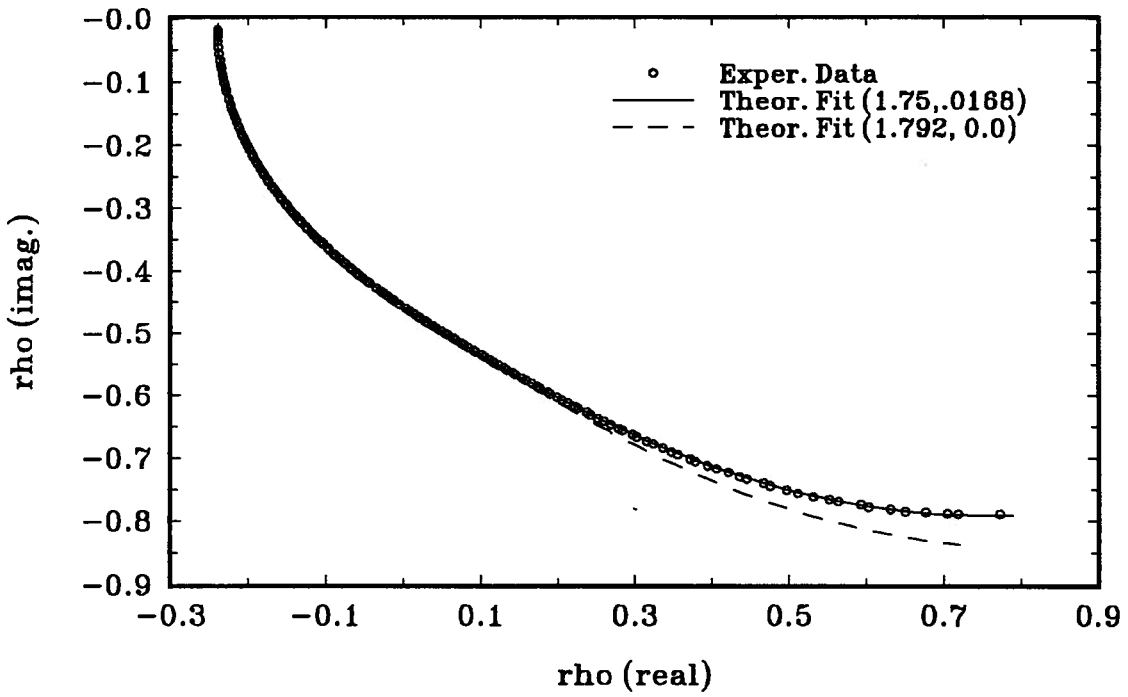

Figure 6.27 Experimental data and two theoretical fits to a carbon film deposited in 33 % CH_4 / 67 % Ar.

Fig 6.27 shows the experimental ellipsometric trajectory of the film deposited in a 33% CH_4 / 67% Ar sputter gas mix. Also show are two theoretical fits. One was accomplished by setting the value of *k* equal to zero and the other through allowing *k* to vary.

It is interesting to take note of the difference in the optical thickness of the two layers, 1547 vs. 1569 angstroms, which is just over a percent difference. This illustrates how ellipsometric measurements are relatively insensitive to small amounts of absorption in the films. However, due to the difference in the optical constants, the difference in the physical thickness is closer to four percent.

6.5 Conclusions

A unique control routine has been developed which uses in-situ ellipsometry to monitor and control the thickness of the individual layers. This technique can be used for both dielectric and absorbing films. However, at this point, the routine develops problems for dielectric coatings with more than ten layers.

This routine is well suited for the deposition of germanium carbide as it can also monitor the refractive index of the individual layers. This should allow for better quality control of films of this nature.

One area of research that the above methods could be extended to is the study of metal-dielectric multilayers. This technique could be used both for control, and as a monitor to determine effects of oxidation of the metal films.

CONCLUSION

Two of the stated objectives of this thesis were achieved: 1) the determination of the optimum conditions for the deposition of diamond-like films through magnetron sputtering and 2) the development of a control system for optical multilayers which can determine both the thickness of the individual layers and their corresponding optical constants. The third objective was not completely achieved in that a method to deposit germanium carbide over the entire alloy range was not accomplished. As a result, the refractive index range of this material was limited from 4.1 to 3. However, a potential solution to this problem was found through depositing alternating layers of carbon and germanium which are thin on the order of the wavelength of interest.

The thesis results showed that the best diamond-like films were deposited at the lower deposition pressures. The increase in transparency at the higher pressures appeared to be, in part, due to hydrogen incorporation and the presence of a polymer phase in the films. In addition, these films were relatively soft and were porous if a substrate bias was not applied. It was determined that the amount of hydrogen incorporation required for the lower pressure films depended upon the degree of trade-off between the hardness and the transparency.

The optical properties of the carbon nitride films were intermediate to those of the hydrogenated and unhydrogenated films. Since these films have a hardness comparable to the hydrogenated films, they do not appear to have any special advantage. However, given the

relatively high deposition rates of these films they may ultimately prove to be the most useful from a commercial point of view; assuming that the adhesion problems can be overcome.

The work on the in-situ ellipsometric monitoring and control of films should be developed further. One area of development would be to increase the robustness of the optimization routines. This would allow for the deposition of more layers and relax the tolerances on the initial guesses of the optical constants. The later property would be useful under conditions where the optical properties were highly dependant on the deposition parameters (i.e. metal coatings).

At this point, the basic characterization of the materials for the infrared protective optical coatings has been established. Therefore the work towards the development of an industrial process should become less scientific and more engineering oriented. The next step should be the deposition of coatings onto specific infrared optical materials such as zinc sulphide; i.e. the creation of a few prototypes. Once this is accomplished, it should be possible to determine the feasibility of a commercial process.

REFERENCES

1 B. Dischler, A. Bubenzer, and P. Koidl, Appl. Phys. Lett. **42**, 636 (1983).

2 L.P Anderson, Thin Solid Films **86**, 193 (1981).

3 M.Ham and K.A.Lou, J. Vac. Sci. Technol. **A8**, 2143 (1990).

4 S.Orzesko, B.N. De, P.G.Snyder, J.A.Woollam, J.J. Pouch and S.A.Alterovitz, J.de Chim. Phys. **84**, 1469 (1987).

5 J.C. Angus and C.C. Hayman, Science **241**, 913 (1988).

6 M.Rubin, C.B.Copper and N.H.Cho, J. Mater. Res. **5**, 2538 (1990).

7 C.B. Collins, F.Davenloo, D.R. Jander, T.J. Lee, H. Park and J.H. You, J. Appl. Phys. **69**, 7862 (1991).

8 S Kumar and T.L. Tansley, Thin Solid Films **256**, 44 (1995).

9 Y. Yongwu; K.A Nelson, F. Adibi, Journal of Materials Research **10**, 41 (1995).

10 P. Koidl, A. Brubenzer, and B. Dischler, Proc. Soc. Photo-Opt. Instrum. Eng. **381**, 186 (1983).

11 G.F. Zhang, L.J. Guo, Z.T. Liu, X.K. Xiu and X. Zheng, J. Appl. Phys. **76**, 705 (1994).

12 F.X. Lu, B.X.Yang, D.G. Cheng, R.Z.Ye, W.X.Yu and J.B.Sun, Thin Solid Films **212**, 220 (1992).

13 A.H. Lettington and G.J. Ball, RSRE Memorandum **3295**, (1981).

14 A.H. Lettington, Proc. Soc. Photo-Opt. Instrum. Eng. **1275**, 14 (1990).

15 H. Nakaue, T. Mitani, H. Kurokawa, T, Yonerawa, and H. Yoshio, Thin Solid Films **212**, 240 (1992).

16 V.I. Polyakov, P.I. Perov, M.G. Ermakov and O.N. Ermakova, V.M. Elinson, and V.V. Sleptsov, Thin Solid Films **212**, 226 (1992).

17 G. Amaratunga, D.Segal, and D. Mackenzie, Appl. Phys. Lett. **59**, 69 (1991).

18 L. Dong, X. Lin, V.P. Dravid, Y.W. Chung, M.Y. Chen, W. Ming-Show and W.D. Sproul, Diamond Films and Technology **4**, 99 (1994).

19 J.T. Cox and G. Hass in *Physics of Thin Films,* Vol **2,** edited by G. Hass and R.E. Thurn, (Academic Press , New York, 1964).

20 H.A. McCleod, *Thin Film Optical Filters,* (Bristol, 2nd ed.,1986).

21 A. Bubenzer, B. Dischler, G. Brandt and P. Koidl, J. Appl. Physics **54**,. 4590 (1983).

22 S.B. White and D.R. Mackenzie, J. Appl. Physics **68**, 3194 (1990).

23 N. Savvides, Thin Solid Films **163**, 13 (1988).

24 B.V. Deryagin and D.V. Fedoseev, J. Cryst. Growth **2**, 380 (1968).

25 J.C. Angus, H.A. Will,W.S. Stanko, J. Appl. Phys. **39**, 2915 (1968).

26 T.Kawato and K.Kondo, Jpn J. Appl. Phys. 26, 1429 (1987).

27 O. Matsumoto, H. Toshima, and Y. Kanzaki, Thin Solid Films **128**, 341 (1985).

28 S.P. Chauhan, J.C. Angus, N.C. Gardener, J. Appl. Phys. **47**, 4746 (1976).

29 S. Aisenberg and R. Chabot, J. Appl. Phys. **42**, 2953 (1971).

30 E.G. Spencer, P.H. Schmidt, D.H. Joy, F.J. Sansalone, Appl. Physics. Lett. **29**, 118 (1976).

31 L. Holland, J. Vac. Sci. Tech. **14**, 5 (1977).

32 A. Friedl, W. Fukarek, W. Moller, A. Koch, Rev.of Sci. Instrum. **65**, 2882 (1994).

33 Y. Catherine, *Diamond and Diamond-like Films and Coatings*, edited by R.E. Clausing, L.L. Horton, J.C. Angus, and P. Koidl (Plenum Press, New York, 1991) p. 193.

34 O. Stenzel, G. Schaarschmidt, F. Wolf, M. Vogel, and T. Wallendorf, Thin Solid Films **203**, 11 (1991).

35 J.P. Hoven, R. Lappalainen, J. Koskinen, A. Anttila, T.R. Jervis and M. Trkula, J. Mater. Res. **5**, 2524 (1990).

36 A. Anders, S. Anders, I.G. Brown, Plasma Sources, Science and Technology **4**, 1 (1995).

37 A. Richter, H.J. Scheibe, W. Pompe, K.W. Brzezinka, and I. Muhling.

38 F. Davenloo, E.M. Juengerman, D.R. Jander, T.J. Lee, and C.B. Collins, J. Mater. Res. **5**, 11 (1990).

39 F. Davenloo, T.J. Lee, D.R. Jander, J.H. You, H. Park, and C.B. Collins, Thin Solid Films **212**, 216 (1992).

40 C.Wyon, R. Gillet and L.Lombard, Thin Solid Films **122**, 203 (1984).

41 H. Tsai and D.B. Bogy, J. Vac. Sci. Technol. **A5**, 3287 (1987).

42 R.R. Parsons in *Thin Film Processes II*, edited by J.L. Vossen and W. Kern, (Academic Press, 1991) Ch. II-3.

43 C.J. Kelly, J.S. Orr, H. Gordan, and L.T. Traub, Proc. Soc. Photo-Opt. Instrum. Eng. **1275**, 122 (1990).

44 R.M.A. Azzam and N.M. Bashara, *Ellipsometry and Polarized Light*, (North-Holland, Amsterdam, 1977).

45 D.E. Aspnes, J.B. Theeten and F. Hottier, Phys. Rev. B **20**, 3292 (1979).

46 B.T. Sullivan and R.R. Parsons, J. Vac. Sci and Tech. **A 4**, 196 (1986).

47 F.W. Smith, J. Appl. Phys. **55**, 764 (1984).

48 P. He, W.A. McGahan, S. Nafis, J.A.Woollam, Z.S. Shan, and S.H. Liou, J. Appl. Phys. **70**, 6044 (1991).

49 D.E. Aspnes and A.A. Studna, Phys. Rev. B **27**, 985 (1983).

50 D.E. Aspnes, S.M. Kelso, R.A.Logan, and R. Bhat, J. Appl. Physics **60**, 754 (1986).

51 V. Chu, M. Fang, and B. Drevillon, J. Appl. Phys. **69**, 3363 (1991).

52 W. Fukarek and H. Kersten, J. Vac. Sci. Technol. **A 12**, 523 (1994).

53 S. Sarvada, M.D. Himel, K.H. Guether and F.K. Urban, Proc. Soc. Photo-Opt. Instrum. Eng **1270**, 133 (1990).

54 P. Houdy, V. Bodart, L. Nevot, D. Corno, B. Pardo, M. Arbaoui, N. Alehyane, R. Barchewitz, Y. Lepetre, and E. Ziegler, Proc. Soc. Photo-Opt. Instrum. Eng. **688**, 122 (1987).

55 G. Herzberg, *Infrared and Raman Spectra*, (Van Nostrand Reinhold Company, New York, 1945) Ch. 3.

56 R.C. Jones, J. Opt Soc. Am. 31, **488** (1941).

57 A. Yariv and P.Yeh, *Optical Waves in Crystals*, (John Wiley and Sons, New York, 1984) Ch. 5.

58 R.M.A. Azzam and N.M. Bashara, *Ellipsometry and Polarized Light*, (North-Holland, Amsterdam, 1977).

59 J.D. Jackson, *Classical Electrodynamics*, (John Wiley and Sons, New York, 1975) pp. 17-22.

60 R.F. Potter in *Handbook of Optical Constants of Solids*, edited by E.D. Palik (Academic Press, 1985) p. 21.

61 J.A. Dobrowolski in *Handbook of Optics*, edited by W.G. Driscoll, (McGraw-Hill Book Co., New York, 1978) Ch. 8.

62 W.D. Westwood, in *Physics of Thin Films*, edited by M.H. Transcombe and J.L. Vossen,. Vol **14** (Academic Press, New York, 1989) p. 1.

63 B. Window and N. Savvides, J.Vac.Sci.Technol. **A 4**, 196 (1986).

64 J.A. Thorton and A.S. Penfield in *Thin Film Processes,* edited. by J.L.Vossen and W.Kern, (Academic Press ,1978) p..80.

65 J.A. Thorton, Ann. Rev. Mater. Sci. **7**, 239 (1977).

66 J.A. Dobrowolski, J.R. Pekelsky, R. Pelletire, M.Ranger, B.T. Sullivan, and A.J.Waldorf, Applied Optics **31**, 3784 (1992).

67 E. Gillam, J. Phys. Chem. Solids **11**, 55 (1959).

68 N. Savvides and B. Window, J.Vac. Sci. Technol. **A 4**, 504 (1986).

69 B. Sullivan, *Spectroscopic Ellipsometry*, Ph.D. Thesis, University of British Columbia (1988).

70 D.E.Aspnes, J. Opt. Soc. Am. **64**, 639 (1974).

71 D.E.Aspnes and A.A.Studna, Appl. Opt. **14**, 220 (1975).

72 P.H. Houdy, Revue Phys. Appl. **23**, 1653 (1988).

73 D.E.Aspnes, Proc. Soc. Photo-Opt. Instrum. Eng. **946**, 84 (1988).

74 Y. Cong, I.An, R.W. Collins, K. Vedam, H.S. Witham, L.J. Pilione and R. Messier, Thin Solid Films **193**, 368 (1990).

75 R.W. Collins, Superlattices and Microstructures **4**, 729 (1988).

76 R.W. Collins, Appl. Phys. Lett. **52**, 2025 (1988).

77 A. Kleinschmidt, *Design of an In-Situ Ellipsometer*, M.A.Sc. Thesis, University of British Columbia (1993).

78 A. Kleinschmidt, G.A. Clarke, N.R. Osbourne, and R.R. Parsons, (Submitted to Applied Optics).

79 D.E. Aspnes, Proc. Soc. Photo-Opt. Instrum. Eng. **276**, 188 (1981).

80 D.E. Aspnes, Am. J. Phys. **50**, 704 (1982).

81 J.D. Jackson, *Classical Electrodynamics*, (Wiley, New York, 1962) Section 4.6.

82 D.E. Aspnes, Thin Solid Films **89**, 249 (1982).

83 H.A. Lorentz, *Theory of Electrons*, 2nd ed. (Teubner, Leipzig, 1916).

84 L. Lorenz, Ann. Phys. Chem. **11**, 70 (1880).

85 D.E. Aspnes, J. Vac. Sci. Tech **18**, 289 (1981).

86 P. Rouard and A. Meessen in *Progress in Optics, Vol. 15*, edited by E.Wolf (North_Holland, Amsterdam, 1977) p. 79.

87 D.A.G. Bruggemen, Ann. Phys. (Leipzig) **24**, 636 (1935).

88 J.C. Maxwell Garnet, Philos. Trans. R. Soc. London **203** , 385 (1904).

89 P.N .Sen, C. Scala, and M.H. Cohen, Geophysics **46**, 781 (1981).

90 D.E. Aspnes and H.G. Craighead, Appl. Opt. **25**, 1299 (1986).

91 O. Wiener, Abh. Math-Phys. K.I. Königl. Sächs. Ges. **32**, 509 (1912).

92 D.E. Aspnes, Phys. Rev. B **33**, 677 (1986).

93 N.W. Ashcroft and N.D. Mermin, *Solid State Physics*, (Holt, Rinehart and Winston, 1976) pp. 16 - 20.

94 J.E. Eldridge and E.D. Palik in *Handbook of Optical Constants of Solids*, edited by E.D.Palik (Academic Press, New York, 1985) p. 777.

95 A.R. Forouhi and I. Bloomer, *Handbook of Optical Constants of Solids* II, edited by E.D.Palik (Academic Press, New York, 1991), p. 151.

96 A.R. Forouhi and I. Bloomer, Phys. Rev. B **34**. 1865 (1988).

97 W.H. Press, S.A. Teukolsky, W.T. Vetterling, B.P. Flannery, *Numerical Recipes in C*, (University Press, Cambridge, 2nd, 1992) p. 685.

98 E.S. Keeping, *Introduction to Statistical Interference* (van Nostrand, Princeton, 1962) Ch. 12.

99 N.B. Colthup, L.H. Daly, S.E. Wiberly, *Introduction to Infrared and Raman Spectroscopy*,3rd. ed. (Boston, Academic Press, 1990).

100 Y. Xie, *The Measurements of the Optical Properties of Diamond-Like Carbon Thin Films By Fourier-Transform Infrared Spectroscopy,* M.Sc. Thesis, University of British Columbia (1994).

101 R.J. Bell, *Introductory Fourier Transform Spectroscopy,* (Academic Press, New York, 1972).

102 O. Stenzil, S. Roth and W. Scharff , Thin Solid Films **190**, 9 (1990).

103 M.Born and E.Wolf, *Principle of Optics,* 5th ed. (Pergamon, Oxford, 1975).

104 M.H. Brodsky, *Amorphous Semiconductors*, (Springer-Verlag, Berlin, 1979).

105 G.A. Clarke and R.R. Parsons, Thin Solid Films **236**, 67 (1993).

106 S.M. Rossnagel, M.A. Russak and J.J. Cuomo, J.Vac.Sci. Technol. **A 5** , 2150 (1987).

107 I.Petrov, V.Orlinov, I.Ivanov, J. Kourtev and J. Jelev, Thin Solid Films **168**, 239 (1989).

108 N. Savvides and B. Window, J. Vac. Sci. Technol **A 4** , 504 (1986).

109 G.A. Clarke, N.R. Osborne and R.R. Parsons, J. Vac. Sci. Technol. **A 9** 1166 (1991).

110 N. Savvides, J. Appl. Phys. **59** 4133 (1986).

111 Semiconductor processing company , 409 E. First St,. Boston, MA USA 02127.

112 Brian Sullivan, Private Communication.

113 J.Ahn and K. L. Mittal, in *Adhesion Measurement of Thin Films, Thick Films and Bulk Coatings* ,edited by K.L. Mittal, (American Society for Testing and Material 1978) pp. 138-149.

114 H .Tsai and D.B. Bogy, J. Vac. Sci. Technol. **A 5**, 3287 (1987).

115 J.A. Thorton, J. Vac. Sci. Technol. **11**, 666 (1974).

116 L.I.Maissel in *Handbook of Thin Filn Technology,* edited by L.I. Maissel and R. Glang (McGraw Hill, 1970) ch 13.

117 B.Chapman, *Glow Discharge Processes* , (Wiley, New York, 1980).

118 J.D. Swift, *Electrical Probes for Plasma Diagnostics*, (London Illife, 1970).

119 J.A. Thorton and A.S. Penfold, in *Thin Film Processes*, edited by J.L. Vossen and W. Kern, (Academic Press, 1978) p. 77.

120 S.A. Alterovitz, N. Savvides, F.W. Smith and J.A. Woollam, in *Handbook of Optical Constants of Solids II* , edited byE.D.Palik, (Acedemic Press, 1991) pp. 837-852.

121 J. Robertson and E.P. O'Reilly , Phys. Rev. B **35**, 2946 (1987).

122 D. Beeman, J. Silverman, R. Lynds and M.R. Anderson, Phys. Rev. B **30**, 870 (1984).

123 J.Tauc in *Optical Properties of Solids*, edited by F.Abeles, (North-Holland, Amsterdam, 1972).

124 J.Tauc, R. Girigorivici and A. Vancu, Phys. Status Solidi **15** 627 (1966).

125 B.T. Sullivan and R.R. Parsons, J. Vac. Sci. Technol. **A 6** 2304 (1988).

126 N. Savvides, Thin Solid Films **163**, 13 (1988).

127 I. Petrov, I. Ivanov, V. Orlinov, J. Kourtev, and J. Jelev, Thin Solid Films **185**, 247 (1990).

128 J. Robertson, Advances in Physics **35**, 317 (1986).

129 N.W. Ashcroft and N.D.Mermin, *Solid State Physics*, (Holt, Rinehart, and Winston, 1976) pp. 175-190.

130 M.A. Tamor and C.H. Wu, J. Appl. Phys. **67**, 1007 (1990).

131 D. Stauffer, *Introduction to Percolation Theory*, (Taylor and Frank, Philadelphia, 1985).

132 G. Galli, R.M. Martin , R. Car and M. Parrinello, Phys. Rev. Lett. **62**, 555 (1989).

133 R. Car and M. Parrinello, Phys. Rev. Lett. **55**, 2471 (1985).

134 Y. Wang, H. Chen, R.W. Hoffman, and J.C.Angus, J. Mater. Res. **5**, 2378 (1990).

135 J. Pluger and J. Fink in *Handbook of Optical Constants of Solids II* , edited byE.D.Palik, (Acedemic Press, 1991) p. 300.

136 S.M. Rossnagel, J. Vac. Sci Technol., **A 7** 205 (1989).

137 C.L. Marquardt, R.T. Williams , and D.J. Nagel, Mater. Res. Soc. Proc. **38**, 325 (1985).

138 G.A. Clarke, Y.Xie, J.E. Eldridge, and R.R. Parsons, (Submitted to Thin Solid Films).

139 E. Pelletier in *Handbook of Optical Constants of Solids II* , edited by E.D.Palik, (Academic Press, 1991) pp. 63-64.

140 *CRC Handbook of Chemistry and Physics,* 74th ed., editor in chief : D.R. Lide, (CRC Press, Boca Raton ,1993-1994) p. 9-123.

141 Takehiko Shimanouchi , *Tables of Molecular Vibrational Frequencies Consolidated Volume I,* Secretary of Commerce (1972).

142 M.A. Tamor, C.H. Wu, R.O. Carter and N.E. Lindsay, Appl. Phys. Lett. **55**, 1388 (1989).

143 S.Craig and G.L. Harding, Thin Solid Films **97**, 345 (1982).

144 M. Pinarbasi, N. Maley, M.J. Kushner, A Myers, J.R. Abelson and J.A. Thorton, J. Vac. Sci. Technol. **A 7**, 1215 (1989).

145 J.C. Angus and F. Jansen, J. Vac. Sci. Technol., **A 6** 1780 (1988).

146 S.Caplan, F..Jansen and M. Machonkin, Appl. Phys. Lett. **47**, 750 (1985).

147 N. Cho, J. Mater. Res. **5**, 2543 (1990).

148 J. Ullmann, G. Schmidt and A. Scharff, Thin Solid Films **214**, 35 (1992).

149 J.J. Coumo, J.P. Doyle, J. Braley, J.C. Liu, Applied Physics Lett. **58**, 466 (1991).

150 S. Kaplan and A. Dilks, J. Appl. Polym. Sci. **38**, 105 (1984).

151 R.S. Yalamanchi and G.K.M. Thutpalli, Thin Solid Films **164**, 103 (1988).

152 B. Dischler, A. Bubenzer, and P. Koidl, Solid State Commun. **48**, 105 (1984)

153 M.A Tamor, C.H. Wu, R.O. Carter and N.E. Lindsay, Appl. Phys. Lett. **55**, 1388 (1989).

154 A.Y.Liu and M.L. Cohen, Phys. Rev. B **41**, 10727 (1990).

155 C.J. Torn, J.M. Siversten, J.H.Judyand, and C.Chang, J. Mater. Res. **8**, 480 (1993).

156 M.Y.Chen, D.Lin, X.Lin, V.P.Dravid, Y.W.Chung, M.S. Wong and W.D. Sproul, J.Vac.Sci. and Technol. **A 11**, 521 (1993).

157 F. Fujimoto and K. Ogata, Jpn. J. Appl. Phys. **32**, L 420 (1993).

158 Y.Y. Tu, T.J. Chuang, and H.F. Winters, Phys. Rev. B **23**, 8223 (1981).

159 F.L. Friere, C.A. Achete, G. Mariotto, and R. Canteri, J. Vac. Sci. Technol. **A 12**, 3048 (1994).

160 R. F. Potter in *Handbook of Optical Constants of Solids II* , edited by E.D.Palik, (Academic Press, 1985) pp. 465-469.

161 Melles Groit *Optics Guide 5*, (1990) section 11.

162 C.J. Kelly, J.S. Orr, H. Gordan, L.T. Traub, and A.H. Lettington, Proc. Soc. Photo. Opt. Eng. **1275**, 122 (1990).

163 D.C. Booth and J.J. Voss, J. Phys. (Paris), Colloqu. **42**, Cy_1033 (1981).

164 R.E. Sah, Ch. Wild, P.Koidl, Proc. Soc. Photo-Opt. Instrum. Eng. **1275**, 59 (1990).

165 J. Tyczkowski and P. Kazimierski, J. Phys. D **27**, 179 (1994).

166 A.H. Lettington, J.C. Lewis, C.J.H.Wort, B.C. Monachan, and A.J.N. Hope,. European Mat. Res. Soc. Proceedings **17**, 469 (1987).

167 E. Gilliam, J. Phys. Chem. Solids **11**, 55 (1959).

168 L.Nevot, B. Pardo, and J. Corno, Revue Phs. Appl. **23**, 1675 (1988).

169 M.S.Aouadi, *Characterization of Inconel-Carbon Multilayer Mirrors For 45 Angstrom Wavelength, Ph.D Thesis*, University of British Columbia (1994).

170 D.E. Savage, N. Schimke, Y.H. Phang, and M.G. Lagally, J. Appl. Phys. **71**, 3238 (1992).

171 P.Boher, P. Houdy, and C.Schiller, J. Appl. Phys. **68**, 6133 (1990).

172 P.Boher, P. Houdy, and C.Schiller, Thin Solid Films **175**, 161 (1989).

173 W.A. McGahan, B. Johs and J.Woollam, Thin Solid Films **234**,443 (1993).

174 E.T. Arakawa, M.W. Williams, and T. Inagaki, J. Appl. Phys. **48**, 3167 (1977).

175 M.A. Tamor, J.A. Haire, C.H. Wu and K.C. Haas, Appl. Phys. Lett. **54**, 9 (1994).

176 B.T. Sullivan and J.A. Dobrowolski, Appl. Opt. **31**, 3821 (1992).

177 H.Schiecker, K.H.Hammann, U.Schnieder, Proc. Soc. Photo-Opt. Instrum. Eng. **1012**, (1988).

178 I. Wu, J.B. Dottellis, M. Dagenais, J.Vac.Sci.Tech. **A 11**, 2398 (1993).

179 M.Yamamoto and Y.Namioka, Appl. Opt. **31**, 1612 (1992).

180 J.A. Thorton and A.S.Penfold in *Thin Film Processes,* edited by J.L.Vossen and W.Kern (Academic Press, New York 1978), pp.107 -109.

181 R.R. Parsons in *Thin Film Process II*, edited by J.L.Vossen and W. Kern. (Academic Press, New York 1991) p. 185.

182 M.M. Yang, J. of Appl. Phys. **62**, 1035 (1987).

183 W.Fukarek and H. Kersten, J.Vac.Sci. Technol. **A 12**, 523 (1994).

184 G. Este and W.D. Westwood, J. Vac. Sci. Technol. **A 6**, 1845 (1988).

185 D.Charlot and A.A.Maruani, Appl. Optics **24**, 3368 (1985).

186 M.S.A. Yousef and A.R.M. Zaghloul, J. of the Optical Society of America **A 6**, 355 (1989).

187 J.D. Paliouras and D.S. Meadows, *Complex Variables for Scientests and Engineers,* 2nd ed. (Macmillan Publishing Company, New York, 1990) Ch. 9.

188 H.A.Macleod, *Thin -Film Optical Filters* , 2nd edition , (Adam Hilger Ltd, Bristol, 1986) pp. 238-257.

189 S.M. Rossnagel, J. Vac. Sci. Tech. **A 6**, 3049 (1988).

190 A.A. Studna, D.E. Aspnes, L.T. Florez, B.J. Wilkens, J.P. Harbison, and R.E.Ryan, J. Vac. Sci. Technol. **A 7**, 3291 (1989).

191 G.N. Maracus, J.L. Edwards, K.Shiralagi, K.Y. Choi, R. Droopad, B. Johs and J.A.Woollam, J. Vac. Sci. Technol. **A 10**, 1832 (1992).

192 M.Yamamoto and T. Namioka, Appl. Opt. **31**, 1612 (1992).

193 S. Sarvada, M.D. Himel, K.H. Guether and F.K. Urban, Proc. Soc. Photo-Opt. Instrum. Eng. **1270**, 133 (1990).

194 D.E. Aspnes, J. of the Opt. Soc. Am. **A 10**, 974 (1993).

195 P.S. Hauge, Surf. Sci. **56**, 148 (1976).

196 P.S. Hauge and F.H. Dill, Optical Communications **14**, 431 (1975).

IN-SITU ELLIPSOMETER ALIGNMENT AND CALIBRATION

A.1 Alignment and Calibration

For a rotating compensator ellipsometer the light intensity incident upon the photodetector can be written as[195]

$$I(t) = I_o(1 + a_2 \cdot \cos 2\omega_c t + b_2 \cdot \sin 2\omega_c t + a_4 \cdot \cos 4\omega_c t + b_4 \cdot \sin 4\omega_c t), \qquad \textbf{(A.1)}$$

where ω_c is the frequency of rotation of the compensator and I_o the dc intensity. The harmonic coefficients can be written in terms of the anaylzer angle A and compensator defect parameters, q,r and s through the relations:[196]

$$a_2 = \frac{-2r(\nu \tan\Delta)\sin 2A + 2s(\cos 2A + \mu)}{2 + q(\nu \sin 2A + \mu \cos 2A)} \qquad \textbf{(A.2a)}$$

$$b_2 = \frac{2r(\nu \tan\Delta)\cos 2A + 2s(\sin 2A + \nu)}{2 + q(\nu \sin 2A + \mu \cos 2A)}, \qquad \textbf{(A.2b)}$$

$$a_4 = \frac{(2-q)(\mu \cos 2A - \nu \sin 2A)}{2 + q(\nu \sin 2A + \mu \cos 2A)}, \qquad \textbf{(A.2c)}$$

$$b_4 = \frac{(2-q)(\mu \sin 2A + \nu \cos 2A)}{2 + q(\nu \sin 2A + \mu \cos 2A)}, \qquad \textbf{(A.2d)}$$

where

$$\mu = \frac{\cos 2P - \cos 2\psi}{1 - \cos 2P \cos 2\psi}, \tag{A.3a}$$

$$\nu = \frac{\sin 2P \cdot \sin 2\psi \cdot \cos\Delta}{1 - \cos 2P \cdot \cos 2\psi}, \tag{A.3b}$$

and where P is the polarizer angle and ψ and Δ the ellipsometric parameters.

The calibration routine used in this thesis requires a metallic sample. In this case linearly polarized light will have its polarization preserved upon reflection if and only if it is aligned to the p or s axis. Under these circumstances the paramenters $(\mu,\upsilon) = (\pm 1,0)$ and the magnitude of the coeffiecents can be written as

$$\sqrt{a_2^2 + b_2^2} = \frac{4s^2(1 + 2\mu + \mu^2)}{(2 + q\mu\cos 2A)^2}, \tag{A.4a}$$

$$\sqrt{a_4^2 + b_4^2} = \frac{(2-q)^2\mu^2}{(2 + q\mu\cos 2A)^2}. \tag{A.4b}$$

The calibration routine is then as follows. The polarizer is first aligned to the p-axis where the magnitude of the second harmonic is at a minimum and equal to zero. Next the analyzer is aligned to the s-axis where the magnitude of the fourth harmonic is at a maximum and ideally equal to one. The minimum in the second harmonic is sharp and can be found simply by searching for it. The maximum in the fourth is broad and a quadratic fit is applied to data points about the maxiumum.

Once the polaizer and analyzer angles have been determined the compensator extraordinary axis must be calibrated. This is detemined by adjusting the compensator axis until $b_4 = 0$.

A.2 Window Corrections

The inclusion of vacuum port windows causes complications due to the stess birefrengence in the window material. If this factor is assumed to be small the Jones matrix of each window in the sample p and s axis orientation is given as

$$T_w = \begin{bmatrix} 1+i\alpha & i\beta \\ i\beta & 1-i\alpha \end{bmatrix}, \tag{A.5}$$

where α and β represent first order effects. As the sample itself can be represented as

$$S = \begin{bmatrix} \rho_s & 0 \\ 0 & 1 \end{bmatrix}, \tag{A.6}$$

the combined window sample system is written as

$$S' = T_{wout} \cdot S \cdot T_{win} , \tag{A.7}$$

To the first order , equation A.7 can be written in matrix form as

$$S' = \begin{bmatrix} \rho \cdot (1+i\alpha) & i \cdot (\rho_s \cdot \beta_i + \beta_o) \\ i \cdot (\rho_s \cdot \beta_o + \beta_i) & (1-i\alpha) \end{bmatrix}. \tag{A.8}$$

In Eq. A.8, β_i and β_o represent the terms for the input and output windows respectivily and α is equal to $\alpha_i + \alpha_o$. Through the use of a bilinear transformation, the exit polarization χ_{so} can be written as

$$\chi_{so} = \frac{(1-i\alpha)\cdot\chi_{si} + i\cdot(\rho_s\beta_o + \beta_i)}{i(\rho_s\beta_i + \beta_o)\cdot\chi_{si} + \rho_s(1+i\alpha)}, \tag{A.9}$$

where

$$\chi_{s'i} = \operatorname{Tan} P. \tag{A.10}$$

By expanding and retaining terms to the first order the actual complex reflectance ratio can be written as

$$\rho_s = -i\beta_o\chi_{si} + \rho_s' + i(\beta_i/\chi_{si} - \beta_i\chi_{si} - 2\alpha)\cdot\rho_s' + i(\beta_o/\chi_{si})\cdot\rho_s'^2, \tag{A.11}$$

where ρ_s' is the measured complex reflectance ratio. If the polarizer is aligned to 45° then the above equation can be simplified to

$$\rho_s = \rho_s' - i\beta_o - 2i\alpha\cdot\rho_s' + i\beta_o\cdot\rho_{si}'^2. \tag{A.12}$$

The presence of the windows can also affect the calibration results . To illustrate this, consider the case where the polarizer angle is close to zero. Under these circumstances equation A.9 can be written as

$$\chi_{so} = \frac{\rho_s P + i\rho_s\beta_i + i\beta_o}{1-i\alpha}, \tag{A.13}$$

which, to the first order, can be simplified to

$$\chi'_{so} = \rho_{sr}P + \rho_{si}\beta_i + i(\rho_{si}P + \rho_{sr}\beta_i + \beta_o). \tag{A.14}$$

For light with its major axis close to the s-axis and which is only slightly elliptically polarized Eq. 2.4 can be writen as

$$\chi = \theta + i\varepsilon. \tag{A.15}$$

Therefore Eq. A.15 can be represented through

$$\theta = \rho_{sr} \cdot (P - P_o) - \rho_{si}\beta_i\,, \tag{A.16a}$$

$$\varepsilon = \rho_{si} \cdot (P - P_o) + \beta_i\rho_{sr} + \beta_o\,. \tag{A.16b}$$

Therefore, as one searches for a zero in Eq. A.4a the calibration routine will give improper angles for A and P. The angles will deviate from the actual angles A_o and P_o by the amounts

$$A - A_o = \rho_{sr} \cdot (P - P_o) - \rho_{si}\beta_i\,, \tag{A.17a}$$

$$0 = \rho_{si} \cdot (P - P_o) + \beta_i\rho_{sr} + \beta_o\,. \tag{A.17b}$$

As the above equations are sample dependant the system can still be calibrated through a suitable choice of two different substrates. If the difference in the complex reflectance ratios is large, then one does not need to be able to measure these values to a great deal of precision and the system can be calibrated through solving the following matrix:

$$\begin{bmatrix} -\rho_{s1i} & 0 & \rho_{s1r} & 1 \\ -\rho_{s1r} & 1 & -\rho_{s1i} & 0 \\ -\rho_{s2i} & 0 & \rho_{s2r} & 1 \\ -\rho_{s2r} & 1 & -\rho_{s2i} & 0 \end{bmatrix} \bullet \begin{bmatrix} P_o \\ A_o \\ \beta_i \\ \beta_o \end{bmatrix} = \begin{bmatrix} -\rho_{s1i} P_1 \\ A_1 - \rho_{s1r} P_1 \\ -\rho_{s2i} P_2 \\ A_2 - \rho_{s2r} P_2 \end{bmatrix} \qquad \textbf{(A.18)}$$

This procedure also solves for β.